

---

# METIS Science Case (FDR)

---

E-REP-ETH-MET-1014

2-0

04-09-2022

Work package: 1.5

Signature and Approval			
	Name	Date	Signature
Prepared	Sascha Quanz & MST	04-09-2022	
Checked	MST	In Polarion	
Approved	B. Brandl, F. Bettonvil	In Polarion	
Released	F. Bettonvil	In Polarion	

## TABLE OF CONTENTS

<b>1</b>	<b>Introduction and scope of the document</b>	<b>5</b>
<b>2</b>	<b>Protoplanetary disks and planet formation</b>	<b>7</b>
2.1	Scientific background and context . . . . .	7
2.2	The physical structure and evolution of protoplanetary disks . . . . .	8
2.2.1	Gas-dust dynamics and planet formation . . . . .	8
2.2.2	Kinematic imaging of gas in planet-forming regions . . . . .	11
2.2.3	Disk winds . . . . .	13
2.2.4	Probing planet formation in early evolutionary phases . . . . .	14
2.3	Signatures of protoplanets . . . . .	14
2.3.1	Continuum detections of forming protoplanets . . . . .	15
2.3.2	Kinematic detections of planets . . . . .	16
2.3.3	Kinematic signatures of circumplanetary disks . . . . .	17
2.4	The chemical composition and evolution of planet-forming material . . . . .	19
2.4.1	Water and organics in the innermost disk . . . . .	19
2.4.2	Imaging of the water ice distribution in disks and resolving the snowline . . . . .	20
2.4.3	Delineating the CO and H <sub>2</sub> O snowlines in edge-on disks . . . . .	21
2.4.4	Isotopic fractionation as a probe of early solar system formation . . . . .	22
2.4.5	Distribution of PAHs and related carbonaceous species . . . . .	23
2.4.6	Crystallization of silicates: when and where? . . . . .	24
2.5	Debris disks around nearby main-sequence stars . . . . .	26
2.5.1	Terrestrial planet formation in warm debris disks . . . . .	26
2.5.2	Exozodiacal dust . . . . .	27
<b>3</b>	<b>Detection and characterization of extrasolar planets</b>	<b>30</b>
3.1	Scientific context . . . . .	30
3.1.1	Planet characterization . . . . .	30
3.1.2	Ground-based techniques . . . . .	31
3.1.3	The power of METIS . . . . .	32
3.2	Planetary demographics . . . . .	32
3.2.1	Direct detection of known gas giant planets . . . . .	33
3.2.2	The occurrence rate of long period gas giant planets . . . . .	36
3.3	Atmospheric properties and climates . . . . .	37
3.3.1	Short-period planets . . . . .	37
3.3.2	Long-period planets . . . . .	39
3.4	Towards other Earths . . . . .	40
<b>4</b>	<b>The formation history of the Solar System</b>	<b>44</b>
4.1	Scientific background and context . . . . .	44
4.2	Scientific Goals . . . . .	44

4.3	Composition and temperature profile and isotopic ratios in the formation disk . . . . .	44
4.4	Large-scale radial mixing of disk material . . . . .	46
4.5	Ice and organics composition of Kuiper Belt objects . . . . .	47
4.6	Thermal inertia and the internal constitution of minor bodies . . . . .	48
4.7	Trace species in the atmosphere of Uranus and Neptune . . . . .	50
4.8	Giant planets as systems . . . . .	51
4.9	The Martian atmosphere . . . . .	53
<b>5</b>	<b>Massive stars and cluster formation</b>	<b>56</b>
5.1	Scientific background and context . . . . .	56
5.2	Science cases . . . . .	56
5.2.1	Cluster formation and the universality of the IMF . . . . .	56
5.2.2	Mapping the immediate environs around massive YSOs . . . . .	58
5.2.3	Physical conditions in the massive YSOs . . . . .	59
5.2.4	Accretion disks around massive YSOs . . . . .	61
<b>6</b>	<b>Evolved stars and their circumstellar environment</b>	<b>62</b>
6.1	Scientific background and context . . . . .	62
6.2	Scientific Goals . . . . .	64
6.2.1	Molecular envelopes of evolved stars . . . . .	64
6.2.2	Dust Structure around evolved stars . . . . .	65
6.2.3	Protoplanetary disk physics around evolved stars: second generation of planets? . . . . .	66
6.3	Gas producing agents in galaxies . . . . .	70
<b>7</b>	<b>The Galactic Center</b>	<b>71</b>
7.1	Introduction and Scientific Background . . . . .	71
7.2	Scientific Goals . . . . .	71
7.3	A Representative Observing Program . . . . .	74
7.3.1	YSO Candidates in the central stellar cluster . . . . .	74
7.3.2	The Nature of Thin Dust Filaments . . . . .	75
7.3.3	Low Luminosity Bow-Shock Sources in the Central Stellar Cluster . . . . .	77
7.3.4	Absorption Line Studies . . . . .	78
7.3.5	The Super-Massive Black Hole . . . . .	78
7.3.6	Comparison with other facilities . . . . .	81
<b>8</b>	<b>The physics of galaxies</b>	<b>82</b>
8.1	Scientific background and context . . . . .	82
8.2	Massive star cluster formation . . . . .	82
8.3	Nuclear star formation . . . . .	84
<b>9</b>	<b>Active Galactic Nuclei</b>	<b>86</b>
9.1	Scientific background and context . . . . .	86
9.2	High-resolution imaging of the AGN “torus” region . . . . .	88

9.3	Black hole masses in nearby obscured AGNs . . . . .	94
9.4	A representative AGN observing program for METIS . . . . .	95
<b>A</b>	<b>APPENDIX: METIS observing modes</b>	<b>97</b>

## 1 INTRODUCTION AND SCOPE OF THE DOCUMENT

The ‘Mid-infrared ELT Imager and Spectrograph’ (METIS) covers the thermal/mid-infrared wavelength range ( $\approx 3 - 13 \mu\text{m}$ ) on the ELT. Focusing on highest angular resolution and high spectral resolution, METIS will provide outstanding observing capabilities, which are complementary to ALMA, MATISSE, JWST and the other ELT instruments. It is obvious that the ELT will open up new parameter spaces for optical/infrared astronomy and enable observations in the thermal/mid-IR range, which have never been possible before. While being a general-purpose science instruments serving a wide range of science cases (cf. Figure 1-1), METIS is expected to excel in particular in research related to circumstellar disks and extrasolar planets. These are the two science themes that mainly drive the science and technical requirements. In particular enabling state-of-the-art high-contrast exoplanet imaging in the L, M and N bands and the related requirements on the achievable contrast performance are technically challenging and led, to some extent, to an increase in instrument complexity that was not foreseen in Phase A. Still, as further detailed below, the scientific prospects of doing mid-infrared exoplanet science with a 39-m telescope more than justify the extra efforts - at least from a scientific perspective.

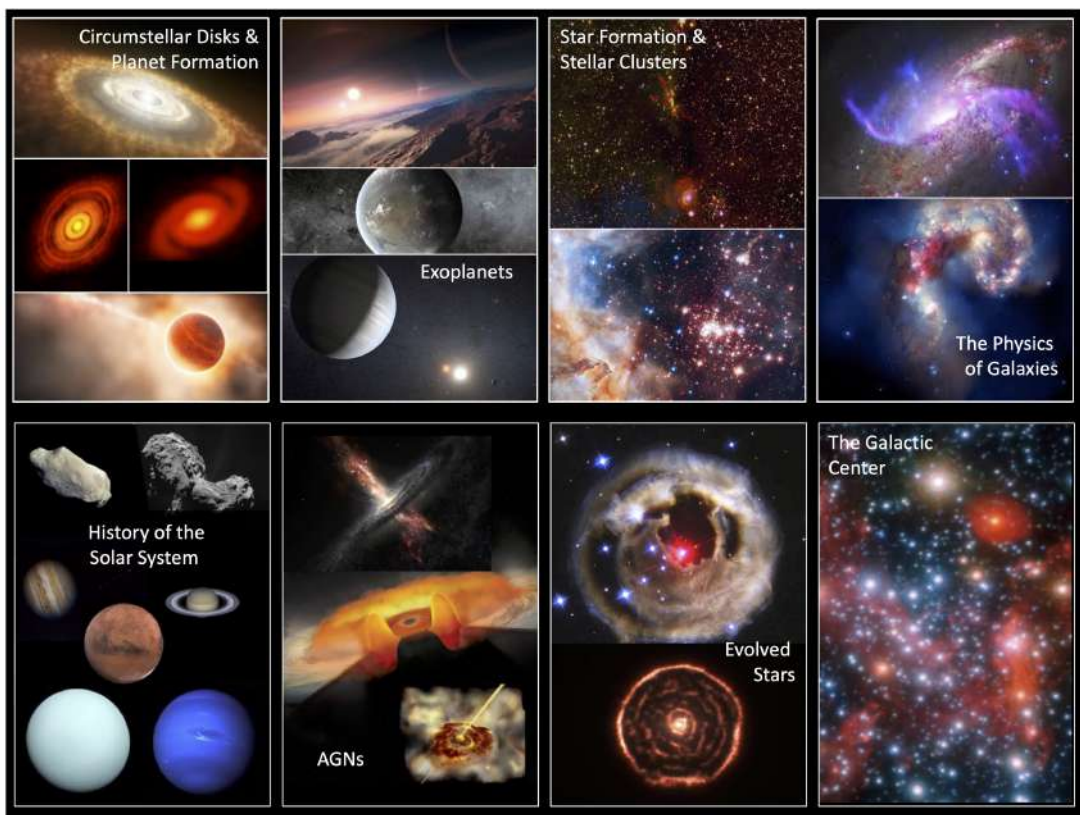


**Figure 1-1:** Overview of key areas of METIS science spanning from Solar System research over galactic sources to extragalactic targets. Circumstellar disks, i.e., the formation sites of planets, as well as exoplanet detection and characterization are the driving science themes.

METIS’ unique contributions to astrophysics in the late 2020s and 2030s will likely be in science areas where high spatial or high spectral resolution, or a combination of both, is crucial. The METIS science case, as conceived around the time of FDR, covers the following science topics:

- Protoplanetary disks and the formation of planets
- Detection and characterization of exoplanets<sup>1</sup>

<sup>1</sup>Some of the science cases discussed for exoplanets are also applicable to Brown Dwarfs (as an extension towards more massive objects); hence, there is no dedicated section on Brown Dwarfs.

- The formation history of the Solar System
- Massive stars and cluster formation
- Evolved stars and their circumstellar environment
- The galactic center
- Physics of galaxies
- Active galactic nuclei

While not all science topics are likely to use all observing modes in equal amounts, prioritizing observing modes by expected scientific benefit is a non-trivial task in the case of METIS. It is exactly its versatility, coupled with the diffraction limited performance, that makes this instrument so powerful and attractive for science questions ranging from Solar System science to distant AGNs and galaxies. While powerful for bright targets, which certainly represent the majority of typical METIS targets, the brightness constraints for the guide stars of the SCAO system do represent a natural limit for METIS' discovery space. In particular Solar System science, massive stars and cluster formation as well as extragalactic science would benefit significantly from the addition of a laser-supported AO-system and increase the number of potential targets.

The objective of this document is to demonstrate both the unique capabilities of METIS in some science areas leading to breakthrough results and a significant advancement of the research field and – at the same time – the breadth of the science that METIS will be able to support covering a wide range of science topics. The instrument performance and capabilities, on which the science cases described in the following sections are based, reflect the instruments baseline as conceived at FDR<sup>2</sup> and in Appendix A we provide for completeness an overview of METIS' observing modes. However, this document does not provide an overview of the technical specifications, the instrument baseline or the derivation of the science requirements for METIS and the reader is referred to other documents for these information.

<sup>2</sup>We note specifically that a laser-supported AO system is not part of the instrument baseline.

## 2 PROTOPLANETARY DISKS AND PLANET FORMATION

### 2.1 Scientific background and context

One of the most surprising findings in exoplanet research is the great diversity of exoplanetary systems, many of which bear little resemblance to our own Solar System. The Kepler satellite has revealed that at least 20% of Sun-like stars have Neptune-sized planets within 0.5 AU (Borucki et al. 2011; Winn & Fabrycky 2015), and many more planets are likely waiting to be discovered by operating and future missions (e.g., TESS, CHEOPS, JWST, PLATO, Roman Space Telescope). The implication of the exoplanet statistics is that essentially every disk around a young star must be forming planets. As our knowledge of exoplanetary properties expands, it becomes increasingly important to understand how planetary architectures depend on initial conditions by observing the evolution of protoplanetary disks. Many (most) of the currently detected planets are also found in close proximity to their host star (< 1 AU) which puts a premium on exploring small angular scales in disk systems that capture the early gas-rich stages of planet formation.

The origin of the diversity of exoplanetary systems must lie in the structure and evolution of the disks out of which they form. The gas and solid components in these disks are inextricably connected and both are key players in the planet formation process. The gas controls the dynamics of dust particles and planetesimal growth, provides the main reservoir of material out of which giant planets form, and enables the migration of planets in the disk (both inwards and outwards) (Armitage 2011; Kley & Nelson 2012; Birnstiel et al. 2016). The solid component forms the basis for pebbles, planetesimals, large planetary cores – required for the formation of giant planets by core accretion (Johansen & Lambrechts 2017) – and rocky planets. Because condensable volatiles, such as water, contribute roughly half of the mass available for planetesimal formation, the phase change and transport/concentration processes of both ices and gases are a central part of planet formation (Ciesla & Cuzzi 2006; Öberg & Bergin 2021; van Dishoeck et al. 2021). It is therefore critical to develop efficient observational tracers of both the solid and gaseous phases of protoplanetary disks on all scales from 0.1 to 100 AU.

Many of the directly imaged planets to date are gaseous Jupiter-like planets, which are thought to form within 1–10 Myr after the formation of the parent star (Pollack et al. 1996; Dawson & Johnson 2018). In the standard core-accretion model, a few rocky cores with masses of 10-20 Earth masses must have formed quickly enough to attract gas to form a gas-rich planet. Over time – at most 20 Myr – the gas in the disk will dissipate and the small grains will coagulate or be blown away. This leads to the debris disk phase in which the disk is optically thin at all wavelengths and the grains are of secondary origin, replenished by collisions of larger objects: asteroid-sized bodies or planetesimals (Wyatt 2008). Rocky planet embryos and planets with masses comparable to those of the Moon or Earth can form by more gradual accretion of these planetesimals during the debris disk stage (Lissauer 1993; Morbidelli et al. 2012), or perhaps by accretion of pebbles in earlier phases (Johansen et al. 2021).

Gas-rich disks around Herbig Ae/Be stars (with ages of 1–5 Myr) are thought to be the immediate progenitors of the classical debris disks around A-type stars, like those around Vega (A0V, ~100 Myr),  $\beta$  Pic (A5V, ~20 Myr) or Fomalhaut (A3V, ~100 Myr). But many more debris disks have now been detected thanks to *Spitzer* and *Herschel*, also around lower mass stars (Matthews et al. 2014; Hughes et al. 2018; Michel et al. 2021). Moreover, transitional disks with large inner dust cavities, which may be the sites of currently forming giant planets, are found around stars from M to A type (van der Marel et al. 2018; van der Marel & Mulders 2021). The protoplanetary disk phase, the transition from gas-rich to gas-poor disks, and the debris disk phases are therefore key pivotal periods during which active planet-formation can be observed across the full mass range of stars.

There are several recent lines of evidence that suggest that planet formation starts at even earlier stages than previously expected. This is demonstrated powerfully by the ALMA detection of gaps in the actively accreting Class I-II HL Tau disk (ALMA Partnership et al. 2015). Such gaps are now also detected in other young gas-rich protoplanetary systems (Fedele et al. 2018; Andrews 2020) and they appear to be common.

Further evidence of significant grain growth in an embedded Class I disk (Harsono et al. 2018) as well as the fact that only embedded Class 0 and I disks have enough solid material to build planetary systems with gas giant planets supports this view (Manara et al. 2018; Tychoniec et al. 2020). More broadly the carbon-poor nature of terrestrial worlds in our solar system also appears to require early formation of the feedstock material of terrestrial planets (Li et al. 2021).

A key science case for METIS is therefore to leverage the high spatial and spectral resolution of the ELT to observe, and image, disk structures as well as the process of planet formation, in the primary planet-forming regions from 0.1–10 AU, at all evolutionary stages, from the embedded phase through the protoplanetary disk phase well into the debris disk phase. Specifically, METIS will have the potential to transform our understanding in five areas:

1. Observe the physical evolution of planet-forming material. This includes imaging the distribution of small grains (a few microns) for direct comparison with large grains (millimetre to centimetre) observed by ALMA, measuring the gas kinematics and amount of warm molecular gas down to 0.1 AU scales in disks (using spectro-astrometric techniques), and quantifying molecular disk winds that affect disk evolution and dissipation.
2. Search for protoplanets embedded in gas-rich disks, either by direct imaging, through their kinematics reflecting dynamical interactions with gas and dust, or through their effects on local disk material (i.e., carving gaps in gas which can be traced in molecular emission line profiles). This includes a search for molecular and atomic emission from circumplanetary disks around Jupiter-mass protoplanets. The physical properties of protoplanets can be directly compared to exoplanet demographics.
3. Measure the chemical composition of planet-forming gas and dust inside of 10 AU. This includes measuring the composition and distribution of warm molecular gas (organics, water) and PAHs in the innermost disk, observations of ices in scattered light and absorption, as well as the crystallinity and composition of small dust grains on 1-10 AU scales.
4. Image warm dust belts in nearby debris disks to determine their properties and radial distribution. This may reveal ongoing terrestrial planet formation and constrain models of the Earth's origin.
5. Search for and image exozodiacal systems around nearby main-sequence stars to determine their demographics in comparison to those of exoplanets.

To achieve these objectives, METIS' unique combination of high spatial and spectral resolution will be crucial: a slice width of 18.3 milli-arcsec at  $4.7\text{ }\mu\text{m}$  with the LMS corresponds to radii of around 1–2 AU in protoplanetary disks in the nearest star-forming regions (e.g., Ophiuchus, Chamaeleon or Lupus). The highest spectral resolution offered by METIS ( $R \sim 100,000$  in the L and M bands) matches the Keplerian velocity in a disk around a  $0.3\text{ }M_{\odot}$  star at 10 AU and can be used via spectro-astrometric techniques to probe gas emission and structure inside of 1 AU. The high spectral resolution is therefore needed to obtain kinematic information at the angular scales spatially resolved by the ELT 39 m aperture.

## 2.2 The physical structure and evolution of protoplanetary disks

### 2.2.1 Gas-dust dynamics and planet formation

METIS will image the thermal emission from micron-sized dust in protoplanetary disks, revealing inner holes and gaps, inner edges of dust walls as well as “hot spots” produced by local heating, all of which are diagnostics of the planet formation process (e.g., Liu et al. 2003; Currie et al. 2022). Recent scattered light studies at near-IR wavelengths tracing small sub-micron sized dust grains are imaging the surface layers of disks down to 10–20 AU. With the advent of VLT-SPHERE, not only the brightest disks around A-type stars are probed but also the T Tauri star disks (e.g., Stolker et al. 2016; Avenhaus et al. 2018; Benisty et al.

2022). These small grains may be present in regions where large mm-sized grains, imaged by ALMA, appear to be missing (Muto et al. 2012; Pinilla et al. 2018). This demonstrates that small dust particles, which are coupled to the gas, filtrate through the gap edge, while larger millimetre to centimetre-sized grains are trapped at larger radii (Garufi et al. 2013; Pinilla et al. 2016).

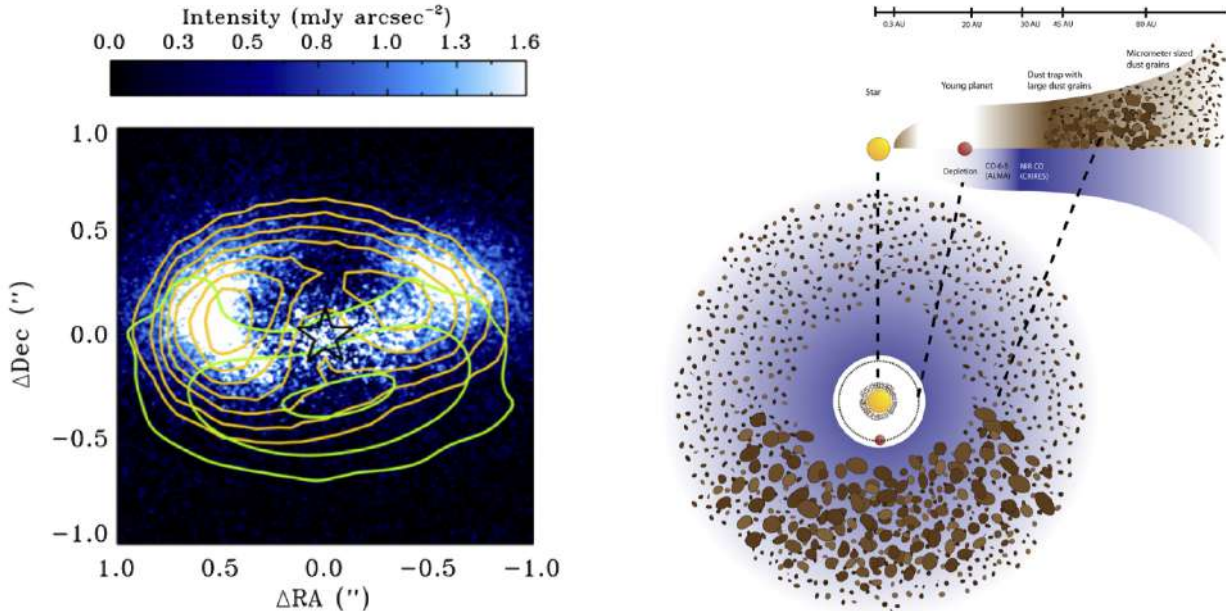


**Figure 2-1:** Left: VLT-VISIR image at 18 micron (orange contours) compared with ALMA 0.85 mm image (green contours) of the Oph IRS 48 transitional disk. The disk has an inclination of  $\sim 50^\circ$  and a  $\sim 60$  AU radius gap. The underlying image is of polarized light at near-infrared wavelengths (Follette et al. 2015). The mm-sized grains seen by ALMA are trapped on one side of the disk whereas the micron-sized grains are spread over the full ring. Such asymmetric dust traps can be caused by gas pressure bumps, likely induced by planets inside the disk (see cartoon on the right). For IRS 48, a  $10\text{-}20 M_{\text{Jupiter}}$  companion located at 20 AU has been suggested (van der Marel et al. 2013). METIS will open up such multi-wavelength studies to a much larger sample of disks.

In addition to radial differences, azimuthal asymmetries of the small and large dust grains have been found. A spectacular example is the IRS 48 disk where the ALMA images reveal a strong azimuthal concentration of mm-sized dust (more than a 100-fold increase in surface density), while the VISIR  $18 \mu\text{m}$  image shows a more complete ring of smaller dust grains (van der Marel et al. 2013) (Figure 2-1). Both radial and azimuthal asymmetries may be due to dust traps formed by the pressure-driven transport of solids in pressure maxima (Birnstiel et al. 2013); ALMA shows that these substructures are common (van der Marel et al. 2021). Within such dust traps, destructive collisions are diminished and small grains can grow rapidly to pebbles, rocks and planetesimals to form the seeds for the next generation of planets. However, while dust-trapping pressure-maxima may be induced by perturbing planets, they may also be the result of other processes such as zonal flows or pressure bumps at the edges of dead zones. It is the *combination* of images at near-infrared, mid-infrared and sub-millimeter wavelengths, mapping the relative spatial distribution of dust grains of different sizes, that is needed to distinguish between disk-sculpting mechanisms (Lyra & Klahr 2011; Rosotti et al. 2016; Pinilla & Youdin 2017).

Figure 2-2 shows simulated METIS N-band and ALMA 0.85 mm images of a disk with embedded planets of varying mass. The images result from full hydrodynamic calculations, including a prescription for dust evolution and dynamics (de Juan Ovelar et al. 2013). The separation between the micron- and mm-sized dust grains is very sensitive to the mass of the (unseen) embedded planet (Facchini et al. 2018), and can be readily imaged by METIS for planets located at  $\sim 5$  AU or larger, the disk region where most giant planets are expected to form.

Similarly, the disk viscosity is a fundamental parameter governing many aspects of disk evolution, including the magnitude of local turbulence and dynamical time scales. Images of the location and sharpness of

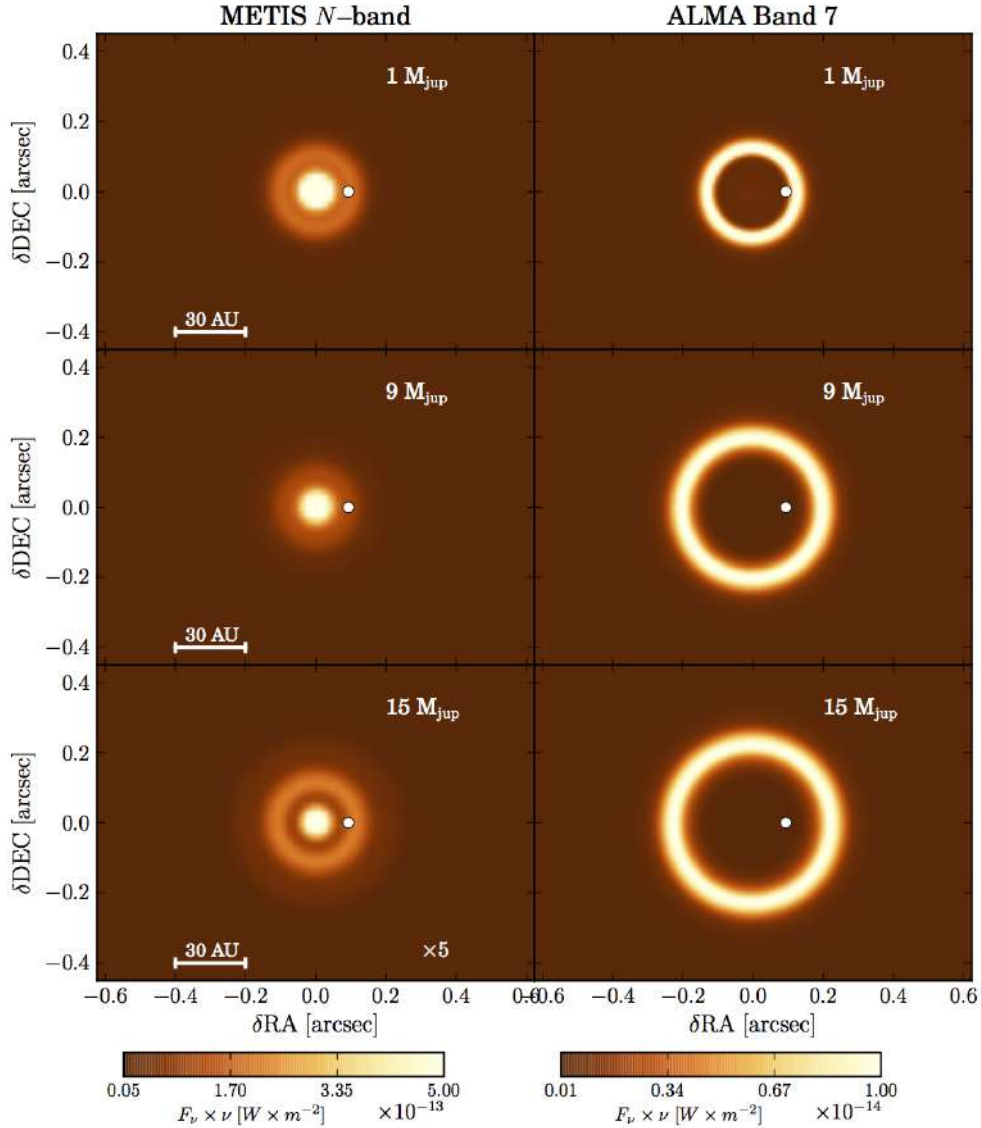


**Figure 2-2:** Simulated images of the disk-planet models for the case of an embedded planet orbiting at 13 AU (white dot) around a solar-mass star. The disk is assumed to be at a distance of 150 pc. Left and right columns correspond to METIS images at N-band (convolved with the METIS PSF) and ALMA images at 0.85 mm, respectively. Top, middle and bottom rows show images obtained for planet masses 1, 9 and 15  $M_{Jupiter}$ , respectively. The model images have been obtained following the procedures of de Juan Ovelar et al. (2013).

the gap wall at multiple wavelengths from near-IR to sub-mm constrain the viscosity by determining the efficiency with which dust grains of different sizes couple to the gas (Pinilla et al. 2012; Birnstiel et al. 2013; Mulders et al. 2013). METIS will have a spatial resolution of 50 mas at N-band, much higher than currently possible, and comparable to that achievable with sensitive ALMA continuum imaging. Another diagnostic may be spiral arms seen in both in scattered light and thermal IR and millimeter emission (e.g., Stolker et al. 2016; Wölfer et al. 2021). This opens the possibility of a strong ELT-ALMA synergy, with the combined data probing grains with sizes covering many orders of magnitude. Together with METIS and ALMA observations of the gas inside the dust gap (van der Marel et al. 2016), it will be possible to constrain most relevant physical parameters, including planet masses, disk viscosities, and even planet ages (Pinilla et al. 2015a). Many disks with gaps and rings located at  $\sim 5$  AU or larger are now known (Andrews 2020) and will be accessible to combined METIS and ALMA studies.

## 2.2.2 Kinematic imaging of gas in planet-forming regions

While dust observations are critical for our understanding of planet formation, the gas component plays an equally important and complementary role. Gas not only drives dust dynamics, but also provides the necessary ingredient for giant planet formation. Moreover, the gas kinematics can probe a plethora of dynamical processes known to occur in disks such as : a) active accretion (viscous? disk wind driven?); b) active ejection (from the star? X-winds? or disk winds?); c) active planet-disk interaction (planet “weather”: accretion shocks? chromospheres?); d) disk perturbations (hydrodynamic? hydromagnetic? orbital?); e) transient phenomena (variable accretion? local disk reorganization? variable irradiation?). METIS will allow probing these effects with roughly an order of magnitude higher angular resolution and two orders of magnitude larger SNR compared with the current state of the art. This critical combination of SNR and angular resolution is fundamental since emission in the line wings holds critical information, is faint and thought to originate in the innermost regions of the planet forming systems.

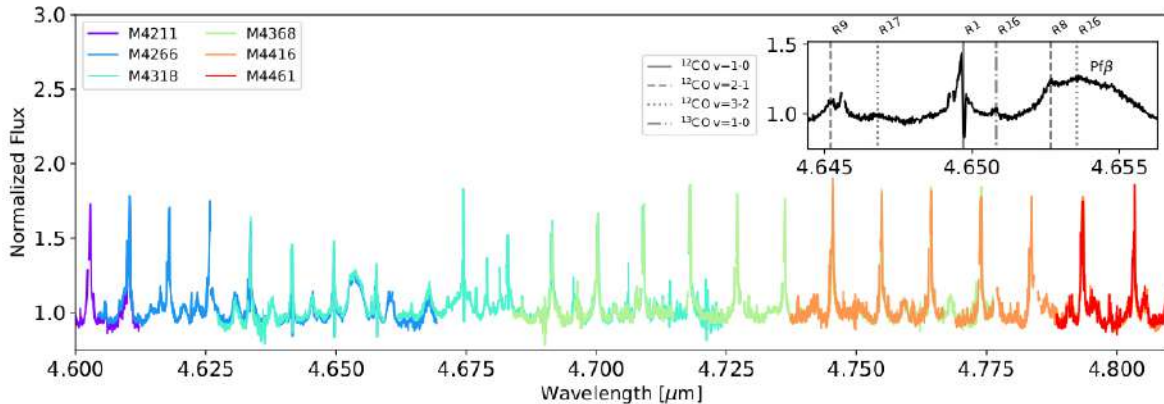


**Figure 2-3:** VLT-CRIRES+ M-band Science Verification spectra at  $R=80,000$  taken in September 2021 illustrating the large variety of detected CO lines arising from the inner 10 AU. H recombination lines and H<sub>2</sub>O lines can also be seen at M band. CRIRES+ complements METIS in its broad wavelength coverage including regions in L and M-band that have not been observed before. It thus provides a pathfinder for selecting individual lines to image with METIS (figure by S. Grant & G. Bettoni).

Gas is uniquely observable by METIS in the inner few AU, a region that ALMA cannot trace. On larger scales of a few 10s of AU, the power of spatially resolving molecular gas emission has already been demonstrated by ALMA. For instance, at typically  $0.2''$ , resolution, Casassus et al. (2013); van der Marel et al. (2016) demonstrate the presence of gas inside the inner dust cavities of transition disks, Qi et al. (2013); van ’t Hoff et al. (2018) image the CO and H<sub>2</sub>O snow lines with molecular tracers, Öberg et al. (2021); Law et al. (2021) show that gas and dust substructures do not follow each other, and Zhang et al. (2021); Sturm et al. (2022) infer highly variable CO abundances from inner to outer disk linked to the presence of dust traps. In comparison to ALMA, METIS will produce full-aperture images of warm molecular gas in protoplanetary disks at angular scales of  $0.05''$ , with high efficiency and sensitivity, allowing for direct imaging of large samples of disks.<sup>3</sup>

The most powerful tracer of this inner planet-forming disk region at 1–10 AU are the CO  $\Delta v=1$  ( $v=1-0, 2-1, \dots$ ) ro-vibrational transitions at  $4.7\text{ }\mu\text{m}$  which trace gas at a few hundred K to about 1000 K (Najita et al. 2003; Blake & Boogert 2004a; Pontoppidan et al. 2008; Brown et al. 2013; Carmona et al. 2017; Banzatti et al. 2022). Figure 2-3 presents part of the new VLT-CRIRES+ science verification spectrum of the young disk S CrA demonstrating the variety of CO lines as well as H recombination lines like Pf  $\beta$ . At somewhat longer wavelength H<sub>2</sub>O lines are detected as well. The CO transitions are excited by collisions, infrared pumping and by UV fluorescent excitation in environments where the UV field is strong (Thi et al. 2013). This leads to strong line emission from small disk radii within 1 AU, and lower, but significant, extended emission from several to 10s of AU, depending on the strength and hardness of the stellar spectrum.

<sup>3</sup>The ELT/METIS angular resolution is a factor  $6-10\times$  that of the JWST/NIRSPEC, precluding such studies with JWST.

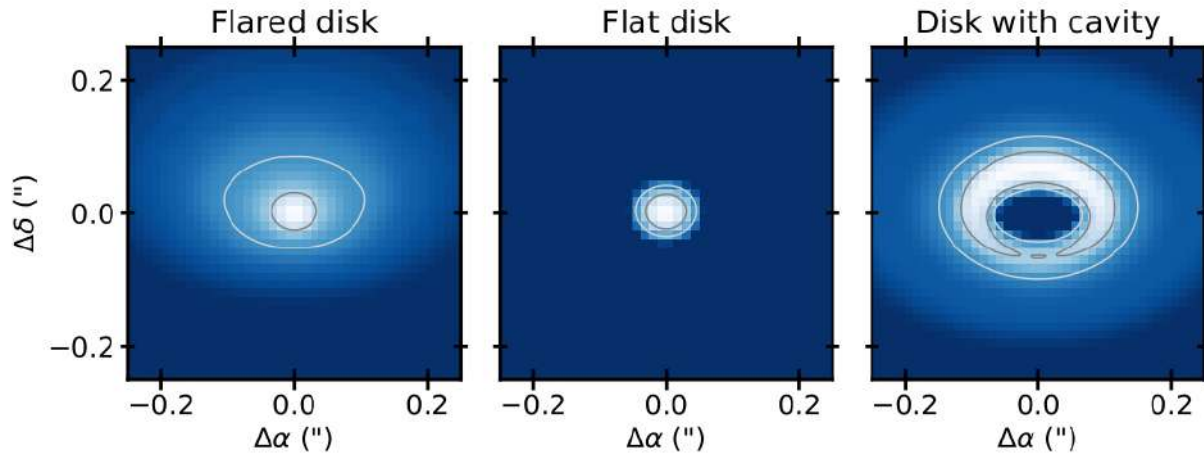


**Figure 2-4:** Simulated METIS CO spectral images for three proposed Herbig disk geometries. Normalised, continuum subtracted and velocity integrated maps of the CO v=1-0 P(10) line are presented. Flat and flared inner disks should be easily distinguished in a 1 hr integration based on these images and the holes inferred for the group I Herbig disks will be resolved in both line and continuum data. A logarithmic colour stretch is used, with the white and grey lines showing 1% and 10% of the peak flux. The model images have been convolved with a Gaussian with a 0.025" FWHM, representative of diffraction limited ELT-METIS observations. A distance of 150 parsec is assumed (from Bosman et al. 2019).

The ro-vibrational CO lines trace the surface of the disk at early evolutionary stages during which the disk is optically thick in the vertical direction, but they may penetrate close to the mid-plane once the gas dissipates or is depleted by the dynamic action of a planet (Salyk et al. 2011). With current facilities, the infrared line emission has been spatially resolved in a number of disks using adaptive optics on scales of  $\sim 10$  AU, in particular those with partially cleared-out inner regions (Goto et al. 2006a; Brittain et al. 2009; Brown et al. 2012). With adaptive optics and the added use of spectro-astrometric techniques, CO gas has been partially imaged down to 0.1 AU scales for a few of the brightest sources (Pontoppidan et al. 2008, 2011a). Some sources show primarily Keplerian rotation of the gas, other disks have additional kinematic signatures superposed (Bast et al. 2011; Banzatti & Pontoppidan 2015; Banzatti et al. 2022). Figure 2-4 illustrates how METIS images can directly distinguish different disk geometries (flat, flared, cavity) that have been proposed for the inner regions of Herbig stars with different spectral energy distributions (Meeus et al. 2001). Overall, ro-vibrational CO is perhaps the best tracer of the structure, kinematics and dissipation of molecular gas in inner disks, and strong correlations are found between the properties of the CO emission and the presence of inner gaps (van der Plas et al. 2015; Banzatti et al. 2017).

In summary, it is well-known that CO ro-vibrational line emission from most disks exhibits extended and complex structures on 1–10 AU scales, but progress is limited by a lack of spatial resolution and sensitivity to image the emission. The METIS integral field unit (IFU) will directly image the kinematics of protoplanetary disks with a spatial resolution 5–10 times better than that offered by current 8m telescopes or line imaging with ALMA. The CO emission extends over 2–32 spaxels with 8–10 m telescopes in favorable cases. The 4–5 times higher spatial resolution with the ELT will, in combination with higher surface brightness sensitivity, lead to spectrally resolved CO line cubes over as many as 82 spaxels or more (see, Figure 2-5). METIS will resolve moving gas structures as small as 2 AU in size at typical distances of 120 pc and as little as 1 AU for the closest disks, with spectro-astrometry providing even higher resolution. Furthermore, the high sensitivity of METIS will ensure that the entire variety of disks will be available to such studies, including faint disks around brown dwarfs and those in transition to the debris disk phase.

Optically thin  $^{13}\text{CO}$  and  $\text{C}^{18}\text{O}$  isotopologues can be imaged as well, probing deeper into the disk. A large sample of at least a hundred protoplanetary disks across the stellar mass range, from brown dwarf disks to disks around young A-stars, can potentially be targeted. As stellar mass is thought to be a key variable in predictive models of disk evolution and planet formation (e.g., Mordasini 2018), observations across the

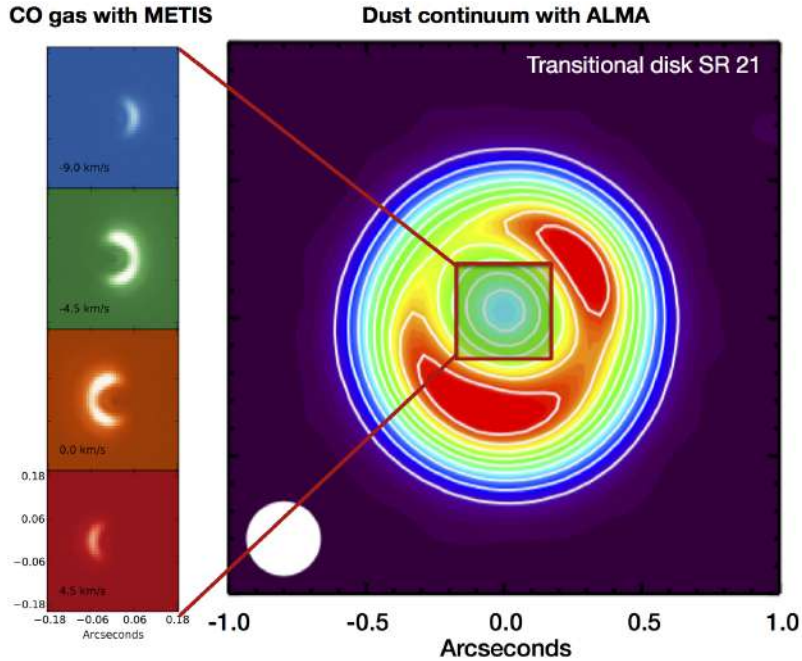


**Figure 2-5:** Model of a METIS observation of CO ro-vibrational emission at  $4.7 \mu\text{m}$  in the transitional disk around SR 21 in Ophiuchus (left panels), compared to the ALMA dust continuum (0.88 mm) image (right panel) from Pinilla et al. (2015b). Note that it is already known from spectro-astrometric observations with CRIRES (Pontoppidan et al. 2008) that the CO gas traces an inner ring at  $\sim 7$  AU (corresponding to the orbits of Jupiter and Saturn in the Solar system), separate from the outer dust ring at  $\sim 35$  AU as seen with ALMA. METIS can now directly image this ring and provide further constraints on any embedded planets shepherding the rings. The CO images represent a two-dimensional non-LTE model with gas/dust thermal decoupling using RADLite/RADMC.

mass spectrum will be a powerful discriminant between models of disk evolution and planet formation.

The high spectral resolution is essential to classify the observed spatial structures: is the emission coming from gas in Keplerian motion, or does it trace an outflow process (see below)? If a localized “hot spot” is detected, is that related to the presence of a compact object, or is it just a disk density or temperature enhancement? High spectral resolution also ensures that the maximum line sensitivity is reached in all cases and that telluric features can be well removed. For instance, the CO lines from the face-on TW Hya disk are 7 km/s wide, and therefore only resolved at  $R > 50,000$ .  $R=100,000$  spectral resolution probes radii of 1–10 AU for a Keplerian disk around a Solar-type star, matching the range of radii that can be resolved by METIS imaging.

### 2.2.3 Disk winds

The upper layers of the disks traced by METIS gas observations provide the connection between the underlying Keplerian disks and the surrounding radial flows, including various types of disk winds (evaporative and magnetically driven centrifugal). Currently, such flows are thought to be observed in CO ro-vibrational lines and Brγ emission, but not yet understood (Pontoppidan et al. 2011a; Salyk et al. 2014; Hone et al. 2017), including how they are linked with the [Ne II]  $12.8 \mu\text{m}$  or [O I]  $6300 \text{\AA}$  kinematic signatures (Alexander et al. 2014; Simon et al. 2016; Nisini et al. 2018; Banzatti et al. 2019). The ionized, atomic and molecular wind tracers likely originate from radially and vertically distinct regions. Such disk winds (rather than MRI) are now frequently invoked to explain disk evolution (e.g., Bai & Stone 2013; Tabone et al. 2022). By directly imaging the flows and their extent in molecular (CO), atomic and ionized species, METIS will allow mass loss rates to be quantified and is therefore likely to dramatically enhance our understanding of disk dissipation and the timescale available to form gas-rich planets. For bright sources, there is a large synergy with VLTI AMBER and GRAVITY(+) which provide sub-AU scale imaging.

Take as an example the case of HL Tau. This source drives a collimated jet (e.g., Movsessian et al. 2012). It is currently accepted that jet engines are magnetically mediated and originate from the star-disk interaction region or the disk itself (now seen by ALMA), a region that METIS can probe. Direct evidence of a molecular disk wind is found with ALMA towards the Class I source TMC1A, launched from radii out to 25 AU (Bjerkeli et al. 2016) and towards the Class I/II source DG Tau, launched from inside 40-70 AU (Güdel et al. 2018). The current state of the art models address jet engines via simulations in the non-ideal MHD regime present in the weakly ionized gas (e.g., Béthune et al. 2017; Yvart et al. 2016; Lesur et al. 2022). It is found that multiple states (e.g., with disk accretion, disk ejection, non-accreting, non-ejection, one disk side only ejection, transient effects, dust free winds) can be present, some of them in the same disk. Because magnetic effects are known to alter disk structure, they directly impact of planet formation.

Evidence of strong disk winds and/or outflows has already been seen in spatially unresolved VLT-CRIRES CO 4.7  $\mu\text{m}$  spectra of a dozen embedded Class I protostars (Herczeg et al. 2011). The model predictions have spatial signatures on 1–30 AU scales that can be directly probed by METIS: a) a wind onion-like structure with lower excitation emission originating further out; b) centroid offsets of the molecular emission from the continuum; c) spatially resolved rotation detected in the molecular emission outflowing from the disk. This is one science case that would greatly benefit from a single laser AO by opening up many more embedded sources for study.

#### 2.2.4 Probing planet formation in early evolutionary phases

At early evolutionary phases ( $t < 1$  Myr), a circumstellar disk continues to accrete gas and dust through infall from the outer region (i.e., from an “envelope”). It is thought that the disk gravitationally fragments when its mass exceeds a certain fraction of the stellar mass (typically  $\sim 10\%$ ; Kratter & Lodato 2016). This would induce the efficient formation of gaseous giant planets even without dust accumulation, formation of planetesimals and core accretion (e.g., Fig. 2-6, left). This formation mechanism may explain the presence of gaseous exoplanets at large orbital radii ( $r > 30$  AU), where planets cannot easily form via the conventional core accretion mechanism (e.g., Durisen et al. 2007; Vorobyov & Elbakyan 2018). Furthermore, numerical simulations show that disk fragmentation can be followed by the formation of multiple rings and gaps in the disk when the disk becomes re-stabilized. This may explain the multiple rings and gaps observed in disks at late evolutionary phases (e.g., Vorobyov et al. 2020).

Some of the gaseous clumps formed in a gravitationally unstable disk would migrate inward, and induce accretion outbursts in the inner disk region (e.g., Vorobyov & Basu 2015). Accretion outbursts identical or similar to this process are observed toward FU Ori-type objects (FUors) that are associated with large accretion luminosities. Although the number of known FUors is small, it has been suggested that many protostars experience FUor outbursts during their evolution (Audard et al. 2014). FUors may thus hold keys for understanding the formation processes of gaseous exoplanets and disk structures described above.

Near-infrared observations (typically at 1.65  $\mu\text{m}$ ) of FUors with 8-m telescopes have recently revealed complicated structures possibly associated with their circumstellar disks (Liu et al. 2016; Takami et al. 2018; Laws et al. 2020, see Fig. 2-6, middle and right for a few examples). METIS will offer coronagraphic capabilities at longer wavelengths (3–10  $\mu\text{m}$ ) with angular resolution improved by up to a factor of  $\sim 2$ . This would yield a breakthrough in the understanding of the physical nature of the FUor disks, and therefore the physical processes of planet formation and disk evolution described above, via searching for the following: (1) disk structures under dusty surface layers, which are responsible for the disk fluxes at shorter wavelengths; and (2) forming gaseous planets (Section 2.3).

### 2.3 Signatures of protoplanets

The unique combination of high spectral and spatial resolution offered by METIS allows spectro-imaging of the distribution of material on AU scales. One of the most exciting prospects, given this capability, is the detection, imaging and kinematic characterization of warm dust and gas directly sculpted by the presence

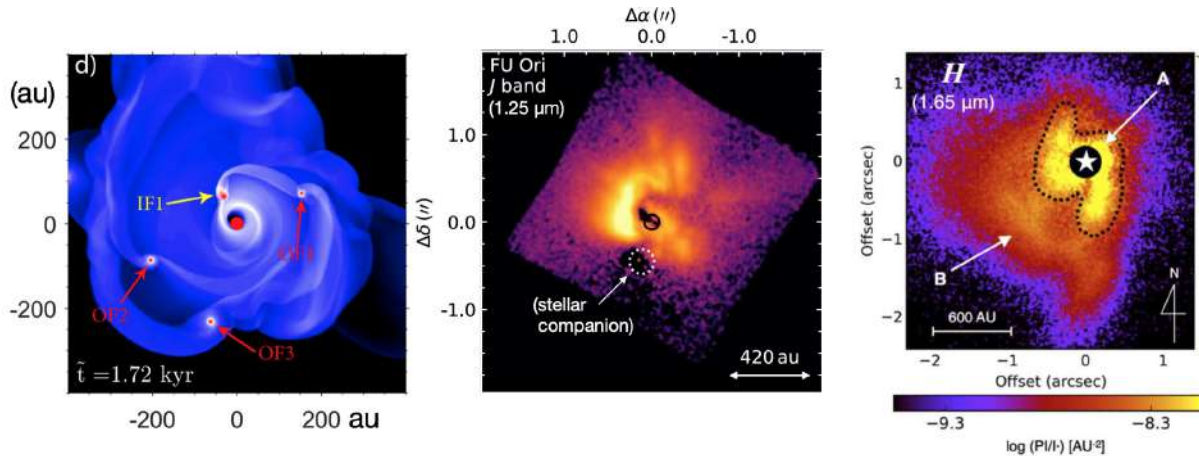


**Figure 2-6:** (left) Numerical simulation of gravitational disk fragmentation with potential embryos of gaseous exoplanets (Vorobyov & Elbakyan 2018); (middle and right) complicated structures possibly associated with gravitationally unstable disks towards some FUors observed using an 8-m telescope (Lawns et al. 2020; Takami et al. 2018).

of still-forming Jupiter-mass planets. This may be accomplished in at least four different ways:

1. Thermal continuum emission from warm protoplanets and their circumplanetary disks (CPDs) may be detected using high contrast imaging.
2. Unseen planets may be detected using spatio-kinematic departures from Keplerian motion, including infall of gas toward the planet from the protoplanetary disk.
3. Detected accreting giant planets may be confirmed and characterized by measuring the Keplerian motion in the circumplanetary disk using CO ro-vibrational lines.
4. Dust imaging, in combination with ALMA, as a function of dust grain size to search for indirect evidence of dynamical sculpting by newly formed planets and dust gaps (Section 2.2.1, Fig. 2-2).

### 2.3.1 Continuum detections of forming protoplanets

Giant planets are surrounded by circumplanetary disks during the protoplanetary disk phase. For instance, it is likely that a Jovian circumplanetary disk was responsible for the formation of the Galilean moons (Canup & Ward 2002; Mosqueira & Estrada 2003). The local Hill sphere of the giant planet sets the radius of a circumplanetary disk ( $R_{\text{CPD}} \sim 0.3 - 0.5 R_{\text{Hill}}$ ), which can be as large as a few AU beyond 10 AU (e.g., Ayliffe & Bate 2009). The circumplanetary disk material is heated by the planetary mass companion, accretion onto it, the central star and the circumstellar disk environment (Wolff et al. 2017; Rab et al. 2019; Portilla-Revelo et al. 2021; Chen & Szulágyi 2021a).

Depending on the, as yet poorly known, properties of protoplanets, METIS may be able to detect them in thermal emission (in contrast to local colder material in the circumstellar disk). Based on high-contrast imaging techniques several candidates for embedded young protoplanets were published in recent years including LkCa 15 b, HD 100546 b, HD 169142 b, and MWC 758 b (e.g., Kraus & Ireland 2012; Quanz et al. 2013, 2015a; Reggiani et al. 2014, 2018). However, in most cases follow-up observations cast some doubts on the true nature of the detected signals (e.g., Thalmann et al. 2016; Rameau et al. 2017; Huélamo et al. 2018; Cugno et al. 2019). In addition, in many other circumstellar disks with prominent morphological or kinematic structures, different groups searched for embedded planets (e.g., HL Tau, HD163296 (see also below); Testi et al. 2015; Guidi et al. 2018), but without success. The only confirmed system with two massive young planets orbiting within the disk gap of its host star is PDS 70 seen through infrared, H $\alpha$  accretion and mm continuum images (see, Figure 2-7; Keppler et al. 2018; Müller et al. 2018; Haffert et al.

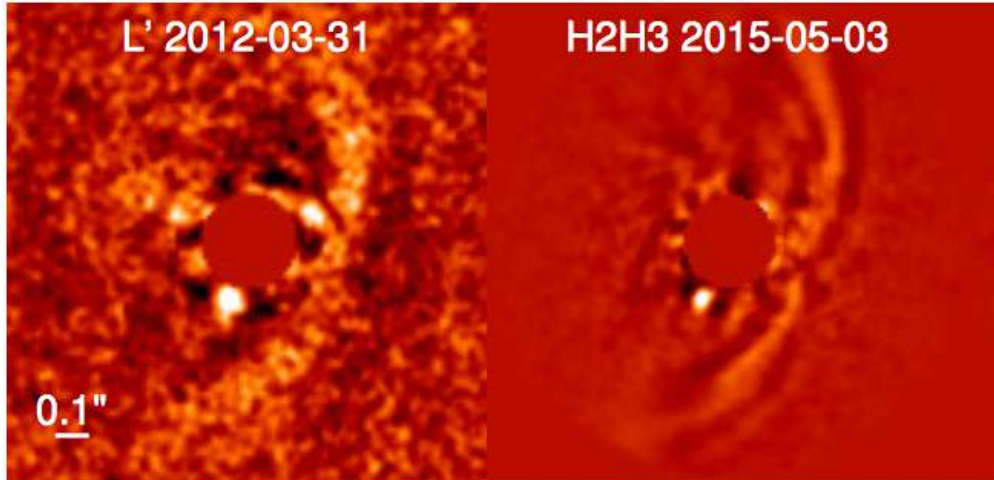


**Figure 2-7:** PDS70 b as seen in the L' band with Gemini/NICI (left) and in the H band with VLT/SPHERE (right) (Keppler et al. 2018). The separation from the central star (which is located in the center and masked out in these images) is  $\sim 22$  AU. In particular in the H band image some scattered light from the circumstellar disk is seen on the right hand side.

2019; Benisty et al. 2021). Recently, additional planetary companion candidates have been added in the AB Aur system (Boccaletti et al. 2020; Currie et al. 2022).

METIS' high sensitivity and spatial resolution will allow us to probe much deeper and much closer to the star than currently possible. This is important as theory would form planets closer in more rapidly than further out. Thus, METIS will allow for (a) a much more robust assessment of the true nature of the known objects and (b) search for additional objects, in particular located within the gaps of transition disks (see also, Figure 2-9). Constraining the luminosity and temperature could place powerful constraints on models of gas giant planet formation. Indeed, objects at orbital separations  $> 10$  AU present challenges to standard formation scenarios (see § 2.2.4). METIS will provide a resolution that enables the detection of objects within 3 AU compared to current limits at  $> 15$  AU (for a distance of 100 pc) probing the physical scales where the bulk of the giant planets in our own solar system are thought to have formed.

In addition to significant uncertainties regarding the luminosity of young, forming gas giant planets, also the properties of the suspected CPDs are largely empirically unconstrained. While some analytical models for CPDs suggest that these objects should be particularly bright at wavelengths  $> 3 \mu\text{m}$  (Eisner 2015; Zhu 2015), the complex 3D morphology of the gas flow onto and around the CPD suggest that more elaborate models are needed to make predictions for the expected MIR SEDs (Szulágyi et al. 2019). Massive gas giants ( $> 5 M_{\text{Jupiter}}$ ) and their CPDs are best detected at mid-IR wavelengths (Chen & Szulágyi 2021b) (Figure 2-8). It is clear that a large wavelength coverage will be essential to disentangle the flux contribution from the young planet from that of the CPD. METIS with its spectroscopic capabilities in the L, M and N band will play a key role here and help constraining the luminosity, and hence temperature and size, of CPDs.

### 2.3.2 Kinematic detections of planets

Continuum or narrow-band detections of protoplanet candidates with METIS are likely to lead to exciting discoveries. However, to fully confirm and characterize protoplanets, spectroscopy is needed. Specifically, attributes such as the planet mass, accretion properties, chemistry and other interactions with any circumplanetary disk may be reachable with spectro-imaging in the 3–5  $\mu\text{m}$  regime.

The kinematic action of an embedded giant planet will not only clear gaps in the protoplanetary disk, but will also perturb the Keplerian motion of disk gas by inducing eccentric gas orbits (Regály et al. 2010), as well as local perturbations near the planet, by as much as 1–2 km/s across a few AU region (Perez et al. 2015). Recently, ALMA detected the kinematic signature of protoplanet candidates in the disk around

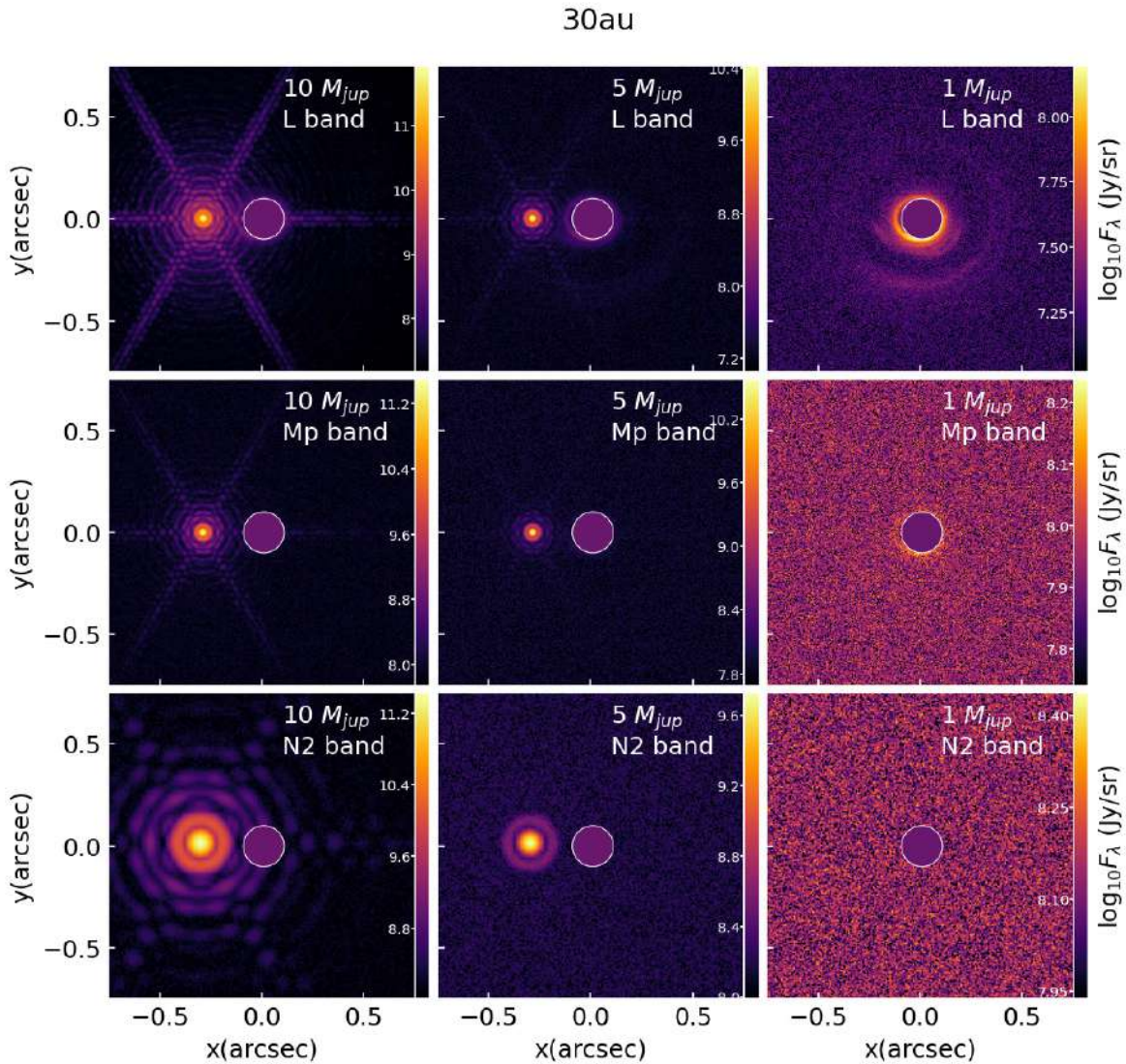


**Figure 2-8:** ELT-METIS synthetic images of a planet with its CPD located at 30 AU in a circumstellar disk at 30° inclination at 100 pc. The columns represent hydrodynamic simulations of different planetary masses (10, 5 and 1  $M_{Jup}$ ) and the rows represent the L, M and N-band filters simulated. The planet is located at 30 AU at 9 o'clock. The central star is masked out with a circle (adapted from (Chen & Szulágyi 2021a).

HD 163296 through CO sub-mm channel maps, which are consistent with perturbations by Jupiter mass planets at  $\approx$  83, 137 and 260 AU (Pinte et al. 2018; Teague et al. 2018; Izquierdo et al. 2022). The METIS wavelength range allows to access the inner disk (warm CO gas inside 30 AU) and is thus highly complementary to ALMA.

The detection of such kinematic signatures may not only confirm the presence of a compact object in a “hot spot” detected by METIS in 10  $\mu$ m continuum imaging, but will also measure its mass. Detecting and measuring the masses of protoplanets while they are forming will provide a transformative comparison to mature exoplanetary systems. Furthermore, the orbital parameter space covered by METIS will match that relevant for giant planets in solar system analogs.

### 2.3.3 Kinematic signatures of circumplanetary disks

Just as protoplanetary disks are intimately linked to the process of star formation, so are circumplanetary disks linked to the formation of gas giant planets and their potential moon systems. Measurements of the gas kinematic signatures in the vicinity of forming protoplanets may test different proposed formation

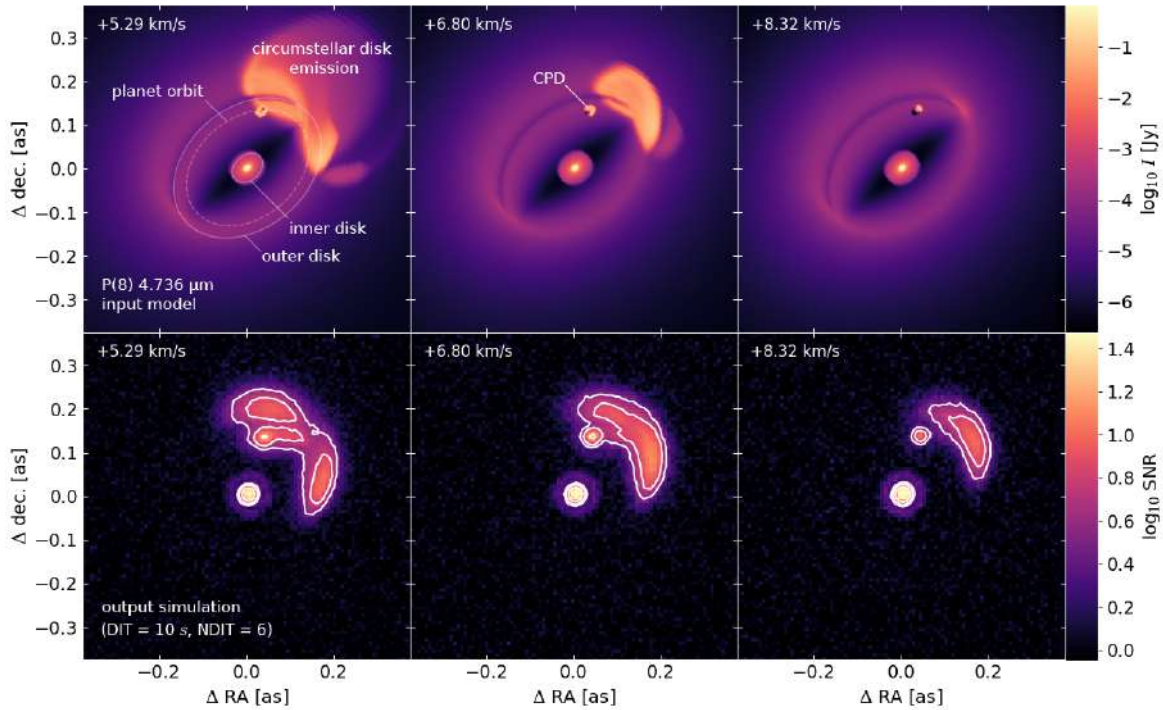


**Figure 2-9:** Synthetic channel maps of the  $v(1-0)P08$  line ( $4.73587 \mu\text{m}$ ) of the HD 100546 circumstellar + circumplanetary disk model. The planet mass is  $10 M_J$  with a corresponding CPD outer radius  $R_{\text{out}} = R_{\text{Hill}}$  (1.62 au). The PRODIMO model (Woitke et al. 2019; Petit dit de la Roche et al. 2021) used as input for SimMetis is in the top row of each sub-figure. The ellipses in the upper-leftmost panel indicate the inner and outer edges of the gap at 4 and 19 au, and the companion orbit at 15 au (dashed line). The corresponding simulated METIS observation panels represent 6 detector integrations of 10 s each in the bottom row of every sub-figure. The white contour lines represent signal-to-noise ratios of 3, 5, and 10. The velocity offset is relative to the stellar reference frame.

scenarios (Canup & Ward 2009; Szulágyi et al. 2014) (see also, Section 2.3.2). METIS may be able to detect warm CO gas in local Keplerian motion in circumplanetary disks. Such a scenario is modeled in Figure 2-9 for a 10 Jupiter mass planet in a pre-transitional disk around a Herbig Ae star (Oberg et al. submitted). An important property of the gas signature from a circumplanetary disk in such a gap is that it will be offset from the local disk velocity by up to 5–10 km/s due to the planet’s own motion around the star, thus avoiding interference from ambient disk gas. METIS can also reveal the kinematics of the gas close to the forming planets and across the gaps; meridional circulation has been detected by ALMA beyond 50 AU (Teague et al. 2019) and is also predicted from 3D hydrodynamical simulations of planet-disk interaction (e.g., Szulágyi et al. 2021). While the signatures of forming protoplanets have been seen in the form of continuum emission, H $\alpha$  accretion signatures, and large-scale non-Keplerian motion (see Section 2.3.1), we still know very little about the internal structure of circumplanetary disks, including their chemical compositions, thermochemistry, and gas masses.

Detections of circumplanetary disks in near-Keplerian rotation may also provide the first evidence for the origin of pro-grade moon systems in disks, such as that of the Jovian system. As the physics of circumplanetary disk accretion may be crucial in limiting planet masses (Morbidelli et al. 2014; Lee & Chiang 2015), these studies are of fundamental importance for constraining models of planet and moon formation.

## 2.4 The chemical composition and evolution of planet-forming material

### 2.4.1 Water and organics in the innermost disk

In addition to providing direct clues concerning the formation of gas giant planets, molecular studies of gas-rich disks can be used to constrain the potential composition of such objects. The bulk chemistry of inner protoplanetary disks — the primary carriers of carbon, oxygen and nitrogen — drive the structure and composition of planets (e.g., Madhusudhan 2019). METIS can therefore link the properties of exoplanets to those of disks, by observing a wide range of abundant gas-phase molecules that are detectable using high resolution spectroscopy, like NH<sub>3</sub>, HCN and CH<sub>4</sub>, as well as water and OH, in the 3–5  $\mu\text{m}$  region (Mandell et al. 2012; Banzatti et al. 2017, Figure 2-10). Most of these key molecules are not observable by ALMA, which is in any case limited to probing volatiles at > 5 AU (e.g., Bruderer et al. 2015).

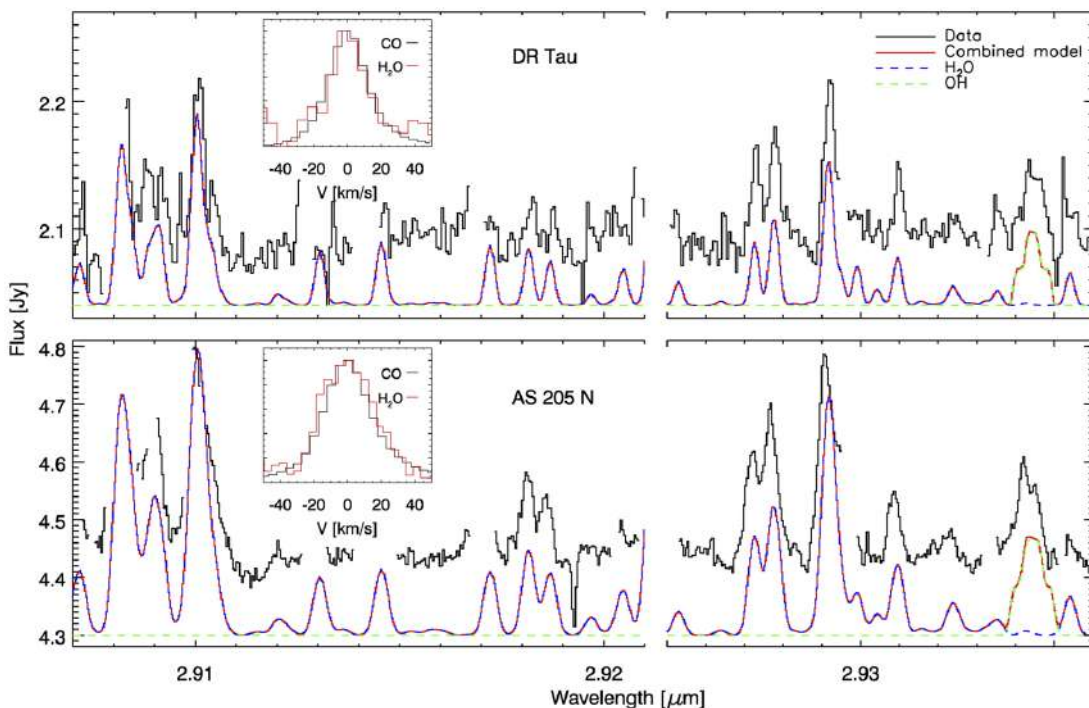


**Figure 2-10:** Keck-NIRSPEC R=25,000 L-band observations of vibration-rotation lines of H<sub>2</sub>O and OH in two protoplanetary disks (Salyk et al. 2008). The inserts indicate the similarity in CO and H<sub>2</sub>O line profiles. These lines arise from the hot inner disk (within  $\sim$ 1 AU); lines further out in the disk will be significantly narrower.

The high sensitivity of METIS can reach disks across the stellar mass-spectrum, down to young brown dwarfs. This is of particular importance, since inner disk chemistry is known to be a strong function of stellar type. Indeed, disks around Herbig Ae stars have an apparently poor chemistry (Pontoppidan et al. 2010; Fedele et al. 2012), while those around solar type stars are rich in both water and organics (Salyk et al. 2011) and brown dwarf disks are rich in organics, but poor in water (Pascucci & Sterzik 2009; Pascucci et al. 2013). Spectrally resolving the line profiles in the inner disk allows us to determine whether lines from different molecular species are tracing the same gas or entirely different disk regions. This is critical for completing molecular budgets as a function of disk radius. As an example, Banzatti et al. (2017) used high resolution VLT-CRIRES spectra of OH and H<sub>2</sub>O at 2.9  $\mu\text{m}$  to infer an inside-out depletion of water within the water snow line during disk dispersal. Thus, METIS spectroscopy is expected to be highly complementary to the lower resolution spectroscopy offered by JWST, which probes the slightly cooler and deeper parts of the disk at mid-infrared wavelengths but lacks the kinematic and spatial information to determine the molecule's location (Antonellini et al. 2015; Bosman et al. 2017; Woitke et al. 2018). Together, they may probe overall C/O, C/N and O/H elemental abundance ratios in the gas as function of disk radius across major snow lines (Pontoppidan et al. 2014). The ultimate goal is to link the composition

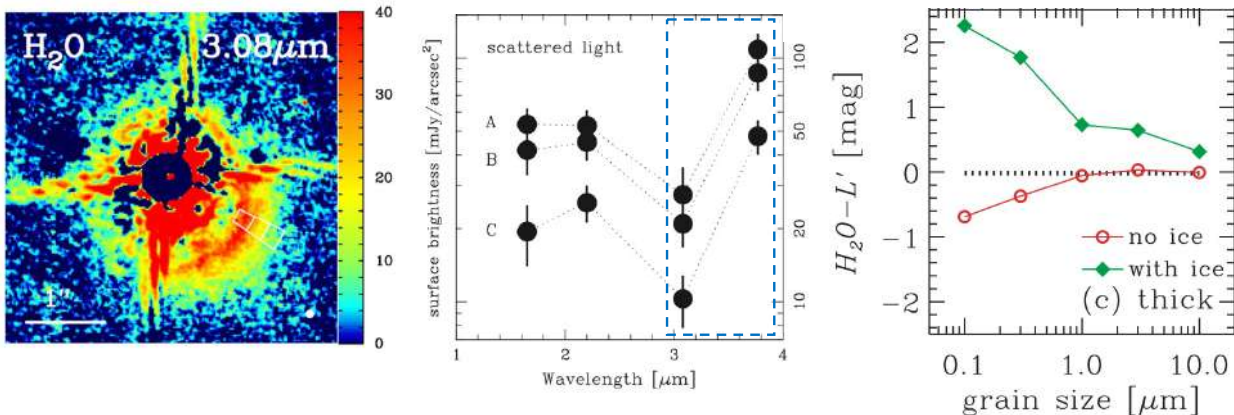


**Figure 2-11:** Left: Narrow-band scattered light imaging investigating the water ice band at  $3.08\mu\text{m}$  in three different locations (A, B and C marked with white squares) in the disk of HD 142527; Center: Multi-band spectrum of the scattered light at same locations A, B and C of the disk. The dash-line blue rectangle shows the spectral coverage of METIS. Figures adapted from Honda et al. (2009). Right: Expected  $\text{H}_2\text{O} - \text{L}'$  color of the scattered light as a function of the dust size for the ice-rich and ice-poor cases. Plot from Inoue et al. (2008).

of mature exoplanets to their formation sites in their natal protoplanetary disks (e.g., Öberg et al. 2011; Helling et al. 2014; Mordasini et al. 2016; Booth et al. 2017; Cridland et al. 2019).

#### 2.4.2 Imaging of the water ice distribution in disks and resolving the snowline

The combination of high spatial resolution and high sensitivity makes METIS a unique tool for imaging not just gas but also solid species in the surfaces of protoplanetary disks. The most important one is water ice. As a dominant solid carrier, the presence of water ice beyond the snowline, where the temperature falls below the condensation temperature of  $\text{H}_2\text{O}$  ( $\sim 150\text{--}170\text{ K}$  at typical pressures of few  $10^{-4}$  bars in the inner regions), enhances locally the dust density, which is thought to be a condition to form the fast-growing cores of the gas giants before the disk's gas dissipates. Theoretical calculations on the location of the water snow line in the inner few AU region have led to conflicting predictions, in part due to the inclusion of dead zones as opposed to the case of fully turbulent disks (Lecar et al. 2006; Martin & Livio 2012). Direct observations of this important transition region in disks, as well as tracing its evolving location across the disk's lifetime, have therefore important repercussions to validating and refining exoplanet formation models.

Measuring the distribution of water in disks is currently a highly active area of research, but one that is almost entirely focused on the vapor phase (Hogerheijde et al. 2011; Du et al. 2017; Banzatti et al. 2017, and see above). Water ice *emission* is only observable in the far-infrared. This was achieved both by ISO (Malfait et al. 1998) and *Herschel* (McClure et al. 2015; Min et al. 2016) but without spatially resolving the disks, leaving therefore unaddressed the question of the radial distribution of water ices.

From the ground, the spatial distribution of icy species in the disk mid-plane, where planetesimal formation occurs, has been attempted by ALMA. For CO ices, the  $\text{N}_2\text{H}^+$  tracer has allowed to resolve the CO snowline in a few disks (Qi et al. 2013, 2019).  $\text{HCO}^+$  can serve a similar role for  $\text{H}_2\text{O}$  ice, but the higher condensation temperature of water compared with CO brings the  $\text{H}_2\text{O}$  snowline closer in, down to a few AU, which ALMA cannot resolve (Leemker et al. 2021). This has led to propose methods based on measurements of a discontinuity in the sub-mm dust emission spectral index to attempt the identification of the water snowline (Banzatti et al. 2015), possibly seen in the out-bursting V883 Ori case (Cieza et al. 2016), but this diagnostic is not unique.

Water ice can be probed as well from the ground in the mid-infrared through the broad *absorption* feature at  $3\mu\text{m}$ , which traces the icy grains population in the disk's upper layers. This has been observed successfully for a number of nearly edge-on disks (Terada et al. 2007; Terada & Tokunaga 2017), with METIS providing unique data, see below. For more face-on systems, the radial ice distribution can be explored

with narrow/broad-band imaging of the disk in scattered light in the  $\sim$ 1.6 to 4  $\mu\text{m}$  region, as the 3  $\mu\text{m}$  absorption feature is clearly imprinted in the scattered light spectrum (Inoue et al. 2008). This technique has been successfully applied to the systems HD 142527 and HD 100546 (Honda et al. 2009, 2016), where PSF-subtracted (coronagraphic) images in the H<sub>2</sub>O (3.1  $\mu\text{m}$ ), L' (3.8  $\mu\text{m}$ ) and K-band filters permitted to extract the spectrum of the scattered light at different radial positions and detect the water ice absorption feature. For these bright Herbig stars, the technique was efficient at large radii ( $>140$  AU) where the images were less affected by PSF-subtraction residuals, but hence limiting the access to the innermost regions.

METIS with its high spatial resolution (0.023'' at 3.5  $\mu\text{m}$ ) and sensitivity opens new perspectives for imaging the water snowline. In Herbig stars with  $T_* \sim 10000$  K, the temperature in the disk upper layer drops below 100 K at  $>100$  AU, which means that this case can be addressed with 8m class telescopes as shown for HD142527 and HD100546. For K-type (T Tauri) stars with  $T_* \sim 4000$  K, H<sub>2</sub>O will condense at  $>10$  AU, which implies that the scattered light has to be detected as close in as 0.1'' to resolve the water snowline in nearby disks, which only METIS can reach. Besides the detection of water ice itself, the potential diversity in feature strength and location will provide key information on the mixing mechanism that efficiently opposes dust settling and transports (sub)micron-sized grain in the upper disk layer (Tazaki et al. 2021).

In contrast to the case in Figure 2-11 for which H to L' band coverage was accessible with the same instrument (CIAO/Subaru or NICI/Gemini), METIS will be limited to the H<sub>2</sub>O and L' imaging filters. Rather than a multi-band spectrum, the H<sub>2</sub>O–L' colors of the disk scattered light at different radii will be exploited to detect a change from bluer to redder (Fig. 2-11). T Tauri stars brighter than  $L=10$  will be targeted (McCabe et al. 2006) in order to guarantee stable AO correction and good quality coronagraphic observations, while the approach will be initially validated on known targets such as HD 142527.

#### 2.4.3 Delineating the CO and H<sub>2</sub>O snowlines in edge-on disks

Highly inclined, or “edge-on” systems, are particularly interesting targets for delineating snowlines, complementary to the more face-on case discussed above. At inclinations greater than 70°, the optically thick mid-plane blocks the thermal emission from both the star and the disk's inner 10 AU, allowing the 3–15  $\mu\text{m}$  fundamental vibrational modes of cold ices beyond 20 AU to be seen in absorption against scattered light from the star or inner dust rim (see spectrum at left in Figure 2-12). However, this optimal inclination makes isolated edge-on disks very faint ( $\sim$ 1 mJy at 5  $\mu\text{m}$  at the distance of the Taurus molecular cloud). Previous space missions were mostly sensitive to edge-on disks with remnant protostellar envelopes (Pontoppidan et al. 2005) or were unable to observe them with sufficient sensitivity to detect ices (Pontoppidan et al. 2007). Ground based observations have successfully revealed water ice features in several bright disks (Terada et al. 2012, and above), and disk models show that the 4.7  $\mu\text{m}$  CO ice feature could be as deep as the 3  $\mu\text{m}$  H<sub>2</sub>O ice feature for edge-on disks (Pontoppidan et al. 2005) but depending on temperature structure (Ballerina et al. 2021). However, the sensitivity of current ground based telescopes at M band is insufficient to observe the 4.7  $\mu\text{m}$  band.

Over the next few years, the JWST NIRSPEC and MIRI IFUs will characterize the anticipated main ice species by mass in protoplanetary disks: JWST has sufficient spectral resolution to detect the narrow features of CO and CO<sub>2</sub>, as well as to measure changes to the broader water ice profile that indicate temperature and grain size variation in the icy grains. However, the spatial scale of JWST is barely enough to resolve the CO snowlines of these disks (e.g. 26 AU, Dutrey et al. 2017) and the water snowline will not be resolved at all. Additionally, both the water and CO feature at 4.7  $\mu\text{m}$  contain blended ice features that will be difficult to disentangle at the spectral resolution of JWST. The CO feature is known to exhibit extra components originating in blends with CO<sub>2</sub> and/or CH<sub>3</sub>OH, as shown in the inset in Figure 2-12. The degree to which CO is mixed with these other ices determines at what temperature the bulk of the CO-rich ices sublimate. This is, in turn, critically important to our understanding of the chemical evolution of carbon-rich ices into less volatile forms as they are transported from the cold outer disk to the planet-forming zones (Bosman et al. 2018). Other major ice features that can be probed from the ground include OCN<sup>-</sup> ice (ammonia salts) and CH<sub>3</sub>OH, both of which should be much less volatile than CO. Finally, at spectral resolutions four

times higher than what JWST NIRSpec will achieve ( $R \approx 10,000$  vs 2700), gas phase lines of CO appear in absorption alongside the sublimating ices. Observing both CO gas and ice at once would allow a detailed investigation into the main carbon carrying solids from which planets form.

With the higher spatial and spectral resolution of METIS, these science cases are possible. Figure 2-12 shows the observed HST scattered light image of a well-known edge-on disk, along with its archival *Spitzer* spectrum and a simulated M band continuum image produced from a model fit to the *Spitzer* spectrum. The FoV of METIS is well-suited to the predicted scattered light emission at M band, and the spatial resolution of  $\sim 0.02''$  yields a 3 AU resolution at 140 pc. This is sufficient to enable the detection of both the water ice and CO ice snowlines in the upper layers of these disks. Furthermore the spectral resolution will be more than sufficient to separate the distinct CO ice components as well as methanol and ammonia salts in each spaxel to see how the ice evolves as it approaches the CO snowline.

#### 2.4.4 Isotopic fractionation as a probe of early solar system formation

Isotope abundance ratios in Solar System objects provide unique probes of certain physical and chemical conditions in the solar nebula (Nomura et al. 2022). Equivalent tracers of isotopologues in protoplanetary disks may provide an important link between our own solar system and exoplanetary systems. The fundamental ro-vibrational lines of the CO isotopologues –  $^{13}\text{CO}$ ,  $\text{C}^{18}\text{O}$ , and  $\text{C}^{17}\text{O}$  – all of which have been detected in disks and young stellar envelopes with VLT-CRIRES, are prime targets of METIS (see Figure 2-13) (Smith et al. 2009b; Young et al. 2011).

The oxygen isotopes are particularly interesting because solar system rocks show an anomalous mass-independent distribution that has defied conclusive explanation since its discovery (Clayton et al. 1973). One leading explanation is isotope-selective photodissociation of CO in the upper layers of the disk, followed by vertical mixing and incorporation into water and rocks (e.g., Lyons & Young 2005; Visser et al. 2009). METIS will be able to determine the CO isotopologue ratios for a much larger number of disks than the couple of disks that were accessible with VLT-CRIRES (Smith et al. 2009b), thus directly tracing the origin of water in the inner solar system and formation history of rocks. This case requires high spectral resolution to fully resolve the line profiles, and thus measure accurate optical depths and isotopologue ratios. JWST lacks the high resolution, and rotational emission lines observed by ALMA are affected by systematic errors driven by complex radiative transfer and excitation processes (e.g., Miotello et al. 2014).

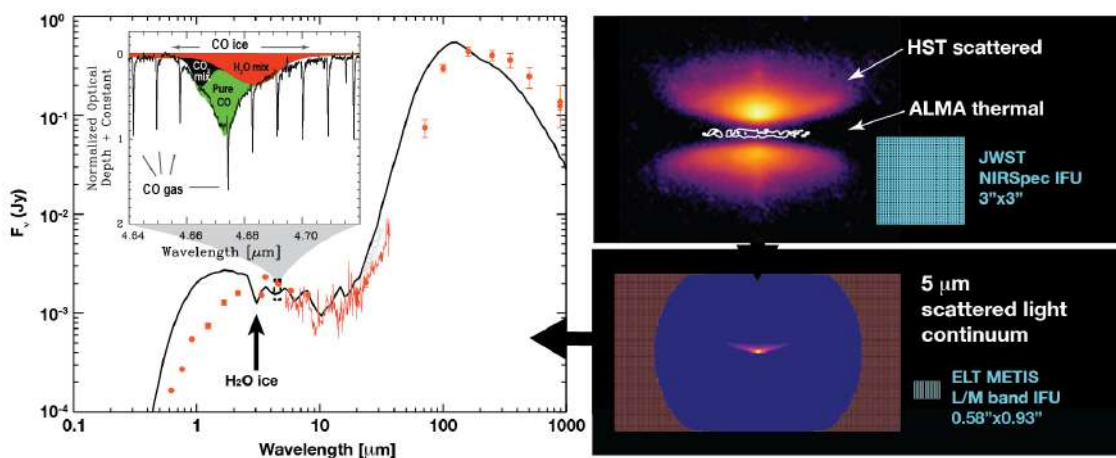


**Figure 2-12:** Left: Archival Spitzer spectrum and radiative transfer model fit of an edge-on disk targeted with JWST in Cycle 1. The water ice feature at  $3\text{ }\mu\text{m}$  is indicated. Inset: Excerpt from Figure 4 of Boogert et al. (2015) showing the CO ice and gas features around  $4.7\text{ }\mu\text{m}$  observed with VLT-ISAAC. Right Top: HST and ALMA images of an edge-on disk (Villenave et al. 2020). Bottom: Simulated M band continuum image of the disk model from the left panel (Harsono, private communication). Footprints of JWST NIRS and ELT METIS are given for comparison. Image credit: M. K. McClure.

#### 2.4.5 Distribution of PAHs and related carbonaceous species

Silicate minerals are ubiquitously detected in protoplanetary disks and have been the main focus of solid phase studies (e.g. Juhász et al. 2010). Carbonaceous dust, the other major cosmic dust species, is known to be present as well in the inner part of disks and in the solar system (e.g., Wirick et al. 2009). Determining the occurrence, nature, and spatial distribution of carbonaceous material in inner disks down to AU-scale is therefore of relevance, as they are primary building blocks of terrestrial planets. Intriguingly, the inner Solar System bodies exhibit a substantial carbon depletion: the C/Si ratio, which is a measure of the organic matter to rock content, displays a strong gradient, rising by several orders of magnitude from the inner (0.5-2 au) to the outer regions ( $\lesssim 40$  AU; Dartois et al. 2018; Li et al. 2021). Observations of carbon in disks (Boutéraon et al. 2019) suggest that this gradient in the Solar System may be a universal attribute of protoplanetary disks. The key questions that METIS has the potential to address are the following :

- In which form(s) are carbon-based species in protoplanetary disks? Options include polycyclic aromatic hydrocarbons (PAH), hydrogenated aromatic and aliphatic carbons, amorphous carbons, graphite, and possibly more exotic species such as fullerenes that have been detected in the ISM. A requirement for delineating different forms is the existence of specific spectral signatures with each species. Graphite and amorphous carbon do not possess such spectral signatures, yet their presence can be inferred indirectly from modeling their contribution to the near-IR continuum and their link to the presence of PAH nanoparticles produced by their destruction.
- What is the relative abundance of solid carbonaceous species ? The somewhat limited objective is to obtain relative abundances of the carbonaceous dust species through their observed signatures.
- What is the spatial (radial) distribution of carbonaceous species? Is the refractory species composition gradient observed in the solar system universal and what are the consequences on the nature and composition of forming planets ?
- What is the lifetime of the carbonaceous material; is replenishing necessary? PAH nanoparticles are relatively fragile and prone to photodestruction in the strong radiation fields of protoplanetary disks' inner regions. Their presence in inner disks would immediately trigger the question whether this replenishment results from the destruction of larger, unseen yet dust particles, or through some gas inflow/accretion, recalling that nano-particles are dynamically well coupled to the gas.

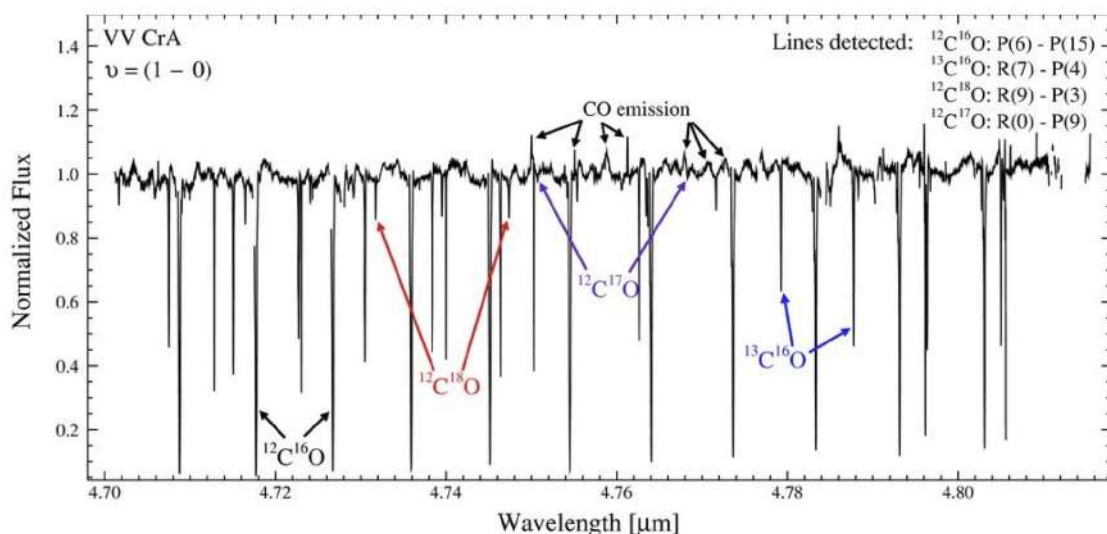


**Figure 2-13:** Infrared absorption spectra of the CO fundamental ro-vibrational bands toward the VV CrA binary object. The line of sight from the primary star passes through the outer cooler part of the disk around the secondary star in which the gas is seen in absorption. Note the detection of lines of all CO isotopologues, including  $\text{C}^{17}\text{O}$  (Smith et al. 2009b).

Within the spectral range covered by METIS, prominent features are seen in many sources at 3.3, 6.2, 7.7, 8.6, 11.3  $\mu\text{m}$  (Geers et al. 2006; Maaskant et al. 2014). They are thought to arise from the cooling of transiently-heated PAHs excited by the intense stellar UV radiation. These macro-molecules are important tracers of complex carbon chemistry and can be used as a proxy for the solid carbon content. Moreover, they control the amount of photoelectric heating in disk surface layers (e.g., Woitke et al. 2009; Bruderer et al. 2012). Measuring the distribution and chemistry (e.g., charge state, amount of dehydrogenation) of PAHs will be an important contribution toward constraining thermo-chemical models. In addition, PAHs play an important role by providing a source of significant UV opacity in the inner disk, thus affecting the disk structure (e.g., amount of flaring). For a flaring disk, the PAHs at the surface of the disk are in direct view of the central star and their emission bands therefore trace the geometry of the disk surface, even at large distances from the star, way beyond that probed by dust mid-infrared thermal emission.

Because 8-10 m class telescopes typically only marginally resolve disks even around luminous young Herbig stars, the geometry and carbonaceous species content, as traced by PAH emission, has been determined for only a handful of disks. Large scale ( $\gtrsim 50$  AU) prominent PAH emission has been traced at an angular resolution of about 0.3'' by direct thermal emission imaging with VLT-VISIR (Lagage et al. 2006). An interesting segregation between PAHs and large grains has been observed for the Oph IRS48 disk, with PAHs only present in a gap or inner hole, potentially cleared out by a planet (Geers et al. 2007a; Schworer et al. 2017) (see Figure 2-14). Comparison of data with detailed radiative transfer modeling shows evidence that the PAH abundance is lower than that in the ISM by an order of magnitude in the cavities of two gapped disks around HD 100546 (Habart et al. 2021) and HD 169142 (Devinat et al. 2022), consistent with earlier work on a large sample of T Tauri disks (Geers et al. 2006). Finally, interferometric observations with MATISSE, although more limited in sensitivity, show the likely presence of carbonaceous nanoparticles in the inner 1-10 AU of the disk around HD 179218 (Kokoulin et al. 2021).

With an angular resolution 5 times better than that of VLT-VISIR and NACO combined with greatly increased sensitivity and high contrast imaging performance, ELT-METIS will be able to image PAH 3.3, 8.6 and 11.2  $\mu\text{m}$  features down to a few AU resolution for a large disk sample, extending the stellar mass to the solar-like progenitors T-Tauri star masses regime ( $0.5\text{-}2 M_{\odot}$ ). The aliphatic amorphous carbon emission feature at 3.4  $\mu\text{m}$  will be traceable down  $\sim$ 5-10 AU from the star. These METIS observations of disk structure will be highly complementary to ALMA dust imaging which predominantly traces large grains in the disk mid-plane: disks such as that of HD 97048 appear symmetric at mm wavelengths (Walsh et al. 2016) but highly asymmetric when observed in PAH emission (Lagage et al. 2006). Thus, only the combination of ALMA and METIS imaging will constrain the vertical stratification and flaring geometry of protoplanetary disks.

Finally, PAHs are known to undergo physical/chemical changes due to UV radiation, including ionization, hydrogen loss and photodestruction to C<sub>2</sub>H<sub>2</sub> as a function of disk radius (e.g., Visser et al. 2007; Zhen et al. 2015; Bouwman et al. 2019). At the other extreme, large PAHs can transform under the influence of UV to fullerenes C<sub>60</sub> and C<sub>70</sub> in a ‘top-down’ interstellar chemistry (Berné & Tielens 2012; Zhen et al. 2014). All of these carbonaceous molecules, from the smallest C<sub>2</sub>H<sub>2</sub> to the largest C<sub>70</sub>, can only be observed at mid-IR wavelengths. The combination of ELT-METIS and JWST-MIRI will provide both the necessary sensitivity, wavelength coverage and spatial resolution (for ELT) to study their distribution across the planet-forming zones of disks.

#### 2.4.6 Crystallization of silicates: when and where?

It is still unclear where and how grain growth and the annealing of silicates take place in protoplanetary disks. In contrast to silicates in the general interstellar medium (e.g. Kemper et al. 2004; Min et al. 2007), a fraction of the silicates in disks is known to be in crystalline form (e.g. Waelkens et al. 1996; Sargent et al. 2009). Thus, the amorphous silicates must be crystallized inside the disk. The most common explanation is annealing at high temperatures ( $>800$  K) in the inner (typically  $<1$  AU) disk (e.g. Gail 1998; Bouwman et al. 2001), but the presence of crystalline silicates in comets (see Solar System section) argues either for

strong mixing or for alternative crystallization processes, such as shocks or planetesimal destruction, which take place at large disk radii (e.g Harker & Desch 2002). Alternatively, transient thermal processing during accretion outbursts in which the central object temporarily becomes many times brighter than in quiescence, can heat the disk surface and crystallize grains (Abrahám et al. 2009).

The N-band contains the resonance of the Si-O stretching mode, which is widely observed in low-resolution disk spectra (e.g. Kessler-Silacci et al. 2007; Oliveira et al. 2011). The shape of this band is particularly sensitive to both grain growth (e.g. van Boekel et al. 2003) – the first step in planet formation – and to crystallization (e.g. Bouwman et al. 2001). Pioneering spatially resolved VLT-MIDI spectroscopy has opened up the completely new field of mineralogy as a function of position in disks (e.g. van Boekel et al. 2004), but this has been possible for only a handful of sources (e.g. Schegerer et al. 2009). Although METIS does not have the ultimate spatial resolution of VLTI-MIDI and MATISSE, it is more than three orders of magnitude more sensitive. It will thus enable the observation of a statistically relevant sample of disks, and constrain the amount of growth and crystallization in the inner versus the outer ( $>5$  AU) disk.

The most prominent example is HD 100546, a transition disk with a large gap possibly carved by a young giant planet (see section 2.3.1), with the inner rim of the outer disk located at  $\approx 11$  AU (e.g. Garufi et al. 2016) and with a small inner disk of  $\lesssim 1$  AU (Panić et al. 2014). In this disk large amounts of cold crystalline silicates are present (e.g. Bouwman et al. 2003; Mulders et al. 2011) but their spatial distribution could so far only be indirectly inferred through SED fitting and is thus poorly constrained. The radius of the outer disk rim is about  $4 \times 5$  AU along the minor  $\times$  major axis; thus, METIS can take high SNR spectra of this rim with  $\sim 15$  independent azimuthal samples along the ring, separately from the inner disk.

Another set of interesting targets are binary young stars (e.g., Ratzka et al. 2005; Duchêne & Kraus 2013), especially those with separations in the interesting 3–30 AU range. With its much higher spatial resolution, METIS will be able to obtain images and spectra of individual circumstellar disks, rather than an unresolved composite of these disks or of the circumbinary disks around wide binaries probed with current generation telescopes (Ratzka et al. 2009). Do the individual disks have similar silicate composition and crystallinity fractions or not? This may provide insight into their formation history, in particular whether they formed through disk fragmentation or cloud core fragmentation. Another aspect is the mass ratio between the two components, which alters the evolution of a binary just like the separation does. The larger the mass ratio deviation from unity, the more the influence of the companion is reduced. A ‘normal’ binary then turns into some kind of a ‘star-planet-system’, and there are indeed many examples where (sub-stellar) companions influence the circumstellar disk around the primary.

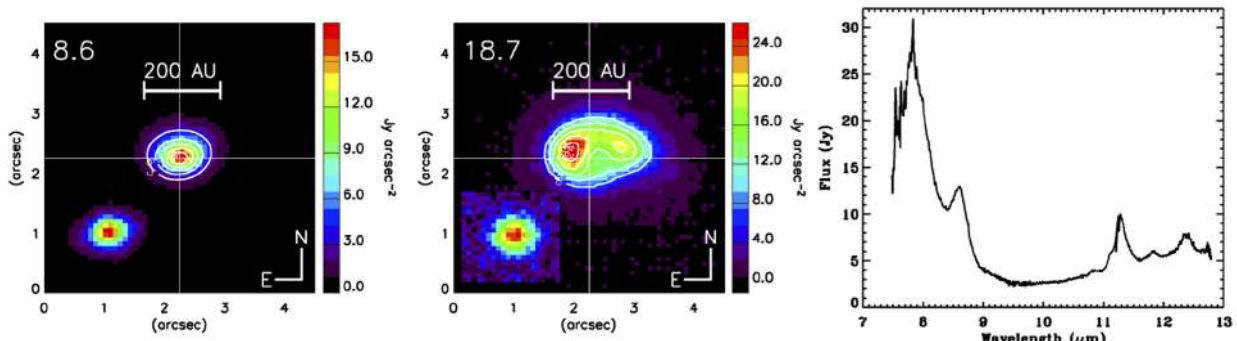


**Figure 2-14:** VLT-VISIR mid-infrared images of the transitional disk around the young Herbig Ae star IRS 48, showing strong centrally peaked PAH emission at  $8.6\text{ }\mu\text{m}$  as well as a 60 AU radius gap devoid of large grains emitting at  $19\text{ }\mu\text{m}$ . The inserts show the PSF of a standard star. The  $8\text{--}13\text{ }\mu\text{m}$  spectrum with the strong PAH features is included. ELT-METIS will be able to provide spatially resolved integral field spectroscopy of the material (gas + dust) present inside and outside gaps down to the terrestrial planet- forming region (figure based on Geers et al. 2007b).

## 2.5 Debris disks around nearby main-sequence stars

The debris disk stage, which follows the gas-rich protoplanetary disk stage, is a phase of planet formation and evolution that is characterized by growth of terrestrial planets and dynamical interactions between planetesimals and giant planets. This leads to the production of belts of debris as planetesimals collide and are ground down to observable amounts of dust. Debris disk belts are known to be located at several distinct radial regions. Cold dust at large distances ( $> 50$  AU) was the first to be discovered and characterized by IRAS (Backman & Paresce 1993) and subsequently imaged by ground-based sub-mm telescopes, *Herschel* (Matthews et al. 2014), and ALMA (Hughes et al. 2018). In particular, the results of the *Herschel* DEBRIS survey showed that approximately 17% of main-sequence stars have a Kuiper belt analog with a fractional luminosity level of at least  $10^{-5}$  (Sibthorpe et al. 2018). Interestingly, more and more detections of warm ( $\sim 150\text{-}300$  K) dust, typically located between the habitable zone and the snow line at a few AU, have been appearing in the literature over the last decade, largely driven by mid-infrared surveys in space using *Spitzer* (Lawler et al. 2009), WISE (Lawler & Gladman 2012) and AKARI (Fujiwara et al. 2013). Hot dust ( $> 300$  K), located within 1 AU, was also discovered around a few tens of main sequence stars with near-infrared interferometry (Absil et al. 2013a; Ertel et al. 2014).

The presence of large amounts of warm dust around main sequence stars is likely related to the presence of asteroid belts, or, for young disks, to the formation of terrestrial planets. METIS should be the first instrument to provide detailed images of warm debris disk belts inside the terrestrial planet region at a couple of AU. Two main goals can be identified, and are discussed in more details below: (i) detailed study of the properties of particularly bright warm debris disks, and (ii) exploration of the faint end of the brightness distribution of warm debris disks (also known as exozodiacal disks).

### 2.5.1 Terrestrial planet formation in warm debris disks

About 1% of all main sequence stars have spectro-photometrically detectable warm debris dust in the terrestrial planet region (Morales et al. 2012; Patel et al. 2014), with a higher fraction around younger stars (Meyer et al. 2008b). While a few dozen examples are currently known, they only represent the tip of the iceberg of a much larger distribution of warm debris disks, and are understood to correspond to the most collisionally active systems. Some of the most well-studied nearby debris disks have dust at  $< 3$  AU, including HD 69830,  $\beta$  Pictoris, and HR 8799, all of which are also famous for hosting planetary systems. Because of the short dynamical/collisional lifetime of dust at such distances from the star, theoretical models show that these warm dust populations must be transient (Wyatt et al. 2007). Possible explanations for their presence range from the late formation of terrestrial planets and major collisions between planetesimals, to the delivery of dust by asteroids and comets in episodes of heavy bombardment.

With METIS, the increase by a factor of 4–5 in spatial resolution over current mid-infrared single-dish imaging facilities, along with an even greater increase in sensitivity and the extreme adaptive optics correction, hold the promise of spectacular continuum images for some nearby warm debris disks, as well as the possibility to measure the sizes of a larger sample of more distant disks. The spatial structure (and perhaps even the variability of the structure) of warm debris disks will constrain the fundamental properties (mass, position, eccentricity, etc) of asteroid belts and terrestrial planets in other planetary systems, and thereby bring much-needed constraints on the origin of warm dust populations. It should also be possible, in some cases, to infer the presence of a hidden (low-mass) planet by revealing structures in the debris dust from high-angular resolution METIS continuum observations at  $10 \mu\text{m}$ . Finally, METIS may also reveal terrestrial planets in formation by observing debris dust distributed asymmetrically in the disk, generated in recent collisions (Lisse et al. 2009; Olofsson et al. 2012; Jackson et al. 2014) or even the resulting hot protoplanet collision afterglows (Mamajek & Meyer 2007; Miller-Ricci et al. 2009).

One example of a particularly bright warm debris disk is the F-star eta Crv located at a distance of  $\sim 18$  pc. It was observed with mid-IR interferometry at the Keck Interferometer and at the Large Binocular Telescope Interferometer (LBTI). Based on these measurements, the location of the dust could be constrained

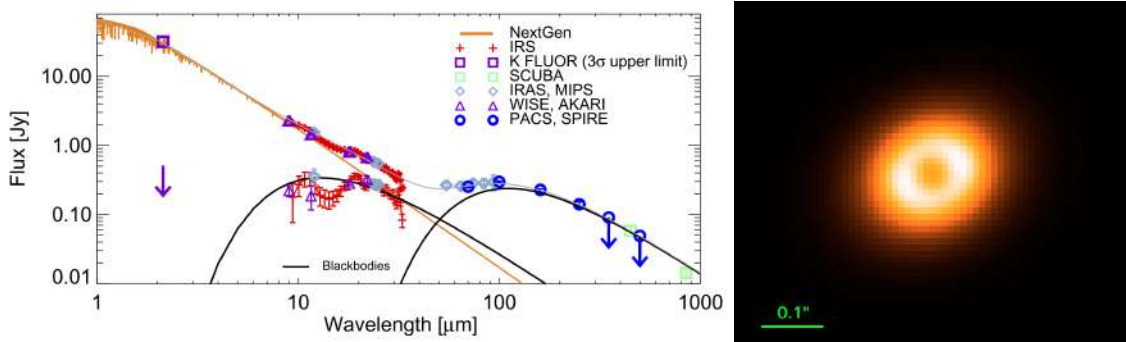


**Figure 2-15:** *Left.* Spectral energy distribution of the eta Crv debris disk (Lebreton et al. 2016b). *Right.* The eta Crv debris disk as seen by METIS in N band in 1 hour of integration time, using standard PSF subtraction based on the observation of a reference star (RDI) of similar type and magnitude, observed under similar conditions. The simulation was performed with the HEEPS end-to-end simulation tool, using the vortex coronagraph, taking into account a representative 1-h sequence of AO residual phase screens. Disk model courtesy of J. Lebreton (pers. comm.).

(Lebreton et al. 2016a): in one of the most probable disk geometries, the dust distribution extends down to 0.8 au ( $\sim 45$  mas). This case was used to test the possibility of obtaining a resolved image of a warm debris disk with METIS. This is illustrated in Figure 2-15, which showcases the capability of METIS to probe the dust distribution when using the vortex coronagraph, assuming residual PSF subtraction based on the observation of a reference star. This particular disk is only detectable at N band, where the total flux of the disk is about 0.4 Jy (at  $10 \mu\text{m}$ ). This results in a flux ratio between the integrated disk flux and the star of around 20%, but the maximum disk flux in any detector pixel is only about 0.1% of the stellar flux. The disk does not produce much thermal emission at shorter wavelengths due to the dust temperature. For instance, at L band, the contrast between the star and disk is about 1000 times higher, which makes it just out of reach of METIS. The disk would be detectable at M band within an hour of integration time, though, thanks to the onset of thermal emission at that band (see Fig. 2-15).

Some other prominent nearby debris disks with warmer dust populations, such as those around  $\zeta$  Lep, HD 69830, or HD 172555, could potentially also be detected at L band. The case of HD 172555 is particularly intriguing, as the system has recently been shown to contain CO gas, which is interpreted as the gaseous aftermath of a major planetesimal collision that happened about 0.2 Myr ago (Schneiderman et al. 2021). METIS will be the first instrument to provide the angular resolution needed to image the warm dust population in this system, located between  $0.^{\circ}03$  and  $0.^{\circ}3$  from the star (Smith et al. 2012). Asymmetries in the dust distribution due to major collisions could thus be revealed for the first time.

### 2.5.2 Exozodiacal dust

Exozodiacal dust disks (“exozodis” for short) are disks of warm ( $\sim 300$  K) dust near the habitable zones (HZ) of main sequence stars. It is expected that most planetary systems harbor small bodies (asteroids and comets) that are remnants of planetary formation. Exozodiacal dust is then supposed to be produced by evaporating comets (Faramaz et al. 2017) or dust migration from a Kuiper or asteroid belt-like debris disk due to Poynting-Robertson (PR) drag (Kennedy & Piette 2015; Rigley & Wyatt 2020) and stellar wind (SW) drag (Reidemeister et al. 2011). Steady state or sporadic production from colliding bodies in the HZ, described in the previous section, can only account for a small fraction of the excesses detected with the most sensitive instruments such as mid-infrared interferometers (Kennedy & Wyatt 2013; Ertel et al. 2018).

Studying the origins, distribution, and properties of exozodiacal dust provides present day insight into the architecture and dynamics of the inner regions of planetary systems, including the nature of HZ rocky exoplanets. Indeed, dust production scenarios have important implications for the environment in which potentially habitable planets exist. For instance, strong cometary activity may both deliver volatiles (e.g., water) to a planet, or render it unsuitable for complex life due to heavy bombardment (Kral et al. 2018; Wyatt et al. 2020). Different origins of the comets (e.g., Kuiper belt vs. Oort cloud) result in different

orbits (i.e., impact velocities), thus distinct and predictable outcomes. Impacts may also provide the energy required to form the molecule HCN, which is considered a primitive building block of life (Ferus et al. 2015). If the majority of the dust is created in an outer debris disk and migrates inward due to PR and SW drag, its radial distribution could allow us to infer the presence of giant planets outside the HZ (Ertel et al. 2012; Shannon et al. 2015; Bonsor et al. 2018). Beyond constraining the architecture of nearby planetary systems that are most relevant for exo-Earth imaging, this again has implications for the habitability of rocky, HZ planets. While Jupiter is generally understood to shield Earth from frequent cometary impacts (although this has been disputed, see Horner & Jones (2008)), other planetary system architectures were found to efficiently scatter minor bodies into the HZ (Bonsor & Wyatt 2012; Marino et al. 2018). Finally, the presence of a collisionally active, yet not depleted (thus dusty) asteroid belt near the HZ of a star at a given age would have strong implications on the architecture (at what separation can what kind of planets exist) and evolution (migration history) of a planetary system, as well as on the impact probability on potentially habitable exoplanets.

In addition to its intrinsic scientific interest, the determination of the prevalence and brightness of exozodiacal dust disks is a very active field because this information is needed for any future space mission aimed at the spectroscopic characterization of terrestrial planets in the HZ around nearby stars. Indeed, the photon noise of exozodiacal disks with densities 100 times higher than that of the zodiacal disk in our Solar System would dramatically limit the sensitivity of such missions (Roberge et al. 2012; Defrère et al. 2010; Stark et al. 2014). Furthermore, if asymmetric, an exozodiacal disk 10 times brighter than that of the Solar System could prevent the characterization of an Earth-like planet (Defrère et al. 2012). Determining the presence, dynamics, and properties of the minor bodies in and near their HZs is thus critical for predicting a true exo-Earth yield for future imaging missions and for determining the highest priority exo-Earth candidates for the time-consuming spectroscopic follow-up observations. The study of exozodiacal disks with spatially unresolved mid-infrared spectro-photometry is limited to disks about 1000 times brighter than the zodiacal disk (“1000 zodis”); the limiting factor is not photon noise, but the accuracy to which the disk emission can be separated from the overwhelming stellar light. This in turn is limited by the photometric accuracy (currently around 1%), as well as by the accuracy of the stellar photosphere model (Beichman et al. 2006). Only spatially resolved observations can probe fainter exozodiacal disks. The angular resolution required for direct imaging of exozodiacal systems is  $< 100$  mas (1 au for a star at 10 pc). This requirement immediately sets the need for a telescope diameter larger than 20 meters when observing at N band<sup>4</sup>. Note that JWST, with its aperture of 6.5 m, is far from providing such high angular resolution.

With their superior angular resolution, ground-based mid-infrared interferometers such as the Keck Interferometer Nuller and the Large Binocular Telescope Interferometer have been funded by NASA to survey the habitable zone of nearby main sequence stars to determine the prevalence of exozodiacal dust (Mennesson et al. 2014; Ertel et al. 2018). In particular, the recent results of the LBTI exozodi survey in the northern hemisphere have shown a detection rate of 26% for a sample of 38 nearby main-sequence stars, with a median  $3\sigma$  sensitivity of about 100 zodis (Ertel et al. 2020). These results put a strong constraint on the median dust level, with is below 27 zodis at 95% confidence. New projects are now being developed for the Very Large Telescope Interferometer to carry out similar surveys in the southern hemisphere (Defrère et al. 2018). While very sensitive, such interferometric observations provide very sparse spatial information, compared to what is achievable with the full aperture imaging promised by the ELT. Thanks to its increased sensitivity (point-source sensitivity around  $50 \mu\text{Jy}$  in 1h at N band), combined with its high angular resolution ( $\lambda/D = 50$  mas at N band), the ELT is *the* machine to study exozodiacal emission in the 1 au region around nearby stars ( $< 10$  pc). Based on the predicted point-source sensitivity and achievable contrast of METIS at N band with its vortex coronagraph, we estimate that 100-zodi disks, boasting a total flux of about 20 mJy at N band and an integrated contrast of about 0.1% with their host star, will be within reach. While METIS on the ELT is probably not the most appropriate instrument to extend blind N-band exozodi surveys to the southern hemisphere, it could be used to better characterize the dust distribution in

<sup>4</sup>Blackbody dust at 1 au heated by a solar-type star would reach an equilibrium temperature of 270 K and would thus have its peak emission around  $10 \mu\text{m}$

the handful of exozodis previously detected with the Keck Interferometer Nuller or the LBTI, or to follow up some nearby WISE detections. The combination of such a program with a planet-hunting research program, as performed in the northern hemisphere on the LBTI with the LBTI Exozodi Exoplanet Common Hunt (LEECH) survey (Stone et al. 2018), would also be particularly time efficient and scientifically valuable by providing simultaneous constraints and/or detection of exoplanets and exozodiacal disks to better understand the nature and evolution of planetary systems (Defrère et al. 2021). Finally, METIS observations of exozodiacal light will be complementary to ALMA observations of the cooler dust in exo-Kuiper belts located at a few tens of au from the star (Hughes et al. 2018). Combining ELT/METIS and ALMA will give a complete picture of debris disks around nearby stars and allow to study, in a statistical way, the link between planet formation and debris disks, as well as the connections between the inner and outer parts of forming planetary systems.

### 3 DETECTION AND CHARACTERIZATION OF EXTRASOLAR PLANETS

#### 3.1 Scientific context

How unique is the Solar system, and Earth in particular? What range of atmospheres do planets have, and why? What are their climates, and what determines whether they are habitable or not? Is there life on other worlds? Excitingly, answers to these existential questions about humanity’s place in the Universe will soon be within reach of astrophysical investigations and they are close to the heart of the science case of the ELT, and METIS in particular.

Within the past generation, a plethora of exoplanet discoveries has shown that planetary systems are very common and diverse (e.g. Dressing & Charbonneau 2015). Ground-based radial velocity surveys (e.g., with ESO’s HARPS spectrograph), transit surveys (e.g., from NASA’s Kepler and TESS missions from space), and high-contrast imaging surveys on 6-12 m-class telescopes (e.g., with SPHERE, GPI) have revealed new classes of planets unknown in our Solar System. These include hot Jupiters, gas giants very close to their host stars, super-Earths or mini-Neptunes, which together represent the majority of exoplanets, and rare massive gas giants on very wide orbits (e.g.,  $>30$  AU). In addition, transit surveys have revealed small rocky planets that are so close to their star that they are disintegrating, showing highly variable tails of dust evaporating off their planet surfaces (Rappaport et al. 2012). They also revealed the existence of compact multi-planet systems, that contain several planets within the orbit of Mercury (Lissauer et al. 2011; Gillon et al. 2017). One of the great goals of exoplanet science is to link this wide variety to formation and evolution theory, including migration scenarios, informed by the ground-breaking observations of protoplanetary disks.

The demographics of planets within a few AU of their parent stars is already relatively well known, with about one in ten of the solar-type stars harbouring gas-giants, one in four harbouring Neptune-mass planets, and most stars having rocky planets (e.g., Petigura et al. 2013; Dressing & Charbonneau 2015). The ubiquity of Earth-size planets is most evident around cool red dwarf stars detectable with radial velocity and transit methods. Combined, they have made two of the most exciting discoveries in recent years; Proxima b, a planet in an 11-day orbit around our nearest neighbour that could sustain liquid water on its surface (Anglada-Escudé et al. 2016), and the TRAPPIST-1 system of seven Earth-size planets, with two or three of these within the star’s habitable zone (Gillon et al. 2017). This immediately raises questions about whether the atmospheres of small planets around late M-dwarfs could support life. Their atmospheres could be eroded by the energetic flares of their host stars. It has also been suggested that they could have lost all their water in the extended pre-main sequence phase during which their host stars were significantly brighter (Segura et al. 2010; Ribas et al. 2016; Turbet et al. 2016). In the coming years, leading up to ELT’s first light, an almost complete census of the local exoplanet population will be achieved, in particular for planets on relatively close-in orbits around late-type stars (e.g., Ribas et al. 2018), by dedicated radial velocity machines (e.g., HARPS, NIRPS, HARPS-N, ESPRESSO, CARMENES, HARPS3), and transit surveys (e.g., TESS, CHEOPS, PLATO, SPECULOOS).

##### 3.1.1 Planet characterization

Tremendous progress also been made in the characterization of extrasolar planets. Most planets are found indirectly, without identifying photons from the planets themselves. However, atmospheric characterization requires separation of planet light from that of the star. To understand habitability, and to be able to unambiguously identify potential bio-marker gases in the future, a deep understanding of atmospheric processes and evolutionary histories of planets is necessary, over a wide range of planet orbit, mass, and stellar host star characteristics. What range of compositions are typical of planetary atmospheres? Do we understand their chemistry? Can we link elemental abundances to formation processes? What are the main

atmospheric circulation patterns? What are their climate like? How important are disequilibrium processes, like haze formation, photochemistry, and mixing? How have the atmospheres evolved over time?

The first successful studies of extrasolar planetary atmospheres were obtained from transmission and secondary eclipse spectra of transiting hot Jupiters using the Hubble Space Telescope (HST) and the Spitzer Space Telescope (e.g., Charbonneau et al. 2002; Deming et al. 2005). These studies revealed absorption from atmospheric sodium, hydrogen, helium, oxygen, carbon and even heavier elements in the extended exospheres of hot Jupiters (e.g., Spake et al. 2018; Nortmann et al. 2018). In addition, molecular absorption features from water vapor have been revealed for more than a dozen planets as well as evidence for Raleigh scattering at UV and optical-blue wavelengths (Sing et al. 2016). Extension of such studies to cooler and smaller planets has proven challenging, possibly due to clouds or metal enhancement that strongly dampen potential transmission features (Kreidberg et al. 2014; Crossfield & Kreidberg 2017). Secondary eclipse spectroscopy and phase curve measurements in the near- and mid-infrared have constrained the day-side temperatures and thermal structures - both vertically and longitudinally - for some of the hottest planets. They provide the first insights in how stellar energy is absorbed by such planet atmospheres and distributed to the night side as a first test for global circulation models (Showman et al. 2009; Knutson et al. 2007; Stevenson et al. 2014). The first thermal phase curves have been measured for rocky planets, revealing that the planet has lost its atmosphere (Kreidberg et al. 2019).

The James Webb Space Telescope (JWST), which launched on 25 December 2021, will provide another leap forward in planet atmospheric studies in the years prior to METIS first light, using transmission and secondary eclipse spectroscopy (evidenced by a large number of accepted Cycle 1 GO and GTO proposals). Its ability to observe a large part of the near-infrared spectrum simultaneously ( $4\times$  increase compared to HST), increased stability from its L2 orbit,  $5\times$  larger collecting area than HST, and in particular its ability to observe over a wide range of MIR wavelengths will be unique. It is expected to provide detailed spectral signatures of the most important detectable molecules for hot and warm Jupiters, and push towards smaller and cooler planets - in particular by observing at long wavelengths where clouds and hazes are less obscuring (e.g., Morley et al. 2017; Benneke et al. 2019). JWST/MIRI will probably be able to detect thermal emission from the hottest planet in the TRAPPIST-1 system and determine whether it has an atmosphere - a first step towards the general assessment of habitability on planets around red dwarf stars (Ribas et al. 2016).

### 3.1.2 Ground-based techniques

In parallel to space-based observations, ground-based techniques play a vital role, including perhaps the fastest route to the first direct images of temperate rocky planets<sup>5</sup>, a goal that will only be achieved in the 2040s in space (National Academies of Sciences & Medicine 2021). High-contrast imaging, through the continuing development of advanced adaptive optics and coronagraphic techniques (e.g., VLT/SPHERE, Gemini/GPI), has now discovered about a dozen planetary systems. In direct imaging, detection means immediate characterization, with multi-wavelength observations revealing molecular absorption signatures from, e.g., water and methane. Direct imaging observations are currently restricted to young (< 300 Myr) systems in which the (gas giant) planets still radiate significant heat of formation. While micro-lensing surveys, radial velocities, and astrometry from GAIA all play an essential role in assessing the demographics of planetary systems (e.g. planet occurrence as well as mass and orbital distributions), only direct imaging provides constraints on luminosities and temperatures (and thus radii), as well as atmospheric composition for long-period planets (those beyond 1 AU).

Another powerful characterization technique developed over the last decade is high-resolution spectroscopy ( $R\sim 100,000$ ; Snellen et al. 2010a; Brogi et al. 2012). The high resolving power is used to separate the much stronger contribution from the star from the planets, remove absorption from the Earth's atmosphere (allowing unambiguous detection of atomic and molecular features), and exploit the Doppler effects from the orbital motion of the planet to further isolate the planet emission. This enables characterization of

<sup>5</sup>Exoplanet Science Strategy Report 2018; National Academy of Sciences

atmospheric winds and circulation, and the spin-rotation of the planet (Snellen et al. 2015). Particularly powerful is the combination of the two methods — high-contrast imaging and high-resolution spectroscopy (e.g., Sparks & Ford 2002; Riaud & Schneider 2007; Kawahara et al. 2014; Snellen et al. 2015; Lovis et al. 2017). Although this technique is still developing (Snellen et al. 2014; Hoeijmakers et al. 2018), it is being implemented with high priority on the VLT, Keck, Subaru, and LBT telescopes (e.g., Jovanovic et al. 2019; Kotani et al. 2020; Vigan et al. 2018) — and now with METIS on the ELT.

### 3.1.3 The power of METIS

METIS will be transformational in exoplanet studies for several reasons:

- The increase in telescope diameter from the VLT to the ELT results in an improvement in angular resolution  $\times 5$ , crossing a critical threshold as most planets are found between 1-10 AU from their host stars.
- The mid-infrared wavelength range probes significantly colder (thus older) planets — with the sensitivity to small mature planets in the direct vicinity of the Sun.
- The integral field spectrograph with a resolving power of  $R=100,000$  is unique in the world, and the ideal tool to combine the high-resolution spectroscopic techniques with high-contrast imaging. Characterization of the temperate planet Proxima b will be within reach (see Section 3.3).

As detailed below, METIS will open up vital new parameter space (cf. Figure 3-1), revealing mature gas giant planets as well as temperate rocky planets around nearby stars. Characterization of the hottest planets will result in atmospheric surface maps, detailed temperature structures as function of longitude, molecular abundance ratios, and even isotopic probes of formation chemistry (Mollière & Snellen 2019). As a primary goal, basic characterization can be extended to temperate rocky planets in the habitable zones of our nearest neighbours, such as Proxima b, revealing whether it has an atmosphere, its day-side temperature, and whether it retains carbon dioxide, methane, and/or water — a first assessment of the habitability of this enigmatic world.

The study of extrasolar planets will be one of the prime science goals of METIS and with its unique combination of spatial resolution, spectral resolution, and unprecedented sensitivity from the ground, METIS will have a ground-breaking impact in both extrasolar planet detection and characterization. Some key science cases are detailed in the following sections. It should be emphasized that the main focus in this chapter is put on mature exoplanets and that science cases related to planet formation and young (proto-)planets are discussed in chapter “Protoplanetary Disks and the Formation of Planets”. Also, the investigation of free-floating planetary mass objects is not discussed, as neither high-spatial nor high-spectral resolution are required to characterize the spectral energy distributions of such objects, perhaps best done by JWST.

## 3.2 Planetary demographics

Given the sensitivity of current AO systems on 6-12 meter telescopes from 1-2.5 microns, gas giant planets  $< 3$  Jupiter mass are only accessible at if they are young ( $< 100$  Myr), found around stars  $<< 1$  kpc, and located at projected separations  $> 5\text{--}10 \lambda/D$ . The nearest stellar samples this young are at distances of 10-100 pc, yielding characteristic orbital distances probed  $> 20$  AU. METIS on the ELT will win in three ways; first with its larger aperture, it will achieve the  $5\times$  finer spatial resolution for the same target at comparable wavelength compared to the VLT (e.g. ERIS at 3–5  $\mu\text{m}$ ). Second, the greater sensitivity and longer wavelengths accessible will enable searches for colder planets, found around older stars. And third, these stars can be found closer to the Sun resulting in an extra physical resolution (and sensitivity) boost in the search. Thus METIS will open up completely new discovery space for exoplanet imaging studies (cf. Figure 3-2).

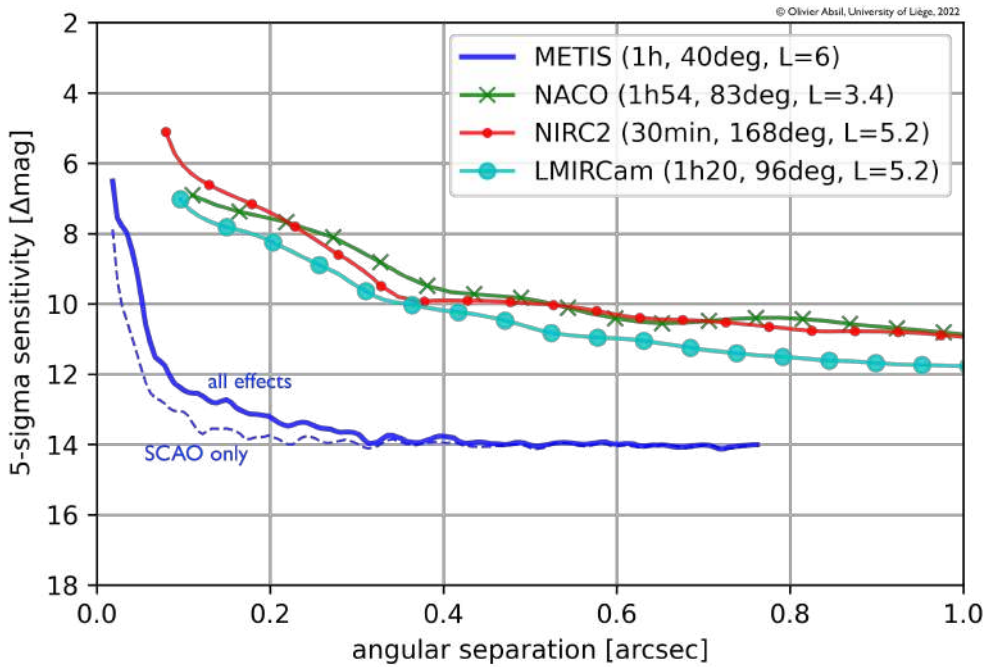


**Figure 3-1:** Illustrating the discovery space of high contrast imaging with METIS in the L band. Comparison between measured contrast curves obtained with VLT/NACO, NIRC2 at Keck, and LMIRCam on the LBT in the L band using an AGPM Vortex coronagraph (e.g. Absil et al. 2013b, yellow curve) and predictions for ELT/METIS in the same filter based on the end-to-end high-contrast simulator with a ring-apodized vector coronagraph (RAVC) for a 1h ADI sequence: the solid line includes all possible complicating effects including random phase variations induced by changes in water vapor column above the telescope, while the dashed line assumes only known limitation of the SCAO system (assuming all other issues have been dealt with in post-processing). The achieved contrast with METIS on the ELT will probably be intermediate between these two extremes.

### 3.2.1 Direct detection of known gas giant planets

**Planets detected by RV or astrometry:** Perhaps the highest priority of the direct imaging community is to constrain temperatures and luminosities of planetary mass companions with dynamical mass constraints. In addition to providing vital information needed for accurate characterization, such data fundamentally calibrate evolutionary models, required to interpret results from direct imaging surveys for demographic studies.

While masses and brightness temperatures are known for numerous hot Jupiters and some warm Neptunes from transit and secondary eclipse studies, dynamical masses are available for only a handful of young low gravity directly imaged exoplanets via astrometry from Hipparcos, Gaia, and VLTI/GRAVITY (Snellen & Brown 2018a; Nowak et al. 2020; Hinkley et al. 2022). Most RV detected planets tend to orbit too close to their host star for current imaging instruments to spatially resolve them (e.g., Zurlo et al. 2018) or they are simply too faint for existing facilities (Mawet et al. 2019). In the case of the HR8799 system we have at least some dynamical constraints on the planets’ mass from stability arguments (Wang et al. 2018). With METIS, this situation will fundamentally change.

A first analysis to estimate how many of the known RV planets are accessible to METIS in at least one filter was presented in Quanz et al. (2015b). In Figure 3-3 we show an example demonstrating that METIS will be able to directly image RV detected planets taking into account updated contrast and sensitivity performance. We went through all RV planets listed in the exoplanet.eu database and computed the most favorable epoch for direct imaging observations given the estimated projected separation given the orbit and distance. We assumed the planet’s effective temperature predicted by evolutionary models based on its age and minimum mass or its equilibrium temperature given its separation and the luminosity of its host

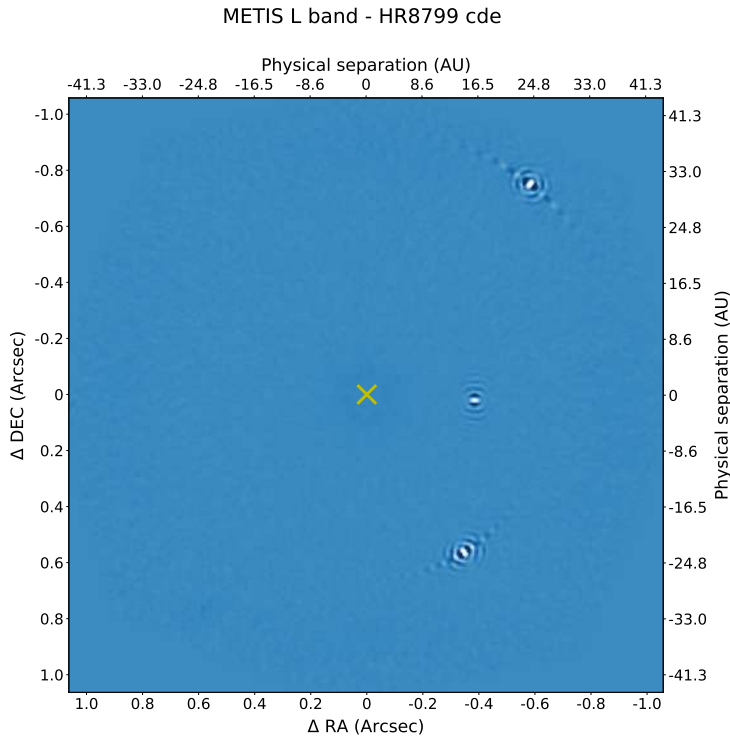


**Figure 3-2:** METIS simulations of the HR8799 planetary system in L band with the ring-apodized vortex (RAVC) using the HEEPS high-contrast imaging simulator and assuming 1h of observing time. The four planets are within the METIS FoV, but our simulations stop at 1.2'' and therefore only show the inner 3 planets (c, d, and e) with SNRs of 49, 21, and 19, respectively. Additional, closer-in planets are easily detectable if they exist.

star and assuming a Bond albedo of 0.3 (whichever was larger). For at least 8 planets (including Eps Ind A b (Feng et al. 2019) and Eps Eri b (Mawet et al. 2019), which are both located close to the background-limited regime), METIS will detect them in the L' and/or M' filter in 1-2 hours observing time. Covering a range in effective temperature and gravity, these detections will provide the fundamental calibration needed to ground the evolutionary models, enabling reliable mass estimates from direct imaging surveys.

In the next several years the list of potential targets will increase dramatically due to emerging astrometry and the longer time baselines of RV surveys. Snellen & Brown (2018b); Kervella et al. (2019) have shown that it is already possible to see the astrometric signal of select known exoplanets by combining Gaia DR2 with Hipparcos.

And new discoveries of long-period gas giants through legacy RV surveys of mature stars provide unique targets such as highly eccentric planets that can be detected directly near apastron (cf. Blunt et al. 2019). A growing body of theoretical work has shown that these planets, which are in super-eccentric orbits possibly due to an external perturbing (third) body (e.g., Socrates et al. 2012; Dong et al. 2014) experience significant *tidal* heating as they pass through periastron. As a result, despite their roughly solar ages, the self-luminosity of these tidally heated planets is dramatically boosted by 2-3 orders of magnitude to star/planet contrasts of  $\sim 10^4\text{-}10^6$ . These vastly more favourable contrasts, combined with the angular separations from their host star of a few  $\lambda/D$  at apastron, places them within reach of the imaging capabilities of METIS at  $3\text{-}5 \mu\text{m}$  (Dong et al. 2013). The population of highly eccentric Jovian planets will place extremely powerful constraints on the interior structure and central concentration of planet interiors, such as the tidal “Q” factor and Love number (e.g., Batygin et al. 2009; Barros et al. 2022) which can, in turn, help to understand the rheology of these planets and disentangle between various formation scenarios.

ESA’s Gaia astrometry mission promises to provide a crucial leap forward in the ability to identify additional targets with dynamical masses which can be directly detected with METIS on the ELT. As the astrometric reflex motion of the star is proportional to the mass ratio of the planet to the star, and orbital

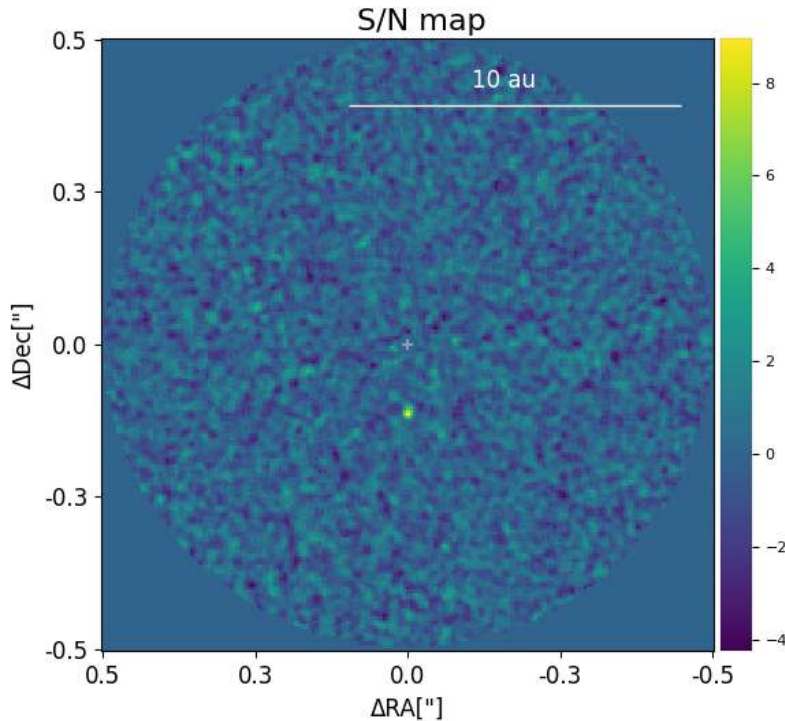


**Figure 3-3:** METIS high-contrast simulations using HEEPS+Scopesim for HD 128311 ( $L' = 5.14$  mag) in the L' filter. One hour of observing time with the ring apodized vortex coronagraph in pupil tracking mode processed with a median subtraction ADI technique. The radial velocity planet HD 128311 c (0.12" separation,  $3.2 M_{\text{Jupiter}}$  and  $5.2 \times 10^{-6}$  contrast) is clearly detected.

separation, wide-orbit gas giants around M dwarfs will be easily detected (Sozzetti et al. 2014). First estimates on the final astrometric performance of GAIA, based on in-flight data, are available<sup>6</sup>. Yet a detailed assessment of the potential yield requires assessment of the Gaia performance as a function of fractional orbital coverage (cf. 10 year mission lifetime < orbital period), and the expected population of planets (peaking between 1–10 AU) Perryman et al. (2014).

The MST is still assessing the potential overlap between new Gaia detected planets as a function of star age and distance, for comparison with the METIS high contrast imaging performance. However, Wallace et al. (2021) has already investigated the detectability of exoplanets in the infrared using several high contrast instruments at VLT, VLTI, Keck, JWST and ELT following their initial astrometric discovery with Gaia. They took a sample of stars of the nearest associations with age  $< 800$  Myr,  $d < 70$  pc and populated them with planets drawn from the statistics from Fernandes et al. (2019). They used the Gaia detection statistics of Perryman et al. (2014) to predict which ones were detectable in the astrometry and afterwards used various detection curves to derive the number of Gaia-discovered planets that would be detected with current and future instruments (including preliminary METIS detection limits). In their sample of over 1700 host stars, about 100 giant planets would exist, 1/3 seen by Gaia, of which 6–10 would be detectable by METIS in L' band (M and N bands were not considered in this paper): a detection rate significantly better than any other existing or forthcoming instruments. This could be an underestimate given that M-band could be substantially more sensitive to cooler planets around slightly older stars. In addition the combination of search techniques including long-term RV, astrometry, and direct imaging has proven to be increasingly valuable through joint analysis (e.g. Hinkley et al. 2022).

<sup>6</sup><https://www.cosmos.esa.int/web/gaia/science-performance>

### 3.2.2 The occurrence rate of long period gas giant planets

At least half of all gas giants are found beyond the ice line, approximately 3 AU around Sun-like stars and it is vital to investigate the dependence of occurrence rates, as well as mass and orbital distributions as a function of host star mass, multiplicity, and composition. As such, direct imaging will continue to play a key role in constraining wide orbit demographics as a crucial test of planetary system formation and evolution theory. For young gas giants of a given age and bolometric luminosity, there is a unique effective temperature for a young planet that depends on the specific entropy of the body which in turn depends sensitivity on its assembly history. Observing the *luminosity* of these objects in the first few million years is essential to constrain models of their initial entropy and temperatures (e.g., Fortney et al. 2008). Finally, observing low-mass companions as early as possible (e.g., Kraus et al. 2014) can help illuminate changes in orbital distributions due to dynamical evolution (e.g., Scharf & Menou 2009; Chatterjee et al. 2008), providing initial conditions for theoretical models.

**Young Star Targets:** To simulate the sensitivity to low-mass (planetary) companions using high contrast imaging with METIS, 35 early-type stars (spectral types A to F) were selected from the de Zeeuw et al. (1999) compilation of objects in the  $\sim$ 11–16 Myr Scorpius-Centaurus Star forming region (hereafter “Sco-Cen”). The selected targets have a mean distance of 130 pc, a membership probability of  $>95\%$  as determined by Rizzuto et al. (2011), and were verified as single stars from the literature (i.e., no unresolved binary companions). An assumed age of 11–16 Myr, was combined with the distance and L-band contrast (cf. Figure 3-1) to determine the gas giant yield for each target using evolutionary models from (Baraffe et al. 2003). The Multi-purpose Exoplanet Simulation System (“MESS”) software (Bonavita et al. 2013) was used to derive a map of our completeness as a function of limiting mass and semi-major axis for the ensemble of 35 stars.

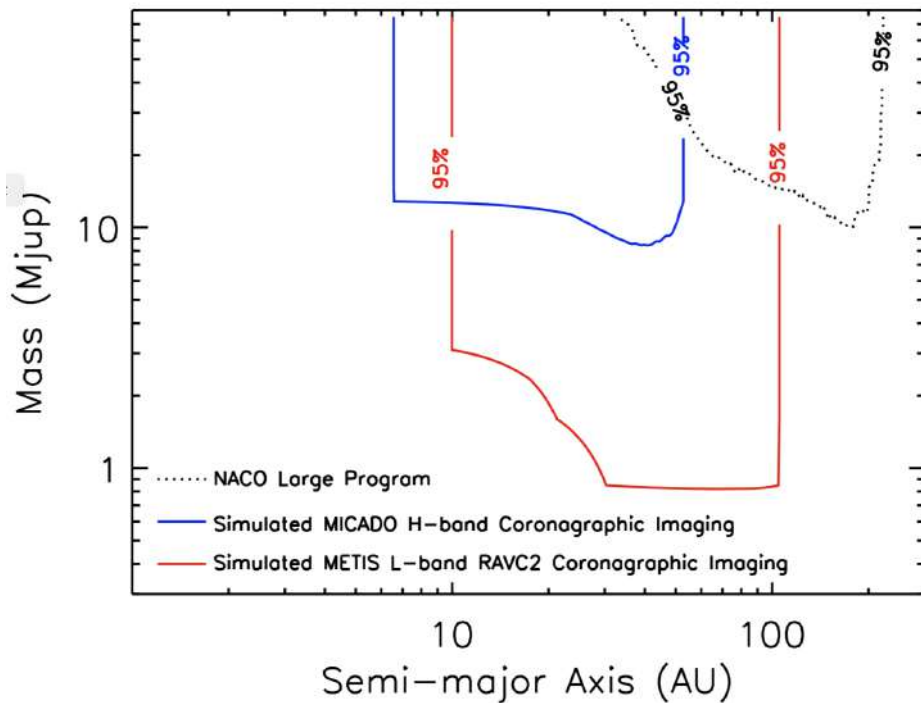


**Figure 3-4:** Simulated discovery space for low-mass companions expressed in terms of 95% completeness contours for a sample of 35 stars in the 11–16 Myr Sco-Cen star forming region using METIS L-band high contrast imaging with the RAVC coronagraph (red line). Also shown is the corresponding sensitivity for the same set of stars using MICADO in the *H*-band (blue). For reference, the corresponding 95% completeness contour for the recently completed VLT NACO Large Program survey (Vigan et al. 2017) is shown in black.

Figure 3-4 shows the results of this exercise, displaying the expected 95% completeness for METIS L-band high-contrast imaging using the RAVC coronagraph, combined with speckle removal at the post-processing

stage (red line). For reference the 95% confidence contour for the NACO Large Program survey (Vigan et al. 2017, black curve) is also shown. We also compare METIS to the estimated H-band contrast performance for MICADO (Perrot et al. 2018) for the same 35 Sco Cen stars. The H-band provides finer angular resolution on the ELT ( $\lambda/D \sim 8$  milliarcseconds at H-band), as well as higher absolute contrast but lower Strehl (e.g.,  $\sim 20\%$  Strehl). Completeness contours were then generated for MICADO in the same manner with MESS, and are plotted in Figure 3-4. Because planets this cold are brighter from 3-4  $\mu\text{m}$  (e.g., Baraffe et al. 2003), METIS operating in L-band is able to detect lower mass planets ( $\lesssim 0.5\text{-}1.0 M_{\text{Jup}}$ ).

Another parameter space worth exploring is to search for gas giant planets around nearby M dwarfs, at older ages of 1-5 Gyr. Here we take advantage of the target distances ( $< 8$  pc), rather than youth, to probe down to low temperatures where M-band observations at 4.8  $\mu\text{m}$  is best. METIS achieves background-limited performance for stars fainter than 5th magnitude in M-band beyond 0.2 arcseconds, or  $> 1$  AU for targets at 5 pc. The background-limited sensitivity in one hour should reach 1 Jupiter mass for stars 1 Gyr, and 3 Jupiter mass for 5 Gyr (cf Bowens et al. 2021). Given that most gas giants around M dwarfs are found beyond 1 AU (Meyer et al. 2018), such a survey of the nearest M dwarfs would yield a near complete census for gas giants. Such information is vital context for designing searches for habitable planets around our nearest neighbors, given the impact a gas giant near the iceline has on the composition of inner rocky planets (Lambrechts et al. 2019).

The goal of this discussion is to demonstrate the possibilities afforded by METIS on the ELT for imaging gas giant planets around nearby stars, young and old. Such a blind survey conducted at the ELT would certainly require the support of a large fraction of the community given the required telescope time. It may be that METIS is restricted to surveying nearby stars where RV and/or Gaia astrometry indicates the presence already of a planet. However, the tremendous increase in imaging sensitivity afforded by METIS, combined with its access to small separations (down to a few AU) would allow us for the first time to probe for exoplanets on Solar System scales around hundreds of nearby stars.

### 3.3 Atmospheric properties and climates

METIS will bring unparalleled instrumental power to the field of exoplanet atmospheric characterization. Its combined high spectral resolution and IFU capabilities make it a unique machine with the potential to deliver game-changing results, from the first atmospheric maps of giant exoplanets (exocartography) to the first detections of possible bio-signatures in our nearest neighbouring rocky worlds, such as LHS 1140 b (Wunderlich et al. 2021) and Proxima b.

At the spectral resolution of METIS ( $R=100,000$ ), the dense forest of lines in molecular bands are individually resolved, revealing the line shape of the planetary spectrum (see Figure 3-5 and Birkby 2018). This probes not only the atmospheric composition and structure, but gives access to a full 3-dimensional view of the planet's atmospheric dynamics and global weather patterns, including day-to-night winds and jet-streams (e.g. Snellen et al. 2010b; Brogi et al. 2016; Flowers et al. 2019), as well as the length of the planet's day or its tidal-locking via rotational spectral broadening (Snellen et al. 2014; Schwarz et al. 2016; Brogi et al. 2016). Current instrumentation limits this work to hot Jupiters and the very brightest of the directly imaged planets. METIS opens the door to smaller, cooler worlds, including the bountiful yet enigmatic super-Earths and mini-Neptunes, and into the Earth-like analogues. Below we discuss these key advancements that METIS will bring by dividing the exoplanet population into short and long orbit systems. The latter requires both the high spatial and spectral resolution of the METIS IFU to disentangle the planet from its host star, while the former relies on the high resolution alone, using only the Doppler shift of the planet's spectrum to extract it from the glare of its host star.

#### 3.3.1 Short-period planets

A major driving force behind the design of the METIS high-resolution ( $R=100,000$ ) L and M band integral field spectrograph is the ground-breaking success of the high spectral resolution technique used with

instruments such as CRIRES(+), to characterize the atmospheres of hot Jupiters. This includes the first unambiguous ground-based detection of water in an exoplanet (Birkby et al. 2013), and the first atmospheric characterization of a non-transiting close-in planet (see Figure 3-5, Brogi et al. 2012). Both of these were key in optimizing METIS to search for bio-signatures of the nearest exoplanets, as these are unlikely to transit their host stars. The technique has also has great potential to determine the full chemical census of exoplanet atmospheres, including rare or less spectrally active components. For example, five C- and O-bearing molecules were recently detected in an hot Jupiter atmosphere (Giacobbe et al. 2021), and seven atomic metals were identified in an ultra-hot Jupiter atmosphere (Hoeijmakers et al. 2020). These detections are the result of integrated signals i.e. the sum of all the spectral lines in the molecular band. METIS' strong increase in sensitivity compared to present-day facilities promises to open a whole new range of measurements. For the first time we will have high signal-to-noise, high-resolution spectra of exoplanet atmospheres where we can measure the strengths of individual lines. This enables detailed atmospheric modeling, including probing the atmosphere as a function of both altitude and longitude, and revealing dawn-to-dusk variations in the planet's chemistry.

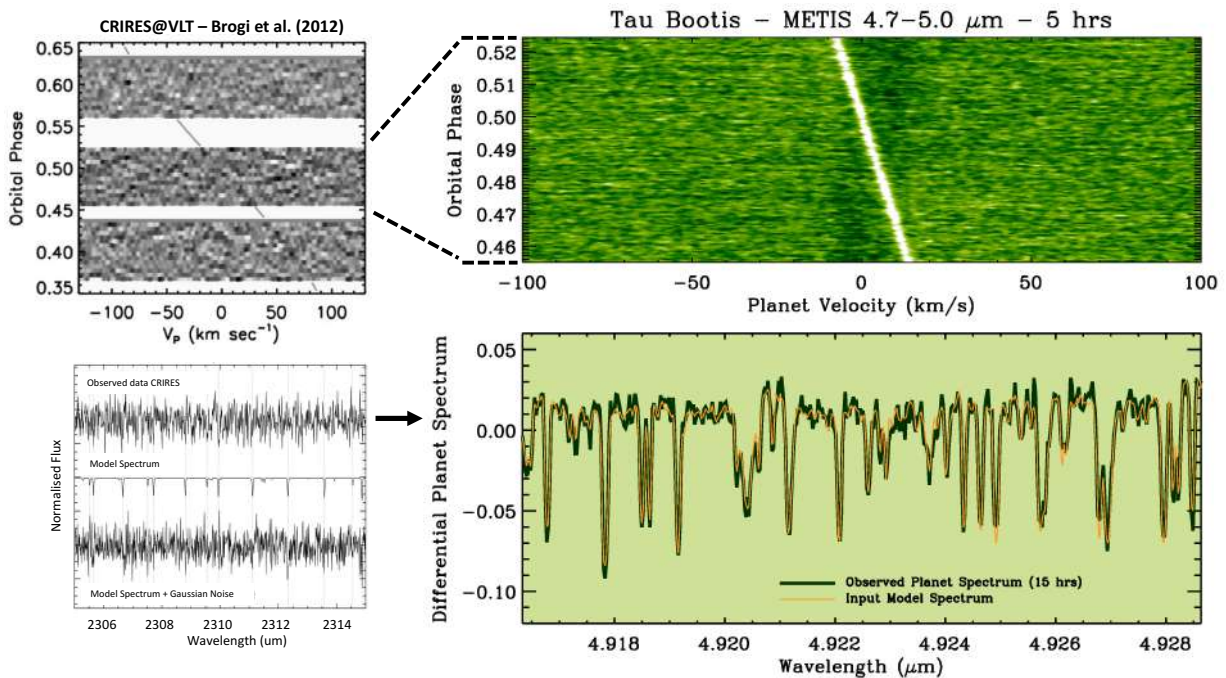


**Figure 3-5:** METIS IFU simulations of dayside spectroscopy of the hot Jupiter Tau Bootis b. The upper and lower left panels show the planet cross-correlation signal as function of orbital phase and the integrated planet spectrum as obtained with CRIRES at 2.3 micron (Brogi et al. 2012). Individual planet lines were visible at about 1 sigma, making the planet detectable only by integrating over time and over all observed lines. The right panels show the same for simulated METIS observations at 4.7-5 micron. The individual planet lines are detected up to 10 sigma, allowing for detailed atmospheric characterization.

Our calculations based on the METIS instrument design and the current sample of known exoplanets indicate that at least 10 short-period gas giants can be studied in this unprecedented detail, with S/N per line  $> 10$  with just a 1-3 half nights of observation (assuming photon-limited statistics). A single planet studied with CRIRES+/VLT to this level would take a half year of observations ( $\sim 185$  nights). Moreover, a key sample of at least 10 mini-Neptune-like planets will become accessible with METIS with integrated signals at  $S/N > 5$  for thorough inventories of their atmospheric constituents and studies of their atmospheric circulation. Again, it would take  $\sim 200$  nights to achieve the same for just one mini-Neptune with CRIRES+. METIS will be the instrument to reveal details about this poorly understood class of exoplanet that are the most common outcome of the planet formation process. The infrared wavelength coverage afforded by METIS will also be key to peering through the clouds and haze that are known to be prevalent on sub-Neptunes, because molecular features are larger at longer wavelengths and high spectral resolution

observations are sensitive to higher altitudes (Benneke et al. 2019; Hood et al. 2020; Gandhi et al. 2020).

The high-dispersion IFU mode of METIS will also be ideal to determine isotopologue ratios in exoplanet atmospheres — a measurement that was recently performed for the first time for 13CO for the super-Jupiter YSES-1b (Zhang et al. 2021). Isotopes of carbon, oxygen and hydrogen can potentially be detected via CO, CO<sub>2</sub>, CH3D and HDO, providing unique insights into the formation history, such as icy body enrichment, and atmospheric evaporation processes, for a wide range of exoplanets (Mollière & Snellen 2019). CH3D can be best targeted at 4.7 microns, and may be detectable in planets below 600 K in equilibrium temperature. In this case, the sky background becomes the dominating noise source for self-luminous planets. HDO is best targeted at 3.7 microns, and is less affected by sky background noise. It may lead to its detection for planets with equilibrium temperatures below 900 K. If Proxima b is water-rich, the HDO isotopologue could be detected with the ELT in less than a few nights of observing time in its reflected-light spectrum (Mollière & Snellen 2019).

METIS observations will also be able to constrain the rotation rate of short-period planets. Close-in planets undergo strong tidal interactions with the parent star and are thus often believed to be tidally locked, making the rotational period of these objects identical to their orbital periods. However, when the eccentricity of the orbit is not exactly zero, a number of spin-orbit resonances emerge that delay the evolution to the synchronous state (e.g., Correia et al. 2014). As a result, short-period planets can also present asynchronous rotation, which can be measured by METIS. This result allow us to put constraints on the internal structure and rheology of these planets, and also directly impacts the habitability of planets around M-dwarfs, such as Proxima b.

All this illustrates the enormous discovery potential for METIS, providing unique information on exoplanets and their atmospheres inaccessible to any other currently planned facility. It should be mentioned that, in particular for this observing mode, METIS will have strong synergies with the ELT ANDES instrument that covers the optical and near-infrared wavelength range. Combined, these instruments will deliver the most detailed probes of the atmospheres of short-orbit planets, covering a vast range of atmospheric pressures and scale heights, temperatures ranges, and molecular species. This will enable a far deeper understanding of the full range of systems possible as end-products of the planet formation process, and give insight into the commonality of other Earth-like worlds.

### 3.3.2 Long-period planets

METIS will also contribute significantly to our understanding of longer period (gas giant) planets. One decade ago, astronomers believed that it would take a space interferometer of several kilometers in size to resolve structures on exoplanets — beyond the dreams of even the biggest optimists. However, work with CRIRES/VLT indicated that Doppler-imaging, a technique regularly used to map star spots on stars, can also be used to map the atmospheric features of field brown dwarfs, as shown in Figure 3-6 (Crossfield et al. 2014). Crossfield (2014) further show that there are at least 10 more brown dwarfs that could be mapped with METIS' IFU using the SCAO. Even more excitingly, simulations by Snellen et al. (2014) show that METIS has the power to map features e.g. large storms like Jupiter's Great Red Spot, in the atmosphere of beta Pic b, one of the brightest directly imaged planets. This could be done twice as fast as it took to map the brown dwarf with the VLT, despite the nearby bright host star. This is thanks to the powerful combination of both high-resolution spectroscopy and high spatial resolution the METIS IFU design.

In addition to mapping the 2D appearance of exoplanet atmospheres, high-resolution spectroscopy showed that another new observable has emerged helping to constrain planet evolution — planetary spin. Observations with CRIRES show that the exoplanet  $\beta$  Pictoris b spins with an equatorial velocity of almost 100.000 km per hour, implying an 8 hour day on this world (Figure 3-6; Snellen et al. 2014). Interestingly, the fact that  $\beta$  Pictoris b spins so fast is well in line with the trend of spin rotation with planet mass seen for the solar system planets, and is likely a relic of the planet formation process during which mass and angular momentum are accreted. METIS will determine the rotation of dozens of exoplanets for a range of masses — an exciting new science case. These planets are also highly suited for dawn-to-dusk and seasonal stud-

ies, monitoring throughout their days and along a large part of their orbits, tracing the seasonal as well as rotational changes in molecular signals.

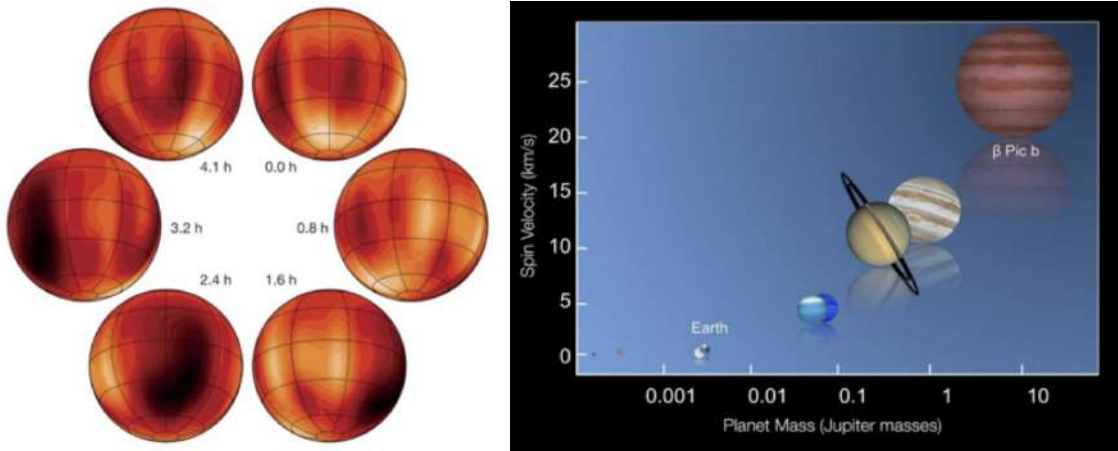


**Figure 3-6:** Left: Illustration of the Doppler Imaging technique with VLT/CRIRES showing a 2D map of the nearby brown dwarf Luhman 16 B (Crossfield et al. 2014). Right: Comparing the spin velocity of the exoplanet  $\beta$  Pictoris b, as measured from high-resolution spectroscopy, with the spin of the Solar System planets (Snellen et al. 2014).

The design of METIS affords one further key advantage in the understanding of the planet formation process. Spectroscopic observations in the L and M band with METIS' long-slit modes provides a spectral resolution of  $R \approx 1500-2000$  over the whole spectral windows, allowing constraints on dozens of giant planet atmospheric compositions and cloud properties (e.g., Lee et al. 2013) and the search for chemical non-equilibrium (e.g., Fortney et al. 2008; Skemer et al. 2012). Until now atmospheric studies of long-period gas giants in the  $3-5 \mu\text{m}$  range was restricted to a small sample of objects and largely based on narrow band photometry (e.g., Skemer et al. 2014, 2016). Chapman et al. (2017) demonstrated that a wavelength coverage from  $0.5-5 \mu\text{m}$  is better, by about an order of magnitude, at constraining atmospheric abundances than coverage limited to wavelengths  $<2.5 \mu\text{m}$ . This is largely due to features of  $\text{CH}_4/\text{CO}_2/\text{CO}$  at  $3.6/4.3/4.8 \mu\text{m}$ , respectively. Possibly even more exciting are the prospects of obtaining an N-band spectrum of the brightest directly imaged exoplanets, such as  $\beta$  Pic b and, depending on the final N-band sensitivities, potentially also HR8799 e and d. JWST/MIRI has the potential to obtain high-quality MIR SEDs for a large number of ultra-cool field objects and wide-separations companions in the background limited regime (e.g., Danielski et al. 2018), but for closer-in companions METIS' superior spatial resolution is key.

METIS spectroscopy will hence provide a new look at the properties of atmospheres of (young) long-period gas giant planets (e.g., C/O ratios, metallicity), which can then be compared to those of hot and warm gas giant planets studied, by for instance JWST, in transmission and secondary eclipse spectroscopy (Todorov et al. 2016). This will enable comparative exoplanetology, such that we may be able to begin an in-depth assessment from a statistical vantage as to the connection between these present day atmospheres and to what extent they can trace back to how and where the planet formed in its protoplanetary disk (e.g., Thiabaud et al. 2015; Eistrup et al. 2018).

### 3.4 Towards other Earths

ELT's ultimate science case is the characterisation of other Earths and the search for evidence of biological activity. If there is one important lesson astronomers have learned over the past decade, it is that worlds similar to Earth (mass, size, irradiation level) are everywhere, possibly tens of billions in the Milky Way alone (e.g. Dressing & Charbonneau 2015). Indeed, radial velocity surveys have already found several Earth-mass planets orbiting small dwarf stars in our direct surroundings, such as Proxima Cen b (Anglada-Escudé et al. 2016) (with possibly two other planets in the system Faria et al. 2022) and Barnard's star (Ribas et al. 2018), which form extremely interesting targets for METIS.

While a planet like Proxima Cen b is only in an 11-day orbit, it receives as much radiation from its host star as a planet between Earth and Mars around the Sun. It could well have liquid water on its surface, be potentially habitable, and host life. However, we have no way of knowing how likely that is. A small dwarf star may not be the best environment for biological activity, with a billion-year-long pre-main sequence phase and strong chromospheric activity that may have erodes any atmosphere and/or water from the planet (e.g. Ribas et al. 2016). Learning as much as possible about Proxima b, and other planets like it, is an enormous step in understanding the place of Earth, life, and humanity in the Universe.

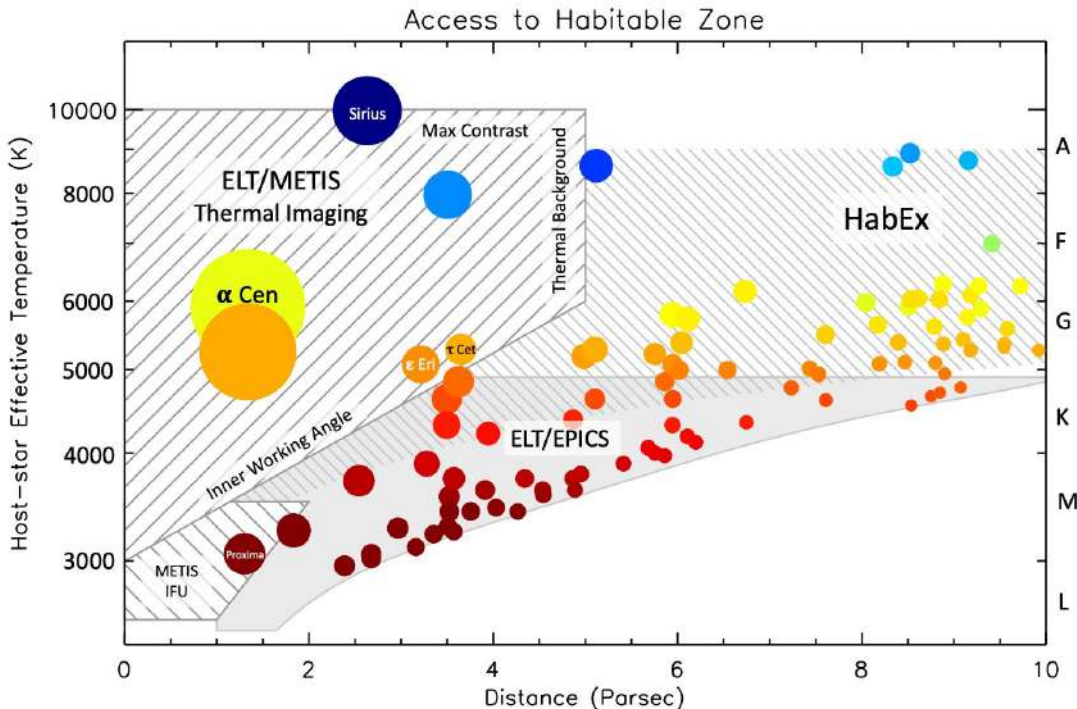


**Figure 3-7:** Accessibility of Earth-size planets in the habitable zone of nearby planets using METIS thermal imaging and IFU spectroscopy. Earth-like planets are the most difficult targets, and METIS will also study hundreds of other planets, both larger and/or warmer.

In the coming years, JWST will take enormous steps forward in the characterisation of exoplanet atmospheres, mostly using time differential techniques such as transit and secondary eclipse spectroscopy and phase curves. Arguably one of the most spectacular observations planned will probe the warmest of the seven Earth-size planets in the TRAPPIST-1 system through secondary eclipse measurements (Lustig-Yaeger et al. 2019) which will be crucial in our understanding to what extent planets around small M-dwarfs can retain their atmospheres.

While JWST will enable great progress in our understanding of transiting Earth-size planets, it will not be capable of spatially resolving them, due to its relatively small aperture. This will be the realm of direct imaging with the ELT and METIS. Figure 3-7 illustrates the accessibility of habitable zone, Earth-size planets for METIS. While METIS thermal imaging is expected to be able to detect rocky planets around the very nearest stars (see below), with METIS-IFU Proxima Cen b can be characterised, probing molecules such as water, methane, and carbon-dioxide. We illustrate with simulations of Proxima b in reflected light, using the HDS+HCI technique with the IFU as shown in Figure 3-8. A planet with a radius of  $1.1 R_{\text{Earth}}$  and an atmosphere identical to that of Earth is observed in the combined high contrast imaging, high spectral resolution IFU mode around  $3.8 \mu\text{m}$  to clearly detectable significance in just 10 hours.

True Earth analogs, seeing worlds like ours that orbit Sun-like stars in reflected light, requires very high contrast performance (e.g.  $10^{-10}$ ). This will require a future generation high-contrast-imaging ELT instrument, such as PCS, or a space telescope, like IROUV anticipated in the 2040s. However, while such a space telescope will reach the required contrast, it will not have the angular resolution to probe Proxima b and

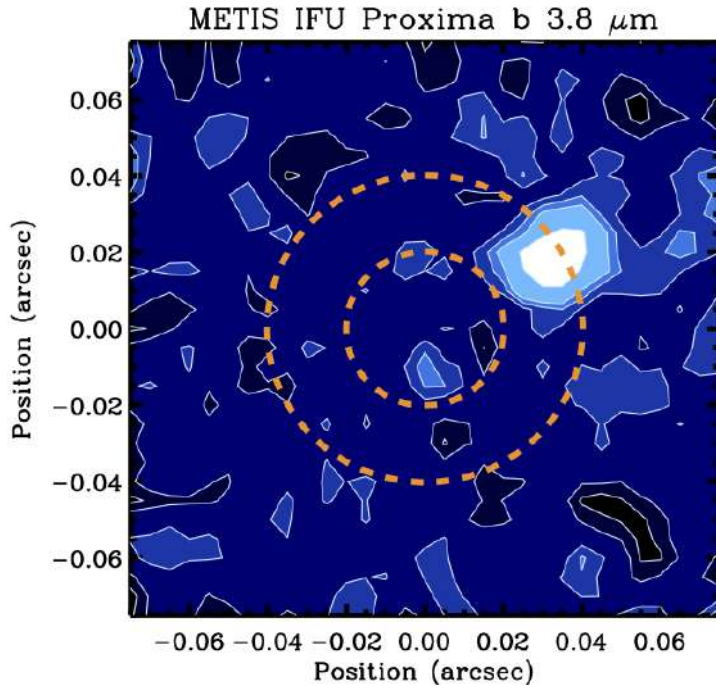


**Figure 3-8:** Simulations of the METIS IFU performance on the Proxima system at  $3.8\mu\text{m}$ . Assuming a  $1.1 R_{\text{Earth}}$  planet radius, an albedo of 0.3, 50% illumination, an achieved coronagraph-aided contrast of 1:500 at  $2 \lambda/D$ , and 10 hours of observing time, the planet is clearly detected in reflected light.

other temperate Earths around nearby red dwarf stars — this will remain the sole hunting ground for the ELT.

Complementary to these reflected light studies, METIS on the ELT will be able to detect rocky,  $< 2$  Earth radii planets around a handful of the nearest AFGK stars (including  $\alpha$  Cen A and B). Bowens et al. (2021) repeated the pioneering work of Quanz et al. (2015b) using more realistic contrast curves in the L-, M-, and N-bands instead of assuming background-limited performance at  $2 \lambda/D$ . Contrary to the previous results, it turns out that the N-band at  $10 \mu\text{m}$  is the best place to conduct the search. The six nearest stars are by far the best targets with the average number of detected planets from an optimized survey being 1.7, some likely detected in multiple bands. This survey, which considers repeated visits for the best targets rather than moving to new targets, would take 11 nights on the ELT, likely revealing the first image of a rocky planet around a nearby Sun-like star. As with reflected light mentioned above, thermal emission studies with the ELT will lead the way for future space-based platforms. While METIS will probe a handful of stars for terrestrial planets, future missions such as LIFE (Quanz et al. 2022) would enable a survey capable of finding and characterizing Earth-like planets around hundreds of FGK stars within 20 pc, building on the legacy of ELT METIS.

In Figure 3-9 we compare the expected flux of an Earth-twin<sup>7</sup> orbiting  $\alpha$  Cen A to the expected contrast and sensitivity achievable with METIS in the N2 filter. This highlights two important points: (a) the habitable zone around  $\alpha$  Cen A lies in the background-limited and not contrast-limited regime; hence observations need to be optimized for throughput and not contrast if the search is focused on habitable zone planets, and (b) METIS has the potential to image an Earth twin if it existed. We note however that an important source of performance degradation for mid-infrared HCI observations is water vapor seeing, which results from the variability in the local column density of water vapor above various parts of the telescope pupil. This effect, described in [E-REP-ULG-MET-1019] (see also, Absil et al. 2022, SPIE), is expected to degrade the N-band HCI performance by one order of magnitude in median atmospheric conditions. The mitigation strategy defined at FDR could significantly improve upon this situation and, if successful, provide HCI performance somewhere between the SCAO-limited and the water vapor-limited situations. In Figure 3-9,

<sup>7</sup>An Earth-sized planet receiving the same amount of flux as Earth and emitting the same spectrum.

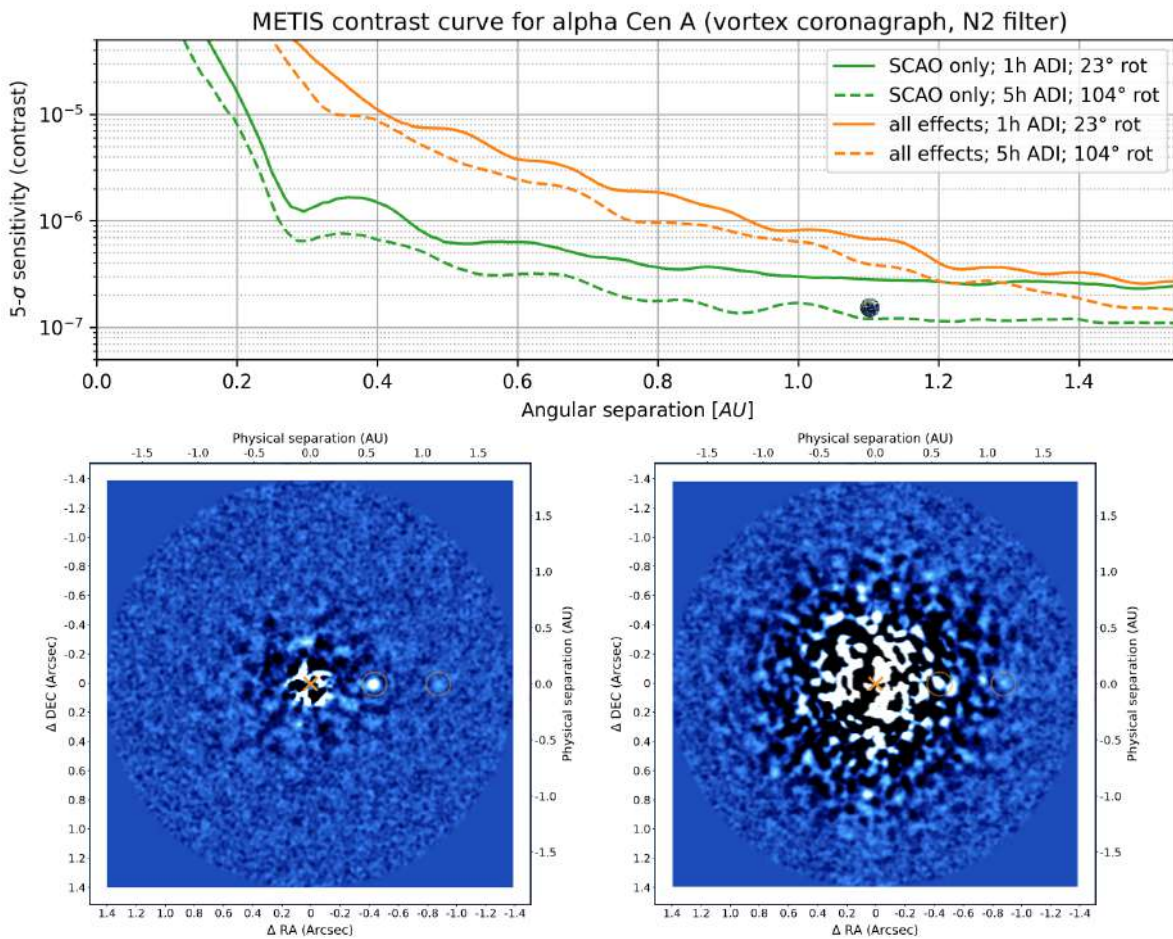


**Figure 3-9:** Feasibility study to investigate if METIS can detect an Earth twin around  $\alpha$  Cen A at quadrature. Given the higher luminosity of the star, an Earth twin (i.e., same size and emission spectrum) would be located at  $\sim 1.1$  AU around  $\alpha$  Cen A. Top: predicted sensitivity limits of the METIS vortex coronagraph in the N2 filter, for two different assumptions in terms of wavefront perturbations (either based on SCAO residuals only in green, or adding uncorrected water vapor seeing on top of SCAO residuals in orange), and for two different durations of the ADI sequence (1h for solid lines, 5h for dashed lines). The contrast and separation of a perfect Earth twin is shown for comparison. We expect the actual METIS performance to lie between the orange and green lines, after partial correction of water vapor seeing. Bottom: final image after classical ADI processing for the 5-h ADI sequences in the absence (left) or in the presence (right) of water vapor seeing, added on top of SCAO residuals. In addition to the Earth twin in the habitable zone (1.1 AU), a second, warmer Earth-like planet was injected at a twice smaller separation (0.55 AU) to illustrate the potential of METIS for the detection of warm rocky planets. The planets are retrieved with an SNR around 6 and 11 respectively, in the SCAO-only case, but not recovered in the presence of water vapor seeing.

we show simulations for the two extreme cases where water vapor seeing is either not included, or not corrected at all (see E-REP-ULG-MET-1019 for details). Our capability to correct for water vapor seeing at N band in METIS will be further investigated in Phase D.

Finally, we note that it is possible, in the next 10 years, for METIS to reveal a sub-Saturn mass planet ( $4 < R_p < 10 R_\oplus$ ) around a larger cohort of stars beyond the nearest six. Such a planet, if found around a star within 20 pc, could also be detectable in reflected light with the Roman Space Telescope (to be launched before first-light with the ELT) and perhaps also Gaia. This would break the radius-albedo degeneracy, and enable a measurement of the total energy budget for the planet — thereby determining whether it possesses an active greenhouse. Such a discovery would be an important milestone on the way towards assessing habitability in planetary atmospheres, a major goal of the LIFE and IRLOUV missions.

## 4 THE FORMATION HISTORY OF THE SOLAR SYSTEM

### 4.1 Scientific background and context

The bodies in the planetary system were formed 4.6 billion years ago in an extended disk, and the formation took only a few ten million years. The physical conditions and the chemical composition of the planetary formation disk at that time is hardly constraint except that strong radial gradients in temperature and density are suggested, ranging from the inner edge close to the Sun, where the terrestrial planets originated, to the region of the gas giants, where the icy bodies like comets and Kuiper Belt objects accreted. The asteroid belt may represent the transition region between the terrestrial and icy environment in the disk. The physical and chemical processing of that formation disk material is at least partially reflected in the atmospheres of the planets and in properties of the most primordial bodies in the solar system that are accessible to observations today, i.e. in minor bodies like comets, asteroids and Kuiper Belt objects. Of particular interest here is how these objects connect to the Earth and its environment for the formation of life.

### 4.2 Scientific Goals

Scientific goals for the exploration of the formation era in our planetary system can be accomplished by:

- Establishing a composition and temperature profile of the planetary formation disk,
- Determining isotope ratios in cometary volatiles, namely the D/H ratio of cometary water as well as the ratios of  $^{12}C/^{13}C$  and  $^{14}N/^{15}N$ , important elements in organic compounds,
- Constraining the large-scale radial mixing of material in the disk,
- Determining the ice composition and the organics in Kuiper Belt objects,
- Constraining the internal constitution of asteroids and comets by estimating thermal inertia of the bodies,
- Searching and estimating trace species in the atmospheres of the outer gas giant planets
- Characterize the relationship between the various components of the gas and ice giant systems

It is also noted that despite the detailed view of space missions in the vicinity of planets, ground-based observations of atmospheric species of for instance Mars can provide the synoptic picture that is necessary for global modeling of the planetary atmosphere and that is essentially not achievable from spacecraft orbit. Moreover, the understanding of the influence of a component of a planetary system (e.g., a volcanic eruption on a moon) on another (e.g., the heating of the polar atmosphere on the planet) requires coordinated observations from both space and from the ground, as a spacecraft can only be at one place at a time.

### 4.3 Composition and temperature profile and isotopic ratios in the formation disk

The ices in comets are expected to reflect best the gaseous composition in the formation disk of the Sun around the time when the gas giants were formed. Sublimation of the ices when a comet gets closer to the Sun, releases volatile species. The richest wavelength domain for studies of these ice volatiles is the IR region between 3 and 5  $\mu m$  (Cochran et al. 2015). Using high-dispersion spectroscopy, a number of parent gas species from cometary ices – including organic compounds – can be measured from the ground, for instance  $H_2O$ ,  $CO$ ,  $NH_3$ ,  $CH_4$ ,  $C_2H_2$ ,  $C_2H_6$ ,  $CH_3OH$ ,  $HCN$  (see Fig. 4-1). Beyond known molecules, emission lines from so far unidentified species are seen in high dispersion 3-5  $\mu m$  spectra of bright comets.

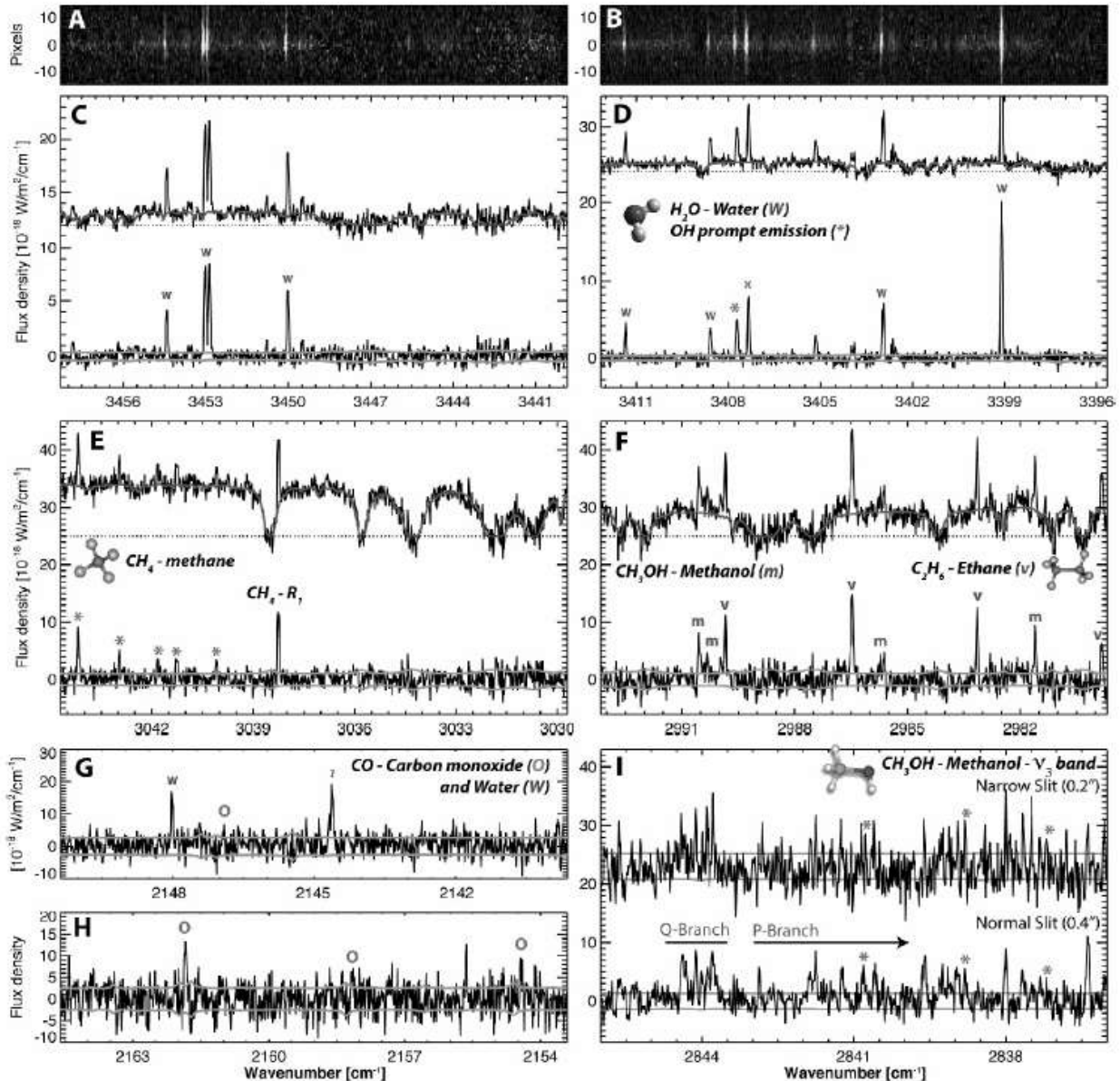


**Figure 4-1:** CRIRES spectra of the coma gases seen in comet 8P/Tuttle (Böhnhardt et al. 2008). Panels A and B show examples of flux calibrated 2D spectra of the comet in the wavelength range of  $\text{H}_2\text{O}$ , panels C to I show extracted 1D spectra for various coma species ( $\text{H}_2\text{O}$ ,  $\text{OH}$ ,  $\text{CH}_4$ ,  $\text{CH}_3\text{OH}$ ,  $\text{C}_2\text{H}_6$ ,  $\text{CO}$ ; dust reflected sunlight removed) as indicated in the various sub-panels. Panel G displays also emission (marked by symbol '?') from an yet unidentified species in the coma.

The Rosetta mission has identified further species of organic and inorganic nature (Altweig et al. 2017) that provide an so far unexplored sample of species for search and quantitative measurements using the high-dispersion spectroscopy option of the METIS instrument.

Considering evolutionary effects of cometary nuclei, the production rates of the known molecules allow to conclude on the ice composition in the outer planetary formation disk. Moreover, through the known sublimation temperatures, they provide a first, coarse idea on the likely temperature in the region where the respective comets were formed. A far better indicator of the temperature domain comes from measurements of the ortho-to-para ratios of parent molecules like  $\text{H}_2\text{O}$  and  $\text{NH}_3$  (Mumma & Charnley 2011) in the 3–5  $\mu\text{m}$  region, since it allows determining the spin temperature of these species that is considered a good proxy for the formation temperature of the respective ices. Temperature models of the formation disk can then provide the link to the likely formation distance of the comet in the proto-planetary disk.

The radial profiles of both the gas composition and the temperature regime in the disk evolve from measurements of a statistically significant and also representative sample of short- and long-periodic comets. Here, over the past ten years, a starting point is already achieved through observations of a few, mostly long-periodic comets from the Oort Cloud. However, progress is slow since the objects must be bright (for CRIRES at VLT brighter than 11 mag in K band) in order to be measurable with existing instrumentation and are thus rare. In particular, short-periodic comets are not well represented in the small sample of measured objects, which can only be overcome by the usage of a high-dispersion L and M band spectrograph like METIS at the ELT.

The same instrumentation is very much suitable to assess the isotopic composition of cometary ices using mostly the same wavelength region as for gas production rate estimations. Here, the D/H ratio in cometary water is of particular interest since it is suspected that terrestrial water may – at least in parts – originate from cometary impacts on the early Earth, for instance during the late heavy bombardment by likely Kuiper Belt objects when the Earth surface was already solidified. The existing D/H measurements (Mumma & Charnley 2011; Paganini et al. 2017) provide a diverse picture that is best compatible with a mixture of impactors with different isotopic compositions and thus from different formation regions. Combining isotopic ratio values in comets – not only D/H, but also  $^{12}\text{C}/^{13}\text{C}$  and  $^{14}\text{N}/^{15}\text{N}$  as important elements in organic molecules – with compositional and temperature radial profile of the formation disk will allow addressing the question of isotopic enrichment and attenuation processes in the disk. The key contribution for the isotopic analysis can only come from measurements of more objects: In particular, short-periodic comets are difficult since they require mostly telescope with apertures larger than currently available.

Taking as reference the experience of observing programs on gas composition in comets using CRIRES at the VLT, one can expect of the order of one half to a full night duration per target of K=11mag objects (here referring to the brightness of the very inner coma of the comet) in order to achieve SNR of 5-10 in the dust continuum signal of the comet. The science goal requires a sample of about 50 comets to be measured, of which about 20 are already done. The remaining 30 comets will have to be observed on an average pace of about 1-to 2 objects per year, the rate of comets that become within reach for the METIS AO system (limited to K=11mag), i.e. this program would last for about a decade or two. Moreover, due to their faintness Jupiter-family comets will be underrepresented in the achievable sample compared to long-periodic and Oort Cloud objects. For an AO system with limiting K magnitude around 15mag, an unbiased sample could be achieved in a much shorter time (since there will be a few comets within reach per night). Isotopic ratios require comet of total K=7mag brightness or brighter for which one can expect 1 object per year or two, observable for METIS at the ELT.

#### 4.4 Large-scale radial mixing of disk material

The compositional mixing of gaseous species in the planetary disk follows from the above mentioned L and M band spectroscopy of gases in cometary comae. The solid, non-volatile component, namely the silicates, can be measured by N band spectroscopy at low resolution. A mixture of amorphous, space-weathered silicates and crystalline ones (Wooden et al. 2017) were found in two long- and one short-periodic comet (Fig. 4-2). The parallel existence of amorphous and crystalline phases in cometary dust suggests that some of the silicates, i.e. the crystalline ones, may have been processed in a hot environment above melting temperature ( $> 1500\text{K}$ ), most likely close to the Sun, just shortly before they got solidified and inserted into the cometary nucleus further away from the Sun. This scenario requires efficient radial mixing of material in the protoplanetary disk, a process that was initially not considered important in the formation scenario of our planetary system. At present, it is completely unknown to which extend the mixing took place and whether it affected the whole disk in a similar way.

Improvement of our knowledge will result from spectroscopic observations of cometary dust comae of a larger sample of comets in N band, an undertaking that given the relative faintness of most targets (in particular of the short-periodic comets) can be accomplished by a low-dispersion mid-IR spectrograph, i.e. METIS at the ELT. The situation is quite similar to the science case on gas and isotopic composition in

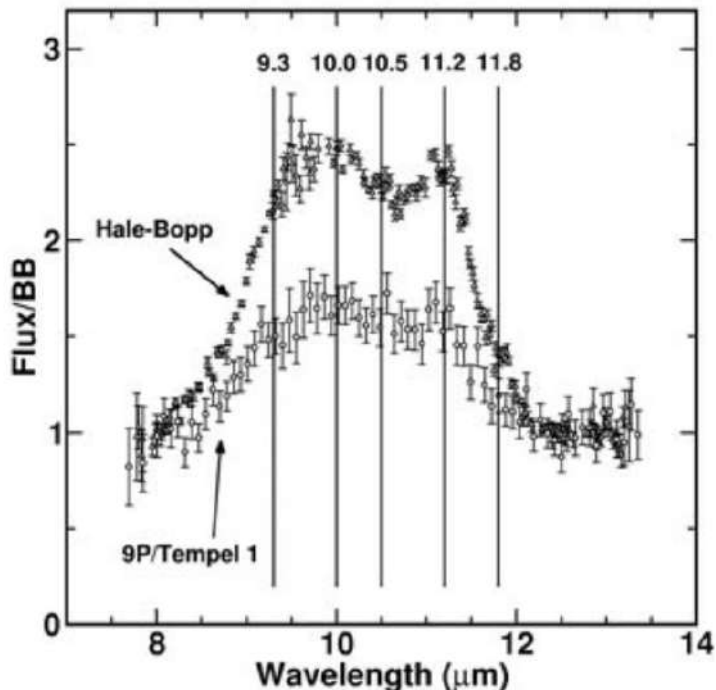


**Figure 4-2:** N band spectra of the dust comae of comets C/1995 Hale-Bopp and 9P/Tempel 1 (Harker et al. 2005). The vertical lines indicate the presence of crystalline silicate grains (olivines and pyroxenes) in the dust comae of the comets, the emission shortwave thereof is produced by amorphous silicates. Dust grains collected at comet 82P/Wild 2 by the Stardust mission, showed examples of crystalline and amorphous dust components in the same grain aggregates.

comets (see section 4.3): required sample size is 40-50 of which about 10 objects have data measured. A comet of K=11mag for the inner coma will require about 1/2 to 1 night for low dispersion N band spectroscopy of the amorphous and crystalline silicate emissions of the cometary dust, i.e. sample completion depends on the availability of suitable targets with K=11mag or brighter and may need two decades or more. A fainter K=15 mag for the AO system will significantly speed up the program execution to about 5 to less than 10 years.

#### 4.5 Ice and organics composition of Kuiper Belt objects

Kuiper Belt objects are considered building stones for the giant planets in the outer solar system. In particular, they are meant to have provided the volatiles of the atmospheres of the gas giants. Moreover, they may have contributed to the so called ‘late heavy bombardment’ after the formation of the planetary system. During the latter period a significant amount of water and organics may have reached Earth via impacts of Kuiper Belt bodies (and comets), possibly scattered into the inner solar system due to the transient event of the 2:1 resonance passage of Saturn with Jupiter Morbidelli et al. (2008).

The ice and organics composition of Kuiper Belt objects is concluded mostly from low dispersion IR spectroscopy using existing large telescope facilities. In JHK bands various species like  $H_2O$ ,  $CH_4$ ,  $N_2$  ices are found among the about 2-3 handful of objects measured so far, and a dichotomy between the large (like Pluto, Eris) and smaller bodies (radius below about 800km) in the belt is noted. Probably, the surface composition of the large objects is affected by rather recent and transient phenomena of atmospheric origin like re-condensation of ices from the vapor phase or aeolic transportation of surface material (Brown 2008). The surfaces of smaller bodies on the other side seem only subject to space weathering and impacts.

Up to now, only a single object has the surface ice composition measured in L and M bands, i.e. Pluto-Charon. While Charon displays a unified water ice surface, Pluto itself shows a  $CH_4$  ice dominated L

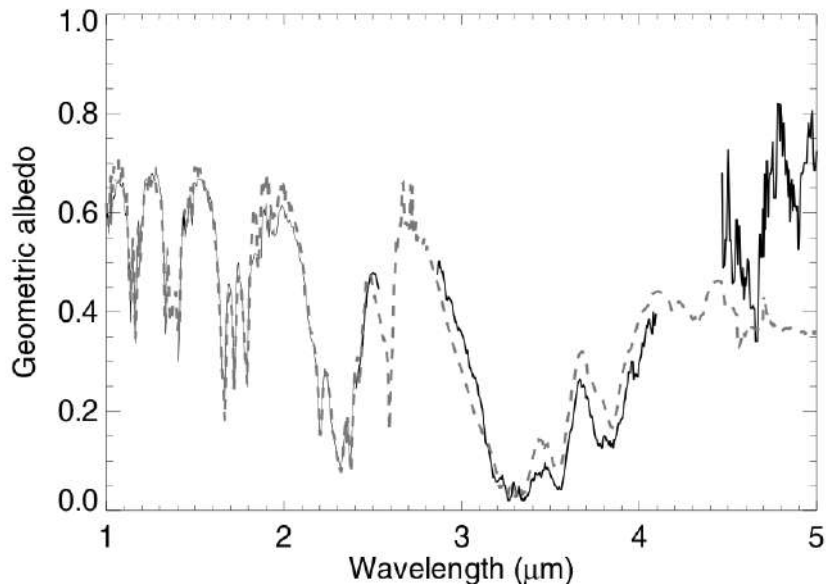


**Figure 4-3:** Near-IR spectrum of Pluto showing deep and wide absorption of methane ice on the surface of the dwarf planet (Protopapa et al. 2008). The observed spectrum (continuous line) is a composite of a JHK band spectrum from the Keck telescope and a LM band spectrum from VLT. The absorption at  $4.6\mu m$  is suspected to be produced by CO ice as well as Nitriles and/or deuterated  $CH_4$  or both. The broken line shows the result of model calculations using a mixture of various surface ices including the mentioned species. Deviations from the observed spectrum beyond  $3.5\mu m$  may indicate the presence of another, yet unidentified absorber material.

band spectrum and an absorption around  $4.6\mu m$  that is tentatively identified as being due to CO ice and very likely Nitrile compounds and/or deuterated methane ice (Fig. 4-3; Protopapa et al. (2008)). The latter two interpretations have intriguing implications: It may either be the first indication of the existence of organic solids involving C-N bearing molecules in a Kuiper Belt object, i.e. of species that play a role in the formation of amino acids in space. Or it may allow for the first time measurements of D/H ratios in these objects that is out of reach for space missions like New Horizons.

Low dispersion IR spectroscopy with METIS at the ELT can open up a new domain for the surface exploration of Kuiper Belt objects. The task of L&M band spectroscopy will be the investigation of the presence of surface ices, namely (1) of the mixing of the expected abundant components like  $CH_4$  (pure and diluted in  $N_2$ ), CO,  $H_2O$ , (2) of organics components like Nitriles, and (3) of deuterated material like  $CH_3D$ . Of the order of 10 objects (Kuiper Belt members and relatives among the Centaur population) will become accessible for L and M band spectroscopy with ELT plus METIS, allowing to address at once the open issues of size-depending surface evolution of Kuiper Belt objects, of the presence of pre-biotic organic compounds and of the D/H ratio in ices at the edge of the known planetary system.

Since the objects to be measured (Kuiper Belt objects and Centaurs) are faint targets ( $V=13$  mag for Pluto), support of an AO system is considered a prerequisite for sensitive measurements in low dispersion spectroscopy mode of the L and M band of METIS. Long-duration approaches of the targets with bright enough background stars may open time windows of the order of one night for the anticipated measurements of a target. Alternatively, on-target AO are preferable provided that a sensitive AO system (about 16mag in K) will become available, then allowing also SNR improvements by extending the total integration time of the spectra to about 4 nights per target. In that case about 10-20 nights of ELT time will be required for the 5-10 targets within reach for this science goal.

## 4.6 Thermal inertia and the internal constitution of minor bodies

Continuous improvements in thermal modeling techniques allow meanwhile to estimate thermal properties of the surfaces of minor bodies from mid-IR photometry. The thermal emission of objects in Earth vicinity

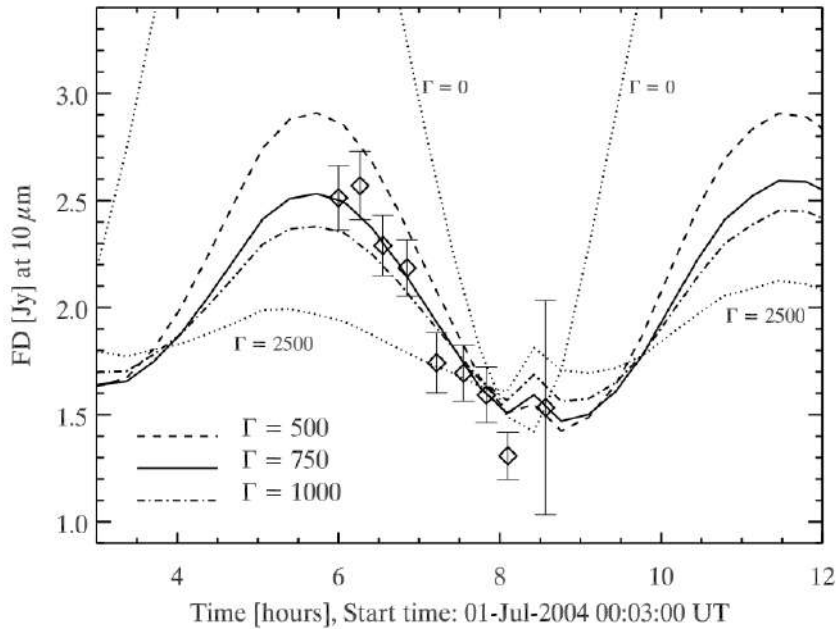


**Figure 4-4:** N band rotation lightcurve (diamond symbols) of asteroid 25143 Itokawa and thermal modeling results for various parameters of thermal inertia  $\Gamma$  (Müller et al. 2005).

out to the asteroid belt and beyond peaks at mid-IR wavelengths and combined N-band measurements at different rotational phases over a range of phase angles are key ingredients for the determination of the thermal inertia of these bodies.

The thermal inertia of large, dust-covered main-belt asteroids is found to be very low, while monolithic bedrock objects have thermal inertia two orders of magnitude higher (Delbo et al. 2015; Scheeres et al. 2015). Rubble-pile objects are expected to have values in between. Tidal forces during encounters with large bodies in the solar system cause regular reorganizations of such rubble piles (Richardson et al. 2002), resulting in thermal properties, which are characteristic for a mixture of dusty and rocky surface regions. The approach of assessing the internal constitution of a body through its thermal inertia will also provide useful results for future interstellar visitors in the solar system like 1I/Oumuamua (Meech et al. 2017) that may become observable more frequently for instance based upon LSST detections.

First indications on the internal constitution of a small body came from N-band observations at a 4m-class telescope (Müller et al. 2005). The thermal inertia of 25143 Itokawa was found to be in the expected range for rubble-pile objects - which was later supported by results from the Japanese spacecraft Hayabusa when visiting this asteroid (Fig. 4-4). The principle capability of constraining the internal structure of minor bodies from the thermal properties is promising since it allows assessing the constitution of rather primordial bodies like cometary nuclei and C- and D-type asteroids as well as more evolved ones like S- and M-type asteroids. Related to this is the intriguing expectation that scenarios for the planetesimal formation in the protoplanetary disk as well as for the impact of the collision history on the body constitution may evolve. Both scenarios will then be constrained by observational results. The key point are accurate thermal measurements of minor bodies for which, given the faintness of the objects, N (and Q) band photometry with METIS at the ELT is required. It is noteworthy that for objects of 10 km and larger, surface resolved measurements will be possible. Terminator regions are of particular interest since they will allow very valuable refinements of the thermal and constitutional properties of the objects by measurement of the sunlit and the dark side of the bodies.

The detection limit of 0.1 Jy in N band at signal-to-noise of about 15 corresponds to a main belt asteroid diameter of order 20km. The observations require 3 filter settings in N band, each with about 2h integration time. I.e. the target needs one night of ELT time for the determination of its physical parameters size, albedo, thermal inertia. A sample of 100 objects covering different taxonomic asteroid classes and a wide

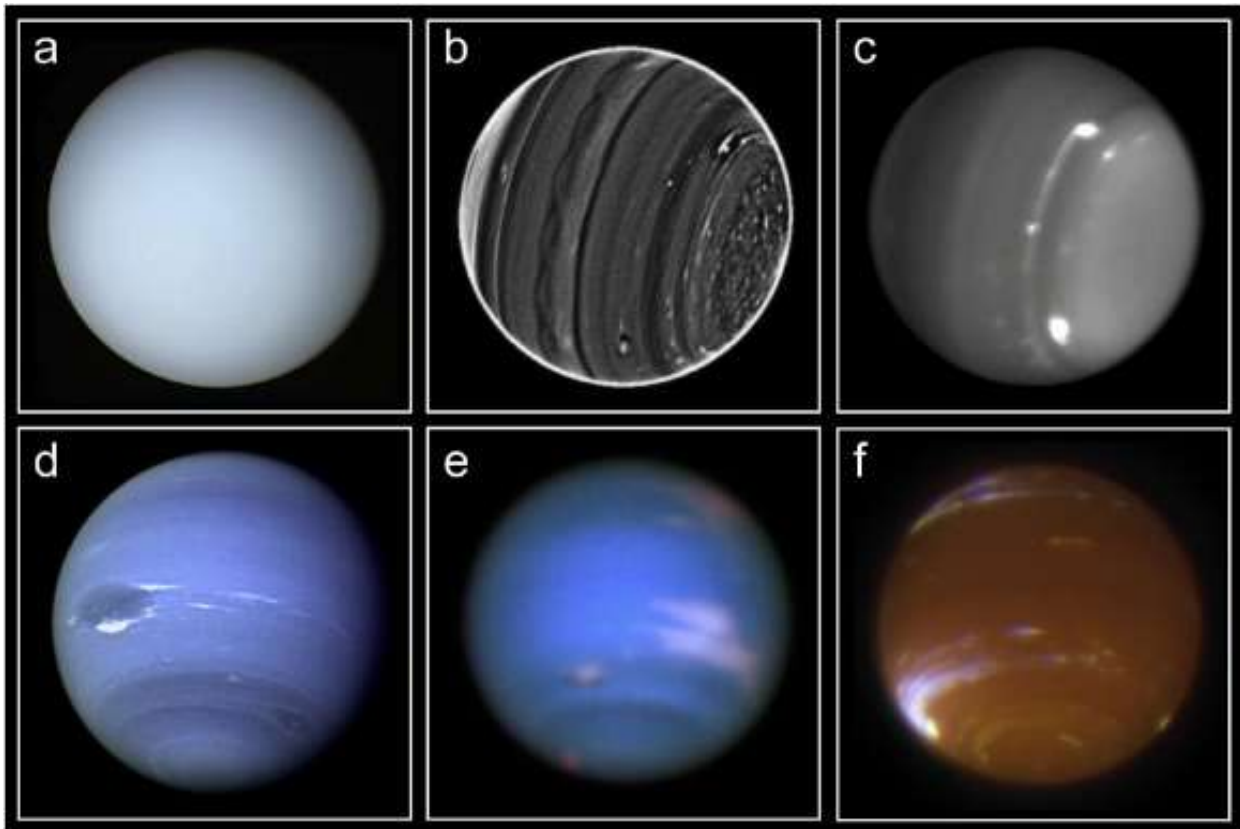


**Figure 4-5:** Uranus and Neptune - global views (Mousis et al. 2018). Upper row Uranus: (a) visible from Voyager 2; (b) atmospheric structures in near IR (Fry et al. 2012); (c) Bright near IR features (de Pater et al. 2014). Bottom row Neptune: (d) visible from Voyager 2; (e) Visible with HST (image credits: NASA, ESA, and M.H. Wong and J. Tollefson from UC Berkeley); (f) near-IR (observations courtesy of I. de Pater).

size range (10 to several 100km) may be achievable for about 50 ELT nights, possibly including also several targets of km-size from the near-Earth asteroid population.

#### 4.7 Trace species in the atmosphere of Uranus and Neptune

The atmospheres of the ice giants are believed to be created from the small body population in the outer solar system. In parts, these bodies may have been collected by the planetary nucleus during the clean-up phase of the formation disk in its gravitational domain. In this respect they reflect the formation environment of the planet's neighborhood. Chemical reactions and mixing in the atmosphere and deeper interior may have altered the original composition (Lellouch et al. 2005; Orton et al. 2015). Nonetheless, elemental abundances, in particular for the heavier species like phosphorus, should be unaffected. It is thus believed that elemental abundance in the giant planets can provide information on their interior and from those clues on their formation scenario.

*PH<sub>3</sub>* and *CO*, trace species in the troposphere of Uranus and Neptune, measured with high-dispersion in the 4-5  $\mu\text{m}$  wavelength region, provide unique constraints on the internal mixing of these planets. Conclusions are drawn on the temperature domain of the planetesimals that created the atmospheric environment and brought in the molecule species when swallowed by the planet embryo from the surrounding planetary formation disk. Both ice giants, Uranus and Neptune (Fig. 4-5), are expected to be enriched in *PH<sub>3</sub>*, but detection and measurement of this species was not yet successful. Since Uranus and Neptune will not be visited by spacecraft during the next decade or two, a challenging search and scientifically interesting detection option is left open for a high dispersion, high resolution spectrograph like METIS at the ELT.

A sensitive search for trace species in the two ice giants Uranus (V=8.3 mag) and Neptune (V=9.5mag),

using the high dispersion L and M band spectroscopy option of METIS at the ELT, may require 5h observing time for a single surface area under seeing limited conditions. Surface sampling may require repetition of the observations in about 4 locations. The total execution time for the trace species search is about 2 nights per planet. It is noted that significant spatial improvement of the search will require AO corrections either during rare alignments of the planets with bright enough background stars or through a sensitive AO system that could make use of bright satellites of the gas giants, for instance of Ariel (V=14.5 mag, S=13 arcsec maximum separation from planet center) or Titania (V=14.0 mag S=30 arcsec) for Uranus and of Triton (V=13.5 mag, S=16 arcsec) for Neptune.

## 4.8 Giant planets as systems

The following discussion assumes that the giant planets can be observed regularly, which requires a SLAO system to be implemented. While stand-alone discoveries concerning giant planets are expected from the unique capabilities of METIS, there is an even greater value in synergistic science, in combination with the future missions designed to explore these outer worlds: JUICE (ESA, expected to arrive at Jupiter in 2031) and Europa Clipper (NASA, expected to arrive at Jupiter in 2030) at Jupiter, Dragonfly at Titan (NASA, expected to land in 2034) and a future Uranus mission, led by NASA, has been strongly recommended in the latest Planetary Science and Astrobiology Decadal Survey 2023-2032 in the USA (National Academies of Sciences 2022), possibly with a significant European contribution. With a spatial resolution ranging from 20 km (at Jupiter) to 170 km (at Neptune) on the planet (or on its moons), its huge collecting area and its spectral resolution on wavelength of great interest for planetary sciences, METIS has the capability to make crucial contributions in domains that will only receive an increasing attention in the coming decades.

Each giant planet possesses its own system, made of the planet itself, from its core to the largest extent of its magnetosphere and its suite of natural satellites. Each part of the system exchanges matter and energy with several others, and Jupiter is an excellent example of these intricate interactions. The strength of the tidal forces on Io's upper mantle generates an enormous amount of heat, at the origin of the most volcanically active body of the solar system. Either directly or indirectly, these volcanic gases populate the faint atmosphere of Io, which then escapes from its gravity. This gas then ionizes and accumulates along Io's orbit, forming the Io plasma torus, before migrating outward to populate the whole Jovian magnetosphere. The complex dynamics of the plasma in the magnetosphere is the source of intense aurorae, which modify the temperature and chemistry of the upper atmosphere, not only locally in the polar regions, but also globally (O'Donoghue et al. 2021). It is thus clear that there are only so many things that a single observer, even a spacecraft orbiting a planet, can do, and progress in understanding the relationship between these different pieces will require coordinated observations from the most up-to-date instruments, both on the ground and in space. It is noteworthy that past experience (e.g. from the Juno mission: Yao et al. (2019)) has shown that perfectly synchronized observations are rarely necessary, as most phenomena have timescales from several hours to days.

METIS is particularly well suited to observe Io's surface in the L-band. Depending on the considered wavelength, METIS will be able to observe individual volcanoes and provide their temperature and lava composition (de Kleer et al. 2017; Pater et al. 2020) (Figure 4-6), but also to map the SO<sub>2</sub> frost and determine its grain size (Carlson et al. 1997; Laver & de Pater 2009). In combination to measurements of the torus (density, composition), either from ground/space telescopes or from orbiters (visible sulfur emissions, or UV emissions from the oxygen and sulfur ions), such measurements could help settle the debate about the origin of the variations of the plasma torus density. While it is expected that volcanic eruptions could be the source of the variability, Io's atmosphere, which serves as a transition between the volcanoes and torus, is remarkably stable through time (Tsang et al. 2013; Roth et al. 2020) and no specific volcanic eruption has ever been identified to explain the brightening of the torus.

On Jupiter, H<sub>3</sub><sup>+</sup> auroral emissions are particularly bright in the L-band. While the instrument's fields of view are much smaller than the planet's projection on the sky, the auroral regions entirely fit into the imagers' (10,5" by 10,5" or 13,91" by 13,91") fields of view and the IFU will be used to focus on selected regions.

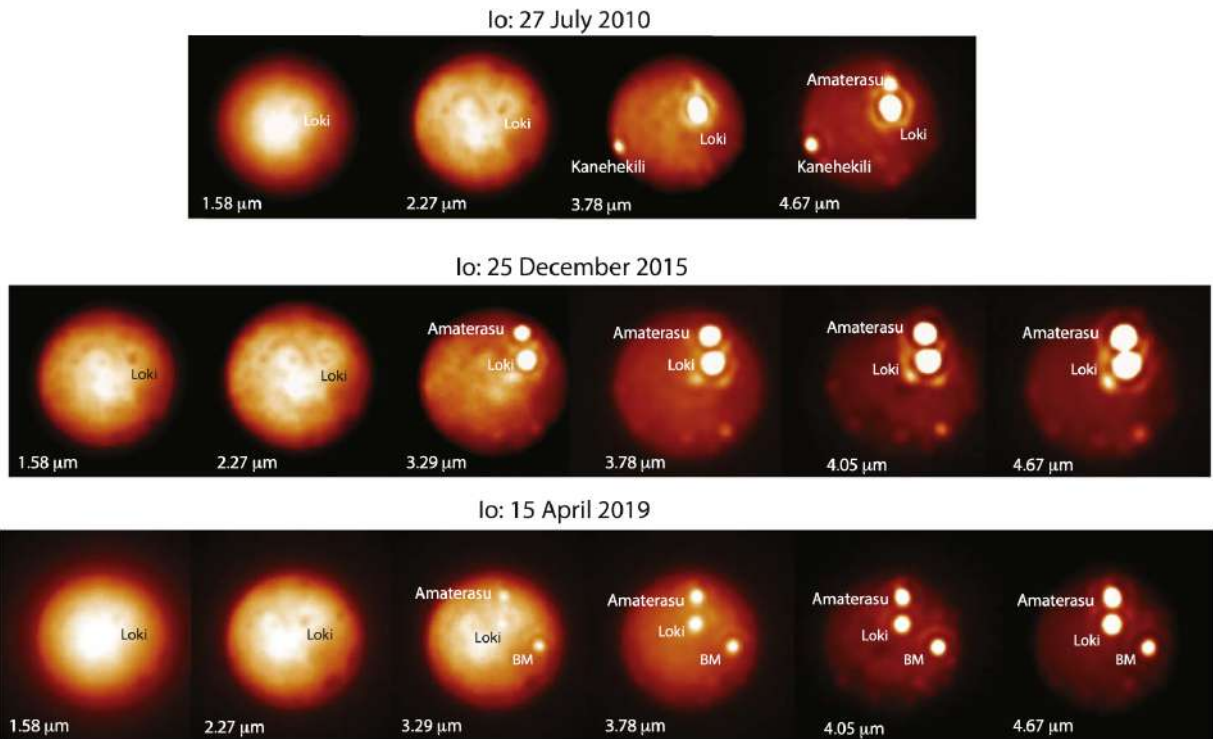


**Figure 4-6:** AO corrected images of Io at different wavelength taken with NIRC2 (Pater et al. 2020).

High resolution image sequences on timescales  $\sim 10$ s is useful to track the dynamics of explosive auroral forms (Bonfond et al. 2016). Observations of the Doppler shift of  $H_3^+$   $v_2$  Q(1,0 $^-$ ) line at  $3.953\ \mu m$ , and thus their velocity along the line of sight, provide access to the ionospheric convection in the polar region (Stallard et al. 2001; Johnson et al. 2017). In addition, the rotational temperature of the  $H_3^+$  ions in Jupiter's upper atmosphere can be obtained from the ratio of the  $v_2$  Q(1,0 $^-$ ) and  $v_2$  Q(3,0 $^-$ ) fundamental emission lines (Johnson et al. 2018). Combined with the  $H_3^+$  density and total emission, these parameters are crucial to understand the magnetosphere-ionosphere-thermosphere electro-dynamic coupling (Ray & Yates 2021). As an example, such measurements could be focused around Europa's or Ganymede's auroral footprints as the Europa Clipper of the JUICE spacecraft would be sampling the state of the magnetospheric plasma along the same field lines, which is impossible with current instruments with similar spectral resolution (such as VLT-CRIRES) because of the lack of spatial and temporal resolution.

Finally, at longer wavelength are several emission lines related to hydrocarbon molecules, which are also bright in the polar stratosphere. These emissions appear related to the aurora since they seem to respond to fluctuations of the solar wind (Sinclair et al. 2019). However, higher spatial resolution images (at least  $\sim 200$  km) would be required to be able to connect these hydrocarbon emissions in the stratosphere to specific auroral features in the thermosphere.

Another key target will be Titan, orbiting Saturn, with the arrival of the Dragonfly helicopter expected by 2034. In the wavelength range upward of  $2.6\ \mu m$ , the atmosphere of Titan gets progressively transparent, providing access to the surface features that are hidden under a veil of hydrocarbon haze at shorter wavelengths (Barnes et al. 2007). High spatial resolution observations of these features will thus provide essential context for NASA's Dragonfly mission, due to land on Titan in 2034. Among others these observations will highlight the potential changes that took place on the planet since the Cassini era.

Most of the science cases exposed here above for Jupiter are also valid for the other three Giant Planet, even if they have not been explored as extensively yet. In particular, Uranus and Neptune are real "terrea incognitae" compared to the other planets of the solar system. The  $H_3^+$  L-band aurorae have only been barely detected in a few spectra (Trafton et al. 1999) (Figure 4-7), and, maybe, a few ambiguous images acquired with the IRTF (Lam et al. 1997). Moreover, no aurora has ever been observed on Neptune (Melin

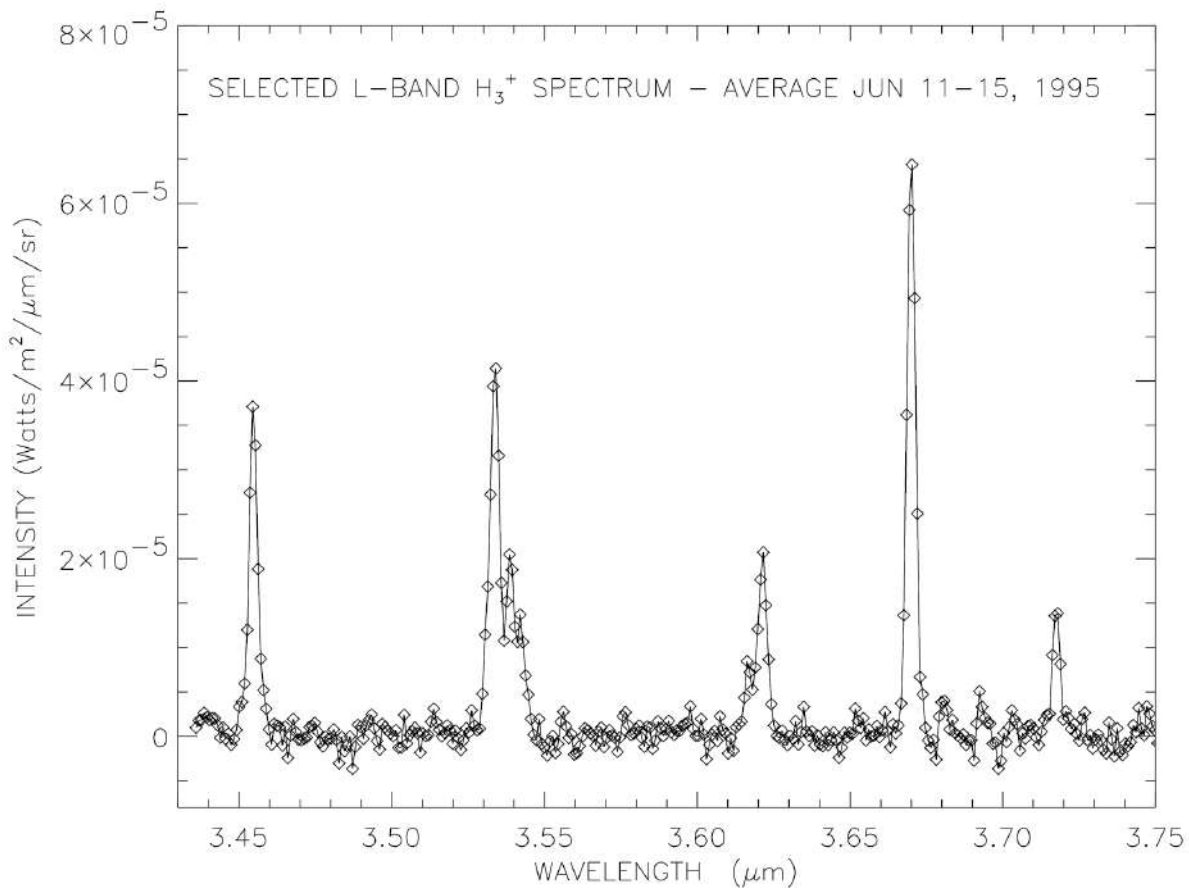


**Figure 4-7:** Spectrum of Uranus from CGS2 in June 1995 (Trafton et al. 1999).

et al. 2018). Characterising these aurorae would not only be a first, but would also provide key clues on how strongly tilted magnetic fields interact with the solar wind.

## 4.9 The Martian atmosphere

The Martian atmosphere is the simplest possible example of a planetary atmosphere. It consists mainly of  $\text{CO}_2$  with a few minor constituents (e.g. 2.7%  $\text{N}_2$ , 1.6%  $\text{Ar}$ , 0.2%  $\text{O}_2$ , 0.07%  $\text{CO}$ , 0.03%  $\text{H}_2\text{O}$ , 0.01%  $\text{NO}$ , 130 ppb  $\text{H}_2\text{CO}$ , 30 ppb  $\text{O}_2$  and 10 ppb  $\text{CH}_4$ ). The total pressure is 6–10 hPa and the scale height is 10km. The surface pressure is varying strongly, as due to the lower mass and gravity when compared to Earth, the Martian topography shows much larger excursions. Variation of the total pressure with time is characterized by minor seasonal effects.

As compared to Earth, understanding this atmosphere should be extremely simple, as there is no energy transport by ocean convection, hardly any by water vapor, apart from occasional dust storms, there are no clouds and there is no plate tectonics (Mangold et al. 2016; Villanueva et al. 2013). Still the atmosphere of Mars is highly enigmatic, beginning with its sheer existence. Due to less gravity the atmosphere is much more weakly bound, and due to the absence of a magnetic field it is subject to the full erosion by the solar wind.

Mostly due to ground-based high-resolution infrared spectroscopy in the 3–5  $\mu\text{m}$  range, many trace constituents could be constrained and e.g. for  $\text{O}_3$ ,  $\text{HDO}$  and  $\text{CH}_4$  high variability with time and location could be found, which, however, cannot be explained by present theory (Fig. 4-8). Explanations range from complex anorganic reactions on or below the Martian surface up to speculations about organic life. Apart from the highly spectacular explanation of the  $\text{CH}_4$  origin or its variability involving organic life, the issue of “understanding” the Martian atmosphere is of extremely high relevance for climate research on Earth.

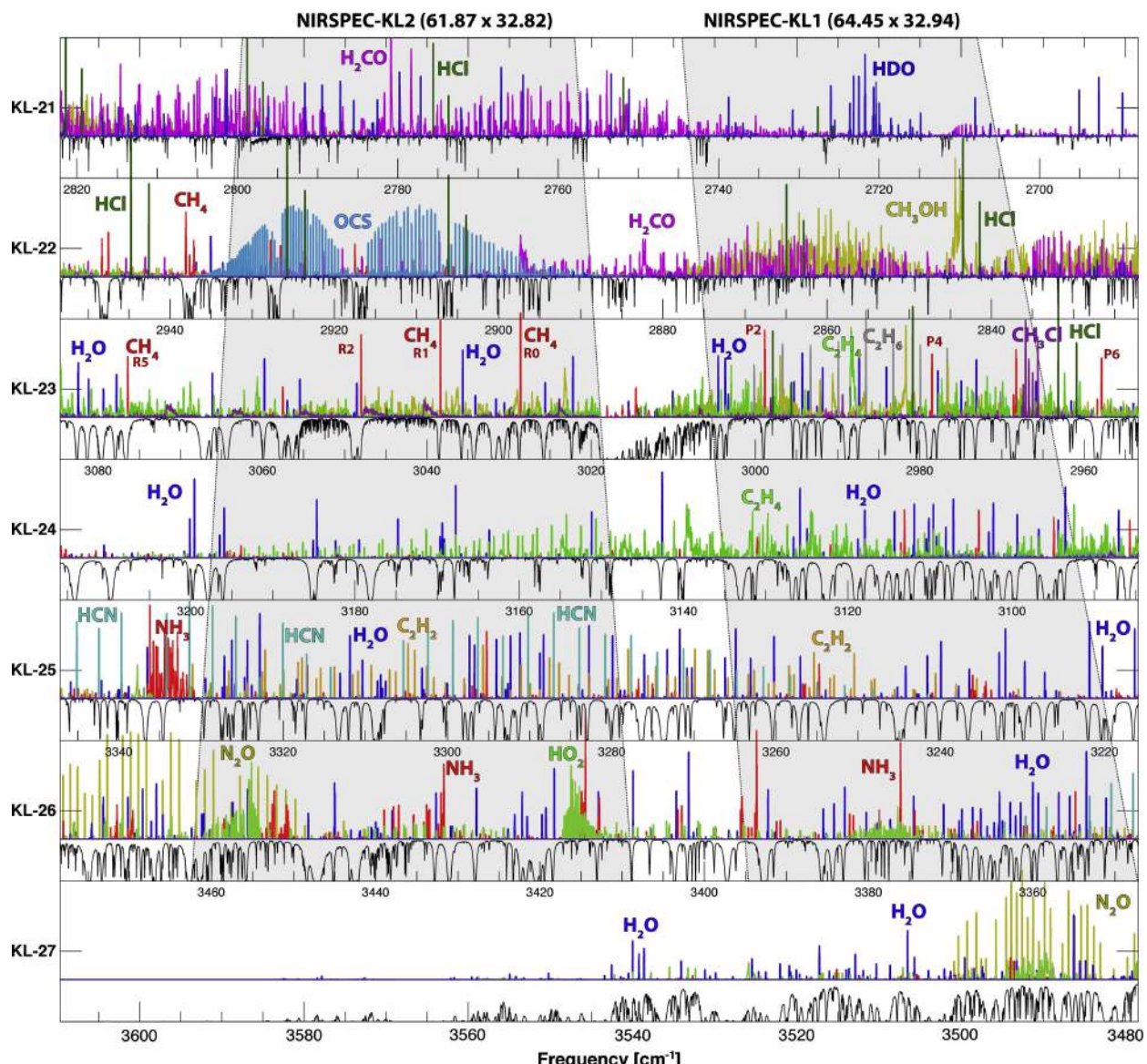


**Figure 4-8:** Trace species on Mars at infrared wavelengths (K and L bands) - simulation representing ground-based observations. Atmospheric transmittance from Mauna Kea (4200 m) is shown with a thin black trace. Grayed areas indicate the spectral coverage of the cross-dispersed NIRSPEC/Keck-2 KL1 and KL2 settings (Villanueva et al. 2013).

Observing the planet by an ELT with a diffraction limited beam ( $\sim 25\text{mas}$  at  $\lambda \sim 5 \mu\text{m}$ ) will yield a spatial resolution of 7-10 km on Mars which is of order of the atmospheric scale height. This will enable limb observations of stable molecules or radicals in the Martian atmosphere, typically a factor of 100 amplified compared to an observation close to the sub-solar point. Molecules can now be observed in fluorescence without the thermal background radiation of the surface. As compared to the closer, more detailed, but very much localized spacecraft data, the telescopic observations can freeze the Martian rotation by measuring the whole limb in about 1h of observing time. Series of such observations to cover diurnal and seasonal variation will then lead to a new quality in the understanding of the chemical and photochemical processes. These observations will also allow us to constrain the 'erosion' processes of the Martian atmosphere and thus will lead to fundamentally new insights into the mechanisms that stabilize the atmospheres of all solar system planets (including the Earth).

Detection of the trace species in the Martian atmosphere from Earth (see for instance the CRIRES measurements of Villanueva et al. (2013)) is possible by sampling the planetary horizon at different latitudes within about 1h. For longitude coverage repetition (12 times or more) of the sampling is required. For the

assessment of seasonal changes in the Martian atmosphere repetition of the whole monitoring observations is required (about 5 times). The challenges of these observations are the proper treatment of the high signal background from light scattered by the planetary disk and the best AO correction. For the latter the Martian moons Phobos and Deimos are available at 9 mag maximum K band brightness reaching maximum separation from the planet center of 25 and 30 arcsec, respectively. Alternatively, the planet horizon may be used (as was exercised with CRIRES at the VLT) for significant AO corrections.

## 5 MASSIVE STARS AND CLUSTER FORMATION

### 5.1 Scientific background and context

In many ways, massive stars ( $>8 M_{\odot}$  and  $>10^3 L_{\odot}$ ) shape the visible Universe. From the phase change of re-ionization (e.g., Bromm et al. 2009), to the formation of the trans-iron elements and the first solid materials in the early Universe (Dunne et al. 2003), as well as with their energetic sculpting of the interstellar medium, massive stars drive galactic evolution. High-mass stars also drive local feedback processes via O-star winds and supernovae. This feedback may trigger the formation of subsequent generations of both low and high-mass stars (e.g., Moore et al. 2007; Thompson et al. 2012), and also may contribute to the regulation of the star-formation efficiency (e.g., Elmegreen 2002; Dale et al. 2015). Understanding high-mass star formation is therefore fundamental to our knowledge of galaxy formation and evolution. Given this profound impact, it is crucial to understand the environmental conditions and processes involved in their formation and the earliest stages of their evolution. Progress in understanding high-mass star formation lags behind the low-mass case, however. There are several reasons for this. Young, high-mass stars are rare and hence tend to be relatively distant. Most high-mass star-forming regions are located beyond 1 kpc and distances of 3 to 7 kpc are common. In addition, massive stars predominantly form in very opaque and highly clustered environments. A characteristic feature of massive star formation is that, in contrast to the low-mass case, the Kelvin-Helmholtz timescale for the onset of nuclear fusion is shorter than the accretion timescale. Thus the pre-main sequence phase takes place deeply embedded within the dusty accreting envelope and the detection of the early phases of massive star formation mostly lies beyond the capabilities of optical and near-infrared instruments. Observations in the thermal infrared are far more suitable since the optical depth falls rapidly to longer wavelengths, and the spectral energy distribution of high-mass YSOs rises steeply in the mid-infrared (see, Figure 5-1). Consequently, thermal infrared observations at high spatial resolution are an essential means to study high mass star formation observationally.

METIS on the ELT will answer key questions related to massive star formation. Its wavelength range and spatial resolution will provide the capability to penetrate high extinction columns, measure the spatial scales, and detect the spectroscopic tracers associated with massive star formation, resolving the cluster members within individual, IR-bright, massive young stellar objects (MYSOs) and their immediate environment, throughout the Milky Way. While ALMA will provide constraints on the physical conditions in the dense gas clumps from which the stars form, METIS will reveal the properties of the resulting protostars and clusters, at matching spatial resolution.

### 5.2 Science cases

#### 5.2.1 Cluster formation and the universality of the IMF

There are theoretical arguments that the Initial Mass Function (IMF) in the early Universe should be weighted toward high mass stars (Bromm & Larson 2004). Early observational results seemed to support this, particularly to explain the evolution of IR and sub-millimetre galaxy luminosity functions (e.g., Lacey et al. 2008). However, this was subsequently put in doubt (Hayward et al. 2013). More recently, Conroy et al. (2013) presented evidence that massive elliptical galaxies exhibit bottom-heavy IMFs compared to that in the disk of the Milky Way (cf. Treu et al. 2010). While in most environments in which it is well measured, the IMF is invariant within the errors (e.g., Bastian et al. 2010), there are persistent suggestions that extreme environments such as the Central Molecular Zone of the Milky Way may produce top-heavy mass distributions (e.g. in the Arches cluster: Hosek et al. 2019). Understanding whether the IMF can vary is vital to the production of a predictive model of star formation and therefore to our comprehension of galaxy evolution and the star-formation history of the Universe. Some theories of massive-star and cluster formation (e.g., competitive accretion; Bonnell & Bate 2006; Bonnell & Smith 2011) require the latter to form already mass-segregated, i.e., high-mass stars form preferentially in the cluster centres. Experimental

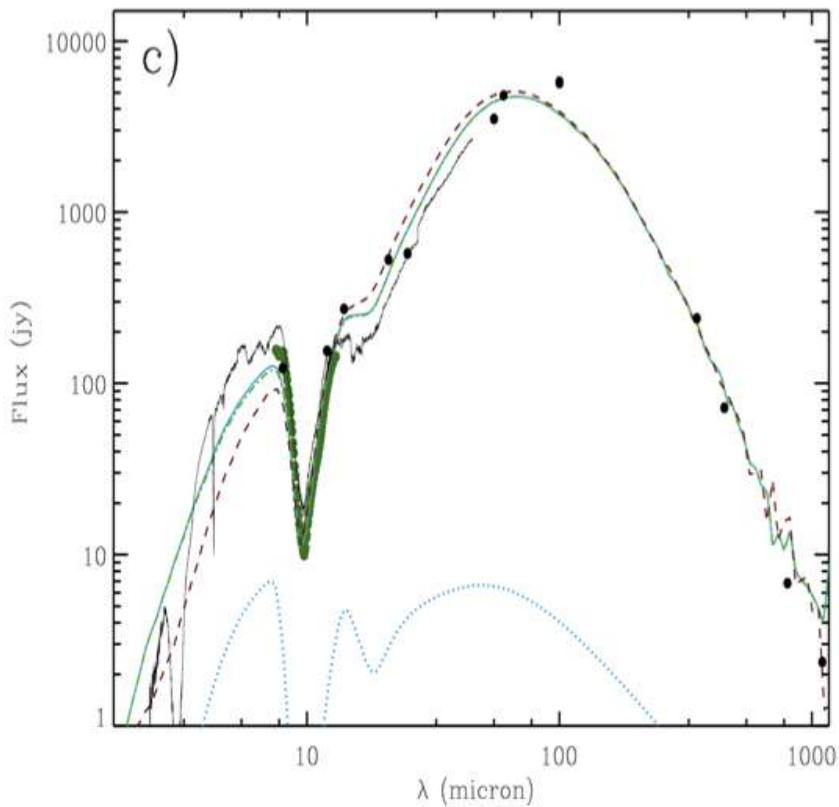


**Figure 5-1:** An example spectral energy distribution of a Massive Young Stellar Object. Most flux is emitted at mid- to far infrared wavelengths, and the object is extremely faint at wavelengths shorter than the L band. Figure: AFGL 2136, taken from de Wit et al. (2011).

evidence for early-time mass segregation would not only constrain the sequence and therefore the process of star formation within clusters (high- or low-mass first or simultaneous) and hence the current models, but would also have fundamental implications for the general idea of a universal IMF on all scales. If the IMF can be position-dependent within a forming cluster then the latter principle will be shown to be invalid. Competing models, such as turbulent core formation, predict less fragmentation, more isolated MYSOs, and a different role for massive star feedback on environment and subsequent star formation (Krumholz et al. 2007). Observations of stellar clusters at visible and near-IR wavelengths show mass segregation, which is probably due to dynamical evolution on short timescales (Allison et al. 2009), so we need to probe the earliest possible evolutionary states to determine the primordial mass structure in clusters. ALMA results have produced mixed results on the mass function of the clumps in proto-clusters, e.g., apparent simultaneous formation of low and high masses but with relatively few low-mass clumps (Cyanowski et al. 2017), only low-mass clumps (Zhang et al. 2015; Sanhueza et al. 2017), and a mass function consistent with a standard IMF (Cheng et al. 2018). A key science project for METIS on the ELT, possibly in conjunction with, e.g., MICADO, is therefore to image the youngest embedded, IR-bright clusters within massive Galactic star-forming regions with sufficient spatial resolution to separate the individual young stars and measure the radial dependence of the luminosity function (see, Figure 5-2 for an example image). Using a sample of such regions, it would also be possible to search for variations in the star-formation rate and efficiency, vital inputs into semi-analytic models of galaxy formation and evolution, and determine the fraction of stars harboring circumstellar disks as a function of cluster age, mass and/or density.

For typical molecular gas densities and temperatures in massive star-forming regions, the Jeans length is of order 0.01 pc. This is equivalent to 0.2'' at 10 kpc, requiring the spatial resolution of METIS to resolve the still-embedded members of young clusters, prior to significant dynamical relaxation and consequent mass segregation. ALMA observations of the pre-stellar stages of star formation are probing spatial scales of this order (e.g., Tan et al. 2013; Cyanowski et al. 2017). At comparable spatial resolution, METIS will measure

the luminosity functions of embedded sources from 3 to 13  $\mu\text{m}$ . Although coarse as a tracer of individual stellar masses via IR luminosities (estimates are good to within a factor of 2-3), thermal IR observations will enable the characterization of the full stellar populations down to sub-stellar masses observed through dozens of magnitudes of visual extinction. By studying multiple young clusters within 10 kpc of the Sun, we can then search for variations as a function of Galactocentric radius and the known radial variations in, e.g., metallicity, pressure, radiation field, and in unique environments (e.g., molecular ring, Galactic centre, sites of triggered star formation), representing a wide range of star-forming sites also relevant to other galaxies. Further, using multi-band photometry and low- to medium-resolution imaging spectroscopy, we can study gradients in the properties of barely resolved, but deeply embedded, massive clusters in the local group. While more evolved star clusters will be better studied in the near-infrared, many of the youngest ultra-compact HII regions, most closely connected to their initial conditions of formation, will only be visible in the mid-IR. Pioneering studies of distant barely resolved embedded regions in the Milky Way conducted with the VLT can be extended with METIS to the LMC/SMC and perhaps M33, opening up unique studies of the IMF and star formation in diverse galactic environments. In the confusion-limit, METIS will be able to probe embedded star clusters in the local group not accessible with JWST.

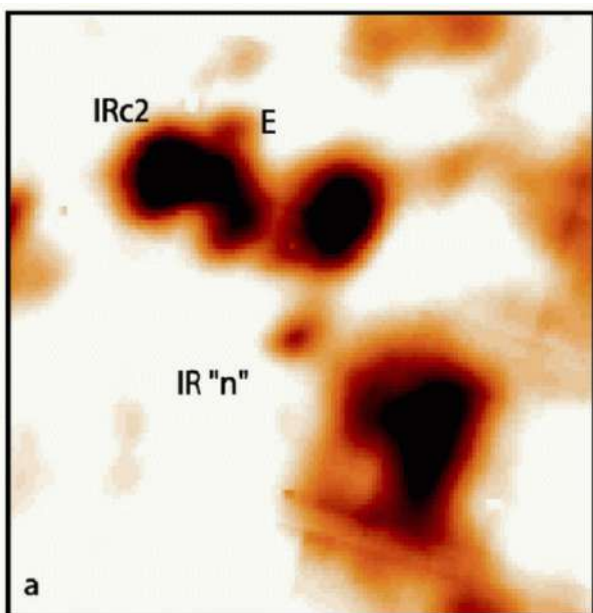


**Figure 5-2:** Keck telescope image of the KL region in Orion at 12.5  $\mu\text{m}$  (Shuping et al. 2004). which breaks up into emission features caused by several embedded protostars. The cutout size is  $10'' \times 10''$ . At 414 pc, Orion is the closest site of massive star formation but most of such regions are several kpc away. If we put Orion at a typical distance of 4.0 kpc, all the fine structure in this image would be contained within a  $1'' \times 1''$  area.

### 5.2.2 Mapping the immediate environs around massive YSOs

Although theory (e.g., Zinnecker & Yorke 2007) and numerical simulations (e.g., Kuiper et al. 2010, 2011; Rosen et al. 2016; Rosen & Krumholz 2020) suggest that high-mass stars may form by disk accretion, observational evidence for the existence of such disks, especially at smaller scales, remains scarce. Only recently, direct evidence for Keplerian rotating, flattened structures at sub-arcsecond scales has started to emerge (e.g., Johnston et al. 2015; Ille et al. 2016; Johnston et al. 2020), all based on mm data. The observations indicate the existence of long-lived large-scale, 100s to 1000 au, cool circumstellar disks, but the inner, hotter, accretion regions and the bases of outflows could not be revealed at these wavelengths. Radio interferometry (Shepherd et al. 2001; Reid et al. 2007) as well as MIR interferometry (Linz et al. 2009; Kraus et al. 2010; de Wit et al. 2011; Boley et al. 2013; Frost et al. 2019) also suggest that potential disks around several massive young stars have diameters smaller than 100s of au. Indeed, Frost et al. (2019, 2021) are the first to find evidence for a disk with a cleared inner hole of 60 au in their MIDI interferometric

data. This discovery provides intriguing evidence for transition disks around massive stars in analogy to lower-mass stars surrounded by forming planets. However, the mid-infrared interferometric studies are limited by sensitivity to only the brightest nearby sources, while extensive mapping of the uv-plane for the sources is prohibitively expensive and will remain so also with the next-generation VLTI instruments like MATISSE. A further complication is that any interferometric observations are constrained to the brightest objects only, and therefore studies are mostly limited to single objects. METIS will allow us to study a large sample of objects, moving away from the anecdotal and start studying statistically meaningful samples, such as the RMS survey that produced a catalogue of 100s of MYSOs, and is complete in the Galaxy for mid-IR bright MYSOs of 15 solar masses and higher (Lumsden et al. 2013). With METIS, we will be able to resolve the disks at sub-100 au scales, even for objects several kpc away, and begin to determine the structure of such disks and their embedding into the envelope material. An additional bonus arising from these imaging observations is that close companions can be detected at high contrast ratios. Although the majority of massive main sequence stars are in binaries, with significant implications for their further evolution (Sana et al. 2012), the origin of multiplicity in high-mass stars is still unclear. Given that dynamic effects may alter the proto-binaries' properties, we need to observe stars in their early phases to obtain observational constraints on binary star formation scenarios (e.g., Meyer et al. 2018; Lund & Bonnell 2018; Oliva & Kuiper 2020). Until recently, we hardly knew anything about the binary properties of MYSOs, with studies being limited to serendipitous detections of binary MYSOs at separations of 30 -100s of au and larger (e.g., Beuther et al. 2017; Kraus et al. 2017; Koumpia et al. 2019). Dedicated surveys had been lacking, A recent survey (Pomohaci et al. 2019) used adaptive-optics-assisted near-IR imaging and found a binary fraction of 30% in the 400 to 40,000 au range, suggesting a very high overall multiplicity. The next step is to complete the parameter space at smaller separations. Next to radial-velocity studies probing the closest sources, high-contrast METIS imaging will be excellent to fill the gap between RV studies, and 8m class images. Utilizing the powerful thermal-infrared imaging of METIS with a 39-m telescope, we finally can observationally address mechanisms to circumvent the radiation pressure problem for the infalling matter onto the central regions. Theorists have proposed outflow cavities, optically thick disks, and/or Rayleigh-Taylor "fingers" to reshape the radiation field and to beam it away from the bulk of the incoming matter (Tan et al. 2014). With the high spatial resolution imaging we will be able to look for such structures at the locations where they matter most for the accretion process: within the innermost hundreds of au. This will put us in a position to better assess the current and future numerical simulations of massive star formation (see, Figure 5-3). ALMA and EVLA will also make significant steps in the study of circumstellar structure (e.g., Krumholz et al. 2007), but sub-mm and cm-wave molecular lines trace mostly the low and intermediate temperature regime appropriate to cool outer-disk regions, pre-stellar objects, and more extended cloud cores, but will provide little information from the inner accretion. METIS, thanks to its high-dispersion IFU mode in the thermal infrared, is complementary to such facilities, rather than competing. Both approaches are needed to obtain a complete picture of the disks around massive YSOs.

### 5.2.3 Physical conditions in the massive YSOs

The benefit of L and M band capability in METIS is twofold. At 3 - 5  $\mu\text{m}$  we trace the hotter material close to the heating sources, which is of special interest when exploring mass transfer onto the central objects and in constraining parameters of continuum radiative transfer models. This is important since the number of free parameters increases drastically when going from one-dimensional models to 2D- or even 3D-simulations (e.g., Indebetouw et al. 2006). Furthermore, the L and M bands contain important spectral lines and ice features, which provide data on disk structure and kinematics. Keplerian rotation is the ultimate evidence for a disk. In this wavelength range, both gaseous and solid-state CO can be detected, the former arises in the inner, warm disk regions (e.g., Blake & Boogert 2004b). Goto et al. (2006b) have spatially resolved the CO emission of the disk of a Herbig Ae star at 100 pc by means of AO-assisted high-resolution spectroscopy. However, in young massive stars, the spectra are dominated by more or less strong CO absorption lines. In order to disentangle these lines from CO emission, a resolution  $R>25000$  is mandatory, and 50,000–100,000 is ideal. Furthermore, one often has to resort to the line series of the

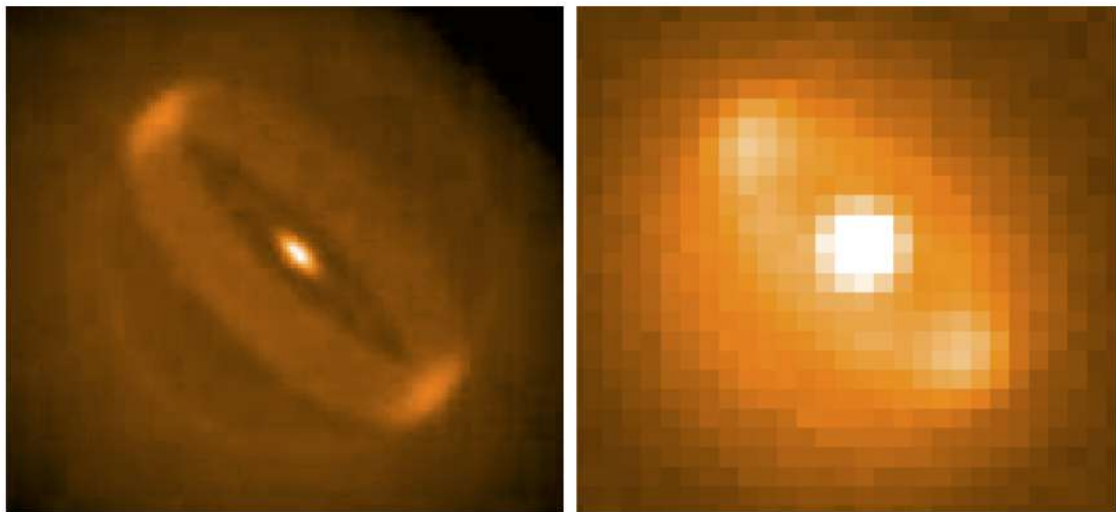


**Figure 5-3:** Left: Model image of the circumstellar environment of a MYSO which reproduced the limited uv-coverage MIDI data and the spectral energy distribution (de Wit et al. 2011). Right: How the object would look like using the ELT. Image computed using the METIS simulator. The image is about 0.25 arcsecond on a side

weaker CO isotopologues in order to make a meaningful excitation analysis. Hence, the combination of high spectral resolution and large collecting power of ELT/METIS is mandatory for this research.

The Pfund- $\beta$  and Brackett- $\alpha$  lines are also covered by the LM bands. These can arise in accretion flows or in a disk wind where the intense radiation from the YSO drives mass loss off the surface of the inner parts of its disk (Drew et al. 1998). Their emission-line profiles and line ratios when computed as function of wavelength already provide indirect evidence for the geometries involved (Lumsden et al. 2012; Pomořáček et al. 2017). However, spatially resolving these line-forming regions with METIS would be a breakthrough for investigating the dynamical structure of the interiors of the youngest massive YSOs, which are too deeply embedded to use near-infrared recombination lines.

Finally, with medium spectral resolution, the ices around massive YSOs can be studied, providing information on the outer disk structure, the composition and thermal history of the ice. Figure 5-4 gives examples for M-band spectra of massive YSOs and indicates important spectral features that are of interest for METIS spectroscopy.

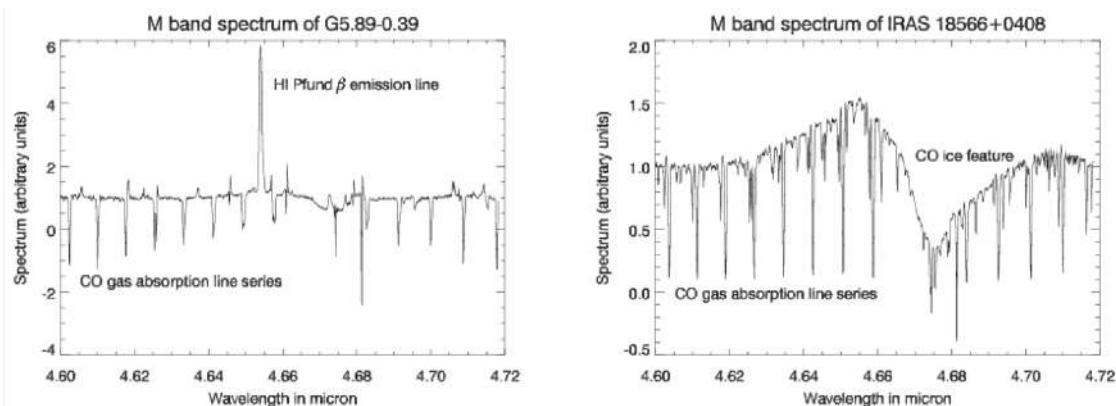


**Figure 5-4:** Examples for M-band spectra of massive YSOs. Left: The UCHII region G5.89-0.39; Right: The high-mass protostellar object IRAS 18566+0408. The most important spectral features accessible with METIS are labelled.

### 5.2.4 Accretion disks around massive YSOs

A major uncertainty concerning the formation of massive stars is how stellar mass is built up through accretion. This requires observations at the smallest possible scales to enable studying the accretion onto the star. A Keplerian circumbinary disk has been seen in the hot-core tracer CH<sub>3</sub>CN at 0.4'' resolution in G35.2-0.74 with ALMA (Sánchez-Monge et al. 2013). Evidence for a disk in this source was also seen in the 2.3- $\mu$ m CO overtone bands by (Ilee et al. 2013). However, given the small scales involved, it is very hard to directly image the accreting material at inner disk radii. Spectro-astrometry, however, is able to measure the photo-center of a spectrum at sub-pixel scales, and both spectrally and spatially resolved spectra allow us to study the inner parts of the circumstellar disks and material. Here, METIS with its IFU for the L-M-band range will make 2D spectro-astrometry possible, a powerful extension of the original technique that has already been pioneered recently for some MYSOs (Davies et al. 2010; Murakawa et al. 2013; Caratti o Garatti et al. 2016, using IFU spectroscopy or using differential phases in VLTI;). Combining such data with sophisticated models will allow us to derive the relevant astrophysical parameters (e.g., Wheelwright et al. 2012, Figure 5-5). Sub-milliarcsec scales have been probed with existing facilities and with METIS micro-arcsec precision can be achieved. This will render disks around a large sample of MYSOs available for study in various atomic (such as hydrogen recombination) and molecular (e.g., CO at 4.6  $\mu$ m) lines. This will provide direct evidence for direct disk accretion for the formation of massive stars (see, e.g., Pontoppidan et al. 2011b), leading to measurement of accretion rates and key tests of rapid- and accelerating-accretion models of high-mass star formation (e.g., McKee & Tan 2003; Hosokawa et al. 2010).

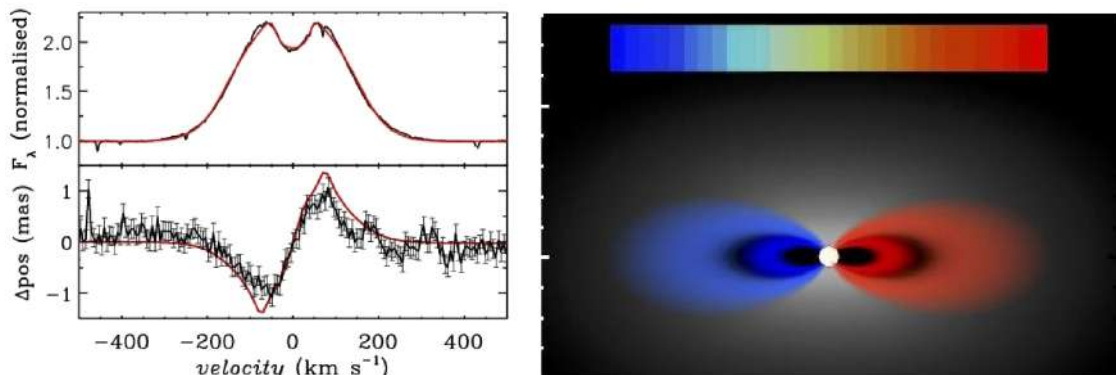


**Figure 5-5:** Left: Example spectro-astrometry of the H $\alpha$  emission line of a Be star. The top panel shows the intensity spectrum, the double peaked profile indicates the presence of a rotating disk. The lower panel shows the offset of the light from the various parts of the disk. As can be seen from the right hand panel, the blue-shifted and red-shifted emission arise from opposite sides from the star. The solid line shows the fit from a 3D non-LTE model (Wheelwright et al. 2012). The precision in the positioning of the photo-centre is at the sub-milli arcsec level, with METIS, micro-arcsecond level should be reachable.

## 6 EVOLVED STARS AND THEIR CIRCUMSTELLAR ENVIRONMENT

### 6.1 Scientific background and context

The final evolution of low- and intermediate-mass stars is a rapid transition from the Asymptotic Giant Branch (AGB) over the post-AGB transit towards the Planetary Nebula Phase (PN), before the stellar remnant cools down as a White Dwarf (WD). In these late phases, it is the external mass-loss that governs the stellar evolution and one of the key ingredients is that in the cool circumstellar envelope (CSE) of AGB stars, dust grains are formed. It is well known that this accumulated mass-loss of lower mass stars is one of the major contributions to the ISM enrichment in gas, dust and chemical species like C, N and the s-process elements beyond the iron peak. This recycling of gas and dust between the ISM and stars is one of the strong evolutionary drivers of a galaxy's visible matter and its chemical and spectral characteristics (see e.g. Meixner et al. 2006; Gordon et al. 2011; Zhukovska et al. 2016; Kobayashi et al. 2019).

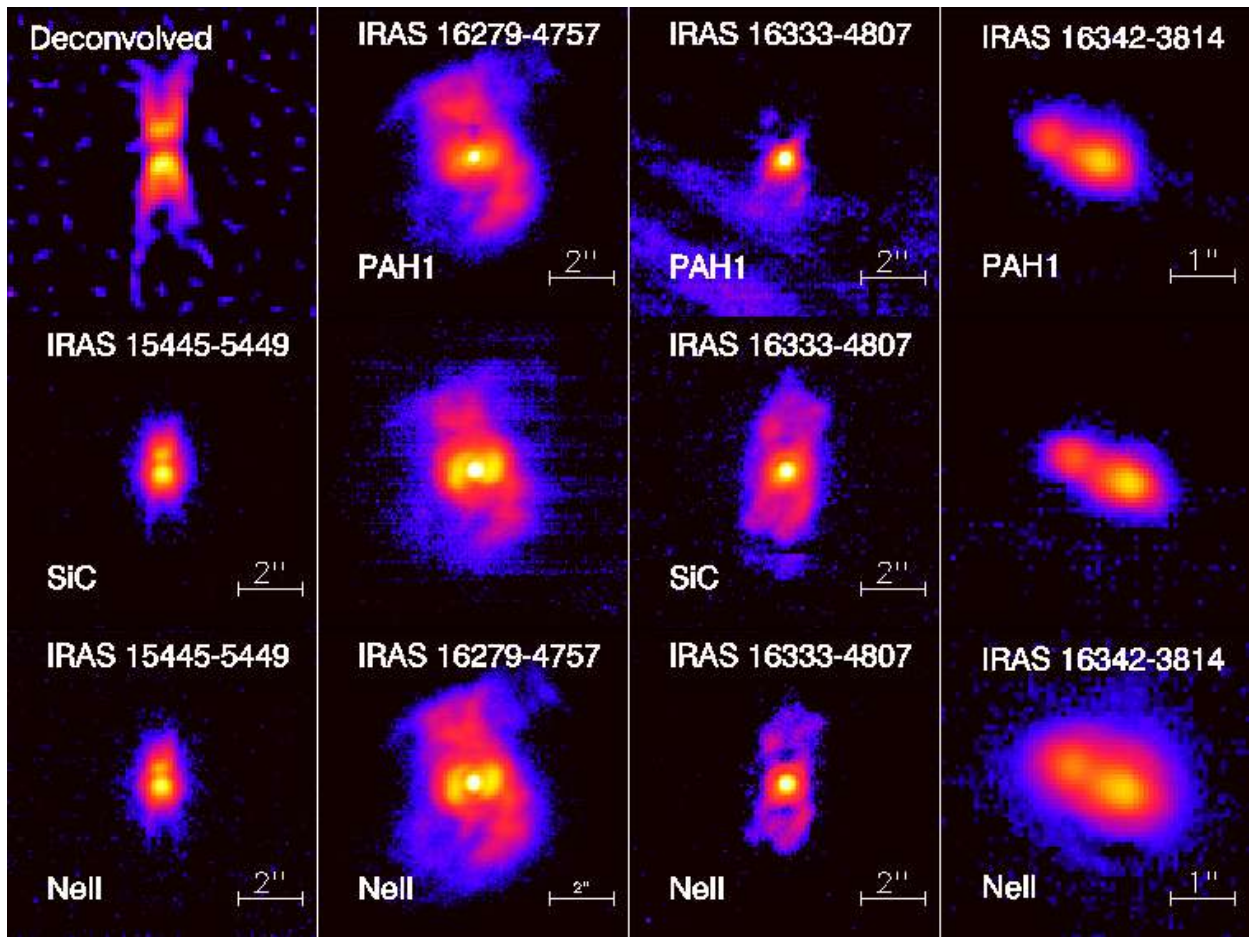


**Figure 6-1:** A small sample of mid-IR images of evolved objects obtained with the VISIR instrument on the VLT. Out of 96 objects observed in this survey, roughly 20 were spatially resolved, i.e. a few objects per evolutionary class (e.g., AGB, post-AGB, PN) (Lagadec et al. 2011).

Although the scheme of the late phases of low-mass stellar evolution may be generally acknowledged, there is no understanding from first principles of the mass-loss process and models still rely on many, rather ad-hoc assumptions. These important processes cover a wide range of scales, from the micro physical levels up to much larger scales, where poorly understood driving and shaping mechanisms work on the whole circumstellar envelope. On the micro scale, the chemical and physical processes in the interface region between the photosphere and the dust forming layers are crucial to generate a dust-driven wind (e.g. Nowotny et al. 2005; Bladh & Höfner 2012; Bladh 2019). In this region, a complex interplay between

non-equilibrium gas-gas and gas-dust interactions are strongly dependent on the local chemical and thermodynamical conditions. Illustrations of our poor knowledge of this crucial part in the mass-loss process are legion. Oxygen-rich stars, for instance, suffer from the "acceleration deficit" dilemma, which states that predicted mass-loss rates due to the formation of silicate dust alone are orders of magnitude smaller than observed ones (Woitke 2006; Höfner 2008) demonstrated that Fe-free silicate grains of sizes larger than 0.1  $\mu\text{m}$  may drive a wind and grains of this size have been detected by Norris et al. (2012).

The detection of AlO in the oxygen-rich mass-losing stars (Tenenbaum & Ziurys 2009; Decin et al. 2017) indicates that small amounts of metal oxides in the gas-phase form and survive the condensation phase of solids (Kamiński 2019), despite their key role as precursors in the nucleation of dust grains (e.g. Tielens 1990). However, the exact path for the formation and growth of oxygen rich grains is still a matter of ongoing research (e.g. Gobrecht et al. 2015; Höfner & Freytag 2019). The formation of C-rich dust is better understood, but also here several uncertainties in the chemical paths exist (Cherchneff 2012). Tracing the molecular "left-overs" of dust formation can thus give crucial hints as to which path leads to carbon and silicate dust at which distance from the star.

On larger scales, our understanding of the processes driving and shaping the whole CSEs, is also still very limited. This is in part due to the high spatial complexity of many of these structures, as illustrated abundantly by the optical images of PNe in scattered light and in nebular optical emission lines by the Hubble Space Telescope (e.g. Balick & Frank 2002; Sahai et al. 2011). For the nearest ones, the thermal emission of the dust component is also resolved with current infrastructure. Also cooler post-AGB stars or proto-planetary nebulae (PPNe) display a surprisingly wide variety in shapes and structure in thermal emission as well as in scattered light (Figure 6-1). This was not expected since the major shaping was thought to occur when the central object is hot enough to generate a fast wind.

The major discussion topic in the PNe community for a while now, is the growing evidence that our view of the Planetary Nebulae physics is in fact dominantly determined by processes only relevant in binary stars (e.g. De Marco 2009; De Marco & Izzard 2017). Binary transition objects do contain bound Keplerian disks (Bujarrabal et al. 2013, 2015), the structure of which resembles protoplanetary disks around young stellar objects (Van Winckel 2018). It is now acknowledged that these disks must play a leading role in the evolution of the systems. Progress on the observational side is now very prominent with ALMA (e.g. Maercker et al. 2012; Ramstedt et al. 2014, 2020). And also on the AGB, unrecognised binary interactions play an important role (Decin et al. 2020) but it is as yet unclear how diverse and widespread these interactions are.

The increase in high-resolution possibilities with the IR interferometers and adaptive optics provide a wealth of new information. The present day interferometers at CHARA (Center for High-Angular Resolution Astronomy) and/or the VLTI (ESO) allow efficient image reconstruction thanks to the 4 to 6-beam combinations. The PIONIER, Gravity and MATISSE instrument at the VLTI of ESO brings progress on high-spatial resolution science, but the stringent flux limit on the correlated flux, will remain an observational challenge. The conclusion of these efforts is that symmetry breaking of the spherical winds occurs very early, but the major driving forces remain unclear.

It is clear that our understanding of the mass loss processes and the deduction of the mass-loss history of low-to-intermediate mass stars is far from understood (e.g. Decin 2021, and references therein). The combination of superb sensitivity, high-spatial spatial resolution and high-spectral resolution of METIS at the ELT is crucial to address the research goals presented in more detail in the following sections. The spectral resolution is needed to resolve the kinematics of the circumstellar material and study the isotopic ratios, which are ideal probes, not only for the AGB nucleosynthesis, but also for the nucleation processes in the circumstellar envelopes and disks. The full N-band spectra will allow us to study the mineralogy of the hot dust component and, for the nearest objects, resolved spectra will allow us to probe the radial dependence of the grain characteristics as well as the detection of density inhomogeneities like rings and spirals.

## 6.2 Scientific Goals

### 6.2.1 Molecular envelopes of evolved stars

Systematic studies of winds around evolved stars include (sub-)millimeter observations of molecular lines, IR spectroscopy of dust emission and molecular lines, and observations of atomic or molecular resonance scattering of photospheric light in the shell. Rotational emission lines of molecular species probe the intermediate and outer wind envelope, beyond 30 stellar radii (e.g. Habing & Olofsson 2003). Non-equilibrium chemistry models predict complex molecules to be formed close to the star, which are subsequently ejected in the outer wind as "parent" molecules Cherchneff (2012); Gobrecht et al. (2019); Decin (2021). A current limitation for testing these models is that the thermo-physical structure close to the target is not well constrained. Using high-resolution IR spectroscopy of rotation-vibration lines and observing scattering resonance lines along the line of sight through the envelope (Decin et al. 2007, 2010; Smith et al. 2009a; Ohnaka 2014; Hron et al. 2015; Ryde et al. 2015; Decin 2021) offer interesting possibilities to explore the thermo-physical, spatial and chemical structures in this inner envelope. The approach has been tested using the high-resolution Phoenix spectrometer on the Gemini South telescope for the oxygen-rich AGB star R Hya (Figure 6-2). The slit was placed at different position angles to image the circumstellar envelope around the star. The intensity of the measured CO rotational-vibrational lines clearly decreases with distance to the star, consistent with a symmetric wind. The fact that the NW, NE, and SE intensities lie above the mean, while the SW, ES, EN, and WS lie below may suggest a bipolar structure, stretching from NW to SE. To investigate this idea, one needs a high-resolution IFU to map the inner wind structure.

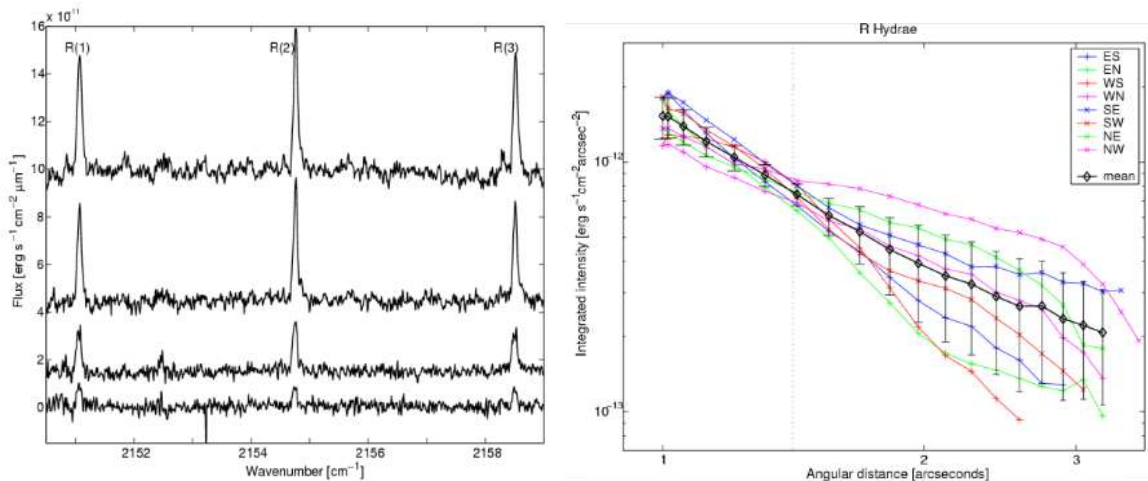


**Figure 6-2:** Left: The set of CO emission spectra at the east-position from R Hya. The spectra are shifted vertically for reasons of clarity. The top spectrum is measured closest to the star, i.e., at 1''. The subsequent spectra are measured at 1.1'', 1.6'' and 2.4'' from the star. Right: The CO line intensity of the circumstellar emission as a function of the angular distance from the star (R Hya) for eight scan directions, and the mean (Decin et al. 2008).

Also, MIR spectroscopy permits the observations of molecules that form in the region that is levitated from the photosphere and whose abundances "freeze out" during the dramatic density drop at the dust formation locus and/or which are depleted onto dust grains. An example for the inner envelope for a prominent AGB star is shown in Figure 6-3. METIS will map the inner wind structure for different molecular species and transitions, thus providing pivotal input in studying stellar mass loss, and in particular high-resolution L and M-band IFU observations are crucial to understand the complex inner wind zone of AGB stars. In comparison with ALMA, MIR spectroscopy gives efficient access to a large number of lines with widely different excitation conditions. Several crucial questions will be answered with the help of METIS:

- What is the structure of the velocity fields in the complex envelopes? Answers to this question can be achieved by spatially and spectrally resolving gas lines, many of which are expected to exhibit P

Cyg profiles or even inverse P Cyg profiles in their absorption and emission portions. Line confusion may be a serious problem that is best met with high spectral resolution.

- What is the density and thermal structure in the envelopes? Various molecules (e.g., CO, H<sub>2</sub>O, C<sub>2</sub>H<sub>2</sub>, CH, SH, HCl, SiO, OH, CO<sub>2</sub>, CS, CH, HF, NH, NO, C<sub>3</sub>) are ideal thermometers and barometers to trace the density and thermal structure in the envelope. The L- and M-bands, accessible with METIS at high spectral resolution, are rich in lines of these molecules. CO, H<sub>2</sub>O, C<sub>2</sub>H<sub>2</sub>, SiO, CH, HCl and OH are of particular importance due to their abundance or relevance for the chemistry and dust formation.
- What are the details of nucleosynthesis and the neutron source driving the s-process in AGB stars, and the dredge-up efficiencies enriching the outer atmospheric layers with nuclear yields? Several isotopologues can be studied to derive the interesting isotopic ratios such as <sup>12</sup>C/ <sup>13</sup>C, <sup>16</sup>O/ <sup>17</sup>O, <sup>16</sup>O/ <sup>18</sup>O, <sup>24</sup>Mg/ <sup>25</sup>Mg, etc. to refine our insight into the nucleosynthesis and mixing in evolved stars and their impact on the chemical evolution of the Galaxy.
- What is the chemistry in the inner envelope of AGB stars? Thanks to the IFU, we will be able to image the inner wind structure and hence measure the line intensities (and abundances) as a function of radius from the photosphere. Thus, we will provide direct measurements of the depletion and freeze-out processes of the different species, and we can study the effect of pulsation-induced shocks, the extent of inhomogeneities, the onset of shaping of the axis-symmetric Planetary Nebula envelope, etc.

### 6.2.2 Dust Structure around evolved stars

An ELT equipped with a mid-IR instrument such as METIS would bring a whole variety of evolved objects within range for direct imaging of their dusty CSE. In that sense, it would supersede the short baseline VLTI, providing an image with several magnitudes higher sensitivity and dynamic range. A prerequisite for this research, however, is that the instrument can deal with the high flux levels of nearby luminous objects (of the order of many Jy). This will require the use of the coronagraphs. For all these objects, complementary ALMA observations would allow us to create a combined gas+dust picture of the CSEs. The scientific questions that METIS will tackle in the study of dusty CSEs can be broken up into the different instrument modes:

- **Imaging:** The imaging modes from L to N offered by METIS will allow a detailed study of the morphology of the ejecta, which is known to be related to stellar pulsation (shells), convection (clumps/plumes), chemical composition (dust and molecules), binarity (disks) and rotation (torii or aspherical shells). It would, for example, extend the current VISIR sample of spatially resolved post-main sequence objects (typically a few per class, see Fig. 1) by a factor of almost 50, finally allowing proper statistical analysis. This is crucial if we want to understand the shaping mechanism of Planetary Nebulae. If a substantial time baseline were available (a few years), it would be possible to directly observe the dynamics (e.g., expansion) of the dust in the CSE, which can then be compared to the dynamics of the gas (cf. the study of the molecular envelope).
- **Low-resolution long-slit spectroscopy:** The low-resolution N-band long-slit spectrograph will allow us to study the dust composition as a function of location within the CSE, by scanning the CSE with the slit. This will provide a direct observation of the dust condensation sequence in dust-driven AGB winds which is the most problematic unknown in all of AGB star research. Also, it will be used to determine the location of crystalline dust in those CSEs where strong dust processing appears to occur. Furthermore, studies of the evolution of dust along the AGB done in galactic globular clusters can be extended to external galaxies.

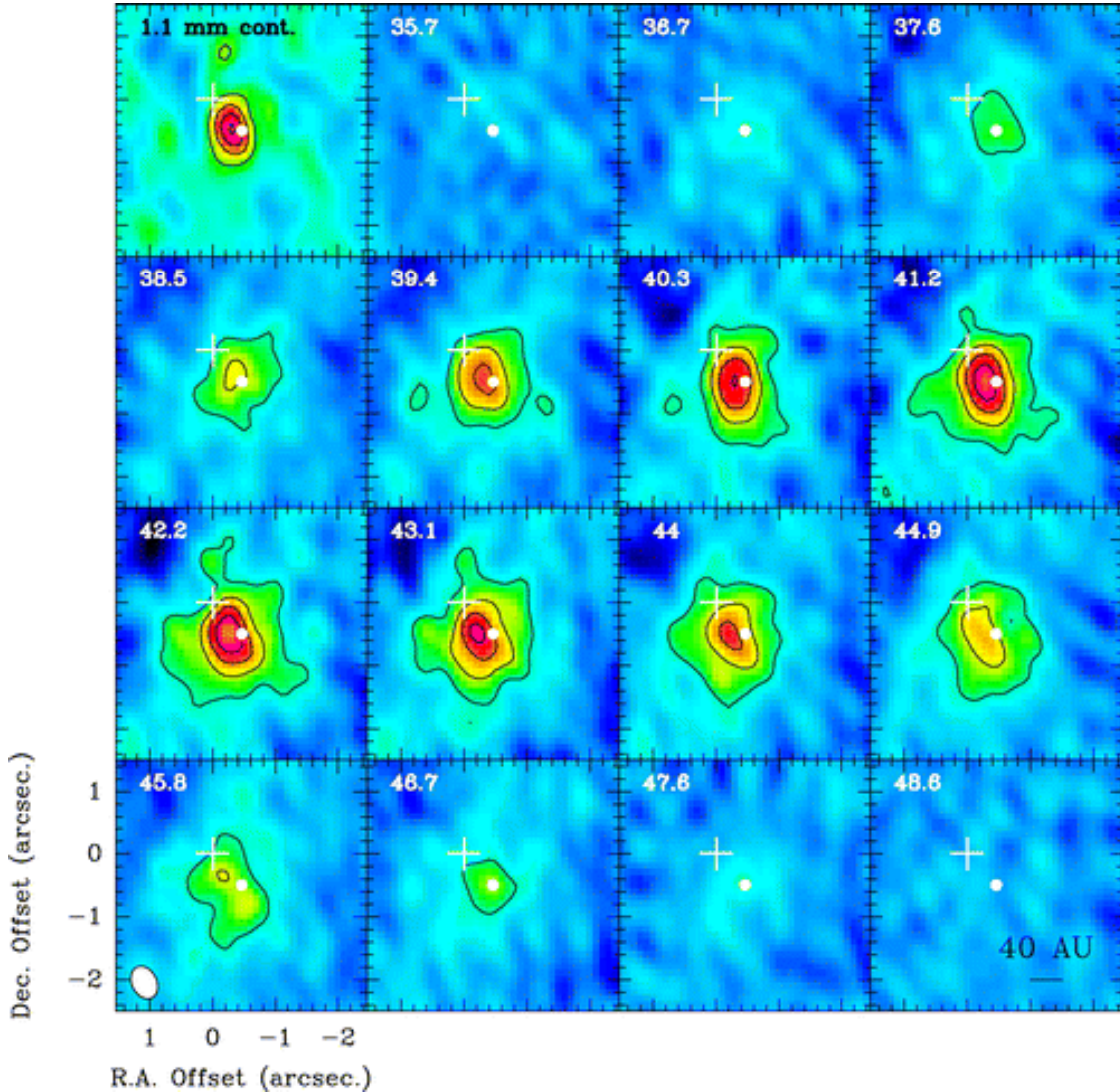


**Figure 6-3:** 1.1 mm continuum emission (top left corner box) and HCN (3-2) channel maps of W Hya as observed with the SMA very extended configuration. Contours are every 25 mJy/beam for the continuum map, and every 0.75 Jy/beam (5 sigma), corresponding to 60 K for the synthesized beam of  $0.55'' \times 0.40''$  (P.A. = 26 deg), for the channel maps. The white cross indicates the position of the phase center, set at the stellar position from the Hipparcos catalogue in the year 2000 (R.A.(J2000) = 13:49:01.998 and Dec.(J2000) = -28:22:03.49). The white dot gives the expected position of the star at the date of our observations in 2008, due to its proper motion. The small offset ( $\sim 0.15''$ ) between this position and the peak emission may be due to baseline errors. The detection of carbon-bearing molecule HCN in the inner envelope of the oxygen-rich AGB star W Hya clearly points to an inner wind origin, possibly due to shock-induced non-equilibrium processes taking place in the inner envelope (from Muller et al. (2008)).

### 6.2.3 Protoplanetary disk physics around evolved stars: second generation of planets?

The focus for the study of planet formation is directed to the disks around young stars, in which planet formation clearly occurs (see chapter on protoplanetary disks). However, it has recently become clear that there are other cases where disks with similar properties can form and might potentially lead to the formation of macro-structures or even planets (Kluska et al. 2022). An interesting, albeit slightly exotic, case is planets around pulsars (Wolszczan & Frail 1992) which are believed to form in a disk formed after a supernova explosion (Wang et al. 2006). More recently, planets have also been discovered around the post-common envelope binary NN Ser (Beuermann et al. 2010), but also around AGB stars like L<sup>2</sup>Pup (Kervella et al. 2016; Homan et al. 2017) with its disk resolved both with ALMA as well as with the extreme-AO instrument at the VLT (SPHERE).

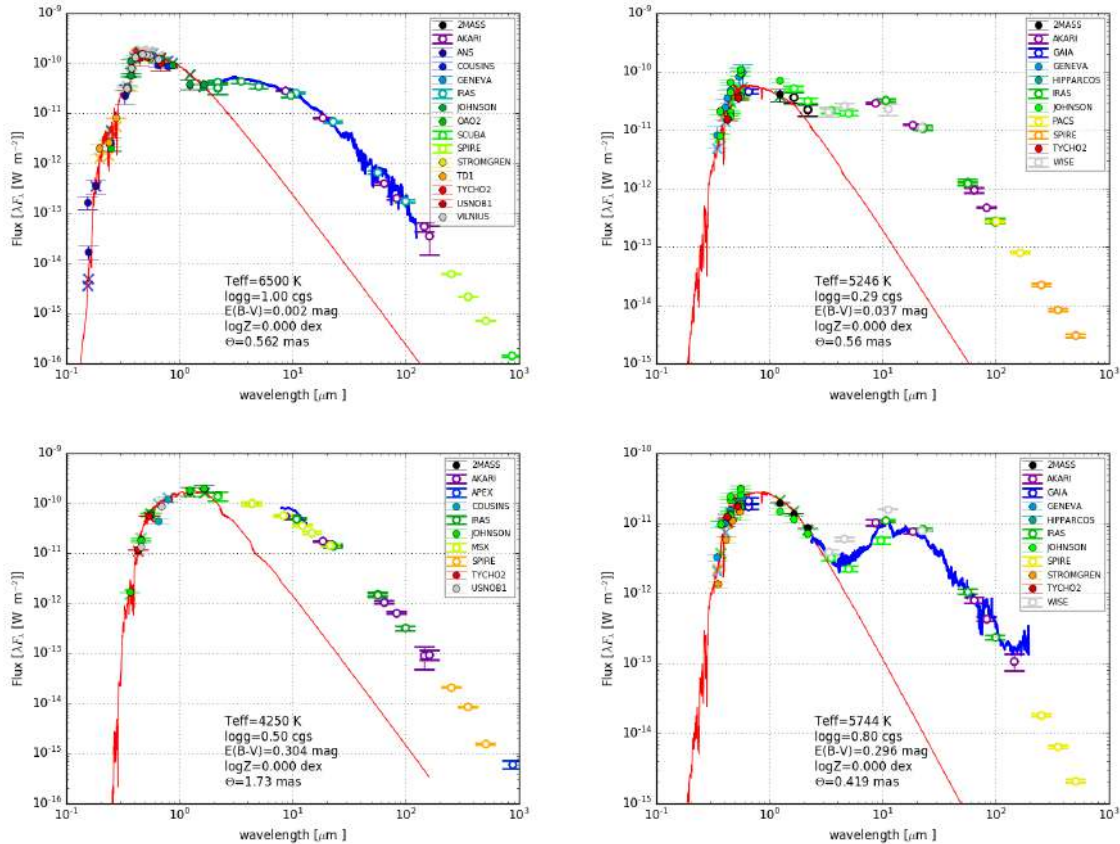


**Figure 6-4:** Characteristic examples of disks around post-AGB stars. The IR excess starts as dust sublimation temperatures, and the peak of the SED is around  $10\text{ }\mu\text{m}$ . Some 90 of these objects are known in the Galaxy (Van Winckel 2018; Kluska et al. 2022) and a significant number has been found in the LMC and SMC (Kamath et al. 2014, 2015).

An even more intriguing case is made by the recent detection of disks around so-called binary post-AGB stars, which in many observational properties seem to be very similar to classical protoplanetary disks. Their distinct SED characteristic (bimodal, with peaks in the visible and mid-IR and a distinct near-IR excess, see Figure 6-4), was used to start a systematic search for binary post-AGB candidates de Ruyter et al. (2006). A follow-up study includes radial velocity monitoring, high-spectral resolution optical and IR studies, and sub-millimeter bolometric observations. All objects show evidence for the presence of long-lived dusty disks (Van Winckel 2003, 2018; Kluska et al. 2022).

Recent interferometric studies confirm the very compact nature of the circumstellar material (Hillen et al. 2013, 2014, 2015, 2017; Kluska et al. 2018, 2019) (Figure 6-6) and SPITZER spectroscopy shows the very high level of processing of the dust grains in the disks (Gielen et al. 2007) (Figure 6-5). Additionally, there is an overresolved component which can be up to 30-40% of the flux in the optical (Hillen et al. 2013) or 15 % in the H-band (Kluska et al. 2018) and which is not accounted for by the state-of-the art radiative transfer models. The binary fraction for this class of objects is 100% (van Winckel et al. 2009; Oomen et al. 2018). The companion stars are likely unevolved main-sequence stars, which do not contribute significantly to the energy budget of the objects. These stars have not become contact binaries yet. However, their orbits are too small to have accommodated an AGB star. Therefore the global picture that emerges is that a binary star evolved in a system that is too small to accommodate a full-grown AGB star. During a phase of strong interaction, that is only poorly understood, a circumbinary dusty disk was formed, but the binary system did not suffer from orbital decay. What we observe now is a F-G type post-AGB supergiant in a binary system surrounded by a circumbinary dusty disk. The objects were likely truncated during their ascent on the AGB branch. Observational hints for that truncated AGB evolution is that in most objects, the circumstellar dust

is oxygen rich (Gielen et al. 2008).

The dynamical interaction between this strong wind and the companion star causes part of the mass loss to be trapped in a circumbinary disk. Millimetre observations of CO lines with the Plateau de Bure interferometer and ALMA showed that these disks appear to be stable, i.e. in Keplerian rotation (Bujarrabal et al. 2013, 2015, 2018). These observations also revealed a disk-wind component suggesting angular momentum transport in the disk. These disks possess dust grains with large sizes (de Ruyter et al. 2005; Gielen et al. 2011; Hillen et al. 2015), and large crystallinity fraction (Gielen et al. 2011) (see also Figure 6-5).

Radiative transfer models of protoplanetary disks (PPDs) around young stellar objects (YSOs) are able to reproduce both the SED and infrared interferometric measurements on a few targets (Kluska et al. 2018). The dust masses found in these disks are of the order of  $10^{-4} - 10^{-3} M_{\odot}$  (Sahai et al. 2011; Hillen et al. 2014). In some cases, time-resolved spectroscopic data indicates the creation of a high velocity outflow (jet) in an accretion disk around the companion (Gorlova et al. 2012, 2015; Bollen et al. 2017).

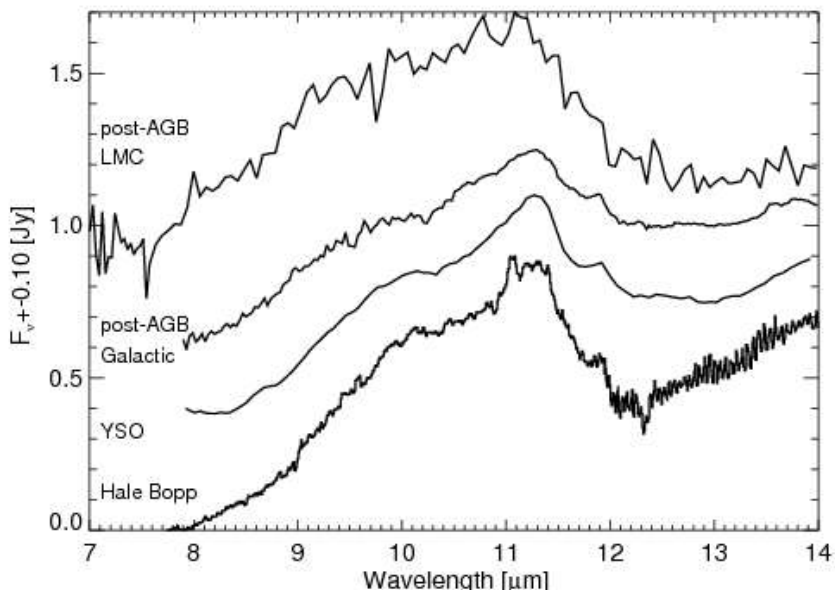


**Figure 6-5:**  $10 \mu\text{m}$  silicate emission profiles of a wide variety of objects: the solar system comet Hale Bopp, a young stellar object (YSO), a Galactic post-AGB binary and a post-AGB star in the LMC. Note the very similar profile indicating that the average silicate grain is quite large with a clear contribution of crystalline silicates as shown by the  $11.3 \mu\text{m}$  forsterite feature. The silicate feature is an ideal tracer for dust processing in the circumstellar disks.

In general, despite very different forming processes, post-AGB disks are in many ways (infrared excess, Keplerian rotation, winds, jets, dust mass, dust mineralogy and grain sizes) similar to protoplanetary disks around YSOs. As the protoplanetary disks are well studied both observationally and theoretically, the very close similarity with the disks around post-AGB binaries rises the question of the universality of physical processes in dusty circumstellar disks and more specifically of their planet formation efficiency. Circumbinary disks around pAGBs can therefore be second generation planet forming disks, especially as several planets are candidates of being formed in such disks (e.g., NN Ser as mentioned above). One way to form planets in those disks would be by gravitational instability (e.g. Schleicher & Dreizler 2014) and METIS, together with ALMA, would be able to probe and constrain such disk instabilities that happen in the outer parts.

The spatial resolution of the ELT, combined with METIS, will allow us to use coronagraphic high contrast imaging of the second generation of circumbinary disk. This will complement the interferometric data and allow for direct detection of structure in the disks which may be induced by the central binary as well as the eventual formation of macroscopic structures. The structure and physical origin of the overresolved flux will be determined as well. In Figure 6-6 we simulate a METIS experiment in the N-band, based on a detailed radiative transfer model of the disk around one of these systems for which the inner rim was resolved

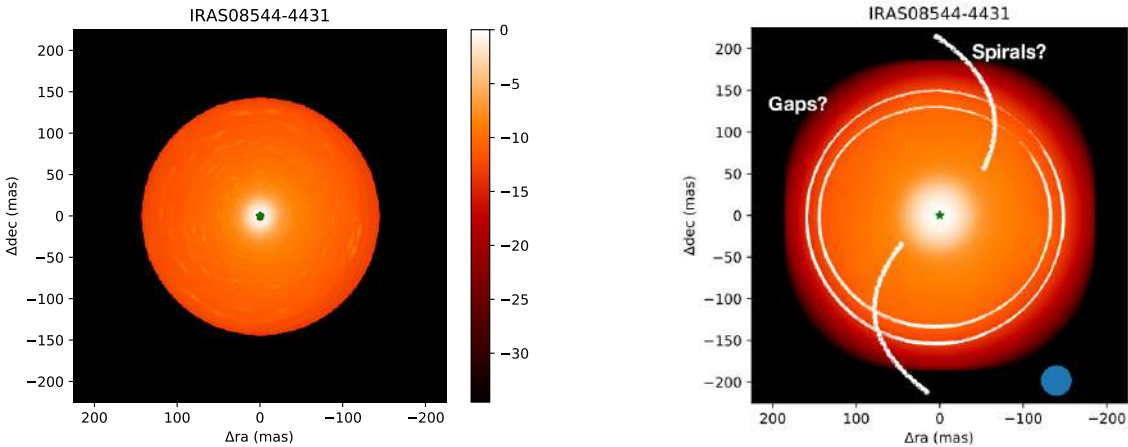


**Figure 6-6:** Left: Full radiative transfer model with a axis-symmetric model of IRAS08544-4431 at  $4 \mu\text{m}$ . (Kluska et al. 2018). Right: The same image but convolved with the METIS beam. METIS with the coronagraph, will allow for direct detection of disk structures like spirals and eventual gaps.

by optical interferometry (Hillen et al. 2015; Kluska et al. 2018). While the IFU in the L band will allow to study the circumstellar gas composition and dynamics of the interacting binaries, the coronagraphic images will directly probe the disk structure and its different components.

We have now identified very similar objects in the LMC and SMC. In the LMC, the disk sources account for about 30% of all post-AGB candidates (van Aarle et al. 2011; Kamath et al. 2014, 2015). Interestingly, disks are also observed at much lower luminosities where they are suggested to be post-RGB systems which have shortcut their evolution on the Red Giant Branch (RGB) (Kamath et al. 2016). This sample is unique as the known distances allow for a full astrophysical test with current (binary) evolution theory. Moreover, some of the objects have disk SEDs, but luminosities that indicate a post-RGB instead of post-AGB nature (Kamath et al. 2015). The large Galactic, LMC and SMC samples prove that circumstellar disk formation must be an important ingredient in the evolution of binaries with a wide range of initial masses, mass ratios and initial orbital parameters.

METIS is an ideal instrument to probe both the gas and dust components of the disks and their interaction with the central stars. The low-resolution spectrum of the N-band will allow mineralogy studies using the 10-micron silicate feature (Figure 6-5). The profile is very sensitive to dust-grain processing both in grain-growth and crystallization (van Boekel et al. 2005; Gielen et al. 2008, 2011). METIS is ideally suited to study the faint objects in the LMC (fluxes in the N-band are down to a few mJy). The disks are very compact, thus at the distance of the LMC and SMC, they are not expected to be resolved with METIS. A systematic study of the whole extragalactic sample will allow detailed correlation studies between dust processing on the one hand, and the positions of the central star in the HR-diagram and the associated evolutionary status on the other hand. Moreover, the metallicity of the initial population will, certainly for the SMC, likely affect the dust processing as well. METIS in high-resolution spectroscopic mode will allow us to study the presence, composition and dynamics of the hot gas component in the disk. The L and M bands contain bands of CO, OH and water lines for the O-rich environments. The high-resolution mode is ideally suited to probe important isotopic abundance ratios of C and O, but also to allow us to compute the temperature and dynamics of the hot circumstellar gas (e.g. Hinkle et al. 2007) for a pilot study of a nearby post-AGB binary). The high-resolution IFU spectra will allow us to probe the expected rotation of the hot circumstellar gas layer and hence probe the gravitational mass of the whole system.

The feedback from the disk on the star is important, as it accounts for the strong depletion of refractory elements in the stellar photosphere. This photospheric chemical peculiarity is characterized by a low abundance of refractory elements like Fe, Ca, and Si, whereas volatile elements like S and Zn are near-solar and are commonly detected in the central stars of the disk sources (e.g. Van Winckel 2003; Maas et al. 2005; Giridhar et al. 2005; Hinkle et al. 2007). Despite being frequently detected, this depletion process

remains very poorly understood. A systematic study of the sample of evolved stars with circumbinary, protoplanetary-like disks in the LMC and SMC will only be possible with the METIS at the ELT. The ultimate goal of the program is to gain insight into the final evolutionary phase of a wide range of binaries. This evolution is intimately connected to the evolution of the circumbinary protoplanetary disk.

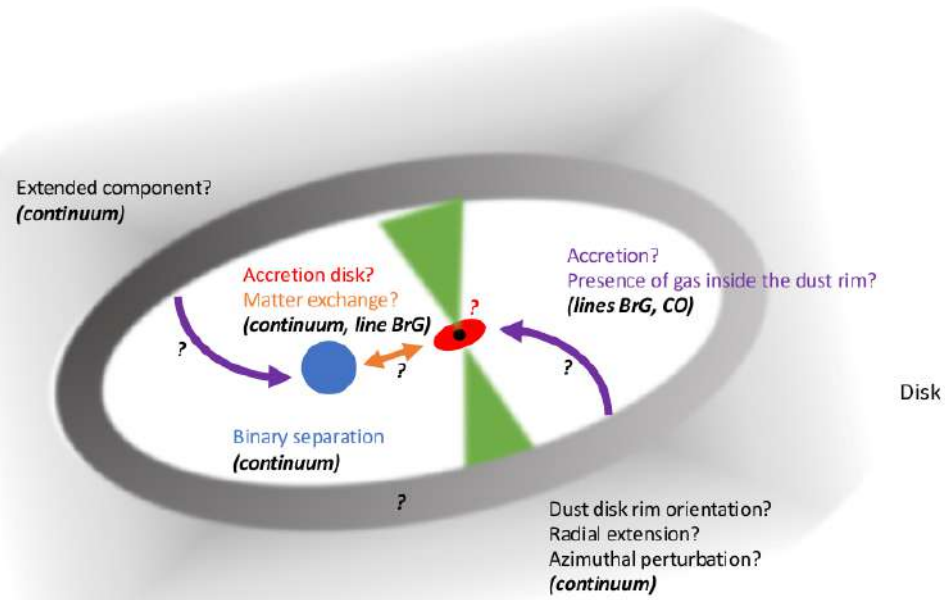


**Figure 6-7:** Cartoon of the physical interplay between the central post-AGB binary and the circumbinary disk. METIS will help constraining the complex interaction processes in these disks (Figure courtesy of J. Kluska).

Since these disks share so many properties with protoplanetary disks, is it conceivable that they, too, form planets? Does that depend on the chemical composition of the disk material? If yes, what will the further evolution of such disks look like? Can they, or the planetary material formed in them, be detected during later evolutionary phases? In Figure 6-7, we show a cartoon of all structural components of binary post-AGB stars and their interaction with the circumbinary disk. METIS on the ELT will focus on the disk structure as well as on the circumstellar gas physics of these interacting binaries.

### 6.3 Gas producing agents in galaxies

While also JWST, and especially the MIRI instrument, will study the individual producing agents in nearby galaxies, only with the spectroscopic mode of METIS, unprecedented details on the chemical and isotopic gas-producing agents are possible. The space observatories ISO and Spitzer provided us with a first glimpse of the gas and dust enrichment of the Galactic ISM in our own Milky Way up to the Fornax dwarf spheroidal galaxy ( $d \sim 140$  kpc) in the  $2-40\ \mu\text{m}$  range. The superb sensitivity of METIS on the ELT (and of MIRI on the JWST beyond  $5\ \mu\text{m}$ ) will allow detailed spectroscopic studies of the gas (and dust) species in a statistically relevant sample of evolved stars in Local Group galaxies (in the field and in clusters). These cover metallicities lower than our Milky Way and the LMC down to metallicities as low as  $1/25$  th of solar. This will enable us to study stellar gas and dust mass-loss rates and dust condensation sequences as a function of the metallicity in galaxies up to  $d \sim 750$  kpc. ALMA will be restricted to the nearest galaxies while MIRI does not cover the most important gas mass loss indicator, i.e., CO. Hence, we will be able to pinpoint the main gas and dust providers in the galactic interstellar media and to look for dependencies upon type of galaxy, interstellar activity, metallicity, etc. The insights gained from these investigations will also have an impact on our understanding of what the main gas and dust producers in starburst galaxies and ultra-luminous infrared galaxies (ULIRGs) are.

## 7 THE GALACTIC CENTER

### 7.1 Introduction and Scientific Background

The Galactic Center region is of great interest not only as the center of our galaxy but also as the environment of the closest (quiescent) super-massive black hole (SMBH) (see recent reviews, e.g., Eckart et al. 2017; Genzel et al. 2010). Largely enshrouded by gas and dust, it can be best explored at radio, sub-millimeter, Mid-to Near-infrared, X-ray and  $\gamma$ -ray wavelengths. The region includes a  $\sim$ 4 million solar mass super massive black hole (Eckart & Genzel 1997; Ghez et al. 1998), three clusters of young massive stars, and massive molecular clouds (see, e.g., Eckart et al. 2005). At a distance of 8 kpc it is the closest nucleus of a Galaxy that we can study in detail. In the central region there are several prominent filaments seen across the wavelength bands. Some of them are the Radio Arc (Yusef-Zadeh et al. 1984) consisting of non-thermally emitting linear filaments perpendicular to the Galactic plane, and the Arched Filaments and Sickle as thermal emitters seen in the light of their radio recombination lines (e.g., Yusef-Zadeh & Morris 1987; Morris & Yusef-Zadeh 1989; Lang et al. 1997, 2001). All constituents of the inner few parsecs, the super-massive black hole (SMBH), surrounding star clusters, streamers of ionized gas, molecular dust ring and a supernova remnant have been studied extensively during the last years (e.g., Melia & Falcke 2001).

### 7.2 Scientific Goals

There are numerous topics of great scientific importance in this complex region, including the stellar dynamics around the SMBH and its associated radio source Sgr A\*, and the formation and evolution of massive young clusters found in the immediate vicinity of the SMBH. Fig. 7-1 shows the near-IR and mid-IR view of the central parsec region, illustrating their complementary nature. The infrared images are close to the diffraction limit of an 8m telescope at their wavelengths. However, METIS would provide approximately the same resolution at mid-IR wavelengths than NAOS-CONICA in the near-IR, enabling the first pan-spectral characterization of the region around Sgr A\*. Highest angular resolution and/or diagnostic spectral line tracers available in the MIR are essential to make further progress in this field (e.g. through absorption features from ices  $H_2O, CH_4, CO, NH_3$  etc.; or through emission features from gaseous molecules like  $H_2, CO, H_2O, CH_4, C_2H_2, HCN, OH, SiO$  etc.). Several of them (e.g.  $CH_4, C_2H_2$  in gas and ice) can be used as probes for stellar disks. For the Galactic Center we have demonstrated the usefulness of the  $H_2O$  line emission and the CO gas and ice absorption to study the extinction towards the Galactic Center and the properties of the GC interstellar medium (Moultaka et al. 2006). In addition to the central stellar cluster and the mini-spiral, the circumnuclear ring (CNR) is also bright in the MIR (see Fig. 7-2).

One issue of particular interest is the accretion and emission mechanisms of the SMBH. Variability and flares have been detected at infrared wavelengths (Genzel et al. 2003). The intrinsic size of Sgr A\* has remained unresolved at centimeter and longer wavelengths because radio waves from Sgr A\* are scattered by the turbulent interstellar plasma along the line of sight. The scattering increases with wavelength as  $\lambda^{-2}$ , pushing observations to shorter and shorter wavelengths. ALMA is expected to be a powerful tool for such observations, and MIR observations at the highest spatial resolution will enormously contribute to this exciting puzzle. Recent broad band observations give upper limits of factors of 2–10 above the theoretically expected SED for Sgr A\*, based on a variety of accretion- and jet models. The limiting flux for these MIR observations was 80 mJy (optimum values are 20 mJy). Depending on the finally chosen site of the ELT, the corresponding point source sensitivity is expected to be 0.06 mJy to 0.08 mJy at  $8.6\mu m$ . The quiescent Galactic center, up to now is not detectable at NIR wavelength, however, during short flare phases the GC has been observed and even polarimetric measurements have been obtained.

While such studies are near the limit of feasibility, monitoring of the quiescent and flaring GC could be easily performed with an ELT. Even medium resolution spectroscopy of Sgr A\* can be obtained. Thus, a very detailed study of the central few Schwarzschild-radii environment of a MBH will be possible.

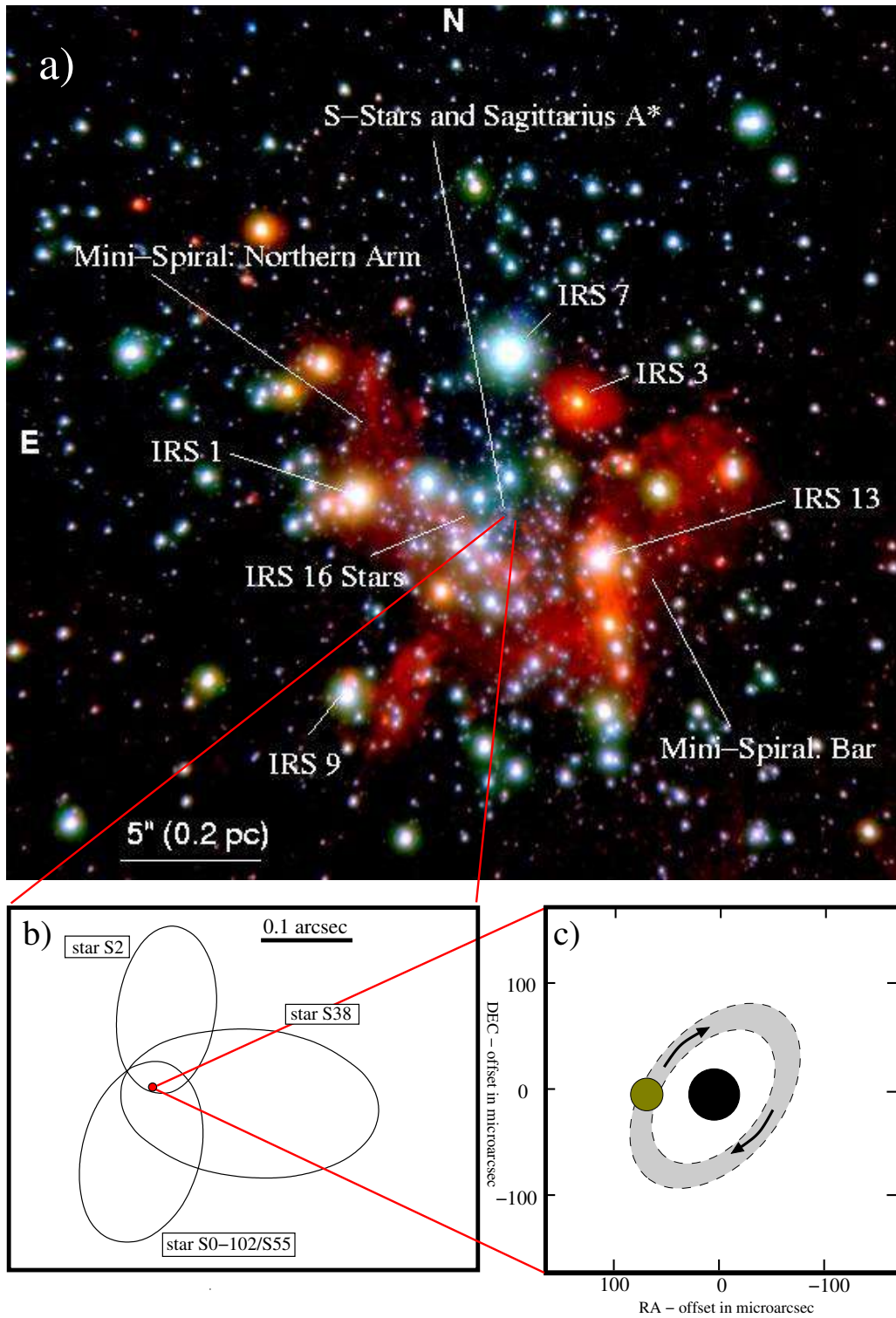


**Figure 7-1:** **a)** The central parsec of the Milky Way seen with the near infrared camera and adaptive optics system NACO at the ESO VLT. Two narrow band images (at  $2.18\mu\text{m}$  and  $2.36\mu\text{m}$ ) were combined with a broad band image at  $3.8\mu\text{m}$  to obtain a pseudo-color image. The red extended emission is due to gas and dust in the mini-spiral or due to circumstellar material of individual stars (see section 3 and references therein). **b)** The orbits of three of the innermost stars orbiting Sgr A\*. Star S2 can be used to determine the relativistic nature of the supermassive black hole environment (see section 4.1; Abuter et al. 2017, 2018; Parsa et al. 2017; Eckart et al. 2018). **c)** Sketch of a possible scenario in the immediate vicinity of Sgr A\* (black circle at the center) with material in orbit around it (grey band with yellowish source component as a hotspot; see section 4.2; Abuter et al. 2017; Meyer et al. 2006a,b; Eckart et al. 2006a,b). (Image from Eckart et al., submitted Conf. Proc.)

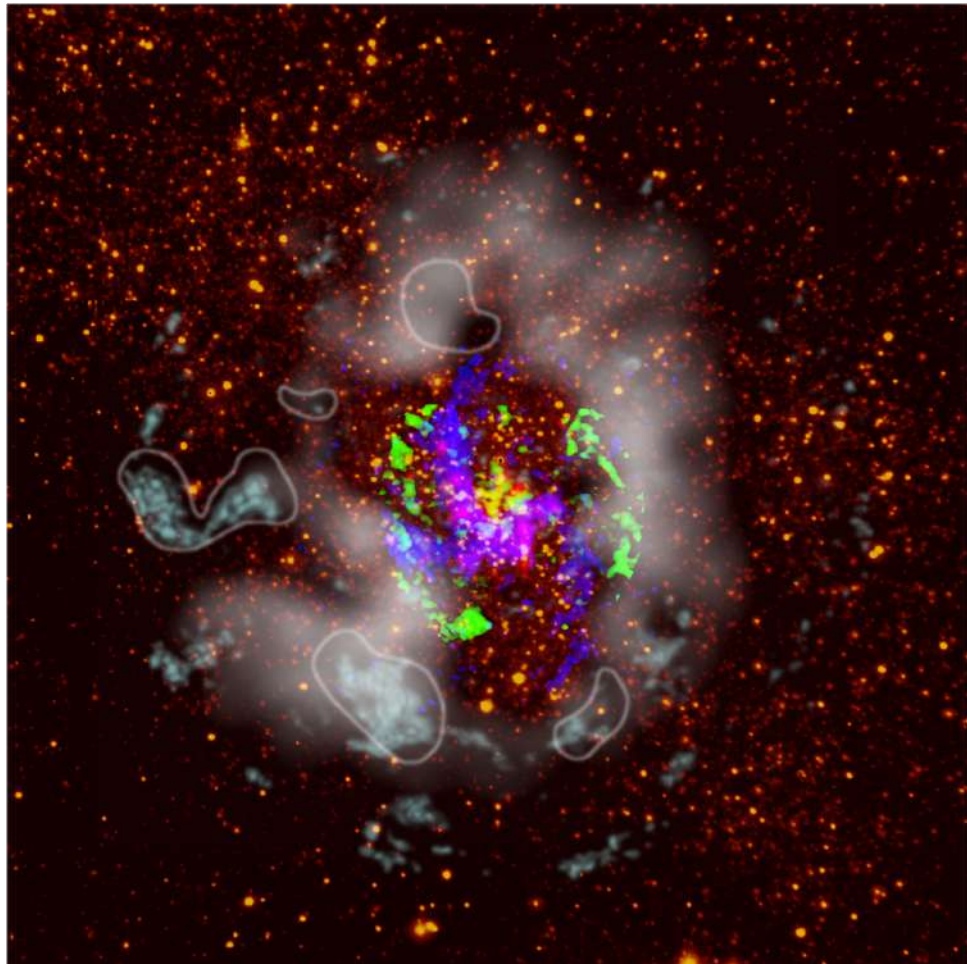


**Figure 7-2:** Sub-millimeter, NIR, and inverted X-ray composite image of the inner 5.6 pc  $\times$  5.6 pc of the Galactic Center. **Yellow:** Stellar background from a combination of ISAAC 1.19 $\mu$ m, 1.71 $\mu$ m, and 2.25 $\mu$ m narrow filters (from Nishiyama & Schödel 2013); **red:** NACO L'-band dust emission. Sub-millimeter ALMA measurements: **blue:** GC mini-spiral is traced by 250 GHz continuum and H39 $\alpha$  ionized emission; **green:** Inner regions of the CNR (in projection) shine in CS(5-4) molecular line; **cyan:** N<sub>2</sub>H<sup>+</sup>(1-0) molecular-gas major structures coincide with foreground dark clouds (Moser et al. 2017). **Extended white shadow:** This shadow shows the footprint of the circumnuclear disk as seen by the depression of the X-ray diffuse emission observed with CHANDRA (Mossoux & Eckart 2018). **Enclosed with white lines:** Prominent dust extinction patches, possibly star-forming regions, visible as dark silhouettes over the bright stellar background are enclosed with white lines. Some emission regions are also identified e.g. the South East Extension (SEE), that towards the west of it (SEW), the V-cloud, the Central Association (CA) and the Triop (see Moser et al. 2017, for more information). (Image from Eckart et al., submitted Conf. Proc.)

**General requirements for METIS:** Galactic center science this is mainly bright science – angular resolution and field of view are essential. In continuum emission one is confusion limited since one looks into the central star cluster. In spectroscopy one may only get into trouble if one uses the highest resolutions possible or faint continuum sources for absorption line studies.

Regarding Adaptive Optics and a possible N-band detector:

- (1) For galactic center SCAO with limiting magnitude of K 12 mag is well suited and sufficient.
- (2) Broad band N band imaging will only be used in a small fraction of the Galactic Center science case and it is of comparatively lower importance (compared to L, M band imaging and spectroscopic studies).

Simulations of the expected images and spectra of the Galactic Center as measured with METIS have started. In Figure 7-3 we show a simulated detector images in N-Band (N2). The image has been derived from a data cube derived from a continuum model of the Galactic Center region simulation extended and stellar components with appropriate continuum scaled template spectra for the extended (GC ISO SWS

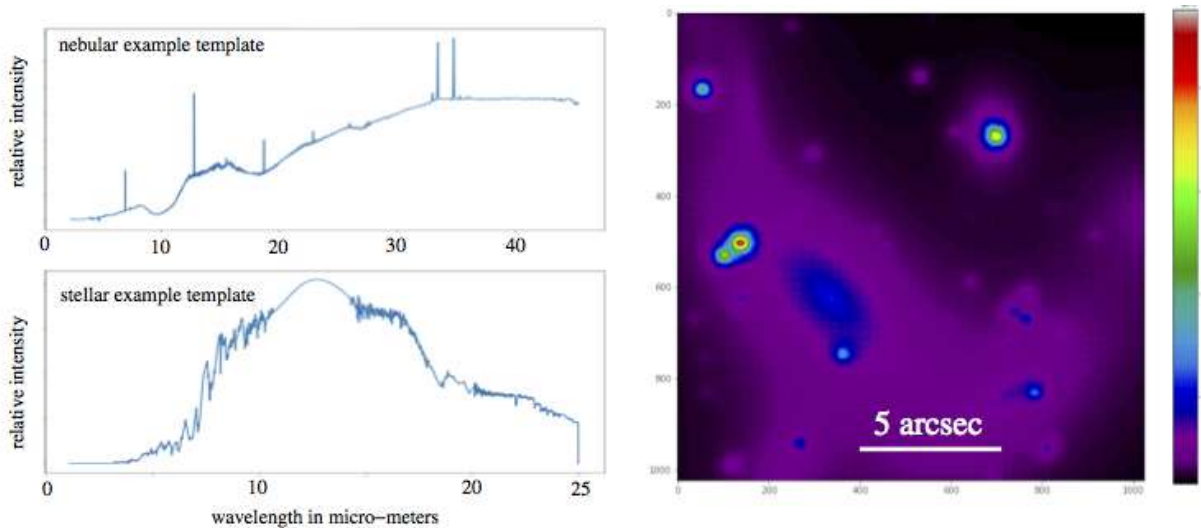


**Figure 7-3:** Example of simulated data for the METIS Galactic Center project. Template input spectra for extended and stellar/ compact components (left) and a simulated N-band continuum image (right).

spectrum) and stellar (as an example here a Pickles M5V spectrum) components including expected detector noise. These simulations will relative intensity relative intensity allow us to extract continuum, color, line, and line to continuum maps with noise. They will allow to address detectability and contrast questions.

### 7.3 A Representative Observing Program

The center of our galaxy (GC) is the closest galactic nucleus that access Control Help can be studied. In addition to a massive black hole, the central half parsec of the Milky Way hosts a surprisingly high number of massive young stars organized in at least one disk-like structure of clockwise rotating stars. The mechanism responsible for the presence of young stars in the strong tidal field of the super-massive black hole (SMBH) at the position of Sgr A\* is not clear. We have been actively publishing on a variety of topics that can ideally be followed up on - or even tackled for the first time using the ELT in the MIR.

#### 7.3.1 YSO Candidates in the central stellar cluster

It is currently unclear how the young stars have been formed in the central stellar cluster. The Galactic center IRS 13E cluster is located 3.2" from Sgr A\*. This cluster harbors sources that are amount the best candidates for young (recently formed) stellar objects in the central cluster (e.g., Mužić et al. 2008); IRS 13E is an extremely dense stellar association containing several Wolf-Rayet and O-type stars, at least four of which show a common velocity. Only half an arcsecond north of IRS 13E there is a complex of extremely red sources so-called IRS 13N. Their nature is still unclear. Based on analysis of their colors, there are two main possibilities: (1) dust-embedded sources older than few Myr or (2) extremely young objects with ages less than 1 Myr. In Mužić et al. (2008) we present the first proper motion measurements of IRS 13N members and four of IRS 13E stars resolved in the L'-band. The L'-band ( $3.8\mu\text{m}$ ) observations were carried out using the NACO adaptive optics system at the ESO VLT. Proper motions were obtained by linear fitting the stellar positions extracted by StarFinder as a function of time, weighted by positional uncertainties. As a result we could show that six of seven resolved northern sources show a common proper motion, thus revealing a new co-moving group of stars in the central half parsec of the Milky Way. The common proper motions of IRS 13E and IRS 13N clusters are significantly ( $>3$ ) different. In Fig. 7-4 we show the IRS13N sources. We also performed a fitting of the positional data for those stars onto Keplerian orbits, assuming Sgr A\* as the center of the orbit. Our results favor the very young stars hypothesis.

Very good candidates for YSOs are the infrared excess sources like the dusty S-cluster object DSO (alias G2). This dusty source had been approaching the black hole Sgr A\* and passed by in 2016. The faint DSO was discovered in 2011 Gillessen et al. (2012) on its way towards the supermassive black hole Sgr A\*. The object is very faint in the NIR K-band, however, well detectable in its Brγ-line emission and considerable brighter continuum emission of the longer wavelength infrared L-band. After its discovery large monitoring programs were started by several groups. We covered the investigation of the source properties between the years 2006 to 2016 using the SINFONI camera at the ESO VLT.

The NIR  $2.2 \mu\text{m}$  continuum emission of the DSO was first found Eckart et al. (2013) making use of the NACO camera at the ESO VLT. A confirmation of its detection could also be achieved using public data of the NIRC system at the Keck telescope (Eckart et al. 2014). Furthermore, the continuum source clearly showed itself in SINFONI data obtained at the VLT. As the source passed by Sgr A\* it showed a very obvious transit from a red- to a blue-shifted Brγ-line emission (Valencia-S. et al. 2015). Given that the source was not disrupted during and after the flyby around Sgr A\*, and given the fact that it stayed very compact in its continuum and line emission (Valencia-S. et al. 2015; Witzel et al. 2014), it became obvious that it is not an extended and core-less cloud as previously claimed (e.g., Gillessen et al. 2012; Pfuhl et al. 2015; Schartmann et al. 2015).

Shahzamanian et al. (2016) could detect and measure the polarization of the DSO as it was descending towards its periapsis close to Sgr A\*. These observations showed that it is very likely a compact dust-enshrouded - probably young - star. The high degree of polarization implies that the scattering material is not distributed highly symmetrically around the source (see e.g., Zajaček et al. 2014, 2016). The data point at a combination of a bow shock and a bipolar wind propagating and surrounding a central star (Shahzamanian et al. 2016; Zajaček et al. 2014, 2016, 2017; Valencia-S. et al. 2015).

Mid-infrared studies of dusty sources in the Galactic Center have been carried out by Peißenker et al. (2022) including the apparent tail of the Galactic Center object G2/DSO (Peißenker et al. 2021b). In Zajaček et al. (2017) show how we can learn of the nature of the Galactic Center NIR-excess sources from broad band NIR/MIR continuum observations. As an example the authors concentrate on the DSO/G2 source.

**The contribution of METIS:** High resolution studies with METIS will allow us to clearly determine the structures of the dust envelopes of these young star candidates. Spectroscopy of PAH and ionic line emission will help us to trace the interaction of the shells with the radiation field from the bright stars in the cluster and Sgr A\*. Goal of these studies will be to consolidate the identification with young stars that are still surrounded by relicts of their dust disks that will certainly suffer from traveling through the dense stellar cluster. Any interaction of the dusty infrared excess sources with the local Galactic Center ISM or a wind from Sgr A\* should be observable at high angular resolution with the ELT. Dusty shells or tails should readily become observable in their dust emission.

### 7.3.2 The Nature of Thin Dust Filaments

Narrow dust filaments in the diffuse ISM of the central stellar cluster allow us to trace its interaction with a wind from the central region through their proper motions (e.g., Mužić et al. 2007). L'-band ( $3.8 \mu\text{m}$ ) images of the Galactic center show a large number of thin filaments in the mini-spiral, located west of the mini-cavity and along the inner edge of the Northern Arm. In Fig. 7-5 we show the location and proper motion of thin dust filaments in the central stellar cluster. One possible mechanism that could produce such structures is the interaction of a central wind with the mini-spiral. Additionally, we identify similar features that appear to be associated with stars. In Mužić et al. (2007) we present the first proper motion measurements of the thin dust filaments observed in the central parsec around Sgr A\* and investigate possible mechanisms that could be responsible for the observed motions. The observations have been carried out using the NACO adaptive optics system at the ESO VLT. The images have been transformed to a common coordinate

system and features of interest were extracted. Then a cross-correlation technique could be performed in order to determine the offsets between the features with respect to their position in the reference epoch.

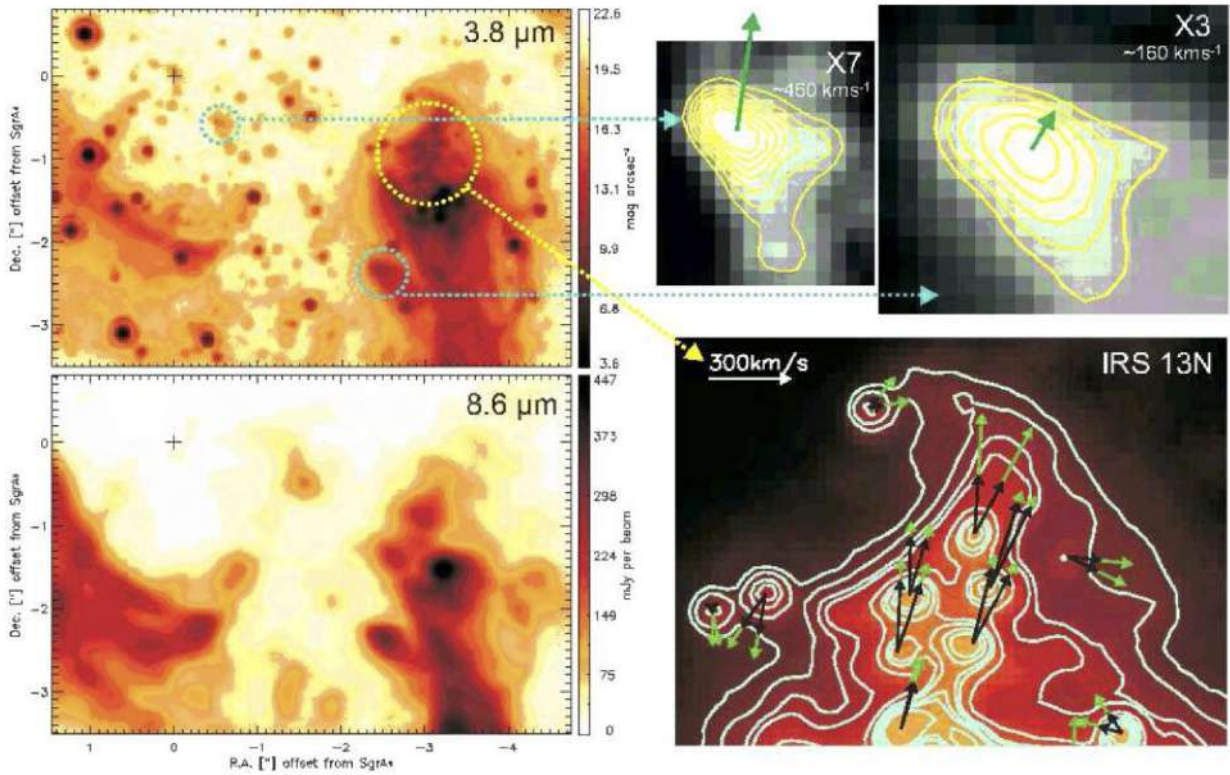


**Figure 7-4:** Left top and bottom: A  $4 \times 6$  arcsec $^2$  section of the central stellar cluster at  $3.8\mu\text{m}$  and  $8.68\mu\text{m}$  wavelength including the position of Sgr A\* and IRS13N just north of the cluster of bright stars of IRS 13 proper. Top right: The sources IRS13N, X3 and X7 in the Galactic Center stellar cluster (Mužić et al. 2007). Bottom right: Proper motions of the dust embedded IRS13N sources (Mužić et al. 2008). The small cluster represents a co-moving group of stars showing that this particular group of stars is not only young with respect of their spectroscopic properties, but that it is also dynamically a young stellar association.

As results we derive the proper motions of a number of filaments and 2 cometary shaped dusty sources close (in projection) to Sgr A\*. We show that the shape and the motion of the filaments does not agree with a purely Keplerian motion of the gas in the potential of the super-massive black hole at the position of Sgr A\*. Therefore, additional mechanisms must be responsible for their formation and motion. We argue that the properties of the filaments are probably related to an outflow from the disk of young mass-losing stars around Sgr A\*. In part, the outflow may originate from the black hole itself. We also present some evidence and theoretical considerations that the outflow may be collimated.

In Fig. 7-4 we also show the cometary shaped bow-shock sources X3 and X7. These sources show bow-shock structures pointing towards Sgr A\* and have proper motions of a few 100 km/s almost perpendicular to the projected connection line towards Sgr A\*. This suggests that these sources interact with a very fast wind (with a velocity of probably larger than  $\sim 1000$  km/s) probably originating in Sgr A\*. The stars are also located within the mini-cavity. In summary this indicates that the sources X3 and X7 are possibly the best probes of the accretion process and an associated wind from Sgr A\*.

Near- and Mid-infrared observations in the inner tenth of a parsec of the Galactic Center and a detection of proper motion of a filament very close to Sgr A\* (Peißker et al. 2020b). Bhat et al. (2022) shows the possibility of measuring proper motions of dust filaments from MIR observations. She can also distinguish between Sources that are in the mini-spiral arms and stellar sources in the cluster.

**The contribution of METIS:** Only a ELT class telescope working in the MIR and long-NIR wavelength range will allow us to study the proper motions of a large number of dust filaments like the ones reported by Mužić et al. (2007). Such a study will then give a complete picture of the wind and outflow activities in

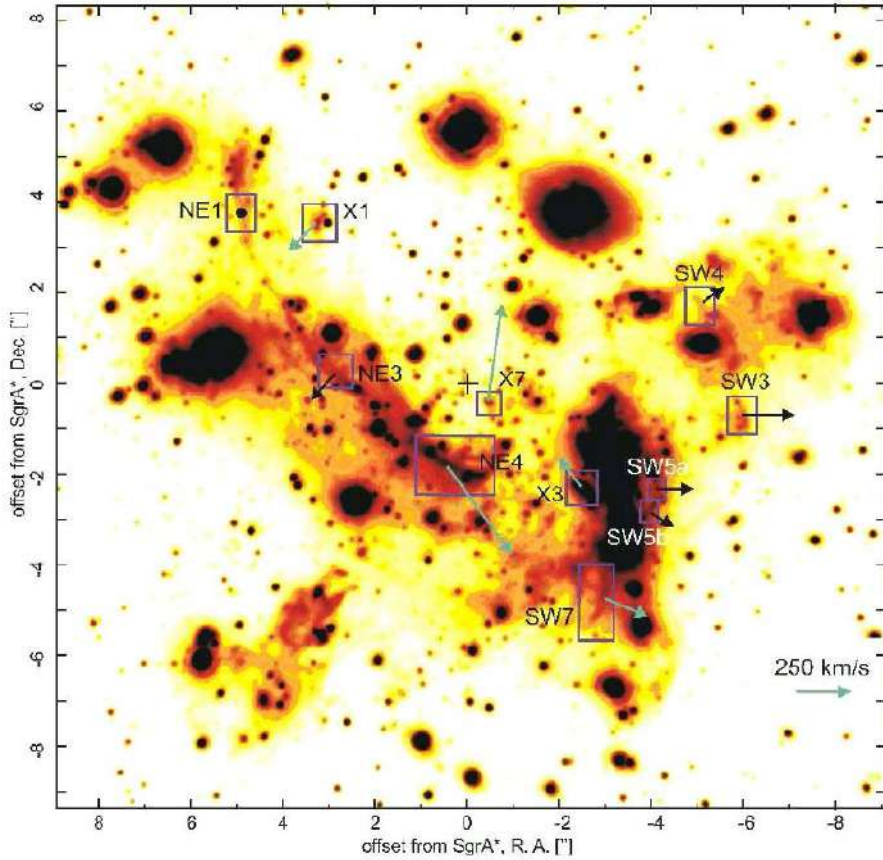


**Figure 7-5:** L'-band image of the Galactic Center. Boxes mark thin filaments with measurable proper motions. Note that boxes in this image are different from those used for measurements. The arrows show proper motions of the thin filaments obtained in our study: light blue arrows stand for the features with measurable proper motion in both directions, while black arrows show only the proper motion component perpendicular to the feature (see, Muzic et al. 2007). The insignificant motion of the Northern Arm filament NE1 is marked with a circle rather than an arrow. The cross marks the position of Sgr A\*.

the central stellar cluster including Sgr A\*.

### 7.3.3 Low Luminosity Bow-Shock Sources in the Central Stellar Cluster

The central stellar cluster contains several bow-shock sources or embedded stars that interact with their immediate ISM (mostly associated with the mini-spiral) (e.g. Perger et al. 2008). Mid-infrared observations of the Galactic Center show among the extended mini-spiral a number of compact sources. Their nature is of interest because they represent an interaction of luminous stars with the mini-spiral material or mass losing sources that are enshrouded in dust and gas shells. Characterizing their nature is necessary to obtain a complete picture of the different stellar populations and the star formation history of the central stellar cluster in general. Prominent compact MIR sources in the Galactic Center are either clearly offset from the mini-spiral (e.g., the M2 super-giant IRS 7 and the bright dust enshrouded IRS 3) or have been identified earlier with bright bow shock sources (e.g., IRS 21, 1W, 10W and IRS 5). There are, however, four less prominent compact sources east of IRS 5, the natures of which were unclear until now. In Perger et al. (2008) we present near-infrared K-band long slit spectroscopy of the four sources east of IRS 5 obtained with the ISAAC spectrograph at the ESO VLT in July 2005. We interpret the data in combination with high angular resolution NIR and MIR images obtained with ISAAC and NACO at the ESO VLT. The K'-band images and proper motions show that the sources are multiple. For all but one source we find dominant contributions from late type stars with best overall fits to template stars with temperatures below 5000 K.

We conclude that the brightest sources contained in IRS 5NE, 5E and 5S may be asymptotic giant branch stars and a part of the MIR excess may be due to dust shells produced by the individual sources. However, in all cases an interaction with the mini-spiral cannot be excluded and their broad band infrared SEDs indicate that they could be lower luminosity counterparts of the identified bow shock sources. In fact, IRS 5SE is associated with a faint bow shock and its spectrum shows contributions from a hotter early type star which supports such a classification.

**The contribution of METIS:** High angular resolution studies that are sensitive to both point like stars and extended emission will allow us to identify and study dust embedded candidates for young stars. A detailed compilation of stand-off distances and proper motion velocities will help to determine the stellar winds that are involved and allow us to narrow down the stellar types even in dust enshrouded systems.

### 7.3.4 Absorption Line Studies

The Galactic Center sources allow for detailed absorption line studies of the intervening material both along the line of sight towards the Galactic Center and very close to/at the Galactic Center (Geballe 1986; Moneti et al. 2001). In our previous works (Moultaka et al. 2004, 2005, 2015), we showed that local absorption occurs probably in the direct environment of the GC infrared sources. As a matter of fact, the spectra of luminous infrared sources in the L-band (from 2.7 to  $4.2\mu\text{m}$ ) revealed absorption features due to water ices and hydrocarbons that we claimed to be present in the local medium of the central parsec. These absorption effects were attributed earlier by other authors to be due to material in the foreground molecular clouds (e.g., Chiar et al. 2000, 2002).

Moultaka et al. (2021) presented the results of CRIRES observations of 13 infrared sources located in the central parsec of the Galaxy. The data provide direct evidence for a complex structure of the interstellar medium along the line of sight and in the close environment of the central sources. In particular we find four foreground cold clouds at radial velocities  $v_{LSR}$  of the order of -145, -85, -60 and  $-40 \pm 15$  km/s that show absorption in the lower transition lines from R(0) to P(2) and in all the observed spectra. We also find in all sources an absorption in velocity range of 50-60 km/s, possibly associated with the 50 km/s cloud in the Galactic Center region. Hence, as the 50km/s cloud is believed to lie behind the GC cluster, parts of it m lie in the line of sight towards it - indicating the the dynamical structure may be very complex. With METIS at the ELT the absorption studies can be extended over a much larger field as now also the SNR for fainter sources will be sufficient to study their absorption line spectrum.

### 7.3.5 The Super-Massive Black Hole

The infrared source associated with the compact radio counterpart of the super massive black hole (SMBH) at the position of Sgr A\* is highly variable in its NIR emission. The identification and investigation of the variability of Sgr A\* will be a prime goal of the Galactic Center ELT observations with METIS (e.g., Eckart et al. 2008). Sgr A\* at the center of the Milky Way is a black hole accreting at extremely sub-Eddington rates (see Fig. 7-6). Measurements of its emission in the infrared and X-ray domains are difficult due to its faintness and high variability.

The optically thin emission in the infrared will allow us to monitor the accretion process in detail and to determine the physical conditions near the black hole and its putative accretion disk or stream (Meyer et al. 2008a). We observed the Galactic center  $8.6\mu\text{m}$  in order to detect a mid-infrared (MIR) counterpart to Sgr A\*, parallel to NIR observations. In Fig. 7-7 we show a Lucy-Richardson de-convolved  $8.6\mu\text{m}$  VLT VISIR image. The goal was to set constraints on possible emission mechanisms. Imaging data were acquired with the adaptive-optics assisted NIR instrument NACO and the MIR instrument VISIR at the ESO VLT. As a result we obtained MIR imaging data of an unprecedented quality in terms of spatial resolution and sensitivity. An extended ridge of emission is found to be present in the immediate vicinity of Sgr A\* thereby rendering any detection of a point source difficult.

No counterpart of Sgr A\* has been detected yet at  $8.6\mu\text{m}$ . At this wavelength, Sgr A\* is located on a dust

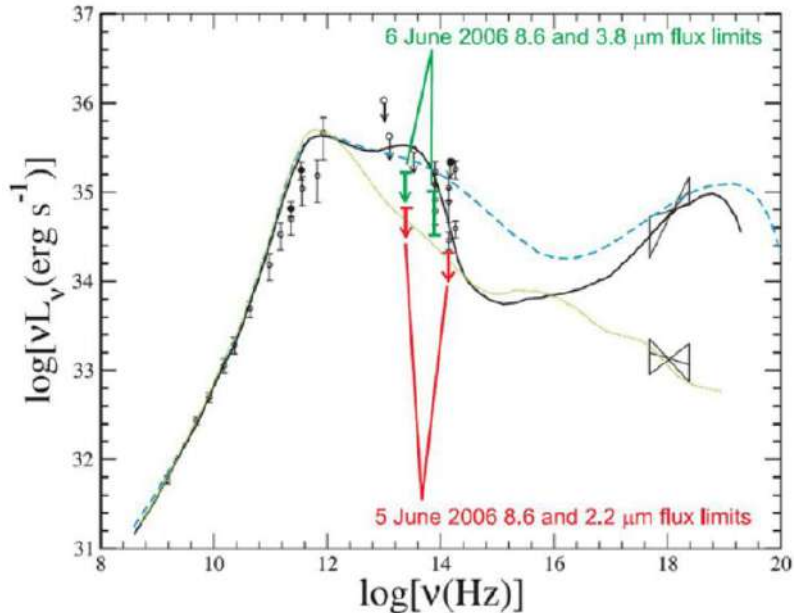


**Figure 7-6:** Emission models for Sgr A\* (Yuan et al. 2003, 2004). The upper limit on the flux of Sgr A\* at  $8.6\mu\text{m}$  determined by Schödel et al. (2007) is indicated together with the simultaneously measured (NACO/VLT) flux at  $3.8\mu\text{m}$  on June 6 and the upper limit on the  $2.2\mu\text{m}$  emission on June 5 superposed onto RIAF models of the quiescent (dotted line) and flaring (dashed and solid lines) emission from Sgr A\*.

ridge, which complicates the search for a potential point source. Schödel et al. (2011) derive an observed  $3\sigma$  upper limit of about 10 mJy for the emission of Sgr A\* at  $8.6\mu\text{m}$ . The de-reddened  $3\sigma$  upper limit, including the uncertainty of the extinction correction, is  $\sim 84$  mJy. Haubois et al. (2012) detect no source in the MIR, but derive a low upper limit for a flare at  $8.6\mu\text{m}$  (22.4 mJy with  $A_{8.6\mu\text{m}} = 1.6 \pm 0.5$ ). Schödel et al. (2011) conclude that, based on the available data, Sgr A\* cannot be detected in the MIR, not even during flares, with currently available instruments. Haubois et al. (2012) explain this behavior by a loss of electrons to the system and/or by a decrease in the magnetic field, as might conceivably occur in fast outflows and/or magnetic reconnection. Yusef-Zadeh et al. (2010) argues that an anticorrelation between the infrared and the sub-millimeter is due to occultation effects of the Sgr A\* source by outbound jet/wind components. Both Haubois et al. (2012); Schödel et al. (2011) spent together a total of  $< 5$  hours of useful integration time on-source in one filter around  $8\mu\text{m}$  wavelength (this is observing time - including inefficiencies due to the observing modes). This time breaks up into  $\leq 4$  integration blocks of typically flare lengths over which the upper limits were derived. Hence, below we can use the  $3\sigma$  limit of 22.4 mJy to derive the detectability of flares over longer observing time periods.

Using the spectral index of  $\alpha = -0.7$  and the upper  $8\mu\text{m}$  flux density limit we obtain a corresponding de-reddened K-band flux limit of  $\sim 8.5$  mJy. We can use the Sgr A\* flare flux histogram in the K-band by (Witzel et al. 2012, Fig. 1b; see Fig. 7-8), published after Haubois et al. (2012); Schödel et al. (2011). Within a total integration time of 0.4% of the 7 years (i.e., 3490 hours) time interval covered by (see also Witzel et al. 2018, 2012) bright flare with a  $\sim 31$  mJy flux was detected. This is  $\sim 100$  times less frequent than the 8.5 mJy K-band MIR flare flux limit. On the other hand, typical frequently occurring K-band flares happen with a rate of 6-8 per day (0.25 to 0.33 per hour). This is  $\sim 8$ -10 times more frequent than our limit, resulting in an estimated 30 hours on source VLT integration time. For METIS this detection could be done in a fifth of the time, i.e. a few hours. Failing to detect Sgr A\* would then speak in favour of alternative scenarios mentioned above.

*Tests for Relativity:* A first indication of the possibility of detection the periapse shift of S2 was given by (Parsa et al. 2017). A detection of the Schwarzschild precession in the orbit of the star S2 near the Galactic centre massive black hole Sgr A\* was achieved with GRAVITY and reported in Gravity Collaboration et al.

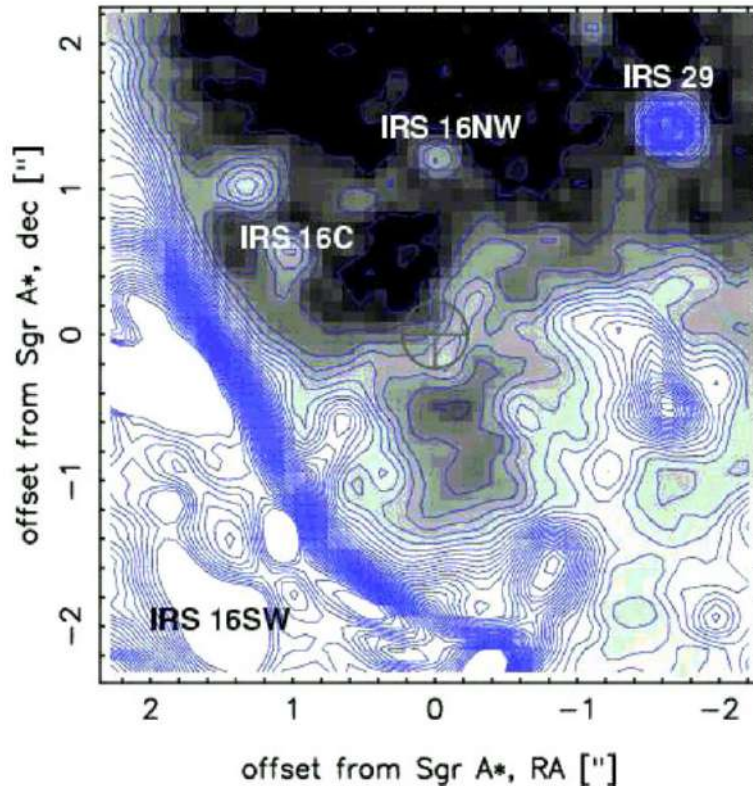


**Figure 7-7:** The Lucy-Richardson de-convolved and beam-restored image taken at a wavelength of  $8.6\mu\text{m}$  using the VLT VISIR system. We derive fluxes of  $22\pm 5$ ,  $21\pm 5$ , and  $180\pm 20$  mJy for the point sources IRS 16C, IRS 16NW, and IRS29 (without extinction correction). Here the angular resolution is 0.25 arcsec. With METIS we will achieve about 75 mas at the same wavelength (which is an ideal match the the 60 mas K-band resolution obtainable with the VLT).

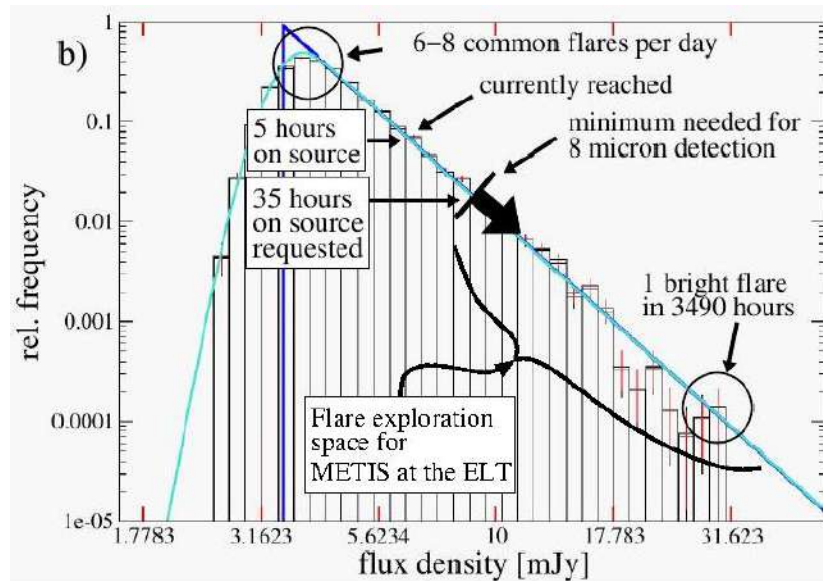


**Figure 7-8:** Our K-band flare flux histogram by Witzel et al. (2012) covering 7 years of observations with an efficiency of 0.4%. The variable NIR emission can be described well by a single stationary power law process. The peak to the left is the detection limit, the noisy edge to the right is the bright under-sampled end of the histogram.

(2020). Detection of the gravitational redshift in the orbit of the star S2 near the Galactic centre massive black hole (GRAVITY Collaboration et al. 2018).

*High Velocity Stars:* Recently, Peißker et al. (2022) published the observation of S4716, a high velocity star with only a 4 year orbit around Sgr A\*. This is by now the shortest orbital timescale known. Other short period stars are S62 and S4711 with orbital periods of 9.9 yr ( $K \approx 16$  mag; see Peißker et al. (2020a, 2021a)) and 7.6 yr ( $K \approx 18$  mag; see Peißker et al. (2020c)), respectively.

**The contribution of METIS:** In the MIR and long-NIR high angular resolution is required to distinguish between the feeble emission from Sgr A\* and the more extended dust emission of the mini-spiral. The spectral index of Sgr A\* in the NIR/MIR is not well known. Here, synchrotron losses may dominate the spectral shape. Also a variability study in the MIR can only be done efficiently with METIS (sensitivity and resolution). Especially in the MIR region the situation will be complicated, since emission and scattering of dust will contribute to the contamination of the signal from Sgr A\*. To get photometric values of Sgr A\*, dithered imaging exposures of about 60 sec single integration time at L, M and N have to be taken over several nights, to monitor the flaring Sgr A\*. Stars within the same FoV can be used as photometric standards. If the Sgr A\* point source turns out to be bright enough, low resolution spectroscopy at L,M and N could provide helpful information to understand the flare mechanism. METIS will improve the situation to observe high velocity stars and to carry out tests for relativity. METIS will help to find more short period stars like S62, and the S4711 to S4716 sources.

### 7.3.6 Comparison with other facilities

In the context of METIS it is important to note that the detectability of Sgr A\* is not limited by the atmospheric background but by the diffuse emission of the surrounding gas and dust. Thus, studies from space are severely limited by the low spatial resolution and the high surface brightness. METIS on the ELT will be able to detect Sgr A\* and measure the broad band fluxes coming from the central  $\leq 17$  Schwarzschild radii at the most critical wavelengths between L and N band Fig. 7-5.

Even though VLTI can provide even higher spatial resolution due to a baseline of about 100m, the sensitivity is by far not sufficient to observe Sgr A\* at MIR wavelengths (MIDI): Its limiting flux at  $10\mu\text{m}$  is around 1 Jy.

Currently, the VLTI project Gravity is working and produced first spectacular results on the Galactic Center (Abuter et al. 2017, 2018). GRAVITY is an adaptive optics assisted, near-infrared VLTI instrument for precision narrow-angle astrometry and interferometric phase referenced imaging of faint objects. With a limiting magnitude of up to  $K=20$  mag, this instrument can provide complementary NIR data on Sgr A\*, however, limited to the NIR domain, Gravity is no competitor to METIS.

MIRI on JWST will allow for sensitive spectroscopic observations of the Galactic Center. However, the angular resolution of the telescope will be inferior compared to the METIS/ELT combination. Detailed spatial information over a decent field of view in the MIR can only be achieved with METIS.

## 8 THE PHYSICS OF GALAXIES

### 8.1 Scientific background and context

Understanding how galaxies formed and evolved remains one of the most challenging issues in modern cosmology. Over the past few years, tremendous progress was achieved in constraining at kilo-parsec scales the nature of the physical processes that drove the build-up of galaxies across cosmic times (e.g., Madau & Dickinson 2014, and references therein). Scaling relations linking fundamental galaxy properties (e.g., stellar mass, star formation rate, gas surface density, central black hole mass, ...) seem to have emerged as soon as the first Gyrs of cosmic evolution (Speagle et al. 2014). They suggest that star formation and black hole growth in the distant Universe were mostly governed by internal processes (e.g., gravitational disk instabilities, secular gas consumption) occurring in isolated galaxies and regulated by the feedback action from supernovae and Active Galactic Nuclei (Lilly et al. 2013). In addition, there is also a global consensus on the importance of environmental effects such as galaxy encounters and clustering, which played a critical role in quenching the star-forming activity of blue galaxies and transforming their morphological structure into passive red sources (Hopkins et al. 2010).

On the intermediate sub-galactic scales though, the local conditions and processes that compress the gas and trigger the formation of new stars are still very uncertain. This shortcoming prevents an accurate description of the recipes required to properly reproduce the physical properties of galaxies in current state-of-the-art hydrodynamic simulations of structure formation (e.g., Schaye et al. 2015a). With the ELT we will finally get a chance to unveil the nature of the physical mechanisms at work in highly star-forming environments, by studying in detail the formation of dense and massive star clusters such as those found in nearby luminous infrared galaxies and circum-nuclear starbursts. In addition, we will be able to probe the presence and the properties of nuclear star formation in the vicinity of active galactic nuclei on scales of the order of  $\sim 10\text{pc}$  or below, which has never been achieved so far. This will allow us to address with unprecedented details how the central star formation connects to the black hole accretion rate, and how the interaction between the two phenomena may have been driving the emergence of the correlation linking the mass of galaxy bulges with the mass of their central super-massive black hole.

### 8.2 Massive star cluster formation

The massive star clusters hosted in luminous starbursting galaxies are likely different from the massive young clusters known within the Local Group: R136 (LMC), NGC 604 (M33), NGC346 (SMC), NGC3603 (MW), and even most of the “super star clusters” in the Antennae galaxies, all of which are located in low density environments like galactic spiral arms or dwarf galaxies. The young clusters with masses well in excess of  $10^{6-7} \text{ M}_\odot$  in the dense environments of luminous starburst galaxies have typical ages up to 10 Myr, luminosities of  $10^{8-10} \text{ L}_\odot$  and visual extinctions up to several tens of  $A_V$ . Due to their large distances, compact sizes, and their dense and dusty environment, these stars are very difficult to observe with existing instruments – a challenge that can be best, or maybe even solely – addressed with the combination of long wavelengths ( $>3\mu\text{m}$ ) and high angular resolution as provided by METIS on the ELT.

For illustration, Fig.8-1 shows the circum-nuclear starburst ring in NGC 7552, a face-on galaxy at approximately 20 Mpc distance, as observed with different instruments and telescopes (Spitzer, VLT) at different wavelengths (near-/mid-infrared). The star formation rate in the nine most mid-IR luminous clusters alone equals about four times the total amount of star formation in the entire Milky Way! With [Ne II] line fluxes of a few times  $10^{-21} \text{ W cm}^{-2}$ , even much fainter clusters will be detected with METIS in a few minutes only. Based on Fig.8-1, two fundamentally important facts need to be stressed, where METIS will make the difference:

- High angular resolution is crucial! Despite diffraction limited performance, the Spitzer Space Telescope cannot resolve the individual clusters. VISIR at  $10\mu\text{m}$  reaches the diffraction limit of the VLT,

corresponding already to about 30 parsecs at NGC 7552. METIS, at the wavelength of the Br-alpha ( $4.05 \mu\text{m}$ ) line will provide an unsurpassed resolution of 3 parsec with minimal susceptibility to dust reddening. At this resolution, we can finally resolve the substructures of and interaction between embedded massive clusters in a representative sample of nearby starburst galaxies.

- Although less sensitive to dust extinction, the K-band ( $\sim 2\mu\text{m}$ ) continuum does not trace the youngest, most massive clusters (M1, M2 in Fig.8-1). Instead, the K-band continuum is dominated by the light from giant and super-giant stars. Even the position of the center of NGC 7552 appears to be offset with respect to the radio peak (and center of the mid-IR ring). In short, wavelengths longer than K-band are essential!

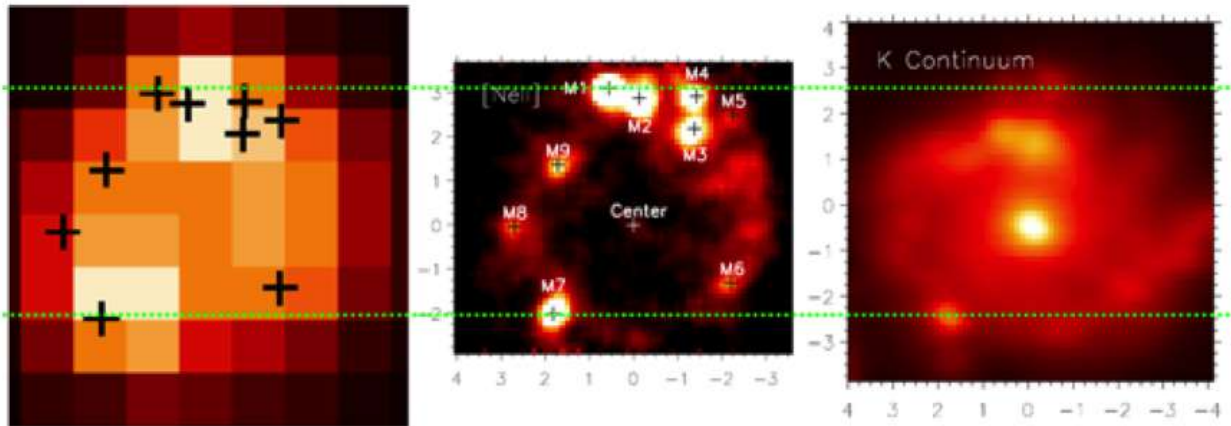


**Figure 8-1:** Infrared imaging of the circum-nuclear starburst ring in NGC 7552. *Left:* Spitzer-IRAC at  $8\mu\text{m}$ . *Center:* VLT-VISIR [ $\text{Ne II}$ ] at  $12.8\mu\text{m}$ . *Right:* VLT-SINFONI K-band ( $\sim 2\mu\text{m}$ ) (Brandl et al. 2012). The black crosses indicate the location of the most mid-IR luminous clusters; the dotted horizontal lines have been added to guide the eye.

Furthermore, METIS on the ELT will provide unique key diagnostics ( $\text{Br}\alpha$ , [S IV], [Ne II], PAHs, silicates, CO), which enable measurements that are very relevant to a better understanding of the “micro-physics” of galaxy evolution. Such key investigations are:

- Study the local temperatures and densities of the ionised gas in the most luminous star forming regions from where the next generation of massive stars will (or will not) form.
- Derive the relative ages of the massive clusters to pin down the local star formation histories with respect to triggering and quenching (positive and negative feedback). This may be particularly relevant in regions where the gas supply is localized, e.g., by transport along the nuclear bars.
- Determine the dynamical properties of the clusters from their line shifts, which will lead to a better (virial) mass estimate as well as general insights into the formation scenario. Although significantly over-resolved,  $\text{Br}\alpha$  observations with the METIS IFU will be ideal for these studies.
- Measure the local physical conditions at the “launching pad” of galactic-scale jets and outflows (“super-winds”) to understand the boundary conditions for these dramatic events, which enriched the intergalactic medium with metals in the early Universe.

### Target selection

The constraints imposed by the Adaptive Optics (AO) system that will equip METIS requires the presence of a relatively bright point source ( $K < \sim 12$  mag) in the close vicinity of the science target ( $r \sim 10''$ ). In

the case of extragalactic objects, this can not be achieved with a foreground star, because the probability to find such a suitable bright star almost aligned with the target is extremely low. This implies that the METIS observations of starburst sources like NGC 7552 will require in principle the availability of a Laser guide star. In the absence of Laser-assisted AO, a possibility is therefore to select star clusters in relatively nearby luminous galaxies also harboring an active galactic nucleus (AGN), and to use this AGN as a reference point source for the AO guiding.

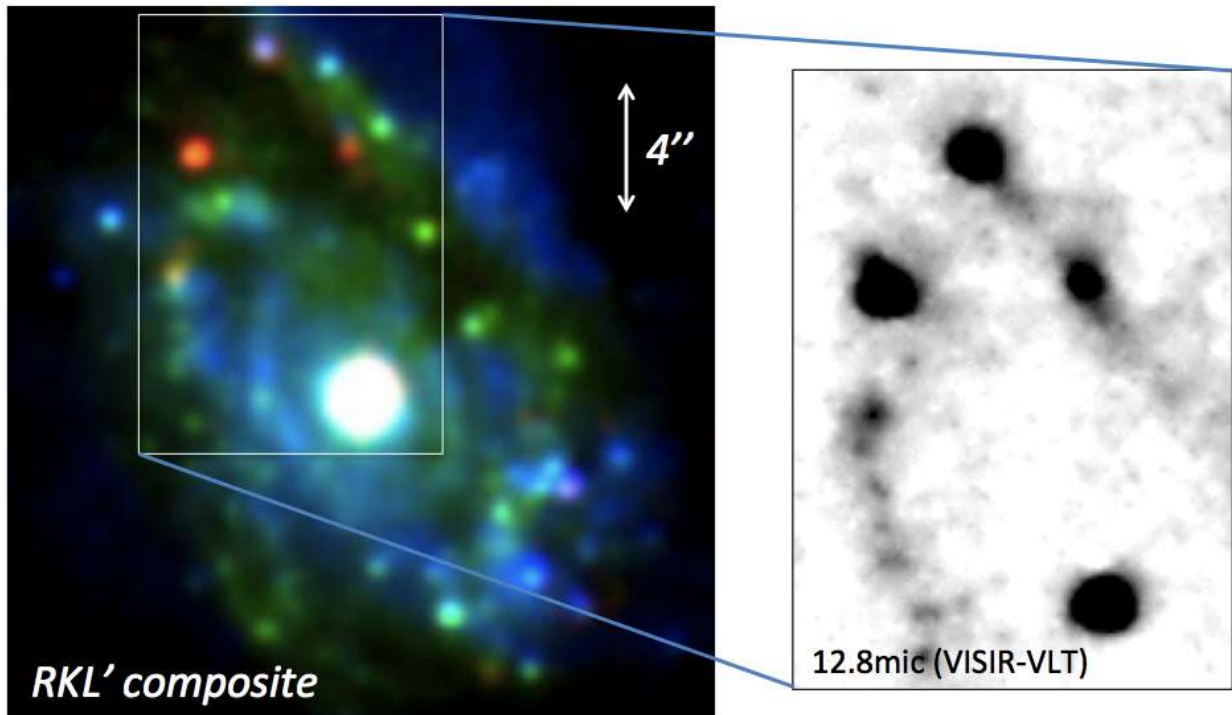


**Figure 8-2:** Composite image of NGC 1365 obtained from  $R$ -,  $K$ - and  $L'$ -band imaging, revealing the bright active galactic nucleus in the core of the galaxy, as well as a large number of massive star clusters throughout the disk. The reddest of these clusters are embedded in dusty regions, requiring observations in the mid-Infrared such as the close-up obtained with VISIR/VLT at  $12.8\mu\text{m}$  (Galliano et al. 2008).

Fig. 8-2 shows the example of NGC 1365, which exhibits a luminous AGN ( $K \sim 10$  mag) as well as a wealth of very massive young star clusters in the disk (Galliano et al. 2008). Similar configurations are also found in many other cases like NGC 253, NGC 7469, NGC 1808, showing that METIS will be able to constrain the physics of star formation in massive clusters over a wide range of environments, age, and galaxy physical conditions.

### 8.3 Nuclear star formation

Over the past few years, observations of local Seyfert's galaxies at high spatial resolution revealed that star formation can be found as close as  $\sim 10$  pc from their central super-massive black hole (see Fig. 8-3). However, we still lack a detailed understanding of the interplay between the AGN activity and the trigger of star formation in the nuclear and circum-nuclear regions of galaxies. Thanks to the exquisite capabilities of METIS on the ELT, we will be able to probe on-going star-forming activity at even higher spatial resolution and shorter distances from galaxy nuclei. Using the spectroscopic mode of METIS in the N-band, we will use the PAH feature at  $11.3\mu\text{m}$  as a key diagnostic for probing star formation and disentangling its signature from that of the nuclear emission (e.g., Mori et al. 2014; Alonso-Herrero et al. 2014; Ramos Almeida et al. 2014). The angular resolution of METIS will allow us to search for recent star formation not only around type 2 AGNs, but presumably also around some type 1 Seyferts. We will explore how this activity of star

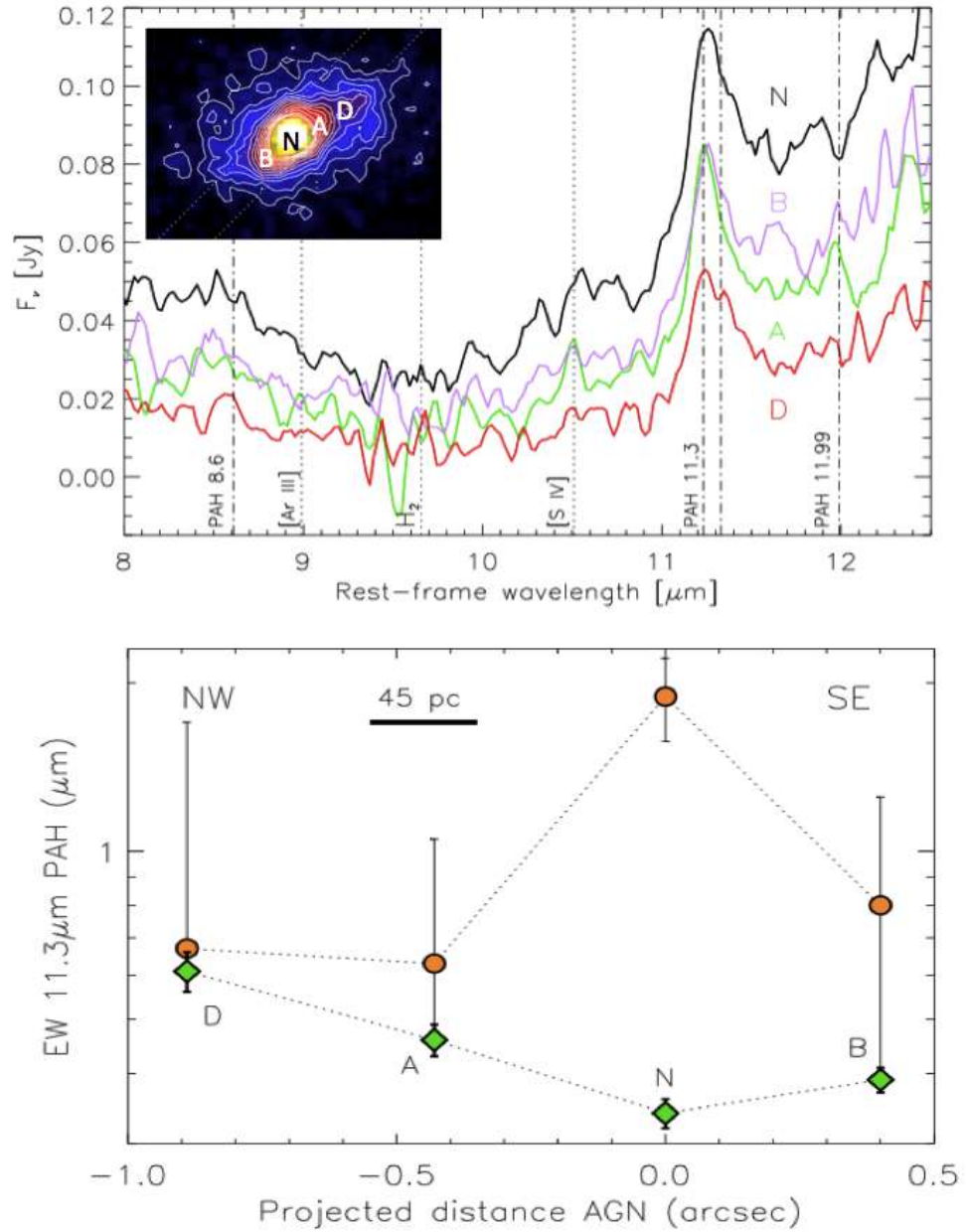


**Figure 8-3:** *Top:* Mid-Infrared spectra obtained in the core region of Mrk 1066, showing the presence of star formation in the vicinity of the nucleus through the detection of the PAH  $11.3\mu\text{m}$ . The spectra were extracted at the 4 locations shown in the inset (A, N, B and D). The distance between B and N is typically  $\sim 100$  pc. *Bottom:* the PAH equivalent width derived from the 4 spectra as a function of the projected distance from the nucleus, before and after subtracting the contribution from the AGN (green and orange symbols, respectively). Adapted from Alonso-Herrero et al. (2014) and Ramos Almeida et al. (2014).

formation correlates with the black hole accretion rate (e.g., Esquej et al. 2014a). Finally, we will investigate if the dust collocated with the gas that fuels the nuclear star formation can play a role in the obscuration of type 2 AGNs (Hicks et al. 2009), and if this dust is partially related to the clumpy torus emission often invoked in the unified scheme of active nuclei.

## 9 ACTIVE GALACTIC NUCLEI

### 9.1 Scientific background and context

In recent years it has become clear that super-massive black holes (SMBHs) form an integral part of galaxy nuclei and that they are closely linked to the large-scale properties of galaxies. The fact that the black hole mass and total galaxy mass are closely related is truly remarkable, given that there is a factor of  $10^8$  between the AU-size Schwarzschild radius of the black hole and the kpc-size dimension of the galaxy. This is generally interpreted as evidence that the formation and growth of the SMBH is directly related to the formation process of the stellar population, e.g. in a violent burst of star formation. While an intimate connection between star formation and SMBH growth nowadays is included in all major cosmological simulations (e.g. Schaye et al. 2015b; Crain et al. 2015), the actual physical processes giving rise to the black hole – spheroid mass correlation are not understood at all. Popular scenarios include feedback from AGNs dispersing the gas that feeds both starburst and AGN, and Eddington-limited starburst activity with radiation pressure from the starburst dispersing the gas (e.g. Murray et al. 2005). To understand this conspiracy, reliable measurements of SMBH masses in a range of galactic nuclei, including inactive galaxies, AGNs and starburst galaxies, are indispensable.

Similarly important, and directly related, is the issue of the immediate vicinity of the SMBH. In the standard model of AGNs, the black hole and its hot accretion disk are surrounded by an obscuring dusty torus, and the dichotomy between type 1 and type 2 AGNs results from different viewing angles. Data on the size and geometry of this torus are extremely scarce; only for the most nearby Seyfert galaxies, the innermost regions have been probed through interferometric VLTI observations (GRAVITY Collaboration et al. 2019; Gámez Rosas et al. 2022; Isbell et al. 2022). Rather than confirming this unification model, these observations have mainly revealed the diversity of the nuclear environments (Burtscher et al. 2013; Leftley et al. 2019).

Finally, on slightly larger scales, the mechanisms by which gas can lose its angular momentum and fall into the nuclear region, fuelling both nuclear starbursts and AGNs, are poorly understood. High-resolution imaging and spectroscopic studies have mapped the morphology and dynamics of some nearby galaxies (e.g. Prieto et al. 2014; Hicks et al. 2013; Rosario et al. 2019; García-Burillo et al. 2021) and studied possible relations between nuclear star formation and nuclear activity (e.g. Jensen et al. 2017; Bing et al. 2019; Burtscher et al. 2021), but the physical mechanism for fuelling AGNs remains far from being understood. There is no consensus on whether AGN fuelling must be synchronous with nuclear star formation (Esquej et al. 2014b), is only sometimes so (Cid Fernandes et al. 2004), follows it during a post-starburst phase (Davies et al. 2007; Vollmer et al. 2008), or is not associated with any recent star formation in the vicinity of the AGN (Sarzi et al. 2007).

High-resolution imaging and integral-field spectroscopic studies of nearby active galaxies are necessary to trace the structure and dynamics of the gas and to resolve star-formation activity in the close vicinity of the AGN. The current instrumentation has allowed us to zoom into the central region of AGNs (see Fig. 9-1), but it has now reached its limits to investigate the nuclear and circum-nuclear regions of galaxies. Fundamental problems are twofold:

- **Obscuration** The nuclear regions of AGNs are often so strongly obscured that even near-infrared observations are not sufficient to peer into the nucleus and witness the fuelling of an AGN and/or starburst. The nearby AGN NGC 4945 is a remarkable example: variable hard X-ray emission unambiguously reveals the presence of an AGN, yet the obscuration is so large ( $A_V > 50$ ) that no evidence for an AGN is found at optical or even near-infrared wavelengths.
- **Spatial resolution** Very high spatial resolution is required to resolve the region of dynamical influence of the black hole. In particular, in order to determine SMBH masses using dynamics (a well-developed technique at shorter wavelengths, using both gas and stellar dynamics) it is necessary to resolve the radius of influence of the SMBH. Using the empirical relation between SMBH mass

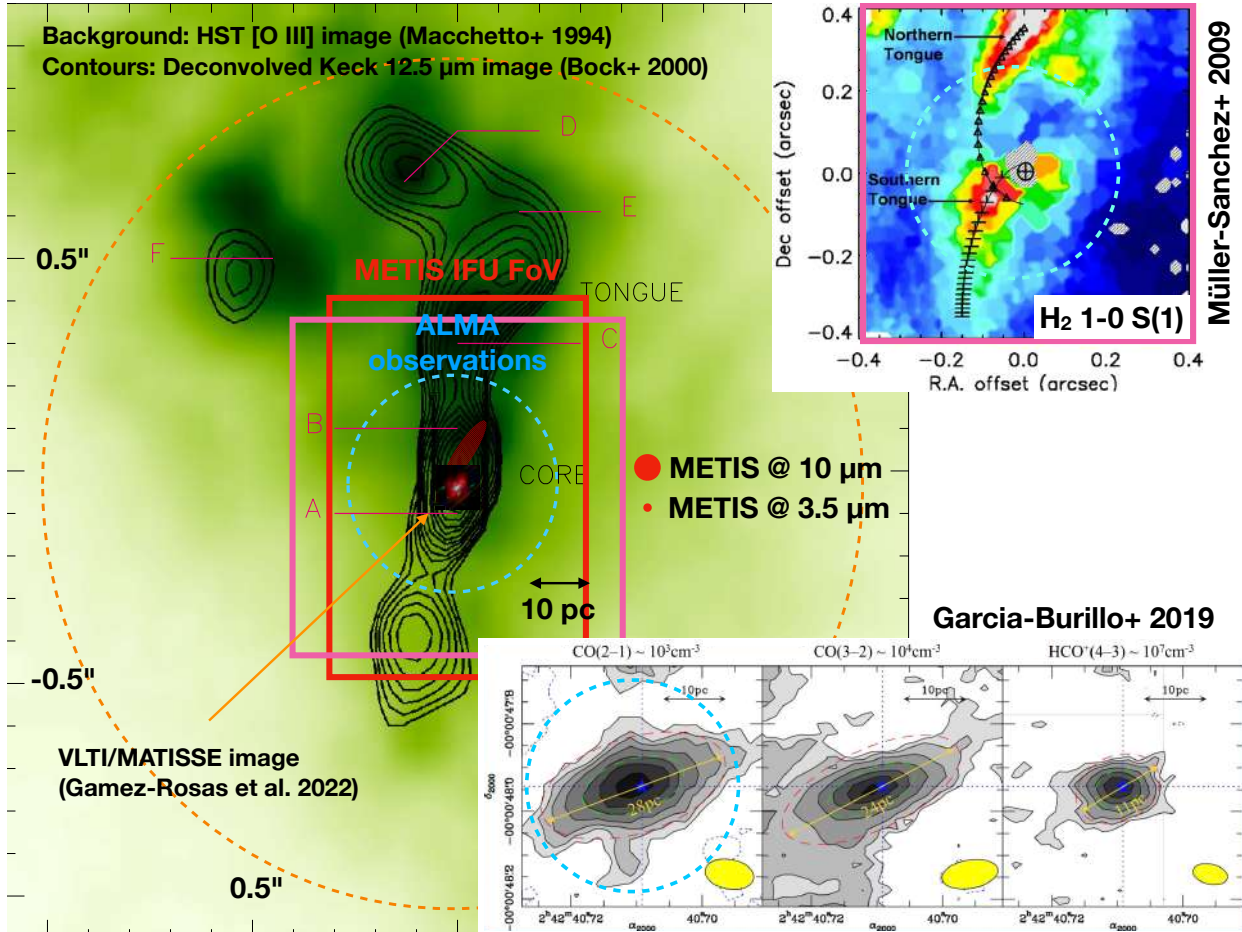


**Figure 9-1:** The modern view of the complex AGN “torus” region: The largest panel shows an overlay of an optical image in the [OIII] line with a deconvolved 12.5  $\mu\text{m}$  image in contours (Bock et al. 2000). On top of the contours, we show the recent image reconstruction based on VLTI/MATISSE observations (Gámez Rosas et al. 2022) (the VLTI field of view is indicated by the large dashed orange circle). The red dots to the center right of this panel show the METIS PSFs at 3.5  $\mu\text{m}$  and at 10  $\mu\text{m}$ , respectively, and the red rectangle indicates the field of view of the METIS *L* and *M* band high-resolution integral-field spectrograph. The blue dashed circle and the purple square allow to compare to the fields of view of the SINFONI (Müller-Sánchez et al. 2009) and ALMA (García-Burillo et al. 2019) observations shown in the upper right and lower right panels, respectively, and to the same scale. While the mid-IR continuum emission is interpreted as being part of the obscuring “torus” as well as outflowing Narrow Line Region, the near-IR “tongues”, seen in the light of hot molecular hydrogen (the 1-0 S(1) line), have been interpreted as inflow. The ALMA observations, on the other hand, show a rotating disk with superposed non-circular motions in the lines of CO and HCO<sup>+</sup>.

and velocity dispersion (Ferrarese & Merritt 2000; Gebhardt et al. 2000), the radius of influence can be written as:

$$\theta_{\text{BH}} = 0.03'' \left( \frac{M_{\text{BH}}}{10^8 M_{\odot}} \right)^{0.5} \left( \frac{100 \text{ Mpc}}{D} \right) \quad (1)$$

With 8m class telescopes, this can only be resolved for the most nearby galaxies and most massive black holes.

METIS at the ELT provides the unique opportunity to investigate the nuclei of local AGNs by mapping gas flows and measuring dynamic black hole masses. The very large obscuration towards these nuclei necessitates the use of the longest accessible wavelengths, and therefore favours METIS. Combined with the spatial resolution provided by an ELT, a direct dynamical probe of black hole masses in obscured galactic nuclei will for the first time be possible. Finally, combining imaging with integral field spectroscopy, the

structures and gas dynamics in the nuclear regions can be mapped and the relation between star formation and black hole growth can be investigated in a systematic way. Specific questions that will be answered include:

1. What are the masses of the SMBHs in the nuclei of nearby AGNs?
2. How is the SMBH fed during the phase of mass buildup?
3. Do stellar mass and SMBH mass build up simultaneously in AGNs, or does one component precede the other?
4. Is the star formation process terminated by feedback from the SMBH?
5. How does feedback from the starburst affect the environment?
6. What is the fate of the gas that is left over after star formation has terminated?
7. (How) is this gas related to the circum-nuclear obscuring torus?
8. What is the size and geometry of the circum-nuclear dusty structure? Is it in fact a torus?
9. Does the circum-nuclear dusty structure have a central cavity and how does gas in this region flow towards the accreting SMBH?
10. How does the warm AGN-heated dust on circum-nuclear scales relate to the cold gas seen by ALMA on similar scales and to the hot dust seen by VLTI on parsec scales?

It is worth noting that an instrument like METIS primarily observes continuum emission from dust at 100-800 K, but is also sensitive to Br  $\alpha$ , coronal lines like [SiIX], [ArVI] and [AlVI], molecular lines of CO and H<sub>2</sub>O, and broad silicate emission and absorption lines. Examples of spectral features in the atmospheric *L*, *M* and *N* bands are shown in Fig. 9-2, 9-6 and 9-7, respectively.

## 9.2 High-resolution imaging of the AGN “torus” region

The AGN “central engine”, in the broader sense, contains many components. In order of increasing size these include the **SMBH**, the (nuclear) radio jet, the surrounding hot accretion disk, the **Broad Line Region** (BLR), the dusty **obscuring structure or torus**, the **Narrow Line Region** (NLR), and the circum-nuclear star-forming region. Material flows inwards, probably in the equatorial plane, while radiation and kinetic energy flow outward into the surrounding galaxy, mostly observed along the “polar” axis. Historically each region has been discovered using different instrumental techniques and often at different wavelengths from radio to gamma rays. Astronomers analyzed the conditions and physical properties independently for each region.

In the past decade theoreticians have begun to break the artificial barrier between the BLR, the “torus” and the NLR, showing that they are part of a single physical system (e.g. Czerny & Hryniwicz 2011; Baskin & Laor 2018; Vollmer et al. 2018). The material travelling inward passes smoothly through a transition where dust sublimates and the nuclear UV ionizes the clouds that form the BLR. In this transition region, the radiation pressure from UV photons reprocessed into the infrared lifts material out of the accretion plane into winds and fountains that redistribute matter and energy into the NLR (e.g. Schartmann et al. 2014; Wada et al. 2016). Besides finally clarifying the mechanism that supports thick dusty accretion disks against the gravity of the SMBH, this model also explains the recently confirmed prevalence of *polar* infrared emission from the central engine region (Asmus et al. 2016; López-Gonzaga et al. 2016; Leftley et al. 2019), see Fig. 9-3. By resolution and sensitivity, METIS will be the ideal instrument to probe this polar dust emission, i.e. the base of the AGN outflow, in a large number of AGNs, see Fig. 9-4.

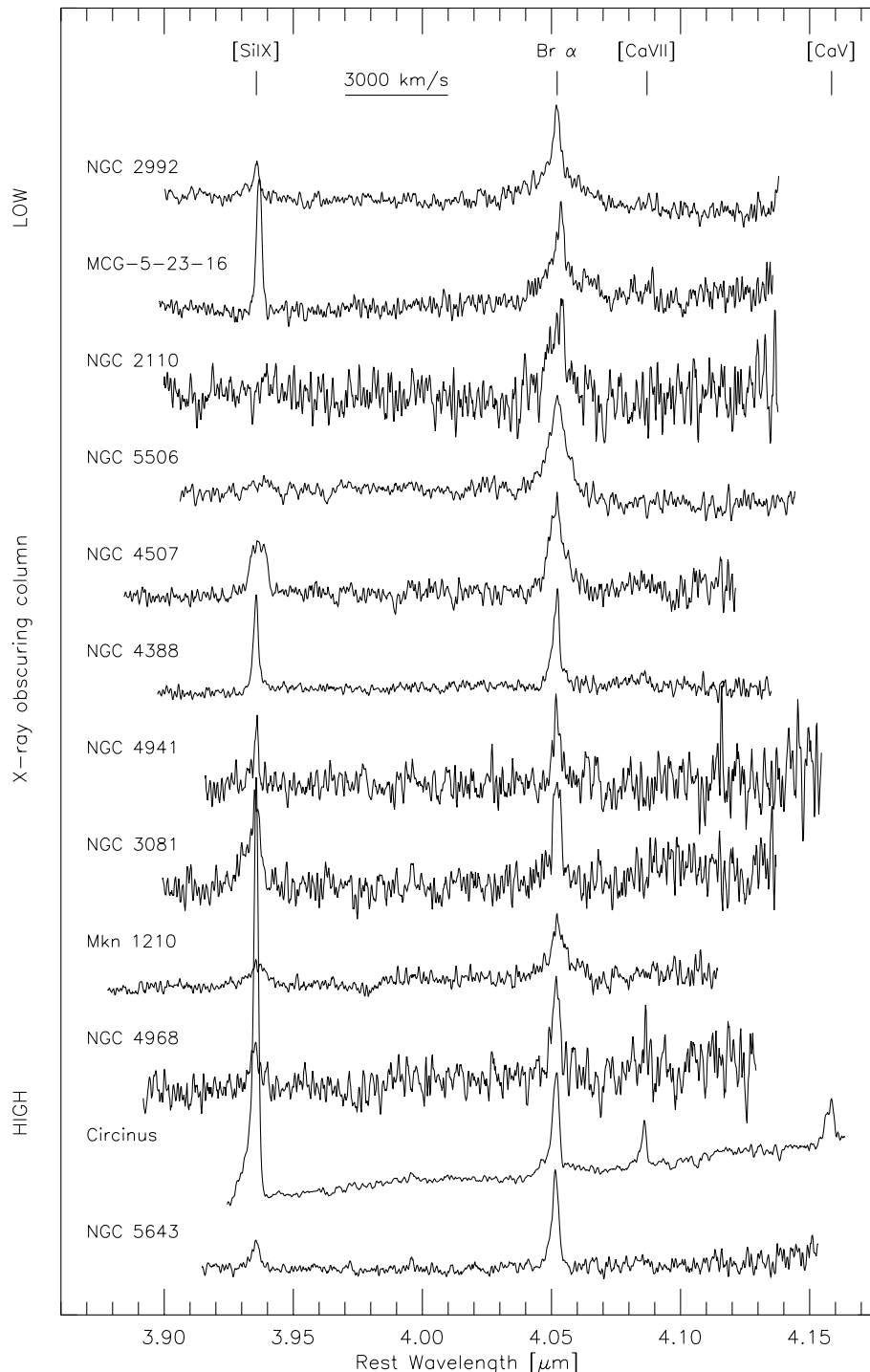


**Figure 9-2:** VLT/ISAAC 4  $\mu\text{m}$  spectra of twelve local Seyfert 2 galaxies showing that Br- $\alpha$  as well as the coronal line [Si IX] are strongly detected in nearly all of these galaxies. From Lutz et al. (2002).

The physics of these regions is particularly relevant to the context of the larger surrounding galaxy because this is where winds and non-relativistic outflows are formed that are the main channels of energy transport to the ISM. Feedback at different epochs and in different environments cannot be understood until the physics of dusty accretion are understood. Key questions include:

- What are the physical conditions of the accreting dust systems that surround AGNs at  $\approx 1 - 100$  pc radius? Are they turbulent? Are they heated by nuclear UV- and X-ray radiation and is infrared

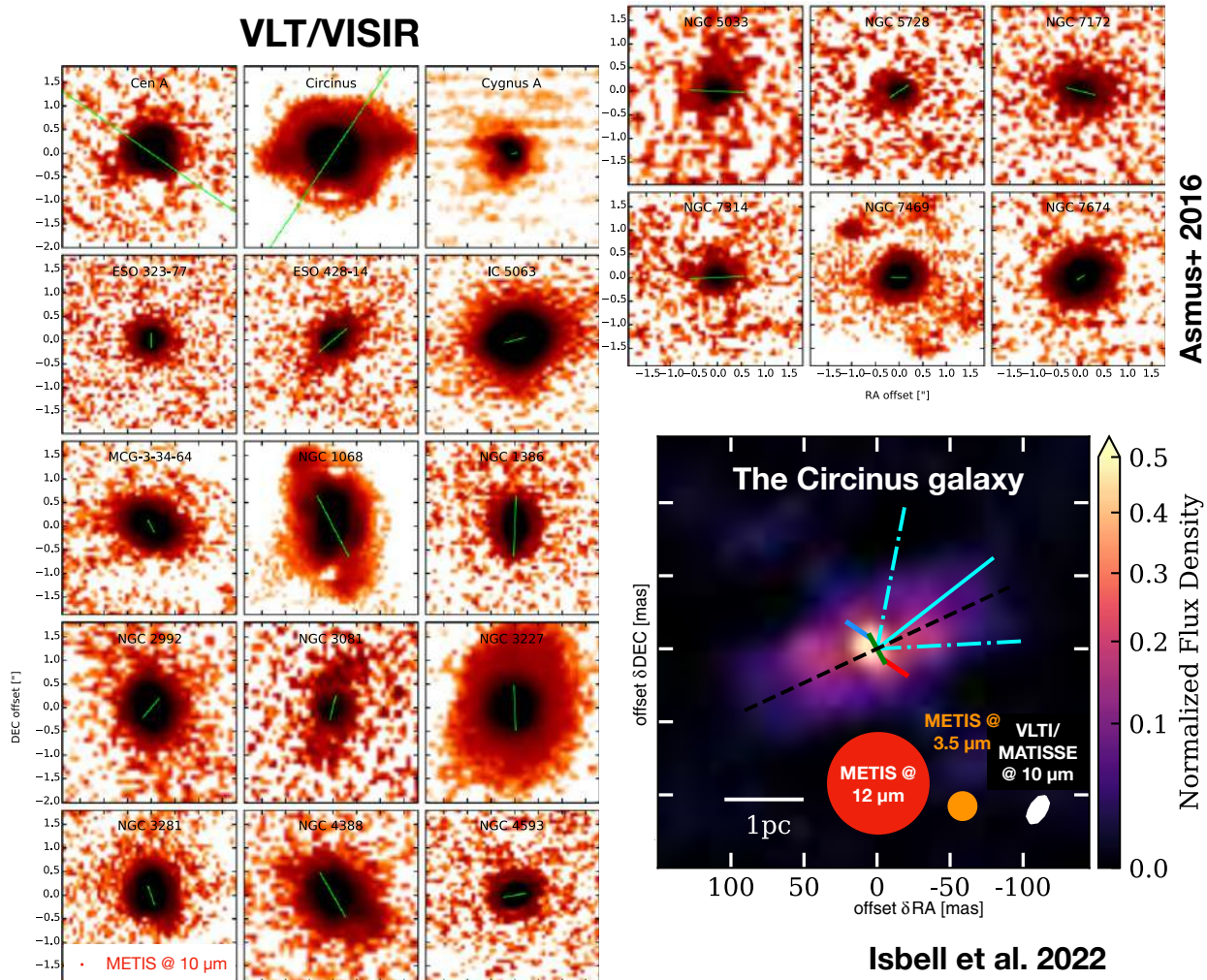


**Figure 9-3:** Polar dust in nearby Seyfert galaxies as seen by VLT/VISIR (Asmus et al. 2016) and VLTI/MATISSE (Isbell et al. 2022) on scales of  $\approx 100$  pc (indicated by the length of the green line) and 1 pc, respectively. In the panel with the MATISSE image, we also show the PSF of METIS at  $L$  and  $N$  band as orange and red disks, respectively, as well as the size of the reconstructed VLTI/MATISSE beam.

radiation pressure as dominant as recent models (e.g. Wada et al. 2016) and observations (e.g. Leftley et al. 2019) predict? Observations with VLTI/MIDI have shown that the structures vary considerably from galaxy to galaxy (Burtscher et al. 2013), and do not always align perpendicular to radio axes (López-Gonzaga et al. 2016). The most recent images from VLTI/MATISSE reveal sub-parsec structure in the two most luminous and nearby AGNs NGC 1068 (Gámez Rosas et al. 2022) and in the Circinus galaxy (Isbell et al. 2022).

- Is the unified model of AGNs still useful or does it rather prohibit us from seeing the full complexity of these regions? Seyfert 1 and Seyfert 2 galaxies are classically interpreted as hosting an identical AGN seen face-on or edge-on, respectively. Statistical investigations have shown, however, that the dust structures in these two types of AGNs are in fact physically different: Seyfert 2 galaxies have more dust clouds that also cover a larger solid angle and may represent a different accretion state (Ramos Almeida et al. 2011).
- Is the dust composition affected by the transition from the outer BLR (the dust sublimation zone) to the dusty outflow? Some silicate absorption features indicate non-standard dust compositions, but the signal-to-noise rate and the spatial resolution of existing observations is too low to make conclusive statements. Existing mid-IR spectra of AGNs typically show a diversity of Silicate absorption and

Angle vs Eddington ratio. Source with 0.1 Jy and 0.4 Myr. 3600 s integration time

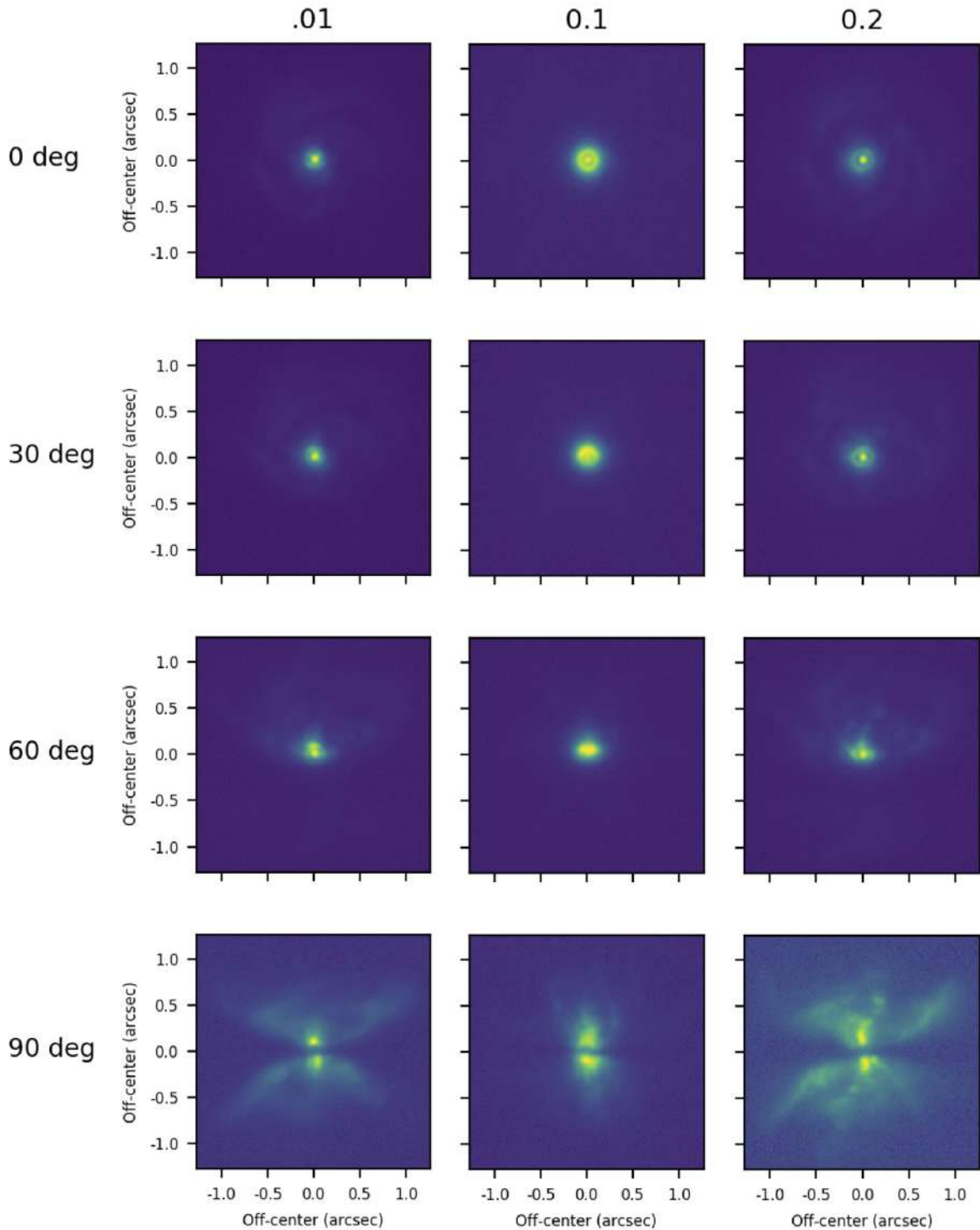


**Figure 9-4:** Simulated METIS images (using the METIS data simulator *SimMETIS*) of the “torus” region of a nearby faint AGN, simulated as a radiation-driven dusty outflow by Schartmann et al. (2014). The rows show different inclinations of the central disk while the columns shown models with Eddington ratios varying from 1% (left) to 10% (center) and 20% (right).

emission features and this is not as straight-forwardly related to the optical (Seyfert 1/2) classification as one might expect (see Fig. 9-7). Due to its unique combination of resolving power and sensitivity, METIS will be the foremost instrument to study the dust chemistry in AGNs in a significant sample of local AGNs, as shown in Figs. 9-5 and 9-8. We expect to be able to resolve the dust chemistry in approximately 100 local active galaxies with AGNs.

- How is energy fed back from the inner regions of AGNs to the surrounding galaxy? The majority of this feedback, at least in lower luminosity AGNs, is probably not from radio jets, but from interaction with winds from the inner edge of the dust disk. Mid-IR observations of a sample of local galaxies show that the majority of the warm dust is located in the outflow region, and not in the “torus” mid-plane (see Fig. 9-3).
- Where does the dusty material come from? The most obvious source is circum-nuclear star clusters. What processes allow material at 100 pc to dump angular momentum? Does this material spiral in quietly or is it grossly turbulent? Why doesn't it form stars? The region outside 10 pc is too big and too faint for MIDI/MATISSE to map dust and CO or Br  $\alpha$  emission lines, but METIS will have the right field of view and sensitivity to bridge the gap between VLTI and ALMA observations.

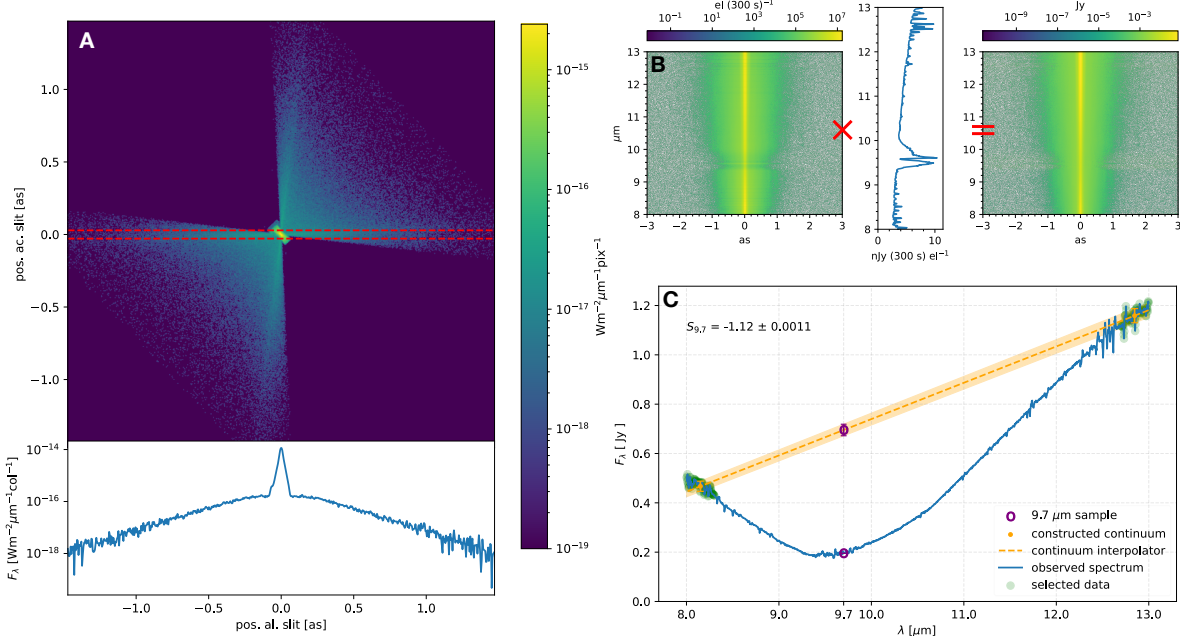


**Figure 9-5:** SimMETIS simulation of an N-band long-slit observation of a nearby AGN. **Panel A:** Input image for the SimMETIS simulation, a Monte Carlo radiative transfer simulation of a dusty AGN disk and a dusty wind from Stalevski et al. (2019). The red dashed lines mark the position angle and width of the long slit (here: slit 'D', 57.1 mas wide). The lower panel shows a cross section of the flux in the image along the slit.

**Panel B:** *left* – The detector image that results from the SimMETIS simulation, here shown with axes already calibrated for spatial / wavelength coordinates; *right* – telluric and flux calibrated 2D spectrum.

**Panel C:** Determination of the silicate absorption depth from the extracted spectrum (blue) and interpolated continuum (yellow). From van der Wielen (2022)

Observations of the obscured central regions, to comparable resolutions, can also be obtained with ALMA, in its most extended configurations, and the most luminous objects. Clear detections of the torus, separated from the surrounded medium, have recently been possible in the continuum, for the bright nearby Seyfert galaxy NGC 1068 (García-Burillo et al. 2016; García-Burillo et al. 2019, see also Fig. 9-1) and for a few other nearby galaxies (García-Burillo et al. 2021). Remarkably, ALMA observations of one of the nearest prominent AGNs, the radio galaxy Centaurus A do not show any emission of molecular lines in the region close to the AGN (McCoy et al. 2017), while near-IR molecular hydrogen emission is strong (Neumayer

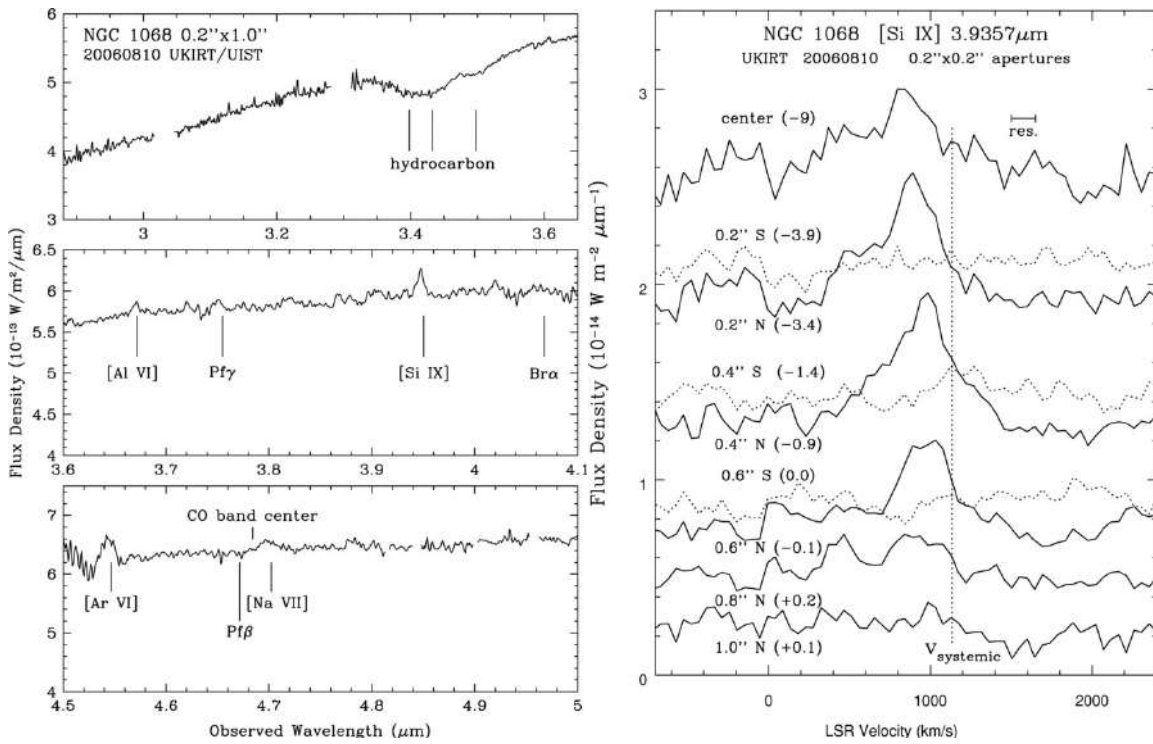


**Figure 9-6:** Left: 3–5  $\mu\text{m}$  spectrum of the central  $0.2'' \times 1.0''$  (EW  $\times$  NS) region of NGC 1068. Wavelengths of atomic lines of interest are shown, as are the three components of the 3.4  $\mu\text{m}$  hydrocarbon feature and the band center of CO, all at the systemic redshift of NGC 1068. Right: Velocity profiles of the [Si IX] line in  $0.2''$  steps along the slit. The continuous lines denote spectra at the center and to the north; the dashed lines indicate spectra to the south. Numbers in parentheses are continuum offsets. The y-axis is flux density in a  $0.2'' \times 0.2''$  aperture. From Geballe et al. (2009).

et al. 2007). The most likely explanation is that molecules other than H<sub>2</sub> are either in extremely highly excited states or, more likely, destroyed in the harsh radiation environment of the AGN. This indicates that molecular lines in the ALMA region are good for probing the torus environment, but not the torus itself, which can be probed through near- and mid-infrared spectroscopy. METIS and ALMA observations are thus highly complementary, and the combination of both is essential for understanding these complex regions.

The specific role of ELT/METIS in unwinding this complexity is its combined high spatial and spectral resolution and high sensitivity. The other relevant instruments that will be operating at the same time are the VLTI (MATISSE+GRAVITY), ALMA, and the JWST. Of these, the VLTI has the highest spatial resolution (2–10 milli-arcseconds in the *K* and *N* bands respectively), but is sensitivity-limited to a few tens of nearby Seyfert galaxies<sup>8</sup>. The sensitivity limit particularly limits possible kinematic studies because the CO and Hydrogen emission line strengths from the inner dust regions seem to be quite low. The resolution of ALMA is only slightly lower and its spectral resolution is high. Its longer wavelength coverage is optimum for studying the colder regions between the star-forming ring and the outer dust disk, rather than the hotter BLR-dust transition where most of the energy is emitted in the infrared. Finally, the JWST has superb sensitivity and spectral coverage, but has a spatial resolution (135–400 milli-arcseconds in the wavelength range that METIS will cover) that is too small to resolve the processes in the “torus” region.

We expect the primary contributions of METIS to be:

<sup>8</sup>In the future, the GRAVITY+ project, will upgrade the VLTI with laser guide stars and state-of-the-art adaptive optics for all unit telescopes to make accessible a larger fraction of the extragalactic sky. The first phase of this project, GRAVITY-wide has recently seen first light (GRAVITY+ Collaboration et al. 2022)

- Follow the kinematics, chemistry, and dynamics of the dusty/molecular accretion flow in nearby Seyfert galaxies from the colder outer regions ( $T \sim 30$  K) towards the sublimation zone ( $T \sim 1500$  K) through mapping of molecular and recombination lines in the mid-IR.
- Similarly, in the same galaxies, follow the acceleration of this material, presumably by radiation pressure, into dusty polar winds towards the NLR.
- Extend these studies, with limited spatial resolution, to hundreds of galaxies, in order to trace how these AGN flows interact with the inward and outward transport of mass, momentum, and energy with the host galaxy and surrounding environment.

### 9.3 Black hole masses in nearby obscured AGNs

As argued in Section 9.1, systematically measuring SMBH masses in significant samples of galaxies is indispensable to understand the link between black hole growth, star formation and galaxy evolution. These samples of galaxies need to contain different sub-samples, including inactive galaxies with “sleeping” SMBHs, AGNs and (U)LIRGs. For the first category, characterized by modest amounts of obscuration, optical or near-infrared observations are suitable and the techniques to measure SMBH masses based on stellar and/or gas kinematics have reached a reasonable level of maturity. AGNs and (U)LIRGs on the other

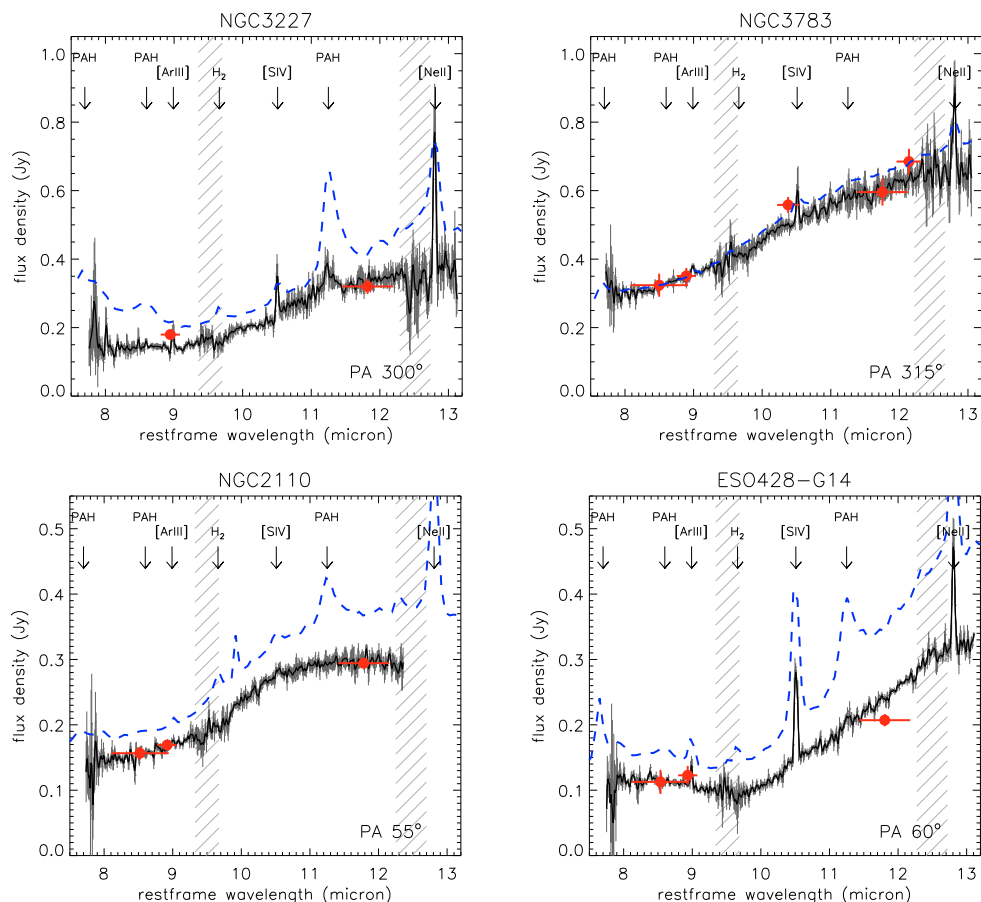


**Figure 9-7:** A collection of  $N$  band spectra from Seyfert 1 (top row) and Seyfert 2 (bottom row). The black line is the spectrum obtained from VLT/VISIR and the blue dashed line is a Spitzer spectrum for comparison. The red dots are photometric measurement from VLT/VISIR. Prominent mid-IR emission lines are marked. In the lower right panel the broad absorption band of Silicates (centered at  $\approx 9.7$   $\mu\text{m}$ ) can easily be seen in the Seyfert 2 galaxy ESO 428-G14. From Höning et al. (2010).

hand are typically obscured by large amounts of dust, such that mid-infrared observations are required to probe their nuclear regions.

Target	D [Mpc]	$M_{\text{BH}}$ $[M_{\odot}]$	$\theta_{\text{BH}}$ ['']	Notes
Cen A	3.5	$4.5 \dots 5.5 \cdot 10^7$	0.6	Neumayer et al. (2007); Cappellari et al. (2009)
Circinus	3.9	$1.3 \cdot 10^6$	0.09	Greenhill et al. (2003)
NGC 4945	7.3	$3.8 \cdot 10^6$	0.09	Greenhill et al. (1997)
NGC 1068	14	$1.0 \cdot 10^7$	0.07	Greenhill et al. (1996)
NGC 7582	21	$5.5 \cdot 10^7$	0.11	Wold et al. (2006)
Arp 220	70	$\approx 10^8$	0.06	Black hole mass estimated
NGC 6240	100	$\approx 10^8$	0.03	Black hole mass estimated

**Table 9-1:** Black hole masses and radii of influence for nearby AGNs and (U)LIRGs.

Tab 9-1 lists relevant parameters of nearby obscured AGNs and (U)LIRGs with representative key METIS observations. The black hole masses of Circinus, NGC 4945 and NGC 1068 in this table come from VLBI measurements of H<sub>2</sub>O maser emission, but the black hole mass of NGC 7582 has been determined using mid-infrared spectroscopy of the [Ne II] 12.8  $\mu\text{m}$  line at the diffraction limit of VISIR/VLT, demonstrating the promise of mid-infrared spectroscopy for these observations (Wold et al. 2006). The high-resolution integral-field spectrograph in the *L* and *M* bands will allow METIS to perform such observations in about 30–100 AGNs.

As can be seen from Tab 9-1, at the resolution of the VLT the radius of influence of the SMBH is approached, but not resolved. However, at the higher resolution provided by an ELT, the full Keplerian motion of the gaseous disk will be revealed. METIS therefore opens up the detailed study of dynamics and gas flow in accreting gas disks in obscured AGNs, and will not be limited to the subset of AGNs that have luminous H<sub>2</sub>O maser emission. This allows a much more statistically robust approach than hitherto possible.

## 9.4 A representative AGN observing program for METIS

1. Mapping of CO or Br-alpha kinematics from warm dusty disks. No kinematic information is currently available, and CO and Br-alpha fluxes are low (Geballe et al. 2009). This information would be the first indication of whether the accretion is smooth or turbulent, whether ionized material is blown off the tops of disks as winds.
2. Mapping of dust continuum emission as well as dust chemistry (Fig. 9-5, Fig. 9-8) beyond radii available to VLTI MIDI/MATISSE. For the VLTI, this is mostly a surface brightness sensitivity issue. The prime interests are to trace the infall of material from the circumnuclear stellar regions, and to trace dust and gas being blown out as winds. One can include in this the mapping of PAH emission. This is not seen at all in MIDI and MATISSE maps, indicating that PAHs near the nucleus are destroyed by nuclear UV/X-rays. Mapping the PAHs at larger radii will diagnose the nuclear radiation fields and its effect on the inflowing gas (Jensen et al. 2017).
3. Map coronal line emission from jet/wind interaction regions. Once again MATISSE sensitivity is probably too low except for the few nearest galaxies. Understanding this interaction is critical to feedback physics.
4. Probe the mid-IR/X-ray relation for AGNs. The mid-IR flux indicates the conversion efficiency of nuclear UV/X-rays to IR, and thus typically measures the dust-covering fraction (fraction of sky covered by dust as seen by the nucleus). This is a critical number for testing AGN unified models, and evolution of accretion phenomenon with cosmic time. Current single dish observations cannot

separate nuclear IR from that at larger radii (circumstellar star regions, spiral arms) and MATISSE is not sensitive enough for a large sample.

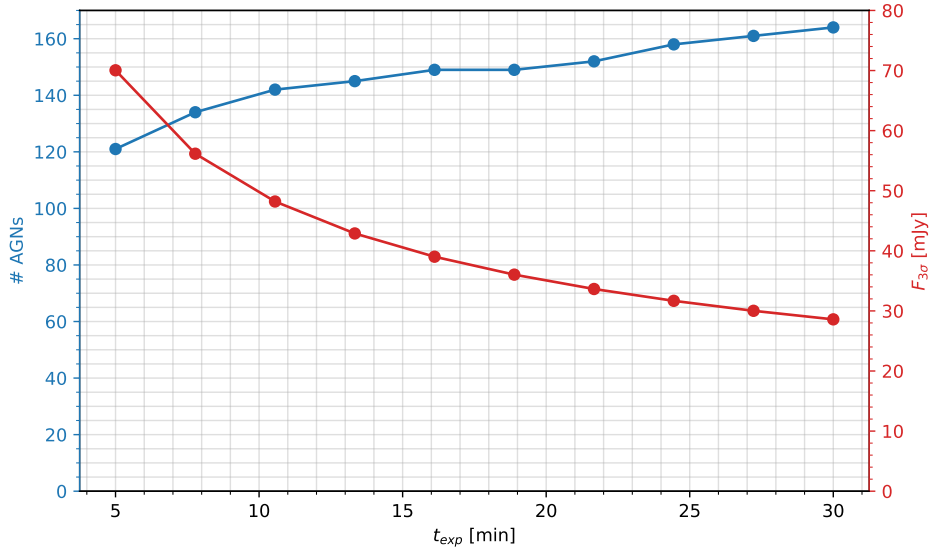


**Figure 9-8:** Number of AGNs (blue curve, left axis) in which METIS will be able to significantly discriminate between a nuclear, silicate-absorption dominated, and an outflow, graphite-dominated (featureless) spectrum, as a function of exposure time. The right axis corresponds to the *total* AGN flux for which this discrimination is possible at the  $3\sigma$  level. From van der Wielen (2022)

## A APPENDIX: METIS OBSERVING MODES

Science Observing Mode	Instrument Configuration						Science Driver
	Sub-Syst.	Band	IFS Setting	HCI Mask	P T	F T	
Direct Imaging	IMG	L,M	N/A	N/A	•	•	circum-stellar (YSOs) and circum-nuclear (AGN) structures, star clusters
	IMG	N	N/A	N/A	•	•	circum-stellar (YSOs) and circum-nuclear (AGN) structures
High Contrast Imaging	IMG	L,M	N/A N/A	RAVC/CVC APP	• •		exoplanets (detection + characterization)
	IMG	N	N/A	CVC	•		exoplanets (detection + characterization)
Longslit spectroscopy	IMG	L,M	N/A	N/A	•		ices in comets and star forming regions
	IMG	N	N/A	N/A	•		physics of circum-stellar and circum-nuclear environments; solid-state chemistry & mineralogy
IFU spectroscopy	LMS	L,M	full IFU field	N/A	•	•	kinematics and chemistry of circum-stellar environments
	LMS	L,M	spectral IFU $\Delta\lambda \sim 300\text{nm}$	N/A	•	•	chemical studies of the interstellar medium
IFU+HCI spectroscopy	LMS	L,M	full IFU field	APP RAVC/CVC	• •		exoplanetary atmospheres at $\theta > 3\lambda/D$ , pp-disks
	LMS	L,M	spectral IFU $\Delta\lambda \sim 300\text{nm}$	APP RAVC/CVC	• •		exoplanetary atmospheres at $\theta \sim 2\lambda/D$ , pp-disks

**Figure 1-1:** The five science observing modes of METIS. The acronyms stand for: CVC – Classical Vortex Coronagraph (bright stars, large angular separations); RAVC – Ring-apodized Vortex Coronagraph (bright stars, small angular separations); APP – Apodized Phase Plate (fainter stars); N/A – not applicable; Pupil tracking (PT) and field tracking (FT) modes are indicated by black dots.

Parallel Observing Mode	Instrument Configuration						Science Driver
	Sub-Syst.	Band	IFS Setting	HCI Mask	P T	F T	
LM&N-Imaging	IMG	L,M,N	N/A	N/A	•	•	circum-stellar (YSOs) and circum-nuclear (AGN) structures, star clusters
LM&N-Longslit Spectroscopy	IMG	L,M,N	N/A	N/A	•		ices in comets and star forming regions physics of circum-stellar and circum-nuclear environments; solid-state chemistry & mineralogy
LM-Imaging & IFU Spect.	IMG, LMS	L,M	full IFU field	N/A	In nominal as well as HCI observations with the IFU, the IMG will be run in parallel for providing an accurate positional reference frame and/or closed-loop positional control (QACITS)		

**Figure 1-2:** Parallel observing modes of METIS. The individual modes are equivalent to the ones listed above in Figure 1-1, but doing two modes in parallel instead of sequentially would increase the observing efficiency.

## REFERENCES

- Abrahám, P., Juhász, A., Dullemond, C., et al. 2009, *Nature*, 459, 224
- Absil, O., Defrère, D., Coudé du Foresto, V., et al. 2013a, *A&A*, 555, A104
- Absil, O., Milli, J., Mawet, D., et al. 2013b, *A&A*, 559, L12
- Abuter, R., Accardo, M., Amorim, A., et al. 2017, *Astronomy & Astrophysics*, 602, A94
- Abuter, R., Amorim, A., Bauböck, M., et al. 2018, *Astronomy & Astrophysics*, 618, L10
- Alexander, R., Pascucci, I., Andrews, S., Armitage, P., & Cieza, L. 2014, *Protostars and Planets VI*, 475
- Allison, R. J., Goodwin, S. P., Parker, R. J., et al. 2009, *ApJL*, 700, L99
- ALMA Partnership, Brogan, C. L., Pérez, L. M., et al. 2015, *ApJ*, 808, L3
- Alonso-Herrero, A., Ramos Almeida, C., Esquej, P., et al. 2014, *MNRAS*, 443, 2766
- Altweig, K., Balsiger, H., Berthelier, J. J., et al. 2017, *Monthly Notices of the Royal Astronomical Society*, 469, S130
- Andrews, S. M. 2020, *ARA&A*, 58, 483
- Anglada-Escudé, G., Amado, P. J., Barnes, J., et al. 2016, *Nature*, 536, 437
- Antonellini, S., Kamp, I., Riviere-Marichalar, P., et al. 2015, *A&A*, 582, A105
- Armitage, P. J. 2011, *ARA&A*, 49, 195
- Asmus, D., Höning, S. F., & Gandhi, P. 2016, *ApJ*, 822, 109
- Audard, M., Ábrahám, P., Dunham, M. M., et al. 2014, in *Protostars and Planets VI*, ed. H. Beuther, R. S. Klessen, C. P. Dullemond, & T. Henning, 387
- Avenhaus, H., Quanz, S. P., Garufi, A., et al. 2018, *ApJ*, 863, 44
- Ayliffe, B. A. & Bate, M. R. 2009, *MNRAS*, 393, 49
- Backman, D. E. & Paresce, F. 1993, in *Protostars and Planets III*, ed. E. H. Levy & J. I. Lunine, 1253–1304
- Bai, X.-N. & Stone, J. M. 2013, *ApJ*, 769, 76
- Balick, B. & Frank, A. 2002, *ARA&A*, 40, 439
- Ballering, N. P., Cleeves, L. I., & Anderson, D. E. 2021, *ApJ*, 920, 115
- Banzatti, A., Abernathy, K. M., Brittain, S., et al. 2022, *AJ*, 163, 174
- Banzatti, A., Pascucci, I., Edwards, S., et al. 2019, *ApJ*, 870, 76
- Banzatti, A., Pinilla, P., Ricci, L., et al. 2015, *ApJ*, 815, L15
- Banzatti, A. & Pontoppidan, K. M. 2015, *ApJ*, 809, 167
- Banzatti, A., Pontoppidan, K. M., Salyk, C., et al. 2017, *ApJ*, 834, 152
- Baraffe, I., Chabrier, G., Barman, T. S., Allard, F., & Hauschildt, P. H. 2003, *A&A*, 402, 701
- Barnes, J. W., Brown, R. H., Soderblom, L., et al. 2007, *Icarus*, 186, 242

- Barros, S. C. C., Akinsanmi, B., Boué, G., et al. 2022, *A&A*, 657, A52
- Baskin, A. & Laor, A. 2018, *MNRAS*, 474, 1970
- Bast, J. E., Brown, J. M., Herczeg, G. J., van Dishoeck, E. F., & Pontoppidan, K. M. 2011, *A&A*, 527, A119
- Bastian, N., Covey, K. R., & Meyer, M. R. 2010, *ARA&A*, 48, 339
- Batygin, K., Bodenheimer, P., & Laughlin, G. 2009, *ApJL*, 704, L49
- Beichman, C. A., Tanner, A., Bryden, G., et al. 2006, *ApJ*, 639, 1166
- Benisty, M., Bae, J., Facchini, S., et al. 2021, *ApJ*, 916, L2
- Benisty, M., Dominik, C., Follette, K., et al. 2022, arXiv e-prints, arXiv:2203.09991
- Benneke, B., Knutson, H. A., Lothringer, J., et al. 2019, *Nature Astronomy*, 3, 813
- Berné, O. & Tielens, A. G. G. M. 2012, *Proceedings of the National Academy of Science*, 109, 401
- Beuermann, K., Hessman, F. V., Dreizler, S., et al. 2010, *A&A*, 521, L60
- Beuther, H., Linz, H., Henning, T., Feng, S., & Teague, R. 2017, *A&A*, 605, A61
- Bhat, H. K., Sabha, N. B., Zajaček, M., et al. 2022, *ApJ*, 929, 178
- Bing, L., Shi, Y., Chen, Y., et al. 2019, *MNRAS*, 482, 194
- Birkby, J. L. 2018, *Spectroscopic Direct Detection of Exoplanets*, 16
- Birkby, J. L., de Kok, R. J., Brogi, M., et al. 2013, *MNRAS*, 436, L35
- Birnstiel, T., Dullemond, C. P., & Pinilla, P. 2013, *A&A*, 550, L8
- Birnstiel, T., Fang, M., & Johansen, A. 2016, *Space Sci. Rev.*, 205, 41
- Bjerkeli, P., van der Wiel, M. H. D., Harsono, D., Ramsey, J. P., & JØrgensen, J. K. 2016, *Nature*, 540, 406
- Bladh, S. 2019, *IAU Symposium*, 343, 99
- Bladh, S. & Höfner, S. 2012, *A&A*, 546, A76
- Blake, G. A. & Boogert, A. C. A. 2004a, *ApJ*, 606, L73
- Blake, G. A. & Boogert, A. C. A. 2004b, *ApJL*, 606, L73
- Blunt, S., Endl, M., Weiss, L. M., et al. 2019, *AJ*, 158, 181
- Boccaletti, A., Di Folco, E., Pantin, E., et al. 2020, *A&A*, 637, L5
- Bock, J. J., Neugebauer, G., Matthews, K., et al. 2000, *AJ*, 120, 2904
- Boley, P. A., Linz, H., van Boekel, R., et al. 2013, *A&A*, 558, A24
- Bollen, D., Van Winckel, H., & Kamath, D. 2017, *A&A*, 607, A60
- Bonavita, M., de Mooij, E. J. W., & Jayawardhana, R. 2013, *PASP*, 125, 849
- Bonfond, B., Grodent, D., Badman, S. V., Gérard, J.-C., & Radioti, A. 2016, *Geophysical Research Letters*, 43, 11,963

- Bonnell, I. A. & Bate, M. R. 2006, MNRAS, 370, 488
- Bonnell, I. A. & Smith, R. J. 2011, in IAU Symposium, Vol. 270, Computational Star Formation, ed. J. Alves, B. G. Elmegreen, J. M. Girart, & V. Trimble, 57–64
- Bonsor, A. & Wyatt, M. C. 2012, MNRAS, 420, 2990
- Bonsor, A., Wyatt, M. C., Kral, Q., et al. 2018, MNRAS, 480, 5560
- Boogert, A. C. A., Gerakines, P. A., & Whittet, D. C. B. 2015, ARA&A, 53, 541
- Booth, R. A., Clarke, C. J., Madhusudhan, N., & Ilee, J. D. 2017, MNRAS, 469, 3994
- Borucki, W. J., Koch, D. G., Basri, G., et al. 2011, ApJ, 736, 19
- Bosman, A. D., Banzatti, A., Bruderer, S., et al. 2019, A&A, 631, A133
- Bosman, A. D., Bruderer, S., & van Dishoeck, E. F. 2017, A&A, 601, A36
- Bosman, A. D., Walsh, C., & van Dishoeck, E. F. 2018, A&A, 618, A182
- Boutéraon, T., Habart, E., Ysard, N., et al. 2019, A&A, 623, A135
- Bouwman, J., Castellanos, P., Bulak, M., et al. 2019, A&A, 621, A80
- Bouwman, J., de Koter, A., Dominik, C., & Waters, L. B. F. M. 2003, A&A, 401, 577
- Bouwman, J., Meeus, G., de Koter, A., et al. 2001, A&A, 375, 950
- Bowens, R., Meyer, M. R., Delacroix, C., et al. 2021, A&A, 653, A8
- Brandl, B. R., Martín-Hernández, N. L., Schaerer, D., Rosenberg, M., & van der Werf, P. P. 2012, A&A, 543, A61
- Brittain, S. D., Najita, J. R., & Carr, J. S. 2009, ApJ, 702, 85
- Brogi, M., de Kok, R. J., Albrecht, S., et al. 2016, ApJ, 817, 106
- Brogi, M., Snellen, I. A. G., de Kok, R. J., et al. 2012, Nature, 486, 502
- Bromm, V. & Larson, R. B. 2004, ARAA, 42, 79
- Bromm, V., Yoshida, N., Hernquist, L., & McKee, C. F. 2009, Nature, 459, 49
- Brown, J. M., Herczeg, G. J., Pontoppidan, K. M., & van Dishoeck, E. F. 2012, ApJ, 744, 116
- Brown, J. M., Pontoppidan, K. M., van Dishoeck, E. F., et al. 2013, ApJ, 770, 94
- Brown, M. E. 2008, The Largest Kuiper Belt Objects, ed. M. A. Barucci, H. Boehnhardt, D. P. Cruikshank, A. Morbidelli, & R. Dotson, 335–344
- Bruderer, S., Harsono, D., & van Dishoeck, E. F. 2015, A&A, 575, A94
- Bruderer, S., van Dishoeck, E. F., Doty, S. D., & Herczeg, G. J. 2012, A&A, 541, A91
- Bujarrabal, V., Castro-Carrizo, A., Alcolea, J., & Van Winckel, H. 2015, A&A, 575, L7
- Bujarrabal, V., Castro-Carrizo, A., Alcolea, J., et al. 2013, A&A, 557, L11
- Bujarrabal, V., Castro-Carrizo, A., Winckel, H. V., et al. 2018, A&A, 614, A58
- Burtscher, L., Davies, R. I., Shimizu, T. T., et al. 2021, A&A, 654, A132

- Burtscher, L., Meisenheimer, K., Tristram, K. R. W., et al. 2013, *A&A*, 558, A149
- Béthune, W., Lesur, G., & Ferreira, J. 2017, *A&A*, 600, A75
- Böhnhardt, H., Mumma, M. J., Villanueva, G. L., et al. 2008, *The Astrophysical Journal Letters*, 683, L71
- Canup, R. M. & Ward, W. R. 2002, *AJ*, 124, 3404
- Canup, R. M. & Ward, W. R. 2009, *Origin of Europa and the Galilean Satellites*, ed. R. T. Pappalardo, W. B. McKinnon, & K. K. Khurana, 59
- Caratti o Garatti, A., Stecklum, B., Weigelt, G., et al. 2016, *A&A*, 589, L4
- Carlson, R. W., Smythe, W. D., Lopes-Gautier, R. M. C., et al. 1997, *Geophysical Research Letters*, 24, 2479, eprint: <https://onlinelibrary.wiley.com/doi/pdf/10.1029/97GL02609>
- Carmona, A., Thi, W. F., Kamp, I., et al. 2017, *A&A*, 598, A118
- Casassus, S., van der Plas, G., M., S. P., et al. 2013, *Nature*, 493, 191
- Chapman, J. W., Zellem, R. T., Line, M. R., et al. 2017, *PASP*, 129, 104402
- Charbonneau, D., Brown, T. M., Noyes, R. W., & Gilliland, R. L. 2002, *ApJ*, 568, 377
- Chatterjee, S., Ford, E. B., Matsumura, S., & Rasio, F. A. 2008, *ApJ*, 686, 580
- Chen, X. & Szulágyi, J. 2021a, arXiv e-prints, arXiv:2112.12821
- Chen, X. & Szulágyi, J. 2021b, arXiv e-prints, arXiv:2112.12821
- Cheng, Y., Tan, J. C., Liu, M., et al. 2018, *ApJ*, 853, 160
- Cherchneff, I. 2012, *A&A*, 545, A12
- Chiar, J. E., Adamson, A. J., Pendleton, Y. J., et al. 2002, *ApJ*, 570, 198
- Chiar, J. E., Tielens, A. G. G. M., Whittet, D. C. B., et al. 2000, *ApJ*, 537, 749
- Cid Fernandes, R., Gu, Q., Melnick, J., et al. 2004, *MNRAS*, 355, 273
- Ciesla, F. J. & Cuzzi, J. N. 2006, *Icarus*, 181, 178
- Cieza, L. A., Casassus, S., Tobin, J., et al. 2016, *Nature*, 535, 258
- Clayton, R. N., Grossman, L., & Mayeda, T. K. 1973, *Science*, 182, 485
- Cochran, A. L., Levasseur-Regourd, A.-C., Cordiner, M., et al. 2015, *Space Science Reviews*, 197, 9
- Conroy, C., Dutton, A. A., Graves, G. J., Mendel, J. T., & van Dokkum, P. G. 2013, *ApJL*, 776, L26
- Correia, A. C. M., Boué, G., Laskar, J., & Rodríguez, A. 2014, *A&A*, 571, A50
- Crain, R. A., Schaye, J., Bower, R. G., et al. 2015, *MNRAS*, 450, 1937
- Cridland, A. J., Eistrup, C., & van Dishoeck, E. F. 2019, *A&A*, 627, A127
- Crossfield, I. J. M. 2014, *A&A*, 566, A130
- Crossfield, I. J. M., Biller, B., Schlieder, J. E., et al. 2014, *Nature*, 505, 654
- Crossfield, I. J. M. & Kreidberg, L. 2017, *AJ*, 154, 261

- Cugno, G., Quanz, S. P., Hunziker, S., et al. 2019, *A&A*, 622, A156
- Currie, T., Biller, B., Lagrange, A.-M., et al. 2022, arXiv e-prints, arXiv:2205.05696
- Cyganowski, C. J., Brogan, C. L., Hunter, T. R., et al. 2017, *MNRAS*, 468, 3694
- Czerny, B. & Hryniewicz, K. 2011, *A&A*, 525, L8+
- Dale, J. E., Haworth, T. J., & Bressert, E. 2015, *MNRAS*, 450, 1199
- Danielski, C., Baudino, J.-L., Lagage, P.-O., et al. 2018, *AJ*, 156, 276
- Dartois, E., Engrand, C., Duprat, J., et al. 2018, *A&A*, 609, A65
- Davies, B., Lumsden, S. L., Hoare, M. G., Oudmaijer, R. D., & de Wit, W.-J. 2010, *MNRAS*, 402, 1504
- Davies, R. I., Mueller Sánchez, F., Genzel, R., et al. 2007, *ApJ*, 671, 1388
- Dawson, R. I. & Johnson, J. A. 2018, *ARA&A*, 56, 175
- de Juan Ovelar, M., Min, M., Dominik, C., et al. 2013, *A&A*, 560, A111
- de Kleer, K., Skrutskie, M., Leisenring, J., et al. 2017, *Nature*, 545, 199, number: 7653 Publisher: Nature Publishing Group
- De Marco, O. 2009, *PASP*, 121, 316
- De Marco, O. & Izzard, R. G. 2017, *PASA*, 34, e001
- de Pater, I., Fletcher, L. N., Luszcz-Cook, S., et al. 2014, *Icarus*, 237, 211
- de Ruyter, S., van Winckel, H., Dominik, C., Waters, L. B. F. M., & Dejonghe, H. 2005, *A&A*, 435, 161
- de Ruyter, S., van Winckel, H., Maas, T., et al. 2006, *A&A*, 448, 641
- de Wit, W. J., Hoare, M. G., Oudmaijer, R. D., et al. 2011, *A&A*, 526, L5
- de Zeeuw, P. T., Hoogerwerf, R., de Bruijne, J. H. J., Brown, A. G. A., & Blaauw, A. 1999, *AJ*, 117, 354
- Decin, L. 2021, *ARA&A*, 59, 337
- Decin, L., Blomme, L., Reyniers, M., et al. 2008, *A&A*, 484, 401
- Decin, L., De Beck, E., Brünken, S., et al. 2010, *A&A*, 516, A69
- Decin, L., Hony, S., de Koter, A., et al. 2007, *A&A*, 475, 233
- Decin, L., Montargès, M., Richards, A. M. S., et al. 2020, *Science*, 369, 1497
- Decin, L., Richards, A. M. S., Waters, L. B. F. M., et al. 2017, *A&A*, 608, A55
- Defrère, D., Absil, O., Berger, J. P., et al. 2018, *Experimental Astronomy*, 46, 475
- Defrère, D., Hinz, P. M., Kennedy, G. M., et al. 2021, *AJ*, 161, 186
- Defrère, D., Absil, O., den Hartog, R., Hanot, C., & Stark, C. 2010, *A&A*, 509, A9
- Defrère, D., Stark, C., Cahoy, K., & Beerer, I. 2012, in *Proc. SPIE*, Vol. 8442, Space Telescopes and Instrumentation 2012: Optical, Infrared, and Millimeter Wave, 84420M
- Delbo, M., Mueller, M., Emery, J. P., Rozitis, B., & Capria, M. T. 2015, Asteroid Thermophysical Modeling, ed. P. Michel, F. E. DeMeo, & W. F. Bottke, 107–128

- Deming, D., Seager, S., Richardson, L. J., & Harrington, J. 2005, *Nature*, 434, 740
- Devinat, M., Habart, É., Pantin, É., et al. 2022, *A&A*, 663, A151
- Dong, S., Katz, B., & Socrates, A. 2013, *ApJL*, 762, L26
- Dong, S., Katz, B., & Socrates, A. 2014, *ApJ*, 781, L5
- Dressing, C. D. & Charbonneau, D. 2015, *ApJ*, 807, 45
- Drew, J. E., Proga, D., & Stone, J. M. 1998, *MNRAS*, 296, L6
- Du, F., Bergin, E. A., Hogerheijde, M., et al. 2017, *ApJ*, 842, 98
- Duchêne, G. & Kraus, A. 2013, *ARA&A*, 51, 269
- Dunne, L., Eales, S., Ivison, R., Morgan, H., & Edmunds, M. 2003, *Nature*, 424, 285
- Durisen, R. H., Boss, A. P., Mayer, L., et al. 2007, in *Protostars and Planets V*, ed. B. Reipurth, D. Jewitt, & K. Keil, 607
- Dutrey, A., Guilloteau, S., Piétu, V., et al. 2017, *A&A*, 607, A130
- Eckart, A., Baganoff, F. K., Schödel, R., et al. 2006a, *A&A*, 450, 535
- Eckart, A., Baganoff, F. K., Zamaninasab, M., et al. 2008, *A&A*, 479, 625
- Eckart, A. & Genzel, R. 1997, in *Bulletin of the American Astronomical Society*, Vol. 29, American Astronomical Society Meeting Abstracts, 1366
- Eckart, A., Horrobin, M., Britzen, S., et al. 2014, in *IAU Symposium*, Vol. 303, The Galactic Center: Feeding and Feedback in a Normal Galactic Nucleus, ed. L. O. Sjouwerman, C. C. Lang, & J. Ott, 269–273
- Eckart, A., Hüttemann, A., Kiefer, C., et al. 2017, *Foundations of Physics*, 47, 553
- Eckart, A., Mužić, K., Yazici, S., et al. 2013, *A&A*, 551, A18
- Eckart, A., Schödel, R., Meyer, L., et al. 2006b, *A&A*, 455, 1
- Eckart, A., Schödel, R., Moultsaka, J., et al. 2005, in *American Institute of Physics Conference Series*, Vol. 783, The Evolution of Starbursts, ed. S. Hüttmeister, E. Manthey, D. Bomans, & K. Weis, 17–25
- Eckart, A., Zajacek, M., Parsa, M., et al. 2018, arXiv e-prints, arXiv:1806.00284
- Eisner, J. A. 2015, *ApJ*, 803, L4
- Eistrup, C., Walsh, C., & van Dishoeck, E. F. 2018, *A&A*, 613, A14
- Elmegreen, B. G. 2002, *ApJ*, 577, 206
- Ertel, S., Absil, O., Defrère, D., et al. 2014, *A&A*, 570, A128
- Ertel, S., Defrère, D., Hinz, P., et al. 2020, *AJ*, 159, 177
- Ertel, S., Defrère, D., Hinz, P., et al. 2018, *AJ*, 155, 194
- Ertel, S., Wolf, S., & Rodmann, J. 2012, *A&A*, 544, A61
- Esquej, P., Alonso-Herrero, A., González-Martín, O., et al. 2014a, *ApJ*, 780, 86

- Esquej, P., Alonso-Herrero, A., González-Martín, O., et al. 2014b, *ApJ*, 780, 86
- Facchini, S., Pinilla, P., van Dishoeck, E. F., & de Juan Ovelar, M. 2018, *A&A*, 612, A104
- Faramaz, V., Ertel, S., Booth, M., Cuadra, J., & Simmonds, C. 2017, *MNRAS*, 465, 2352
- Faria, J. P., Suárez Mascareño, A., Figueira, P., et al. 2022, *A&A*, 658, A115
- Fedele, D., Bruderer, S., van Dishoeck, E. F., et al. 2012, *A&A*, 544, L9
- Fedele, D., Tazzari, M., Booth, R., et al. 2018, *A&A*, 610, A24
- Feng, F., Anglada-Escudé, G., Tuomi, M., et al. 2019, *MNRAS*, 490, 5002
- Fernandes, R. B., Mulders, G. D., Pascucci, I., Mordasini, C., & Emsenhuber, A. 2019, *ApJ*, 874, 81
- Ferrarese, L. & Merritt, D. 2000, *ApJ*, 539, L9
- Ferus, M., Nesvorný, D., Šponer, J., et al. 2015, *Proceedings of the National Academy of Science*, 112, 657
- Flowers, E., Brogi, M., Rauscher, E., Kempton, E. M. R., & Chiavassa, A. 2019, *AJ*, 157, 209
- Follette, K. B., Grady, C. A., Swearingen, J. R., et al. 2015, *ApJ*, 798, 132
- Fortney, J. J., Marley, M. S., Saumon, D., & Lodders, K. 2008, *ApJ*, 683, 1104
- Frost, A. J., Oudmaijer, R. D., de Wit, W. J., & Lumsden, S. L. 2019, *A&A*, 625, A44
- Frost, A. J., Oudmaijer, R. D., de Wit, W. J., & Lumsden, S. L. 2021, *A&A*, 648, A62
- Fry, P. M., Sromovsky, L. A., de Pater, I., Hammel, H. B., & Rages, K. A. 2012, *The Astronomical Journal*, 143, 150
- Fujiwara, H., Ishihara, D., Onaka, T., et al. 2013, *A&A*, 550, A45
- Gail, H.-P. 1998, *A&A*, 332, 1099
- Galliano, E., Alloin, D., Pantin, E., et al. 2008, *A&A*, 492, 3
- Gámez Rosas, V., Isbell, J. W., Jaffe, W., et al. 2022, *Nature*, 602, 403
- Gandhi, S., Brogi, M., & Webb, R. K. 2020, *MNRAS*, 498, 194
- García-Burillo, S., Alonso-Herrero, A., Ramos Almeida, C., et al. 2021, *A&A*, 652, A98
- García-Burillo, S., Combes, F., Ramos Almeida, C., et al. 2019, *A&A*, 632, A61
- García-Burillo, S., Combes, F., Ramos Almeida, C., et al. 2016, *ApJ*, 823, L12
- Garufi, A., Quanz, S. P., Avenhaus, H., et al. 2013, *A&A*, 560, A105
- Garufi, A., Quanz, S. P., Schmid, H. M., et al. 2016, *A&A*, 588, A8
- Geballe, T. R. 1986, *A&A*, 162, 248
- Geballe, T. R., Mason, R. E., Rodríguez-Ardila, A., & Axon, D. J. 2009, *ApJ*, 701, 1710
- Gebhardt, K., Kormendy, J., Ho, L. C., et al. 2000, *ApJ*, 543, L5
- Geers, V. C., Augereau, J.-C., Pontoppidan, K. M., et al. 2006, *A&A*, 459, 545
- Geers, V. C., Pontoppidan, K. M., van Dishoeck, E. F., et al. 2007a, *A&A*, 469, L35

- Geers, V. C., van Dishoeck, E. F., Visser, R., et al. 2007b, *A&A*, 476, 279
- Genzel, R., Eisenhauer, F., & Gillessen, S. 2010, *Reviews of Modern Physics*, 82, 3121
- Genzel, R., Schödel, R., Ott, T., et al. 2003, *Nature*, 425, 934
- Ghez, A. M., Klein, B. L., Morris, M., & Becklin, E. E. 1998, *ApJ*, 509, 678
- Giacobbe, P., Brogi, M., Gandhi, S., et al. 2021, *Nature*, 592, 205
- Gielen, C., Bouwman, J., van Winckel, H., et al. 2011, *A&A*, 533, A99
- Gielen, C., van Winckel, H., Min, M., Waters, L. B. F. M., & Lloyd Evans, T. 2008, *A&A*, 490, 725
- Gielen, C., van Winckel, H., Waters, L. B. F. M., Min, M., & Dominik, C. 2007, *A&A*, 475, 629
- Gillessen, S., Genzel, R., Fritz, T. K., et al. 2012, *Nature*, 481, 51
- Gillon, M., Triaud, A. H. M. J., Demory, B.-O., et al. 2017, *Nature*, 542, 456
- Giridhar, S., Lambert, D. L., Reddy, B. E., Gonzalez, G., & Yong, D. 2005, *ApJ*, 627, 432
- Gobrecht, D., Bromley, S. T., Plane, J. M. C., Decin, L., & Cristallo, S. 2019, *IAU Symposium*, 343, 119
- Gobrecht, D., Cherchneff, I., & Sarangi, A. 2015, in *Astronomical Society of the Pacific Conference Series*, Vol. 497, Why Galaxies Care about AGB Stars III: A Closer Look in Space and Time, ed. F. Kerschbaum, R. F. Wing, & J. Hron, 321
- Gordon, K. D., Meixner, M., Meade, M. R., et al. 2011, *AJ*, 142, 102
- Gorlova, N., Van Winckel, H., Gielen, C., et al. 2012, *A&A*, 542, A27
- Gorlova, N., Van Winckel, H., Ikonnikova, N. P., et al. 2015, *MNRAS*, 451, 2462
- Goto, M., Usuda, T., Dullemond, C. P., et al. 2006a, *ApJ*, 652, 758
- Goto, M., Usuda, T., Dullemond, C. P., et al. 2006b, *ApJ*, 652, 758
- GRAVITY+ Collaboration, :, Abuter, R., et al. 2022, arXiv e-prints, arXiv:2206.00684
- GRAVITY Collaboration, Abuter, R., Amorim, A., et al. 2018, *A&A*, 615, L15
- Gravity Collaboration, Abuter, R., Amorim, A., et al. 2020, *A&A*, 636, L5
- GRAVITY Collaboration, Pfuhl, O., Davies, R., et al. 2019, arXiv e-prints, arXiv:1912.01361
- Güdel, M., Eibensteiner, C., Dionatos, O., et al. 2018, *A&A*, 620, L1
- Guidi, G., Ruane, G., Williams, J. P., et al. 2018, *MNRAS*, 479, 1505
- Habart, E., Boutéraon, T., Brauer, R., et al. 2021, *A&A*, 649, A84
- Habing, H. J. & Olofsson, H., eds. 2003, *Asymptotic giant branch stars*
- Haffert, S. Y., Bohn, A. J., de Boer, J., et al. 2019, *Nature Astronomy*, 3, 749
- Harker, D. E. & Desch, S. J. 2002, *ApJ*, 565, L109
- Harker, D. E., Woodward, C. E., & Wooden, D. H. 2005, *Science*, 310, 278
- Harsono, D., Bjerkeli, P., van der Wiel, M. H. D., et al. 2018, *Nature Astronomy*, 2, 646

- Haubois, X., Dodds-Eden, K., Weiss, A., et al. 2012, *A&A*, 540, A41
- Hayward, C. C., Narayanan, D., Kereš, D., et al. 2013, *MNRAS*, 428, 2529
- Helling, C., Woitke, P., Rimmer, P. B., et al. 2014, *Life*, 4, 142
- Herczeg, G. J., Brown, J. M., van Dishoeck, E. F., & Pontoppidan, K. M. 2011, *A&A*, 533, A112
- Hicks, E. K. S., Davies, R. I., Maciejewski, W., et al. 2013, *ApJ*, 768, 107
- Hicks, E. K. S., Davies, R. I., Malkan, M. A., et al. 2009, *ApJ*, 696, 448
- Hillen, M., de Vries, B. L., Menu, J., et al. 2015, *A&A*, 578, A40
- Hillen, M., Menu, J., Van Winckel, H., et al. 2014, *A&A*, 568, A12
- Hillen, M., Van Winckel, H., Menu, J., et al. 2017, *A&A*, 599, A41
- Hillen, M., Verhoelst, T., Van Winckel, H., et al. 2013, *A&A*, 559, A111
- Hinkle, K. H., Brittain, S. D., & Lambert, D. L. 2007, *ApJ*, 664, 501
- Hinkley, S., Lacour, S., Marleau, G. D., et al. 2022, arXiv e-prints, arXiv:2208.04867
- Hoeijmakers, H. J., Schwarz, H., Snellen, I. A. G., et al. 2018, *A&A*, 617, A144
- Hoeijmakers, H. J., Seidel, J. V., Pino, L., et al. 2020, *A&A*, 641, A123
- Höfner, S. & Freytag, B. 2019, *A&A*, 623, A158
- Hogerheijde, M. R., Bergin, E. A., Brinch, C., et al. 2011, *Science*, 334, 338
- Homan, W., Richards, A., Decin, L., et al. 2017, *A&A*, 601, A5
- Honda, M., Inoue, A. K., Fukagawa, M., et al. 2009, *ApJ*, 690, L110
- Honda, M., Kudo, T., Takatsuki, S., et al. 2016, *ApJ*, 821, 2
- Hone, E., Kraus, S., Kreplin, A., et al. 2017, *A&A*, 607, A17
- Hood, C. E., Fortney, J. J., Line, M. R., et al. 2020, *AJ*, 160, 198
- Hopkins, P. F., Bundy, K., Croton, D., et al. 2010, *ApJ*, 715, 202
- Horner, J. & Jones, B. W. 2008, *Astronomy and Geophysics*, 49, 1.22
- Hosek, Jr., M. W., Lu, J. R., Anderson, J., et al. 2019, *ApJ*, 870, 44
- Hosokawa, T., Yorke, H. W., & Omukai, K. 2010, *ApJ*, 721, 478
- Hron, J., Utenthaler, S., Aringer, B., et al. 2015, *A&A*, 584, A27
- Hughes, A. M., Duchêne, G., & Matthews, B. C. 2018, *ARA&A*, 56, 541
- Huélamo, N., Chauvin, G., Schmid, H. M., et al. 2018, *A&A*, 613, L5
- Höfner, S. 2008, *A&A*, 491, L1
- Hönig, S. F., Kishimoto, M., Gandhi, P., et al. 2010, *A&A*, 515, A23+
- Ilee, J. D., Cyganowski, C. J., Nazari, P., et al. 2016, *MNRAS*, 462, 4386

- Ilee, J. D., Wheelwright, H. E., Oudmaijer, R. D., et al. 2013, MNRAS, 429, 2960
- Indebetouw, R., Whitney, B. A., Johnson, K. E., & Wood, K. 2006, ApJ, 636, 362
- Inoue, A. K., Honda, M., Nakamoto, T., & Oka, A. 2008, PASJ, 60, 557
- Isbell, J. W., Meisenheimer, K., Pott, J. U., et al. 2022, A&A, 663, A35
- Izquierdo, A. F., Facchini, S., Rosotti, G. P., van Dishoeck, E. F., & Testi, L. 2022, ApJ, 928, 2
- Jackson, A. P., Wyatt, M. C., Bonsor, A., & Veras, D. 2014, MNRAS, 440, 3757
- Jensen, J. J., Höning, S. F., Rakshit, S., et al. 2017, MNRAS, 470, 3071
- Johansen, A. & Lambrechts, M. 2017, Annual Review of Earth and Planetary Sciences, 45, 359
- Johansen, A., Ronnet, T., Bizzarro, M., et al. 2021, Science Advances, 7, eabc0444
- Johnson, R. E., Melin, H., Stallard, T. S., et al. 2018, Journal of Geophysical Research: Space Physics, 123, 5990
- Johnson, R. E., Stallard, T. S., Melin, H., Nichols, J. D., & Cowley, S. W. H. 2017, Journal of Geophysical Research: Space Physics, 122, 7599
- Johnston, K. G., Hoare, M. G., Beuther, H., et al. 2020, ApJ, 896, 35
- Johnston, K. G., Robitaille, T. P., Beuther, H., et al. 2015, ApJL, 813, L19
- Jovanovic, N., Delorme, J. R., Bond, C. Z., et al. 2019, arXiv e-prints, arXiv:1909.04541
- Juhász, A., Bouwman, J., Henning, T., et al. 2010, ApJ, 721, 431
- Kamath, D., Wood, P. R., & Van Winckel, H. 2014, MNRAS, 439, 2211
- Kamath, D., Wood, P. R., & Van Winckel, H. 2015, MNRAS, 454, 1468
- Kamath, D., Wood, P. R., Van Winckel, H., & Nie, J. D. 2016, A&A, 586, L5
- Kamiński, T. 2019, IAU Symposium, 343, 108
- Kawahara, H., Murakami, N., Matsuo, T., & Kotani, T. 2014, ApJS, 212, 27
- Kemper, F., Vriend, W. J., & Tielens, A. G. G. M. 2004, ApJ, 609, 826
- Kennedy, G. M. & Piette, A. 2015, MNRAS, 449, 2304
- Kennedy, G. M. & Wyatt, M. C. 2013, MNRAS, 433, 2334
- Kepler, M., Benisty, M., Müller, A., et al. 2018, A&A, 617, A44
- Kervella, P., Arenou, F., Mignard, F., & Thévenin, F. 2019, A&A, 623, A72
- Kervella, P., Homan, W., Richards, A. M. S., et al. 2016, A&A, 596, A92
- Kessler-Silacci, J. E., Dullemond, C. P., Augereau, J.-C., et al. 2007, ApJ, 659, 680
- Kley, W. & Nelson, R. P. 2012, ARA&A, 50, 211
- Kluska, J., Hillen, M., Van Winckel, H., et al. 2018, A&A, 616, A153
- Kluska, J., Van Winckel, H., Coppée, Q., et al. 2022, A&A, 658, A36

- Kluska, J., Van Winckel, H., Hillen, M., et al. 2019, *A&A*, 631, A108
- Knutson, H. A., Charbonneau, D., Allen, L. E., et al. 2007, *Nature*, 447, 183
- Kobayashi, C., Haynes, C. J., & Vincenzo, F. 2019, *IAU Symposium*, 343, 247
- Kokoulina, E., Matter, A., Lopez, B., et al. 2021, *A&A*, 652, A61
- Kotani, T., Kawahara, H., Ishizuka, M., et al. 2020, in Society of Photo-Optical Instrumentation Engineers (SPIE) Conference Series, Vol. 11448, Society of Photo-Optical Instrumentation Engineers (SPIE) Conference Series, 1144878
- Koumpia, E., Ababakr, K. M., de Wit, W. J., et al. 2019, *A&A*, 623, L5
- Kral, Q., Wyatt, M. C., Triaud, A. H. M. J., et al. 2018, *MNRAS*, 479, 2649
- Kratter, K. & Lodato, G. 2016, *ARA&A*, 54, 271
- Kraus, A. L. & Ireland, M. J. 2012, *ApJ*, 745, 5
- Kraus, A. L., Ireland, M. J., Cieza, L. A., et al. 2014, *ApJ*, 781, 20
- Kraus, S., Hofmann, K.-H., Menten, K. M., et al. 2010, *Nature*, 466, 339
- Kraus, S., Kluska, J., Kreplin, A., et al. 2017, *ApJL*, 835, L5
- Kreidberg, L., Bean, J. L., Désert, J.-M., et al. 2014, *Nature*, 505, 69
- Kreidberg, L., Koll, D. D. B., Morley, C., et al. 2019, *Nature*, 573, 87
- Krumholz, M. R., Klein, R. I., & McKee, C. F. 2007, *ApJ*, 665, 478
- Kuiper, R., Klahr, H., Beuther, H., & Henning, T. 2010, *ApJ*, 722, 1556
- Kuiper, R., Klahr, H., Beuther, H., & Henning, T. 2011, *ApJ*, 732, 20
- Lacey, C. G., Baugh, C. M., Frenk, C. S., et al. 2008, *MNRAS*, 385, 1155
- Lagadec, E., Verhoelst, T., Mékarnia, D., et al. 2011, *MNRAS*, 417, 32
- Lagage, P.-O., Doucet, C., Pantin, E., et al. 2006, *Science*, 314, 621
- Lam, H. A., Miller, S., Joseph, R. D., et al. 1997, *The Astrophysical Journal*, 474, L73, publisher: American Astronomical Society
- Lambrechts, M., Morbidelli, A., Jacobson, S. A., et al. 2019, *A&A*, 627, A83
- Lang, C. C., Goss, W. M., & Morris, M. 2001, *AJ*, 121, 2681
- Lang, C. C., Goss, W. M., & Wood, O. S. 1997, *ApJ*, 474, 275
- Laver, C. & de Pater, I. 2009, *Icarus*, 201, 172
- Law, C. J., Loomis, R. A., Teague, R., et al. 2021, *ApJS*, 257, 3
- Lawler, S. M., Beichman, C. A., Bryden, G., et al. 2009, *ApJ*, 705, 89
- Lawler, S. M. & Gladman, B. 2012, *ApJ*, 752, 53
- Laws, A. S. E., Harries, T. J., Setterholm, B. R., et al. 2020, *ApJ*, 888, 7
- Lebreton, J., Beichman, C., Bryden, G., et al. 2016a, *ApJ*, 817, 165

- Lebreton, J., Beichman, C., Bryden, G., et al. 2016b, *ApJ*, 817, 165
- Lecar, M., Podolak, M., Sasselov, D., & Chiang, E. 2006, *ApJ*, 640, 1115
- Lee, E. J. & Chiang, E. 2015, *ApJ*, 811, 41
- Lee, J.-M., Heng, K., & Irwin, P. G. J. 2013, *ApJ*, 778, 97
- Leemker, M., van't Hoff, M. L. R., Trapman, L., et al. 2021, *A&A*, 646, A3
- Leftley, J. H., Höning, S. F., Asmus, D., et al. 2019, *ApJ*, 886, 55
- Lellouch, E., Moreno, R., & Paubert, G. 2005, *Astronomy and Astrophysics*, 430, L37
- Lesur, G., Ercolano, B., Flock, M., et al. 2022, arXiv e-prints, arXiv:2203.09821
- Li, J., Bergin, E. A., Blake, G. A., Ciesla, F. J., & Hirschmann, M. M. 2021, *Science Advances*, 7, eabd3632
- Lilly, S. J., Carollo, C. M., Pipino, A., Renzini, A., & Peng, Y. 2013, *ApJ*, 772, 119
- Linz, H., Henning, T., Feldt, M., et al. 2009, *A&A*, 505, 655
- Lissauer, J. J. 1993, *ARA&A*, 31, 129
- Lissauer, J. J., Fabrycky, D. C., Ford, E. B., et al. 2011, *Nature*, 470, 53
- Lisse, C. M., Chen, C. H., Wyatt, M. C., et al. 2009, *ApJ*, 701, 2019
- Liu, H. B., Takami, M., Kudo, T., et al. 2016, *Science Advances*, 2, e1500875
- Liu, W. M., Hinz, P. M., Meyer, M. R., et al. 2003, *ApJ*, 598, L111
- Lovis, C., Snellen, I., Mouillet, D., et al. 2017, *A&A*, 599, A16
- Lumsden, S. L., Hoare, M. G., Urquhart, J. S., et al. 2013, *ApJs*, 208, 11
- Lumsden, S. L., Wheelwright, H. E., Hoare, M. G., Oudmaijer, R. D., & Drew, J. E. 2012, *MNRAS*, 424, 1088
- Lund, K. & Bonnell, I. A. 2018, *MNRAS*, 479, 2235
- Lustig-Yaeger, J., Meadows, V. S., & Lincowski, A. P. 2019, *AJ*, 158, 27
- Lutz, D., Maiolino, R., Moorwood, A. F. M., et al. 2002, *A&A*, 396, 439
- Lyons, J. R. & Young, E. D. 2005, *Nature*, 435, 317
- Lyra, W. & Klahr, H. 2011, *A&A*, 527, A138
- López-Gonzaga, N., Burtscher, L., Tristram, K. R. W., Meisenheimer, K., & Schartmann, M. 2016, *A&A*, 591, A47
- Maas, T., Van Winckel, H., & Lloyd Evans, T. 2005, *A&A*, 429, 297
- Maaskant, K. M., Min, M., Waters, L. B. F. M., & Tielens, A. G. G. M. 2014, *A&A*, 563, A78
- Madau, P. & Dickinson, M. 2014, *ARA&A*, 52, 415
- Madhusudhan, N. 2019, *ARA&A*, 57, 617
- Maercker, M., Mohamed, S., Vlemmings, W. H. T., et al. 2012, *Nature*, 490, 232

- Malfait, K., Waelkens, C., Waters, L. B. F. M., et al. 1998, *A&A*, 332, L25
- Mamajek, E. E. & Meyer, M. R. 2007, *ApJ*, 668, L175
- Manara, C. F., Morbidelli, A., & Guillot, T. 2018, *A&A*, 618, L3
- Mandell, A. M., Bast, J., van Dishoeck, E. F., et al. 2012, *ApJ*, 747, 92
- Mangold, N., Baratoux, D., Witasse, O., Encrenaz, T., & Sotin, C. 2016, *The Astronomy and Astrophysics Review*, 24, 15
- Marino, S., Bonsor, A., Wyatt, M. C., & Kral, Q. 2018, *MNRAS*, 479, 1651
- Martin, R. G. & Livio, M. 2012, *MNRAS*, 425, L6
- Matthews, B. C., Krivov, A. V., Wyatt, M. C., Bryden, G., & Eiroa, C. 2014, *Protostars and Planets VI*, 521
- Mawet, D., Hirsch, L., Lee, E. J., et al. 2019, *AJ*, 157, 33
- McCabe, C., Ghez, A. M., Prato, L., et al. 2006, *ApJ*, 636, 932
- McClure, M. K., Espaillat, C., Calvet, N., et al. 2015, *ApJ*, 799, 162
- McCoy, M., Ott, J., Meier, D. S., et al. 2017, *ApJ*, 851, 76
- McKee, C. F. & Tan, J. C. 2003, *ApJ*, 585, 850
- Meech, K. J., Weryk, R., Micheli, M., et al. 2017, *Nature*, 552, 378
- Meeus, G., Waters, L. B. F. M., Bouwman, J., et al. 2001, *A&A*, 365, 476
- Meixner, M., Gordon, K. D., Indebetouw, R., et al. 2006, *AJ*, 132, 2268
- Melia, F. & Falcke, H. 2001, *ARA&A*, 39, 309
- Melin, H., Fletcher, L. N., Stallard, T. S., et al. 2018, *Monthly Notices of the Royal Astronomical Society*, 474, 3714
- Mennesson, B., Millan-Gabet, R., Serabyn, E., et al. 2014, *ApJ*, 797, 119
- Meyer, D. M.-A., Kuiper, R., Kley, W., Johnston, K. G., & Vorobyov, E. 2018, *MNRAS*, 473, 3615
- Meyer, L., Do, T., Ghez, A., et al. 2008a, *ApJL*, 688, L17
- Meyer, L., Eckart, A., Schödel, R., et al. 2006a, *A&A*, 460, 15
- Meyer, L., Schödel, R., Eckart, A., et al. 2006b, *A&A*, 458, L25
- Meyer, M. R., Carpenter, J. M., Mamajek, E. E., et al. 2008b, *ApJ*, 673, L181
- Michel, A., van der Marel, N., & Matthews, B. C. 2021, *ApJ*, 921, 72
- Miller-Ricci, E., Meyer, M. R., Seager, S., & Elkins-Tanton, L. 2009, *ApJ*, 704, 770
- Min, M., Bouwman, J., Dominik, C., et al. 2016, *A&A*, 593, A11
- Min, M., Waters, L. B. F. M., de Koter, A., et al. 2007, *A&A*, 462, 667
- Miotello, A., Bruderer, S., & van Dishoeck, E. F. 2014, *A&A*, 572, A96
- Mollière, P. & Snellen, I. A. G. 2019, *A&A*, 622, A139

- Moneti, A., Cernicharo, J., & Pardo, J. R. 2001, *ApJL*, 549, L203
- Moore, T. J. T., Bretherton, D. E., Fujiyoshi, T., et al. 2007, *MNRAS*, 379, 663
- Morales, F. Y., Padgett, D. L., Bryden, G., Werner, M. W., & Furlan, E. 2012, *ApJ*, 757, 7
- Morbidelli, A., Levison, H. F., & Gomes, R. 2008, The Dynamical Structure of the Kuiper Belt and Its Primordial Origin, ed. M. A. Barucci, H. Boehnhardt, D. P. Cruikshank, A. Morbidelli, & R. Dotson, 275–292
- Morbidelli, A., Lunine, J. I., O’Brien, D. P., Raymond, S. N., & Walsh, K. J. 2012, *Annual Review of Earth and Planetary Sciences*, 40, 251
- Morbidelli, A., Szulágyi, J., Crida, A., et al. 2014, *Icarus*, 232, 266
- Mordasini, C. 2018, *Planetary Population Synthesis*, 143
- Mordasini, C., van Boekel, R., Mollière, P., Henning, T., & Benneke, B. 2016, *ApJ*, 832, 41
- Mori, T. I., Imanishi, M., Alonso-Herrero, A., et al. 2014, *PASJ*, 66, 93
- Morley, C. V., Kreidberg, L., Rustamkulov, Z., Robinson, T., & Fortney, J. J. 2017, *ApJ*, 850, 121
- Morris, M. & Yusef-Zadeh, F. 1989, *ApJ*, 343, 703
- Moser, L., Sánchez-Monge, A., Eckart, A., et al. 2017, *A&A*, 603, A68
- Mosqueira, I. & Estrada, P. R. 2003, *Icarus*, 163, 198
- Mossoux, E. & Eckart, A. 2018, *MNRAS*, 474, 3787
- Moultaka, J., Eckart, A., & Sabha, N. 2015, *MNRAS*, 448, 3363
- Moultaka, J., Eckart, A., Schödel, R., Viehmann, T., & Najarro, F. 2005, *A&A*, 443, 163
- Moultaka, J., Eckart, A., Tikare, K., & Bajat, A. 2021, in *Astronomical Society of the Pacific Conference Series*, Vol. 528, *New Horizons in Galactic Center Astronomy and Beyond*, ed. M. Tsuboi & T. Oka, 121
- Moultaka, J., Eckart, A., Viehmann, T., et al. 2004, *A&A*, 425, 529
- Moultaka, J., Eckart, A., Viehmann, T., & Schödel, R. 2006, in *Journal of Physics Conference Series*, Vol. 54, *Journal of Physics Conference Series*, ed. R. Schödel, G. C. Bower, M. P. Muno, S. Nayakshin, & T. Ott, 57–61
- Mousis, O., Atkinson, D. H., Cavalié, T., et al. 2018, *Planetary and Space Science*, 155, 12
- Movsessian, T. A., Magakian, T. Y., & Moiseev, A. V. 2012, *A&A*, 541, A16
- Mulders, G. D., Min, M., Dominik, C., Debes, J. H., & Schneider, G. 2013, *A&A*, 549, A112
- Mulders, G. D., Waters, L. B. F. M., Dominik, C., et al. 2011, *A&A*, 531, A93
- Muller, S., Dinh-V-Trung, He, J.-H., & Lim, J. 2008, *ApJ*, 684, L33
- Mumma, M. J. & Charnley, S. B. 2011, *Annual Review of Astronomy and Astrophysics*, 49, 471
- Murakawa, K., Lumsden, S. L., Oudmaijer, R. D., et al. 2013, *MNRAS*, 436, 511
- Murray, N., Quataert, E., & Thompson, T. A. 2005, *ApJ*, 618, 569
- Muto, T., Grady, C. A., Hashimoto, J., et al. 2012, *ApJ*, 748, L22

- Mužić, K., Eckart, A., Schödel, R., Meyer, L., & Zensus, A. 2007, *A&A*, 469, 993
- Mužić, K., Schödel, R., Eckart, A., Meyer, L., & Zensus, A. 2008, *A&A*, 482, 173
- Müller, A., Keppler, M., Henning, T., et al. 2018, *A&A*, 617, L2
- Müller, T. G., Sekiguchi, T., Kaasalainen, M., Abe, M., & Hasegawa, S. 2005, *Astronomy and Astrophysics*, 443, 347
- Müller-Sánchez, F., Davies, R. I., Genzel, R., et al. 2009, *ApJ*, 691, 749
- Najita, J., Carr, J. S., & Mathieu, R. D. 2003, *ApJ*, 589, 931
- National Academies of Sciences, E. & Medicine. 2021, *Pathways to Discovery in Astronomy and Astrophysics for the 2020s*
- National Academies of Sciences, E. a. M. 2022, *Origins, Worlds, and Life: A Decadal Strategy for Planetary Science and Astrobiology 2023-2032* (Washington, DC: The National Academies Press)
- Neumayer, N., Cappellari, M., Reunanen, J., et al. 2007, *ApJ*, 671, 1329
- Nishiyama, S. & Schödel, R. 2013, *A&A*, 549, A57
- Nisini, B., Antoniucci, S., Alcalá, J. M., et al. 2018, *A&A*, 609, A87
- Nomura, H., Furuya, K., Cordiner, M. A., et al. 2022, arXiv e-prints, arXiv:2203.10863
- Norris, B. R. M., Tuthill, P. G., Ireland, M. J., et al. 2012, *Nature*, 484, 220
- Nortmann, L., Pallé, E., Salz, M., et al. 2018, *Science*, 362, 1388
- Nowak, M., Lacour, S., Lagrange, A. M., et al. 2020, *A&A*, 642, L2
- Nowotny, W., Aringer, B., Höfner, S., Gautschy-Loidl, R., & Windsteig, W. 2005, *A&A*, 437, 273
- Öberg, K. I. & Bergin, E. A. 2021, *Phys. Rep.*, 893, 1
- Öberg, K. I., Guzmán, V. V., Walsh, C., et al. 2021, *ApJS*, 257, 1
- Ohnaka, K. 2014, *A&A*, 561, A47
- Oliva, G. A. & Kuiper, R. 2020, *A&A*, 644, A41
- Oliveira, I., Olofsson, J., Pontoppidan, K. M., et al. 2011, *ApJ*, 734, 51
- Olofsson, J., Juhász, A., Henning, T., et al. 2012, *A&A*, 542, A90
- Oomen, G.-M., Van Winckel, H., Pols, O., et al. 2018, *A&A*, 620, A85
- Orton, G. S., Fletcher, L. N., Encrenaz, T., et al. 2015, *Icarus*, 260, 94
- O'Donoghue, J., Moore, L., Bhakyapaibul, T., et al. 2021, *Nature*, 596, 54, number: 7870 Publisher: Nature Publishing Group
- Paganini, L., Mumma, M. J., Gibb, E. L., & Villanueva, G. L. 2017, *The Astrophysical Journal Letters*, 836, L25
- Panić, O., Ratzka, T., Mulders, G. D., et al. 2014, *A&A*, 562, A101
- Parsa, M., Eckart, A., Shahzamanian, B., et al. 2017, *ApJ*, 845, 22

- Pascucci, I., Herczeg, G., Carr, J. S., & Bruderer, S. 2013, *ApJ*, 779, 178
- Pascucci, I. & Sterzik, M. 2009, *ApJ*, 702, 724
- Patel, R. I., Metchev, S. A., & Heinze, A. 2014, *ApJS*, 212, 10
- Pater, I. d., Kleer, K. d., & Ádámkovics, M. 2020, *The Planetary Science Journal*, 1, 29, publisher: IOP Publishing
- Pei ker, F., Eckart, A., & Ali, B. 2021a, *ApJ*, 918, 25
- Pei ker, F., Eckart, A., & Parsa, M. 2020a, *ApJ*, 889, 61
- Pei ker, F., Eckart, A., Sabha, N. B., Zaja ek, M., & Bhat, H. 2020b, *ApJ*, 897, 28
- Pei ker, F., Eckart, A., Zaja ek, M., Ali, B., & Parsa, M. 2020c, *ApJ*, 899, 50
- Pei ker, F., Eckart, A., Zaja ek, M., & Britzen, S. 2022, *ApJ*, 933, 49
- Pei ker, F., Zaja ek, M., Eckart, A., et al. 2021b, *ApJ*, 923, 69
- Perez, S., Dunhill, A., Casassus, S., et al. 2015, *ApJ*, 811, L5
- Perger, M., Moultaka, J., Eckart, A., et al. 2008, *A&A*, 478, 127
- Perrot, C., Baudoz, P., Boccaletti, A., et al. 2018, arXiv e-prints, arXiv:1804.01371
- Perryman, M., Hartman, J., Bakos, G.  ., & Lindegren, L. 2014, *ApJ*, 797, 14
- Petigura, E. A., Howard, A. W., & Marcy, G. W. 2013, *Proceedings of the National Academy of Science*, 110, 19273
- Petit dit de la Roche, D. J. M., Oberg, N., van den Ancker, M. E., et al. 2021, *A&A*, 648, A92
- Pfuhl, O., Gillessen, S., Eisenhauer, F., et al. 2015, *ApJ*, 798, 111
- Pinilla, P., Birnstiel, T., Ricci, L., et al. 2012, *A&A*, 538, A114
- Pinilla, P., Birnstiel, T., & Walsh, C. 2015a, *A&A*, 580, A105
- Pinilla, P., Klarmann, L., Birnstiel, T., et al. 2016, *A&A*, 585, A35
- Pinilla, P., Tazzari, M., Pascucci, I., et al. 2018, *ApJ*, 859, 32
- Pinilla, P., van der Marel, N., P  rez, L. M., et al. 2015b, *A&A*, 584, A16
- Pinilla, P. & Youdin, A. 2017, in *Astrophysics and Space Science Library*, Vol. 445, *Astrophysics and Space Science Library*, ed. M. Pessah & O. Gressel, 91
- Pinte, C., Price, D. J., M nard, F., et al. 2018, *ApJ*, 860, L13
- Pollack, J. B., Hubickyj, O., Bodenheimer, P., et al. 1996, *Icarus*, 124, 62
- Pomohaci, R., Oudmaijer, R. D., & Goodwin, S. P. 2019, *MNRAS*, 484, 226
- Pomohaci, R., Oudmaijer, R. D., Lumsden, S. L., Hoare, M. G., & Mendigut a, I. 2017, *MNRAS*, 472, 3624
- Pontoppidan, K. M., Blake, G. A., & Smette, A. 2011a, *ApJ*, 733, 84
- Pontoppidan, K. M., Blake, G. A., & Smette, A. 2011b, *ApJ*, 733, 84

- Pontoppidan, K. M., Blake, G. A., van Dishoeck, E. F., et al. 2008, *ApJ*, 684, 1323
- Pontoppidan, K. M., Dullemond, C. P., van Dishoeck, E. F., et al. 2005, *ApJ*, 622, 463
- Pontoppidan, K. M., Salyk, C., Bergin, E. A., et al. 2014, *Protostars and Planets VI*, 363
- Pontoppidan, K. M., Salyk, C., Blake, G. A., et al. 2010, *ApJ*, 720, 887
- Pontoppidan, K. M., Stapelfeldt, K. R., Blake, G. A., van Dishoeck, E. F., & Dullemond, C. P. 2007, *ApJ*, 658, L111
- Portilla-Revelo, B., Kamp, I., Rab, C., et al. 2021, arXiv e-prints, arXiv:2111.08648
- Prieto, M. A., Mezcua, M., Fernández-Ontiveros, J. A., & Schartmann, M. 2014, *MNRAS*, 442, 2145
- Protopapa, S., Boehnhardt, H., Herbst, T. M., et al. 2008, *Astronomy and Astrophysics*, 490, 365
- Qi, C., Öberg, K. I., Espaillat, C. C., et al. 2019, *ApJ*, 882, 160
- Qi, C., Öberg, K. I., Wilner, D. J., et al. 2013, *Science*, 341, 630
- Quanz, S. P., Amara, A., Meyer, M. R., et al. 2015a, *ApJ*, 807, 64
- Quanz, S. P., Amara, A., Meyer, M. R., et al. 2013, *ApJ*, 766, L1
- Quanz, S. P., Crossfield, I., Meyer, M. R., Schmalzl, E., & Held, J. 2015b, *International Journal of Astrobiology*, 14, 279
- Quanz, S. P., Ottiger, M., Fontanet, E., et al. 2022, *A&A*, 664, A21
- Rab, C., Kamp, I., Ginski, C., et al. 2019, *A&A*, 624, A16
- Rameau, J., Follette, K. B., Pueyo, L., et al. 2017, *AJ*, 153, 244
- Ramos Almeida, C., Alonso-Herrero, A., Esquej, P., et al. 2014, *Monthly Notices of the Royal Astronomical Society*, 445, 1130
- Ramos Almeida, C., Levenson, N. A., Alonso-Herrero, A., et al. 2011, *ApJ*, 731, 92
- Ramstedt, S., Mohamed, S., Vlemmings, W. H. T., et al. 2014, *A&A*, 570, L14
- Ramstedt, S., Vlemmings, W. H. T., Doan, L., et al. 2020, *A&A*, 640, A133
- Rappaport, S., Levine, A., Chiang, E., et al. 2012, *ApJ*, 752, 1
- Ratzka, T., Köhler, R., & Leinert, C. 2005, *A&A*, 437, 611
- Ratzka, T., Schegerer, A. A., Leinert, C., et al. 2009, *A&A*, 502, 623
- Ray, L. C. & Yates, J. N. 2021, in *Magnetospheres in the Solar System* (American Geophysical Union (AGU)), 485–498, section: 31 eprint: <https://onlinelibrary.wiley.com/doi/pdf/10.1002/9781119815624.ch31>
- Reggiani, M., Christiaens, V., Absil, O., et al. 2018, *A&A*, 611, A74
- Reggiani, M., Quanz, S. P., Meyer, M. R., et al. 2014, *ApJ*, 792, L23
- Regály, Z., Sándor, Z., Dullemond, C. P., & van Boekel, R. 2010, *A&A*, 523, A69
- Reid, M. J., Menten, K. M., Greenhill, L. J., & Chandler, C. J. 2007, *ApJ*, 664, 950

- Reidemeister, M., Krivov, A. V., Stark, C. C., et al. 2011, *A&A*, 527, A57
- Riaud, P. & Schneider, J. 2007, *A&A*, 469, 355
- Ribas, I., Bolmont, E., Selsis, F., et al. 2016, *A&A*, 596, A111
- Ribas, I., Tuomi, M., Reiners, A., et al. 2018, *Nature*, 563, 365
- Richardson, D. C., Leinhardt, Z. M., Melosh, H. J., Bottke, Jr., W. F., & Asphaug, E. 2002, Gravitational Aggregates: Evidence and Evolution, ed. W. F. Bottke, Jr., A. Cellino, P. Paolicchi, & R. P. Binzel, 501–515
- Rigley, J. K. & Wyatt, M. C. 2020, *MNRAS*, 497, 1143
- Rizzuto, A. C., Ireland, M. J., & Robertson, J. G. 2011, *MNRAS*, 416, 3108
- Roberge, A., Chen, C. H., Millan-Gabet, R., et al. 2012, *PASP*, 124, 799
- Rosario, D. J., Togi, A., Burtscher, L., et al. 2019, *ApJ* (accepted)
- Rosen, A. L. & Krumholz, M. R. 2020, *AJ*, 160, 78
- Rosen, A. L., Krumholz, M. R., McKee, C. F., & Klein, R. I. 2016, *MNRAS*, 463, 2553
- Rosotti, G. P., Juhasz, A., Booth, R. A., & Clarke, C. J. 2016, *MNRAS*, 459, 2790
- Roth, L., Boissier, J., Moullet, A., et al. 2020, *Icarus*, 350, 113925, arXiv: 2006.10193
- Ryde, N., Lambert, J., Richter, M. J., et al. 2015, in Astronomical Society of the Pacific Conference Series, Vol. 497, Why Galaxies Care about AGB Stars III: A Closer Look in Space and Time, ed. F. Kerschbaum, R. F. Wing, & J. Hron, 67
- Sahai, R., Morris, M. R., & Villar, G. G. 2011, *AJ*, 141, 134
- Salyk, C., Blake, G. A., Boogert, A. C. A., & Brown, J. M. 2011, *ApJ*, 743, 112
- Salyk, C., Pontoppidan, K., Corder, S., et al. 2014, *ApJ*, 792, 68
- Salyk, C., Pontoppidan, K. M., Blake, G. A., et al. 2008, *ApJ*, 676, L49
- Sana, H., de Mink, S. E., de Koter, A., et al. 2012, *Science*, 337, 444
- Sanhueza, P., Jackson, J. M., Zhang, Q., et al. 2017, *ApJ*, 841, 97
- Sargent, B. A., Forrest, W. J., Tayrien, C., et al. 2009, *ApJS*, 182, 477
- Sarzi, M., Allard, E. L., Knapen, J. H., & Mazzuca, L. M. 2007, *MNRAS*, 380, 949
- Scharf, C. & Menou, K. 2009, *ApJL*, 693, L113
- Schartmann, M., Ballone, A., Burkert, A., et al. 2015, *ApJ*, 811, 155
- Schartmann, M., Wada, K., Prieto, M. A., Burkert, A., & Tristram, K. R. W. 2014, *MNRAS*, 445, 3878
- Schaye, J., Crain, R. A., Bower, R. G., et al. 2015a, *MNRAS*, 446, 521
- Schaye, J., Crain, R. A., Bower, R. G., et al. 2015b, *MNRAS*, 446, 521
- Scheeres, D. J., Britt, D., Carry, B., & Holsapple, K. A. 2015, Asteroid Interiors and Morphology, ed. P. Michel, F. E. DeMeo, & W. F. Bottke, 745–766

- Schegerer, A. A., Wolf, S., Hummel, C. A., Quanz, S. P., & Richichi, A. 2009, *A&A*, 502, 367
- Schleicher, D. R. G. & Dreizler, S. 2014, *A&A*, 563, A61
- Schneiderman, T., Matrà, L., Jackson, A. P., et al. 2021, *Nature*, 598, 425
- Schwarz, H., Ginski, C., de Kok, R. J., et al. 2016, *A&A*, 593, A74
- Schworer, G., Lacour, S., Huélamo, N., et al. 2017, *ApJ*, 842, 77
- Schödel, R., Eckart, A., Mužić, K., et al. 2007, *A&A*, 462, L1
- Schödel, R., Morris, M. R., Muzic, K., et al. 2011, *A&A*, 532, A83
- Segura, A., Walkowicz, L. M., Meadows, V., Kasting, J., & Hawley, S. 2010, *Astrobiology*, 10, 751
- Shahzamanian, B., Eckart, A., Zajaček, M., et al. 2016, *A&A*, 593, A131
- Shannon, A., Mustill, A. J., & Wyatt, M. 2015, *MNRAS*, 448, 684
- Shepherd, D. S., Claussen, M. J., & Kurtz, S. E. 2001, *Science*, 292, 1513
- Showman, A. P., Fortney, J. J., Lian, Y., et al. 2009, *ApJ*, 699, 564
- Shuping, R. Y., Morris, M., & Bally, J. 2004, *AJ*, 128, 363
- Sibthorpe, B., Kennedy, G. M., Wyatt, M. C., et al. 2018, *MNRAS*, 475, 3046
- Simon, M. N., Pascucci, I., Edwards, S., et al. 2016, *ApJ*, 831, 169
- Sinclair, J. A., Orton, G. S., Fernandes, J., et al. 2019, *Nature Astronomy*
- Sing, D. K., Fortney, J. J., Nikolov, N., et al. 2016, *Nature*, 529, 59
- Skemer, A. J., Hinz, P. M., Esposito, S., et al. 2012, *ApJ*, 753, 14
- Skemer, A. J., Marley, M. S., Hinz, P. M., et al. 2014, *ApJ*, 792, 17
- Skemer, A. J., Morley, C. V., Zimmerman, N. T., et al. 2016, *ApJ*, 817, 166
- Smith, N., Hinkle, K. H., & Ryde, N. 2009a, *AJ*, 137, 3558
- Smith, R., Wyatt, M. C., & Haniff, C. A. 2012, *MNRAS*, 422, 2560
- Smith, R. L., Pontoppidan, K. M., Young, E. D., Morris, M. R., & van Dishoeck, E. F. 2009b, *ApJ*, 701, 163
- Snellen, I., de Kok, R., Birkby, J. L., et al. 2015, *A&A*, 576, A59
- Snellen, I. A. G., Brandl, B. R., de Kok, R. J., et al. 2014, *Nature*, 509, 63
- Snellen, I. A. G. & Brown, A. G. A. 2018a, *Nature Astronomy*, 2, 883
- Snellen, I. A. G. & Brown, A. G. A. 2018b, *Nature Astronomy*, 2, 883
- Snellen, I. A. G., de Kok, R. J., de Mooij, E. J. W., & Albrecht, S. 2010a, *Nature*, 465, 1049
- Snellen, I. A. G., de Kok, R. J., de Mooij, E. J. W., & Albrecht, S. 2010b, *Nature*, 465, 1049
- Socrates, A., Katz, B., Dong, S., & Tremaine, S. 2012, *ApJL*, 750, 106
- Sozzetti, A., Giacobbe, P., Lattanzi, M. G., et al. 2014, *MNRAS*, 437, 497

- Spake, J. J., Sing, D. K., Evans, T. M., et al. 2018, *Nature*, 557, 68
- Sparks, W. B. & Ford, H. C. 2002, *ApJ*, 578, 543
- Speagle, J. S., Steinhardt, C. L., Capak, P. L., & Silverman, J. D. 2014, *ApJS*, 214, 15
- Stalevski, M., Tristram, K. R. W., & Asmus, D. 2019, *MNRAS*, 484, 3334
- Stallard, T., Miller, S., Millward, G., & Joseph, R. D. 2001, *Icarus*, 154, 475
- Stark, C. C., Roberge, A., Mandell, A., & Robinson, T. D. 2014, *ApJ*, 795, 122
- Stevenson, K. B., Désert, J.-M., Line, M. R., et al. 2014, *Science*, 346, 838
- Stolker, T., Dominik, C., Avenhaus, H., et al. 2016, *A&A*, 595, A113
- Stone, J. M., Skemer, A. J., Hinz, P. M., et al. 2018, *AJ*, 156, 286
- Sturm, J. A., McClure, M. K., Harsono, D., et al. 2022, *A&A*, 660, A126
- Szulágyi, J., Binkert, F., & Surville, C. 2021, arXiv e-prints, arXiv:2103.12128
- Szulágyi, J., Dullemond, C. P., Pohl, A., & Quanz, S. P. 2019, *MNRAS*, 487, 1248
- Szulágyi, J., Morbidelli, A., Crida, A., & Masset, F. 2014, *ApJ*, 782, 65
- Sánchez-Monge, A., Cesaroni, R., Beltrán, M. T., et al. 2013, *A&A*, 552, L10
- Tabone, B., Rosotti, G. P., Cridland, A. J., Armitage, P. J., & Lodato, G. 2022, *MNRAS*, 512, 2290
- Takami, M., Fu, G., Liu, H. B., et al. 2018, *ApJ*, 864, 20
- Tan, J. C., Beltrán, M. T., Caselli, P., et al. 2014, *Protostars and Planets VI*, 149
- Tan, J. C., Kong, S., Butler, M. J., Caselli, P., & Fontani, F. 2013, *ApJ*, 779, 96
- Tazaki, R., Murakawa, K., Muto, T., Honda, M., & Inoue, A. K. 2021, *ApJ*, 921, 173
- Teague, R., Bae, J., & Bergin, E. A. 2019, *Nature*, 574, 378
- Teague, R., Bae, J., Bergin, E. A., Birnstiel, T., & Foreman-Mackey, D. 2018, *ApJ*, 860, L12
- Tenenbaum, E. D. & Ziurys, L. M. 2009, *ApJ*, 694, L59
- Terada, H. & Tokunaga, A. T. 2017, *ApJ*, 834, 115
- Terada, H., Tokunaga, A. T., Kobayashi, N., et al. 2007, *ApJ*, 667, 303
- Terada, H., Tokunaga, A. T., Pyo, T.-S., et al. 2012, *AJ*, 144, 175
- Testi, L., Skemer, A., Henning, T., et al. 2015, *ApJ*, 812, L38
- Thalmann, C., Janson, M., Garufi, A., et al. 2016, *ApJ*, 828, L17
- Thi, W. F., Kamp, I., Woitke, P., et al. 2013, *A&A*, 551, A49
- Thiabaud, A., Marboeuf, U., Alibert, Y., Leya, I., & Mezger, K. 2015, *A&A*, 574, A138
- Thompson, M. A., Urquhart, J. S., Moore, T. J. T., & Morgan, L. K. 2012, *MNRAS*, 421, 408
- Tielens, A. G. G. M. 1990, in *From Miras to Planetary Nebulae: Which Path for Stellar Evolution?*, ed. M. O. Mennessier & A. Omont, 186–200

- Todorov, K. O., Line, M. R., Pineda, J. E., et al. 2016, ApJ, 823, 14
- Trafton, L. M., Miller, S., Geballe, T. R., Tennyson, J., & Ballester, G. E. 1999, The Astrophysical Journal, 524, 1059, publisher: IOP Publishing
- Treu, T., Auger, M. W., Koopmans, L. V. E., et al. 2010, ApJ, 709, 1195
- Tsang, C. C. C., Spencer, J. R., Lellouch, E., et al. 2013, Icarus, 226, 1177
- Turbet, M., Leconte, J., Selsis, F., et al. 2016, A&A, 596, A112
- Tychoniec, Ł., Manara, C. F., Rosotti, G. P., et al. 2020, A&A, 640, A19
- Valencia-S., M., Eckart, A., Zajaček, M., et al. 2015, ApJ, 800, 125
- van Aarle, E., van Winckel, H., Lloyd Evans, T., et al. 2011, A&A, 530, A90
- van Boekel, R., Min, M., Leinert, C., et al. 2004, Nature, 432, 479
- van Boekel, R., Min, M., Waters, L. B. F. M., et al. 2005, A&A, 437, 189
- van Boekel, R., Waters, L. B. F. M., Dominik, C., et al. 2003, A&A, 400, L21
- van der Marel, N., Birnstiel, T., Garufi, A., et al. 2021, AJ, 161, 33
- van der Marel, N. & Mulders, G. D. 2021, AJ, 162, 28
- van der Marel, N., van Dishoeck, E. F., Bruderer, S., et al. 2016, A&A, 585, A58
- van der Marel, N., van Dishoeck, E. F., Bruderer, S., et al. 2013, Science, 340, 1199
- van der Marel, N., Williams, J. P., Ansdell, M., et al. 2018, ApJ, 854, 177
- van der Plas, G., van den Ancker, M. E., Waters, L. B. F. M., & Dominik, C. 2015, A&A, 574, A75
- van der Wielen, T. 2022, Master's thesis, Leiden Observatory
- van Dishoeck, E. F., Kristensen, L. E., Mottram, J. C., et al. 2021, A&A, 648, A24
- van 't Hoff, M. L. R., Persson, M. V., Harsono, D., et al. 2018, A&A, 613, A29
- Van Winckel, H. 2003, ARA&A, 41, 391
- Van Winckel, H. 2018, arXiv e-prints, arXiv:1809.00871
- van Winckel, H., Lloyd Evans, T., Briquet, M., et al. 2009, A&A, 505, 1221
- Vigan, A., Bonavita, M., Biller, B., et al. 2017, A&A, 603, A3
- Vigan, A., Otten, G. P. P. L., Muslimov, E., et al. 2018, in Society of Photo-Optical Instrumentation Engineers (SPIE) Conference Series, Vol. 10702, Ground-based and Airborne Instrumentation for Astronomy VII, ed. C. J. Evans, L. Simard, & H. Takami, 1070236
- Villanueva, G. L., Mumma, M. J., Novak, R. E., et al. 2013, Icarus, 223, 11
- Visser, R., Geers, V. C., Dullemond, C. P., et al. 2007, A&A, 466, 229
- Visser, R., van Dishoeck, E. F., Doty, S. D., & Dullemond, C. P. 2009, A&A, 495, 881
- Vollmer, B., Beckert, T., & Davies, R. I. 2008, A&A, 491, 441
- Vollmer, B., Schartmann, M., Burtscher, L., et al. 2018, A&A, 615, A164

- Vorobyov, E. I. & Basu, S. 2015, *ApJ*, 805, 115
- Vorobyov, E. I. & Elbakyan, V. G. 2018, *A&A*, 618, A7
- Vorobyov, E. I., Elbakyan, V. G., Takami, M., & Liu, H. B. 2020, *A&A*, 643, A13
- Wada, K., Schartmann, M., & Meijerink, R. 2016, *ApJ*, 828, L19
- Waelkens, C., Waters, L. B. F. M., de Graauw, M. S., et al. 1996, *A&A*, 315, L245
- Wallace, A. L., Ireland, M. J., & Federrath, C. 2021, *MNRAS*, 508, 2515
- Walsh, C., Juhász, A., Meeus, G., et al. 2016, *ApJ*, 831, 200
- Wang, J. J., Graham, J. R., Dawson, R., et al. 2018, *AJ*, 156, 192
- Wang, Z., Chakrabarty, D., & Kaplan, D. L. 2006, *Nature*, 440, 772
- Wheelwright, H. E., Bjorkman, J. E., Oudmaijer, R. D., et al. 2012, *MNRAS*, 423, L11
- Winn, J. N. & Fabrycky, D. C. 2015, *ARA&A*, 53, 409
- Wirick, S., Flynn, G. J., Keller, L. P., et al. 2009, *Meteoritics and Planetary Science*, 44, 1611
- Witzel, G., Eckart, A., Bremer, M., et al. 2012, *ApJs*, 203, 18
- Witzel, G., Ghez, A. M., Morris, M. R., et al. 2014, *ApJl*, 796, L8
- Witzel, G., Martinez, G., Hora, J., et al. 2018, *ApJ*, 863, 15
- Woitke, P. 2006, *A&A*, 460, L9
- Woitke, P., Kamp, I., Antonellini, S., et al. 2019, *PASP*, 131, 064301
- Woitke, P., Kamp, I., & Thi, W.-F. 2009, *A&A*, 501, 383
- Woitke, P., Min, M., Thi, W. F., et al. 2018, *A&A*, 618, A57
- Wold, M., Lacy, M., Käufl, H. U., & Siebenmorgen, R. 2006, *A&A*, 460, 449
- Wölfer, L., Facchini, S., Kurtovic, N. T., et al. 2021, *A&A*, 648, A19
- Wolff, S. G., Ménard, F., Caceres, C., et al. 2017, *AJ*, 154, 26
- Wolszczan, A. & Frail, D. A. 1992, *Nature*, 355, 145
- Wooden, D. H., Ishii, H. A., & Zolensky, M. E. 2017, *Philosophical Transactions of the Royal Society of London Series A*, 375, 20160260
- Wunderlich, F., Scheucher, M., Grenfell, J. L., et al. 2021, *A&A*, 647, A48
- Wyatt, M. C. 2008, *ARA&A*, 46, 339
- Wyatt, M. C., Kral, Q., & Sinclair, C. A. 2020, *MNRAS*, 491, 782
- Wyatt, M. C., Smith, R., Greaves, J. S., et al. 2007, *ApJ*, 658, 569
- Yao, Z. H., Grodent, D., Kurth, W. S., et al. 2019, *Geophysical Research Letters*, 46, 11632
- Young, E. D., Gounelle, M., Smith, R. L., Morris, M. R., & Pontoppidan, K. M. 2011, *ApJ*, 729, 43
- Yuan, F., Quataert, E., & Narayan, R. 2003, *ApJ*, 598, 301

- Yuan, F., Quataert, E., & Narayan, R. 2004, ApJ, 606, 894
- Yusef-Zadeh, F. & Morris, M. 1987, ApJ, 322, 721
- Yusef-Zadeh, F., Morris, M., & Chance, D. 1984, Nature, 310, 557
- Yusef-Zadeh, F., Wardle, M., Bushouse, H., Dowell, C. D., & Roberts, D. A. 2010, ApJL, 724, L9
- Yvart, W., Cabrit, S., Pineau des Forêts, G., & Ferreira, J. 2016, A&A, 585, A74
- Zajaček, M., Britzen, S., Eckart, A., et al. 2017, A&A, 602, A121
- Zajaček, M., Britzen, S., Eckart, A., et al. 2017, A&A, 602, A121
- Zajaček, M., Eckart, A., Karas, V., et al. 2016, MNRAS, 455, 1257
- Zajaček, M., Karas, V., & Eckart, A. 2014, A&A, 565, A17
- Zhang, K., Booth, A. S., Law, C. J., et al. 2021, ApJS, 257, 5
- Zhang, Q., Wang, K., Lu, X., & Jiménez-Serra, I. 2015, ApJ, 804, 141
- Zhen, J., Castellanos, P., Paardekooper, D. M., et al. 2015, ApJ, 804, L7
- Zhen, J., Castellanos, P., Paardekooper, D. M., Linnartz, H., & Tielens, A. G. G. M. 2014, ApJ, 797, L30
- Zhu, Z. 2015, ApJ, 799, 16
- Zhukovska, S., Dobbs, C., Jenkins, E. B., & Klessen, R. S. 2016, ApJ, 831, 147
- Zinnecker, H. & Yorke, H. W. 2007, ARAA, 45, 481
- Zurlo, A., Mesa, D., Desidera, S., et al. 2018, MNRAS, 480, 35
- Öberg, K. I., Murray-Clay, R., & Bergin, E. A. 2011, ApJL, 743, L16